An improved 3D embedded beam element with explicit interaction surface

A study into the improvement of a numerical modelling technique that enables simplified modelling of pile foundations

C.M. Smulders

Delft University of Technology

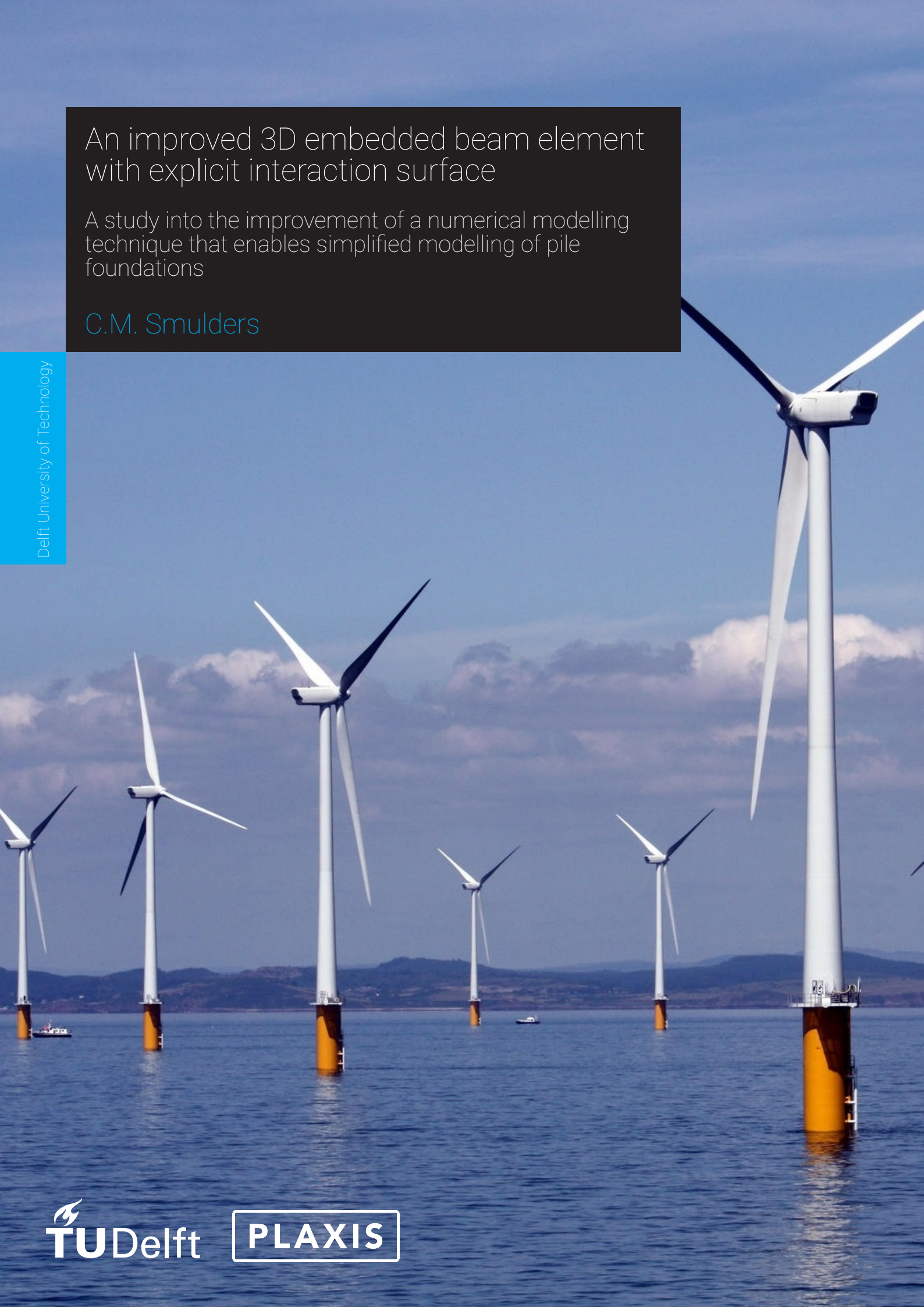

TU Delft PLAXIS

An improved 3D embedded beam element with explicit interaction surface

A study into the improvement of a numerical modelling technique that enables simplified modelling of pile foundations

by

C.M. Smulders

to obtain the degree of Master of Science
in Civil Engineering - Structural Mechanics
at the Delft University of Technology.

to be defended publicly on Friday June 1, 2018 at 4 p.m.

Student number:	4211855	
Project duration:	September 4, 2017 – June 1 2018	
Thesis committee:	Prof. dr. ir. L. J. Sluys,	TU Delft, chairman
	Dr. ir. R. B. J. Brinkgreve,	TU Delft & Plaxis BV
	Ir. J. M. Houben,	TU Delft
	Dr. S. Hosseini,	Plaxis BV

TU Delft Delft University of Technology

PLAXIS

Preface

This thesis is written as the final work to complete the Master's programme Structural Engineering with specialisation Structural Mechanics of the faculty of Civil Engineering at Delft University of Technology. The subject for this research was formulated in cooperation with Plaxis BV. They provided me with the means necessary to achieve my research goals and supported me throughout the entire duration of the research.

This report would not lie here in front of you without the help and support of many people. I would like to thank my graduation committee first for their guidance and supervision. First and foremost I would like to thank my daily supervisor Saman Hosseini, who's been there for me during all my ups and downs. I wouldn't have accomplished the same without his guidance and I'm going to miss our talks and laughs. Second, I know that I can count myself very lucky to have had Ronald Brinkgreve in my graduation committee. His involvement and interest in my research was unparalleled and he pushed me to learn and achieve more than I would have thought possible. His enthusiasm for geo engineering motivated me to dig deeper again and again. The experienced vision of Bert Sluys was indispensable and his comments and remarks have often helped me focus on the right details. And last but not least, I would like to thank Lambert Houben for listening to all my presentations and asking the right questions when necessary.

Furthermore, I would like to thank my colleagues at Plaxis BV. Most importantly, the assistance of Paul Bonnier to help me understand all the dark and incomprehensible parts of the PLAXIS source code. He has saved me multiple times from nasty bugs and your knowledge of soil mechanics has often helped me find the source of my problems. Also, many thanks to all the interns that I have seen coming and going at Plaxis and the group of colleagues from 'upstairs' that were there during lunch breaks or after work. I have enjoyed working with them a lot and it wouldn't have been the same without them.

Last, I would like to thank my family and friends for their unconditional love and support throughout my studies. Especially Chris, for listening to my unintelligible stories and all my (often unfounded) complaints. I have enjoyed my years as a student so much because of all of you and I wouldn't have missed it for the world.

C.M. Smulders
Delft, June 2018

Abstract

Numerical modelling of pile foundations can be done in several ways. In commercial finite element packages two main options are available; using volume elements with interface elements between the pile and soil domains and the embedded beam approach. The embedded beam element was first proposed by Sadek and Shahrour (2004) and considers a beam element that can cross a solid element at any arbitrary location with any arbitrary inclination. This has several advantages to the volume pile method, such as the need for fewer elements and the mesh uncoupling of the pile and soil, which make this method much more efficient and leads to a significant reduction in calculation time. However, the embedded beam element also deals with a number of limitations and drawbacks. This research focusses on overcoming the mesh sensitivity, which is caused by the stress singularity that is introduced in the soil by the beam element. Also, the inability to take into account the pile surface will be resolved, aiming to improve the lateral pile-soil interaction.

The idea of Turello et al. (2016a,b) of an embedded beam element with explicit interaction surface is extended and generalised leading to a new embedded beam formulation. In the proposed model the beam displacements at the interaction surface are obtained by a mapping scheme that takes into account Timoshenko beam theory and which is generalised to model inclined piles as well. A constitutive equation that describes the relation between the interface stresses and relative displacements between the pile and soil is defined along the shaft and at the foot of the pile. Along the shaft of the pile a shear stress limit is defined based on the Mohr-Coulomb failure criterion in order to incorporate plasticity in lateral direction. Furthermore, a more practical and efficient assembly procedure is proposed.

The components of the proposed model are evaluated separately in a parametric study. First of three interesting findings is the fact that the proposed foot interface leads to a stiffer response of the embedded beam model in case of axial loading. Reduction of the foot interface stiffness is proposed to obtain a response that is equivalent to the existing embedded beam method and measurement data. A short parameter study yields the expectation that the foot stiffness in the proposed method is one order of magnitude lower than the foot stiffness in the existing embedded beam element. However, it is recommended to define a generally applicable definition of the foot interface stiffness in future research.

Second, an investigation into the proposed method to include plasticity in lateral direction along the shaft of the pile has proven to yield an incorrect failure mechanism. The ambition to model soil slippage around the pile is not met.

At last, evaluation of the mesh sensitivity in case of an axially loaded pile proofs that the proposed embedded beam element is considerably less mesh sensitive than the existing embedded beam model. Therefore, the proposed model clearly solves one of the two most important drawbacks of the existing embedded beam model.

Next, the proposed method is applied to a practical application; a laterally loaded offshore monopile foundation. The response of the proposed embedded beam model is stiffer than the response of the existing embedded beam model. A stiffer behaviour is in better agreement with a full 3D model without interfaces. Especially near the foot of the pile a stiffer response is considered a great improvement.

However, the proposed embedded beam model is unable to capture lateral interface behaviour equivalent to a full 3D model with interfaces. In addition, the computation time of the proposed embedded beam model is similar to the computation time of the full 3D model. The embedded beam principle aims to provide a more efficient modelling technique than a full 3D model, which is not achieved with the proposed formulation. Therefore, the proposed embedded beam element is not suitable to replace full 3D models yet.

In conclusion, a significant improvement in terms of mesh sensitivity for axially loaded piles and an improvement in the overall response of laterally loaded piles is obtained, considering the response without interfaces. It is recommended to investigate alternative methods to include lateral plasticity and to optimise the code in order to reduce the computation time. Furthermore, the description of the interaction surface opens up many new possibilities for future research, such as modelling the true cross-section shape.

Contents

List of Symbols

Symbols and abbreviations used in the text are defined below. Some symbols are used to represent different quantities at different places. In the text the symbols are defined to avoid misinterpretation.

Bold capital symbols indicate a matrix and bold lower case symbols indicate a vector, otherwise the symbol signifies a scalar quantity or function. When necessary, a distinction between local and global coordinate systems is made by a sub- or superscript and by definition in the text.

List of Latin symbols

Symbol	Description	Units
A	Area of the pile cross-section, factor for the loading condition	m^2, -
$\boldsymbol{A}, \boldsymbol{S}$	Transformation matrices used in the Turello et al. (2016a,b) formulation of the embedded beam element	-
$\boldsymbol{B}$	Deformation matrix that contains the beam and soil interpolation functions	-
C_1, C_2, C_3	Coefficients depending on the friction angle	-
D	Pile diameter	m
$\boldsymbol{D^e}$	Elastic material stiffness matrix of the interface	kN/m^2, kN/m^3
D_f, D_F	Stiffness terms that describe the relation between vertical displacement and distributed and point load	kN/m^3, kN/m
$\widetilde{D}_{ijkl}$	Elastic constitutive relation between total strain and stress rate containing a continuous and discontinuous contribution (CLED)	kN/m^2
E, E_p	Soil and pile Young's modulus respectively	kN/m^2
E_{50}^{ref}	Secant stiffness of Hardening soil model	kN/m^2
$E_{oed,i}$	Oedometer stiffness of interface element	kN/m^2
E_{oed}^{ref}	Oedometer stiffness for Hardening soil model	kN/m^2
E_{ur}^{ref}	Unloading-reloading stiffness of Hardening soil model	kN/m^2
F_{foot}	Force at the foot of the pile	kN
F_{max}	Ultimate base resistance	kN
G^*, G_c	Modified and characteristic shear modulus	kN/m^2
G_{soil}, G_i	Shear modulus of the soil and interface respectively	kN/m^2
H	Horizontal force applied at the top of the pile	kN
$\boldsymbol{H}$	New beam interpolation matrix for the explicit interaction surface	-
$\boldsymbol{H_u}, \boldsymbol{H_f}$	Mapping matrices that map the nodal beam displacements (u) and forces (f) to the interaction surface	-
I_2, I_3	Moments of inertia of the pile cross-section in the two directions perpendicular to the pile axis	m^4
I_{avg}	Average moment of inertia of the pile cross-section	m^4
J	Dimensionless empirical constant	-
$\boldsymbol{J}$	Jacobian matrix	-
$\boldsymbol{K}$	Global stiffness matrix of the total FE model	kN/m
$\boldsymbol{K_b}$	Beam stiffness matrix	kN/m
$\boldsymbol{K_{bs}}$	Beam stiffness matrix expressed in solid kinematics	kN/m
$\boldsymbol{K^e}$	Element stiffness matrix	kN/m
K_{foot}	Interface stiffness at the foot of the pile	kN/m
K_p, K_a	Coefficients of passive and active earth pressure	-
K_s, K_n, K_t	Axial (s), normal (n) and transversal (t) interface stiffness along the shaft of the pile	kN/m^2, kN/m^3
L	Length of the pile	m

Symbol	Description	Units
L_c	Critical length	m
M	Moment applied at the top of the pile	kNm
M_i	Local enrichment function of node i (XFEM)	-
M_p	Plastic bending moment in pile	kNm
$\boldsymbol{M_u}, \boldsymbol{M_f}$	Mapping matrices that map the displacement (u) and force (f) field at the beam axis to the interaction surface	-
N_i^*	Partition of unity function of node i (XFEM)	-
$\boldsymbol{N^s}, \boldsymbol{N^b}$	Interpolation matrices containing the shape functions of the solid (s) or beam (b) element	-
$\boldsymbol{dN_i^s}$	Gradient of the soil shape function at node i	m^{-1}
N_i	Shape function of node i	-
$\boldsymbol{N_s^{int}}$	Transformation matrix combining nodal soil displacements	-
$\boldsymbol{N_u}, \boldsymbol{N_f}$	Interpolation matrices that define the beam displacement (u) and force (f) field at the beam axis in terms of nodal displacements	-
$O\left(h^2\right)$	Second order truncation error	m
P_{ab}, P_{bc}	Equivalent resistance forces of soil reactions working on the pile	kN
P_u	Ultimate soil force working on the pile per unit length	kN/m
R	Pile radius	m
R_{eq}	Equivalent pile radius	m
R_{inter}	Strength reduction factor for the interface in PLAXIS 3D	-
$\boldsymbol{R_\varphi}$	Rotation matrix that describes transformation from the local coordinate system at the beam axis to the local coordinate system at the explicit interaction surface	-
$\boldsymbol{T}$	Transformation matrix that describes transformation from global to local coordinate system	-
$T_{bot,max}$	Ultimate skin resistance at the foot of the pile	kN/m
$T_{top,max}$	Ultimate skin resistance at the head of the pile	kN/m
$\boldsymbol{V_1}, \boldsymbol{V_2}, \boldsymbol{V_3}$	Local unit vectors in ξ,η,ζ-coordinate system	-
$\boldsymbol{W_2}, \boldsymbol{W_3}$	Matrices used to transform the cross products of $\boldsymbol{\theta}$ and $\boldsymbol{V_2}$, $\boldsymbol{V_3}$ to dot products	-
$\boldsymbol{X_m}$	Vector containing the coordinates of the beam axis	m
$\boldsymbol{X_r}, \boldsymbol{X_p}$	Vector describing the mapping from the beam axis to the interaction surface in case of a circular cross-section (m) or rectangular (p)	m
Z_r	Transition depth	m
$\boldsymbol{\Delta a}$	Nodal displacement jump between the beam and soil at the embedded beam interface	m
$\boldsymbol{a^b}, \boldsymbol{a^s}$	Nodal beam (b) and soil (s) DOFs	m
$\boldsymbol{a^e}$	Nodal displacement vector, containing both the nodal beam and soil displacements and beam rotations	m
a_i	Unknown displacement in node i	m
b	Dimension of the beam in local ζ-direction (width)	m
b_i	Additional unknown displacement in node i (XFEM)	m
c_{soil}, c_i	Cohesion of the soil and interface	kN/m^2
c_u	Undrained shear strength of the soil	kN/m^2
e	Eccentricity of applied force, error at the end of an iteration	m, -
f	Distributed load over an area	kN/m^2
$\boldsymbol{f_{ex}}$	External force vector	kN
$\boldsymbol{f_{in}}$	Internal force vector	kN
$\boldsymbol{f^{int}}$	Interaction force field at the interaction surface	kN
h	Distance between ground level and plastic hinge in pile, dimension of the beam in local η-direction (height)	m
h_i	Thickness of the narrow domain (ring) around the pile	m
k	Spring stiffness in the subgrade reaction approach	kN/m^3

Symbol	Description	Units
l_{ab}, l_{bc}	Distance between ground level and height of equivalent resistance forces P_{ab} and P_{bc}	m
m	Factor that controls the change of stiffness related to the stress level	-
n	Gradient of the average ultimate soil pressure	kN/m^3
$\boldsymbol{n}$	Normal vector	-
$\boldsymbol{p_{bs}}$	Nodal beam interaction load vector in terms of solid kinematics	kN
$\boldsymbol{p_b}, \boldsymbol{p_s}$	Nodal beam (b) and solid (s) interaction load vectors	kN
$\boldsymbol{p^{es}}, \boldsymbol{p^{eb}}$	External forces working on the soil (s) and beam (b) nodes	kN
$\boldsymbol{p^{int}}$	Nodal interaction forces at the interaction surface	kN
$\boldsymbol{q^{int}}$	Nodal interaction force vector introduced by displacement jump	kN
s	Scaling factor	-
s, n, t	Local Cartesian coordinates	m
$\boldsymbol{t}$	Skin tractions along the beam axis	kN/m
t_i	Virtual thickness of the interface element	m
$\boldsymbol{t^{int}}$	Interaction force field at the interaction surface introduced by displacement jump	kN
$\boldsymbol{t^{int*}}$	Equivalent reduced interaction force vector	kN
$t_{s,max}$	Ultimate shear traction at the interface	kN/m
t_s, t_n, t_t	Shear (s), normal (n) and transversal (t) tractions in the interface along the shaft	kN/m
$\boldsymbol{\Delta u}^*$	Equivalent reduced displacement jump vector	m
$\boldsymbol{u_b^e}$	Nodal beam displacements (excluding beam rotations)	m
$\boldsymbol{u_b}, \boldsymbol{u_s}$	Beam (b) and soil (s) displacements at the embedded beam interface	m
$u_{foot}^{b,s}$	Displacement at the foot of the pile of the beam (b) or soil (s) element	m
$\boldsymbol{u_m}$	Beam displacements at the beam axis	m
$\boldsymbol{u_{rel}}, \boldsymbol{\Delta u}$	Relative displacement/displacement jump between the beam and soil at the embedded beam interface	m
$\boldsymbol{u_s^\omega}$	Solid displacement field evaluated over the interaction surface ω and mapped onto the beam axis	m
u_x, u_y, u_z	Displacement fields in x,y,z-directions respectively	m
w_i	Weights used in the Newon-Cotes integration scheme	-
x, y, z	Global Cartesian coordinates	m

List of Greek symbols

Symbol	Description	Units
Γ_{foot}	Multiplier on the foot interface stiffness, also denoted as FacKfoot	-
Γ_s, Γ_n	Multiplier for the axial and normal interface stiffness	-
Δ_s, Δ_n	Input values that are added to the axial and normal interface stiffness	-
α_j	Enriched DOF that is added to interface node j (IGFEM)	m
β_k	Enrichment DOF at node k representing the size of the jump in the discontinuity (DE-FEM)	m
γ	Rotation due to shear deformations in the beam, unit weight of beam	°, kN/m^3
$\gamma_{(un)sat}, \gamma'$	Unit weight below/above phreatic level and effective unit weight	kN/m^3
$\dot{\varepsilon}_{ij}$	Total strain rate (CLED)	s^{-1}
$\dot{\tilde{\varepsilon}}_{ij}, \dot{\tilde{\varepsilon}}_{ij}$	Continuous and discontinuous part of total strain rate (CLED)	s^{-1}
$\boldsymbol{\varepsilon_i}$	Strains in the interface	-
$\boldsymbol{\theta}$	Vector containing beam rotations around x,y,z-axes	°
$\boldsymbol{\theta^e}$	Vector containing nodal beam rotations around x,y,z-axes	°
θ_x	Beam rotation around x-axis	°
ν, ν_i	Poisson's ratio of the soil and interface	-
ξ, η, ζ	Local, iso-parametric coordinates	m

Symbol	Description	Units
ρ_c	Parameter reflecting the degree of homogeneity in the soil stiffness	-
σ_1, σ_3	Major and minor principal stresses in the soil	kN/m^2
σ'_3	Minor effective principal stress	kN/m^2
$\dot{\sigma}_{ij}$	Total stress rate (CLED)	kN/m^2 s^{-1}
σ_{foot}	Stresses in the foot interface	kN/m^2
$\boldsymbol{\sigma_i}$	Stresses in the interface along the shaft of the pile	kN/m^2
σ_n^{avg}	Average normal stress at the beam axis	kN/m^2
σ'_n, σ'_t	Effective stress in the soil around the pile perpendicular to the pile axis	kN/m^2
$\sigma_s, \sigma_n, \sigma_t$	Stresses at the interaction surface in the local coordinate system	kN/m^2
$\boldsymbol{\sigma'_v}$	Effective vertical stress in the soil	kN/m^2
τ	Shear stress in the interface	kN/m^2
φ	Angle between local ζ axis and point on the interaction surface	°
$\varphi_{soil}, \varphi_i$	Friction angle of the soil and interface	°
ϕ	Scalar level-set function	-
ϕ_j	Enrichment function for interface node j (IGFEM)	-
χ_k	Strong enrichment functions (DE-FEM)	-
ψ	Global enrichment function (IGFEM), dilatancy angle	-, °
ω, ω^e	The interaction surface around the beam (element)	m^2

List of abbreviations

Abbreviation	Description
API	American Petroleum Institute
CLED	Constitutive Law with Embedded Discontinuity
DE-FEM	Discontinuity-Enriched Finite Element Method
DEM	Discrete Element Method
DOF	Degree of freedom
EB	Embedded beam
FDM	Finite Difference Method
FE	Finite Element
FEM	Finite Element Method
FVM	Finite Volume Method
HS	Hardening soil (soil model)
IGFEM	Interface-Enriched Generalized Finite Element Method
MC	Mohr Coulomb (soil model)
MoDeTo	Monopile Design Tool
MPM	Material Point Method
NC	North Carolina
nCirDiv	Number of points that are considered at the explicit interaction surface
PISA	Pile Soil Analysis
VP	Volume pile
XFEM	Extended Finite Element Method, also known as Special FEM, Partition of Unity FEM (PUFEM) or Generalized FEM (GFEM)

1 Introduction

The use of pile foundation to secure structures and reduce hazards can be traced far back in time. In ancient times people used pile foundations especially on weak soils near rivers. Since food, water and transport are readily available near lake shores and rivers, people built complete piled settlements on these weak soils. Also later, cities such as Venice and Amsterdam are built entirely on pile foundations from the founding on.

Since the nineteenth century many new piling techniques evolved and improvements and new techniques are still being developed. Research in this area is now conducted by specialised engineers, who use advanced modelling techniques to predict and assess the settlement behaviour of single piles or complex pile groups. Accurate modelling of pile foundations can result in better designs in which the dimensions of the piles are optimised. This leads to possible reductions in material use and thereby in transportation and installation costs, see for instance the PISA project in Section G.1.

Many techniques to model the mechanical behaviour and capacity of pile foundations in a soil medium have been developed and used in the past. These methods range from simple methods, such as techniques based on the Winkler's hypothesis that models the soil as independent springs along the pile (Appendix A), to very complex finite element techniques, taking into account the non-linear behaviour of the pile-soil interaction.

Nowadays, finite element models are most frequently used. Early finite element methods to model pile foundations consider piles modelled as solid elements. These elements can be assigned concrete or steel properties and are surrounded by solid elements representing the soil. It is possible to model interface elements between the pile and soil elements in order to capture slip between the two more accurately. In this report this method is referred to as the volume pile method. It provides accurate results, but is inefficient; in addition to the large number of elements that is generated, the meshing process is more difficult due to the required mesh alignment between pile and soil. This makes this method unnecessarily time consuming.

To solve this problem, Sadek and Shahrour (2004) proposed a three-dimensional embedded beam element. The beam is now modelled as a line element with zero thickness. This embedded beam element does not influence or depend on the mesh of the surrounding solid elements, but can cross a solid element at any arbitrary location with any arbitrary inclination. Furthermore, they introduce interface elements to describe the possibility of the occurrence of slip and separation between the soil and the pile in axial direction.

Based on this formulation Plaxis implemented embedded beam elements in PLAXIS 2D and 3D, that models pile foundations as line beam elements.

1.1. Problem statement

Although the embedded beam element is outstanding in its ability to simplify the modelling of pile foundations, the existing embedded beam element in PLAXIS 3D still deals with a couple of limitations and drawbacks.

An important limitation of the existing embedded beam element is that a line element can not distinguish between the two directions perpendicular to the axis of the beam (normal and transversal to the pile circumference). Therefore, the pressure differences along the circumference cannot be taken into account accurately in the interaction between pile and soil.

Another problem that influences the results significantly is the fact that a line element introduces stress singularities along the pile and at the foot of the pile. This causes the embedded beam element to be mesh sensitive. Consequently, the embedded beam formulation does not converge to the exact solution when the mesh is refined.

Furthermore, the existing embedded beam element is primarily intended for axially loaded piles, but users of finite element software have started using the embedded beam elements also for laterally loaded piles. The inability to distinguish between the two directions perpendicular to the beam axis makes it impossible to describe this lateral behaviour accurately. Also, no interface is defined in lateral direction, so no slippage of the soil around the pile can be modelled.

Applications in which a lateral loading component arises are getting more common. Lateral loading on foundation piles may be caused by an external load or by movement of the soil surrounding the pile. The first type is called 'active' loading, as the soil resists the load. An example of actively loaded pile foundations are monopile foundations of offshore wind turbines, since wind and wave loading are dominant. The second type is called 'passive' loading, as the soil movements cause stresses in the pile. Passive loading on piles can be caused by unequal loading of the soil around the pile by, for instance, an embankment or excavation pit.

In earlier research (Engin et al., 2007) the problems concerning stress singularities and even premature failure due to numerical problems have been identified and an elastic zone approach was proposed to solve them. This elastic zone approach forces the soil that lies inside the pile radius to remain elastic. However, this has not solved the problems entirely. This research will address the remaining problems. There are four problems that this research will focus on:

- The most important problem is the remaining mesh sensitivity. When the mesh is refined, the results of a finite element model should converge to the exact solution. This does not happen in the existing embedded beam formulation, not even for perfectly vertical piles with axial loading. The non-convergence is caused by the fact that a line element introduces stress singularities in the soil which become infinitely large when the soil mesh size goes to zero.
- The embedded beam element is supposed to be used for axially loaded piles only. Therefore, the lateral pile-soil interaction has never been given much attention. This research aims to improve this behaviour.
- The possibility to model slip of the soil along the pile in lateral direction will be investigated.
- In the existing embedded beam implementation, it is possible to choose between different cross-section types, but the real cross-section shape is not taken into account. Instead of using the real cross-section shape, an equivalent radius is computed and used. This research will look into possibilities to model the cross-section shape more accurately.

1.2. Aim of the research

Based on the idea of an embedded beam element with an explicit interaction surface by Turello et al. (2016a), a new three-dimensional embedded beam formulation is developed. This new formulation aims to solve the problems concerning mesh sensitivity and improve the lateral deformation behaviour of the pile-soil model.

The formulation of Turello et al. (2016a) only includes the possibility to model perfectly vertical piles. For inclined piles, different mapping functions need to be defined. This research proposes a new formulation that is generalised to be able to model inclined piles as well. Additionally, instead of using the Euler-Bernoulli hypothesis, the embedded beam formulation proposed in this report takes into account shear deformations based on the Timoshenko beam theory.

Not only an explicit interaction surface along the shaft of the pile is considered, but also at the foot of the pile. In addition, possibilities to incorporate lateral plasticity along the shaft of the pile are investigated. Turello et al. (2016a) proposed two methods (one based on beam kinematics and one on solid kinematics) to model lateral deformation behaviour more accurate. However, these methods are not readily applicable to the PLAXIS 3D embedded beam elements and the possibility to regulate the interface strength by means of one input parameter (R_{inter}) is not taken into account.

The final proposed new embedded beam formulation is implemented in PLAXIS 3D by the development of new subroutines that can be linked to the existing kernel. Subsequently, the new embedded beam model is validated and the influence of relevant parameters is investigated.

The objective of this research is therefore to improve the existing formulation of the three-dimensional embedded beam element, dealing with the issues of

mesh sensitivity

and unrealistic lateral pile-soil interaction behaviour

by developing a new formulation of the three-dimensional embedded beam element with an explicit interaction surface, that has

improved interface behaviour around the shaft and at the foot,

takes into account Timoshenko beam theory,

and is generalised for possibly inclined piles

and different cross-section shapes

by implementing a prototype and validating it by comparing it to

existing FE models and

available measurement data.

1.3. Research question

The main research question that is addressed in this research is:

How can the original embedded beam element be improved and generalised in order to overcome its limitations and drawbacks?

Several sub-questions are formulated for every phase of the research:

Literature review

- Which numerical modelling techniques to model discontinuities exist and how does the embedded beam element relate to them?
- What are the fundamentals and current state-of-the-art in embedded beam elements?
- How is the existing three-dimensional embedded beam element modelled in PLAXIS 3D and what are its limitations?

Model development

- How can the pile-soil interaction be modelled on the explicit interaction surface in a generalised manner?
- How can the stress singularity at the foot of the pile be solved?
- How can lateral plasticity (slippage) be modelled at the interaction surface and what are appropriate limits for the stress components in the interface?

Parametric study

- What is the best method to calculate the soil displacements and stresses on the interaction surface in terms of accuracy?
- Which of the proposed lateral plasticity methods performs best?
- What are appropriate values for the interface stiffnesses in the new model?
- To what extend is the proposed model an improvement compared to existing FE models?

Application

- How well does the proposed model perform compared to the real behaviour (case study)?

1.4. Scope

- This research will focus on the three-dimensional embedded beam implementation in PLAXIS 3D. Other FE software packages may have variations of an embedded beam element, such as FEA DIANA with bond-slip embedded reinforcements. Though, in order to limit the span of this research, the focus will only be on the formulation and implementation in PLAXIS 3D. Nonetheless, the proposed embedded beam element is generally applicable.

- The focus of this research is on investigating the capabilities, performance and potential of the new embedded beam formulation with explicit interaction surface. Therefore, the goal is not to come to a final implementation, but just a prototype which still needs additional verification and validation. Also, code optimisation or similar activities are not part of this research.

- Cyclic loading has a negative effect on the soil bearing capacity (Offshore Standard DNV-OS-J101, 2010) and therefore also on the bearing capacity of the pile. However, this type of loading will not be considered in this research. The focus will be on static loading.

- In this research only active lateral loading will be considered in order to limit the complexity of the research.

- In this research the proposed embedded beam element is only validated for single pile foundations. Pile group behaviour is not evaluated.

- One of the existing limitations in the current implementation of the three-dimensional embedded beam element in PLAXIS 3D is the inability to take into account the influence of installation effects. This limitation will not be part of this research.

- Other FE models that will be used for comparison are the existing embedded beam element in PLAXIS 3D and the volume pile method described in Section 4.4.

1.5. Research approach and outline of the report

The structure of the report follows the three main topics of the research; Part I of the report contains the literature study; Part II explains the theory and implementation of the proposed embedded beam element; Part III presents results of simple validation cases, which lead to conclusions on certain methods and parameters; Part IV considers the evaluation of a case study model to which the embedded beam element is applied.

Part I: Literature Review

In this phase a desk research, specifically a literature survey, is carried out to gain insight in all existing knowledge and theories concerning the subject. This part of the report is gradually zooming in on the real topic. First, a broader view of discontinuity modelling is presented (Chapter 2); different methods that are available to model discontinuities are explained, and features of the embedded beam concept are compared to them. Second, the original embedded beam element as proposed by Sadek and Shahrour (2004) is presented, followed by a recent publication that proposes a new embedded beam formulation that considers an explicit interaction surface (Chapter 3). At last, a closer look is taken at the existing embedded beam element implementation in PLAXIS 3D in Chapter 4.

In this literature survey, all problems and limitations of the existing embedded beam element are identified. Additionally, possible methods to improve the existing formulation are presented and investigated.

Part II: Model Development

The idea of an explicit interaction surface (Turello et al., 2016a,b) is extended and incorporated in the existing embedded beam formulation in PLAXIS 3D. The theory for the new embedded beam formulation is presented in Chapter 5. The formulation is divided in the kinematics, constitutive model and equilibrium equations of the element. In addition, a distinction is made between the shaft and foot interface.

Part III: Parametric Study

This phase focusses on the validation of the new implementation of the three-dimensional embedded beam element with explicit interaction surface. A distinction is made between axially (Chapter 6) and laterally (Chapter 7) loaded piles. First, the influence of the different components of the new formulation are evaluated

separately in order to make a choice for the most favourable methods. Subsequently, the performance of the complete proposed embedded beam formulation is evaluated for simple test cases.

Axial loading

In case of an axially loaded model, first the different methods to obtain the soil displacements are compared and then the influence of the foot interface is evaluated separately. In addition, the influence of the incorporation of lateral plasticity in the interface along the shaft is evaluated for axially loaded models. The incorporation of lateral components shouldn't influence the results of an purely axially loaded model.

Furthermore, the performance of the complete new embedded beam element is evaluated by means of a simple test case. Special attention is given to the skin traction evolution and foot resistance mobilisation.

Lateral loading

In case of a laterally loaded model the performance of the incorporation of lateral plasticity is evaluated separately.

Furthermore, the relative improvement of the new embedded beam model compared to the existing one and the volume pile method is evaluated, while varying certain model parameters. Also, a laterally loaded inclined pile model is evaluated in order to verify if the generalisation does indeed work and yields accurate results.

Part IV: Application

At last, a more complex case study model is used to validate the proposed embedded beam element (Chapter 8). A realistic model of a monopile foundation of an offshore wind turbine with a very large diameter is evaluated. The deformation behaviour, force distribution, mesh sensitivity and computation time are elaborated.

Part V: Conclusions & Recommendations

This part will sum up all conclusions that are drawn during the research based on obtained results. The research question and the sub-questions are answered. In addition, an overview of all recommendations for further research is presented.

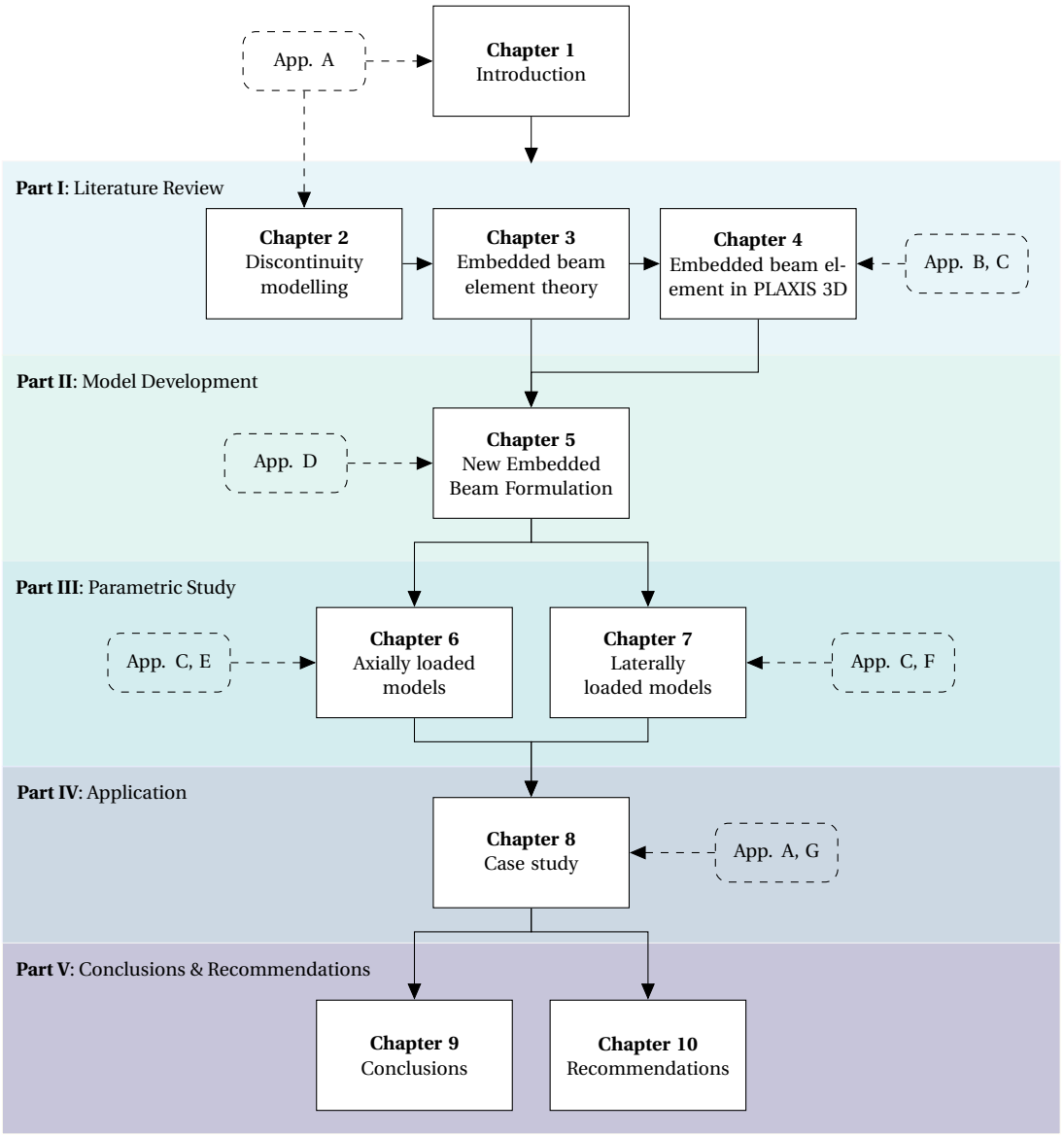

Figure 1.1: Outline of the report

I

Literature Review

2

Discontinuity modelling

In geotechnical engineering an understanding of discontinuities is crucial, because discontinuities influence the failure behaviour of soil and rock masses significantly. Think of shear bands, cracks, joints or faults. The influence of discontinuities is not only present in geotechnical engineering, but also in other civil engineering disciplines. For example the use of concrete as building material introduces challenges in discontinuity modelling, such as crack propagation and reinforcement bars.

With the rise and growth of processing power of computers, a variety of numerical modelling techniques have arisen that are nowadays widely adopted to calculate and predict displacements and stresses in structures. The finite element method (FEM, Courant (1943)) is one of the oldest and still the most used numerical modelling technique in the last decades. However, other methods are available as well, such as the Material Point Method (MPM, Sulsky et al. (1994)), Finite Difference method (FDM, Courant et al. (1928)), Finite Volume Method (FVM, Eymard et al. (2000)) or Discrete Element Method (DEM, Cundall and Strack (1979)). All methods have their own advantages and disadvantages, most are very suited for certain applications, but less suited for others or are very expensive in terms of computation time or storage. One of the big advantages of FEM compared to the others is that FEM is a very general method, making it applicable to a wide range of applications. The focus in this research is on the modelling of pile foundations in PLAXIS 3D, which is a FEM package. Therefore, other methods are not elaborated any further.

Numerical modelling of cracking in concrete started in the 1960's (De Borst and Sluys (2015)) with the introduction of smeared and discrete crack models by Ngo and Scordelis (1967) and Rashid (1968). This is a good starting point for the overview of numerical discontinuity modelling techniques in this report. First, two ways to distinguish between different types of discontinuities is explained. Next, Section 2.2 presents a brief overview of literature and current state-of-the-art in discrete FEM discontinuity modelling techniques. Subsequently, Section 2.3 explains smeared FEM discontinuity modelling techniques in short. At last, in Section 2.4 the embedded beam approach is explained shortly and related to the current state-of-the-art in discrete FEM discontinuity modelling techniques.

2.1. Discontinuity characterisation

There are several ways to distinguish between different types of discontinuities. In this report a coarse distinction between structural and material discontinuities is used, based on the physics of the problem. A structural discontinuity is a plane or surface that marks a change in physical or chemical characteristics, for example pores, cracks, joints and shear bands (Schultz and Fossen, 2008). At such a discontinuity the structure is slightly stronger or weaker than the rest of the structure. A material discontinuity is the plane or surface where a change in material properties occurs. In this type of discontinuity there is some interaction between the two materials present. For example, a pile foundation in soil.

Another distinction that is often made in research is between weak and strong discontinuities (see for example Soghrati et al. (2010)). This distinction is based on how the discontinuity shows up in the displacement field. A weak discontinuity shows a kink in the solution and a strong discontinuity shows a jump in the solution. Figure 2.1 shows the two types of discontinuities.

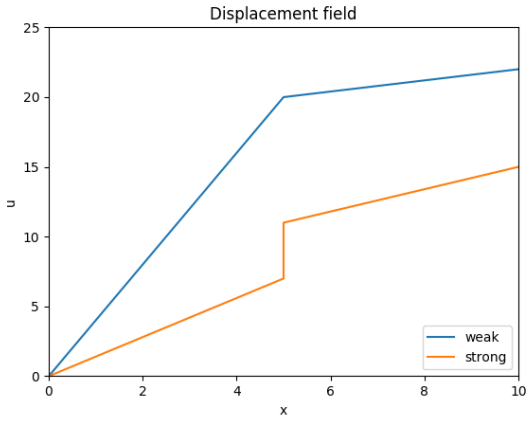

Figure 2.1: Two types of discontinuities

2.2. Discrete Finite element methods

In the basic discrete crack model (Ngo and Scordelis, 1967) a crack is assumed to occur when the maximum tensile stress is exceeded at a node or element boundary in the model. At the nodes where this happens, new nodes are inserted and the old and new nodes are allowed to separate. This effectively models the relative displacement between two sides of a crack or other kind of discontinuity.

However, this method has two big disadvantages. The first disadvantage of this method is the necessity to remesh the model every time a crack occurs or propagates. The second disadvantage is that the occurrence of a crack and its propagation is limited to the element boundaries.

These problems have been tried to solve and different methods have been developed that model a discrete crack without these two big drawbacks. For example Ingraffea and Saouma (1985) introduced an algorithm that enables automatic remeshing and Blaauwendraad and Grootenboer (1981) proposed a technique in which discrete cracks can extend through finite elements. Cundall and Strack (1979) proposed a distinct element method in which every element is surrounded by potential discrete cracks, so that a crack can propagate anywhere between the elements.

However, the problem that is addressed in this research doesn't consider a propagating crack for which the direction is not known beforehand. Therefore, the previously mentioned drawbacks are not relevant and it is possible to use a numerical method in which the location of the discontinuity needs to be known. The next sections present several discrete numerical modelling techniques that are able to capture discontinuities. Developments in this area of research evolve quickly and more related methods might be available already. All methods described in the following sections possess some advantages and disadvantages that may or may not make them suitable to model the problem that is considered in this report; pile foundations.

2.2.1. Interface elements

A numerical method to model cracking in concrete for which the location and orientation are known is proposed by Rots (1991). This method includes the use of interface elements that are inserted at locations where a discontinuity is present. An interface element is an element with zero thickness, so each pair of nodes lie exactly on top of each other. As long as the stresses in the integration points of the interface elements are below the maximum capacity, the interface element behaves elastic. To minimise the deformations that happen in the interface elements in this elastic stage, the interface elements are given a high stiffness. When the maximum capacity is exceeded, the excessive stresses may cause displacements between the two nodes. The interface element can model opening of a gap and sliding between the two sides of the interface.

Interface elements can either be used for structural discontinuities such as cracks or material discontinuities. In case of cracking, this method obviously solves the necessity to update the mesh every time a crack occurs or propagates. A disadvantage is that the crack path needs to be known before calculation. The crack path can be estimated using smeared crack models or experimental data, but this still is a big limitation of this method. Material discontinuities are often known beforehand, which makes this method very suitable for material interaction problems.

In the interface element description that is currently incorporated in PLAXIS 3D (Brinkgreve et al., 2015; Van Langen and Vermeer, 1991), the material stiffness describes the relation between the stresses at the interface and relative displacements. This makes it necessary for the material interface stiffnesses to have the unit [kN/m^3], incorporating the virtual thickness of the interface element. The stiffnesses are defined as follows:

$$\begin{aligned} K_s &= \frac{G_i}{t_i} \\ K_n = K_t &= \frac{E_{oed,i}}{t_i} \end{aligned} \tag{2.1}$$

with

$$\begin{aligned} E_{oed,i} &= 2G_i \cdot \frac{1-\nu_i}{1-2\nu_i} \\ G_i &= R_{inter}^2 \cdot G_{soil} \end{aligned} \tag{2.2}$$

This gives:

$$K_n = K_t = \frac{2G_i \cdot \frac{1-\nu_i}{1-2\nu_i}}{t_i} = 2 \cdot K_s \cdot \frac{1-\nu_i}{1-2\nu_i} \tag{2.3}$$

Here t_i is the virtual thickness of the interface element. The virtual thickness of an interface element is an imaginary dimension, which influences the amount of elastic deformations; the higher the virtual thickness is, the more elastic deformations are generated. The virtual thickness generally is very small, since the interface elements are not supposed to generate large elastic deformations, but too small values might cause numerical problems. R_{inter} is a strength reduction factor that reduces the strength of the interface compared to the surrounding material.

2.2.2. Extended Finite Element Method (XFEM)

The method was developed in the 1990's and was given several names, such as Special FEM (Babuška et al., 1994), Partition of Unity FEM (PUFEM, Melenk and Babuška (1996)) and Generalized FEM (GFEM, Duarte et al. (1998); Strouboulis et al. (2000)). Moës et al. (1999) was the first to name it the extended finite element method (XFEM). The information in this section is based on the information provided by Fries (2013).

The XFEM extends the standard FEM according to:

$$u(x) = \underbrace{\sum N_i(x) \cdot a_i}_{\text{Standard FEM}} + \underbrace{\sum M_i(x) \cdot b_i}_{\text{Extension}} \tag{2.4}$$

Here $M_i(x)$ are local enrichment functions at node i and b_i are additional nodal unknowns. The local enrichment function at node i has the form:

$$M_i(x) = N_i^*(x) \cdot \psi(x) \tag{2.5}$$

where $N_i^*(x)$ are called partition of unity functions, and $\psi(x)$ is the global enrichment function. $N_i^*(x)$ are standard finite element shape functions, which don't have to be the same as N_i in the standard FEM part of the discretisation. The sum of the partition of unity functions is one.

Whether or not an element contains a discontinuity is checked using the level-set method. A level-set function (ϕ) is a scalar function within a domain, which is zero at the location of the discontinuity. On one side of the discontinuity the level-set function is negative, on the other side the level-set function is positive. The level-set function is discretised similarly as the displacement field in the finite element method; $\phi = \sum N_i \phi_i$, where N_i are the standard finite element shape functions and ϕ_i are the nodal values of the level-set function. Elements that contain a discontinuity are elements for which:

$$\min(\phi_i) \cdot \max(\phi_i) < 0. \tag{2.6}$$

Different choices for global enrichment functions are possible. For example, when there is a jump in the displacement field, which is the case for cracking, the Heaviside-function of the level-set function can be used. In case of weak discontinuities the global enrichment function can be chosen as the absolute value of the level-set function. These possibilities make XFEM applicable for the modelling of both weak and strong discontinuities.

This method solves both disadvantages that come with the standard discrete crack model. Therefore, this method is a very good alternative to model discrete discontinuities in structures. However, this method is mainly intended to model structural discontinuities and is therefore less applicable for modelling material discontinuities.

2.2.3. Interface-Enriched Generalized Finite Element Method (IGFEM)

This method (Soghrati et al., 2010) is very closely related to the Extended Finite Element Method. Similar as in XFEM, the relevant elements are enriched. However, different enrichment functions are used, which are only applied at interface nodes. These interface nodes are found at the intersection of the phase interface with element edges. Figure 2.2 shows how this enrichment is applied at an element in IGFEM. The phase

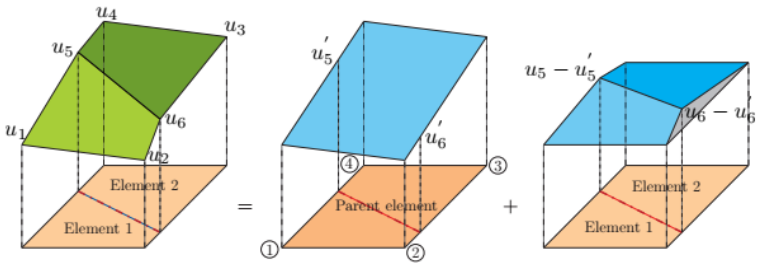

Figure 2.2: Capturing a weak discontinuity at the phase interface, (Soghrati et al., 2010)

interface resembles the line on which the discontinuity takes place. To be able to catch this discontinuity using standard FEM an element boundary must be located there, but using IGFEM (or XFEM) this is not necessary.

An enrichment in IGFEM is given by:

$$u(x) = \sum N_i(x) a_i + \sum s\phi_j(x)\alpha_j \tag{2.7}$$

Here s is a scaling factor, ϕ_j are enrichment functions and α_j are generalised DOFs. Equation (2.4) shows that in XFEM the nodal values are given by $a_i + \psi(x)b_i$, but Equation (2.7) shows that in IGFEM the nodal values are given by a_i. The generalised DOFs α_j are added at the interface nodes. In Figure 2.2 this would mean that $\alpha_1 = a_5 - a_5'$ and $\alpha_2 = a_6 - a_6'$.

The enrichment functions ϕ_j are a linear combination of the Lagrangian shape functions of the two sub-elements at the interface nodes. For example, look again at Figure 2.2. The solution field can be found by:

$$\begin{aligned} u(x) =& N_1^{(1)} a_1 + N_2^{(1)} a_2 + N_3^{(2)} a_3 + N_4^{(2)} a_4 + \left(N_4^{(1)} + N_1^{(2)}\right) a_5 + \left(N_3^{(1)} + N_2^{(2)}\right) a_6 \\ \Longrightarrow\ & N_1^{(p)} a_1 + N_2^{(p)} a_2 + N_3^{(p)} a_3 + N_4^{(p)} a_4 + \left(N_4^{(1)} + N_1^{(2)}\right) \alpha_1 + \left(N_3^{(1)} + N_2^{(2)}\right) \alpha_2 \end{aligned} \tag{2.8}$$

The scaling factor is necessary to avoid numerical problems when the interface node is close to one of the nodes of the parent element. When the interface node is close to one of the nodes of the parent element the scaling factor is decreased to avoid an ill-conditioned stiffness matrix.

This method is only able to capture weak discontinuities. The method that is described in the next section solves this limitation. Furthermore, like XFEM this method is intended for structural discontinuities and is therefore less applicable for modelling material discontinuities.

However, this method does have several advantages compared to XFEM. Soghrati et al. (2010) names for instance lower computational cost and easier implementation. Handling of Dirichlet boundary conditions is more straightforward as well, because no additional nodal unknowns are included as in XFEM.

2.2.4. Discontinuity-Enriched Finite Element Method (DE-FEM)

Aragón and Simone (2017) proposed an extension of IGFEM to include the possibility to model not only weak discontinuities, but strong discontinuities as well. The same advantages that IGFEM has compared to XFEM are maintained. In DE-FEM the solution field is also enriched:

$$u(x) = \sum N_i(x) a_i + \underbrace{\sum s\phi_j(x)\alpha_j}_{weak} + \underbrace{\sum \chi_k(x)\beta_k}_{strong} \tag{2.9}$$

The IGFEM enrichment can be easily recognised as the enrichment for the weak discontinuity. The enrichment for the strong discontinuity consists of χ_k as the strong enrichment function and β_k as the strong enriched DOFs. The enrichment functions are again constructed from a linear combination of Lagrangian shape functions in the sub-elements. The enriched DOFs β_k represent the size of the jump in the discontinuity.

Although, this method is able to capture both weak and strong discontinuities, it is mainly intended to model structural discontinuities, just like XFEM.

2.2.5. Constitutive Law with Embedded Discontinuity (CLED)

Pietruszczak and Haghighat (2014) proposed a finite element in which the constitutive law is enriched with an embedded discontinuity in a discrete sense. The concept of a discontinuous strain measure has been applied before to describe localised deformations in a smeared sense, but by coupling this method with the level-set method it is possible to describe crack propagation in a discrete way.

The discontinuous strain measure is introduced by decomposing the total strain rate into a continuous part and a discontinuous one:

$$\dot{\varepsilon}_{ij} = \dot{\tilde{\varepsilon}}_{ij} + \dot{\tilde{\varepsilon}}_{ij} \tag{2.10}$$

After imposing the correct conditions and including the interface properties, a modified constitutive relation is found:

$$\dot{\sigma}_{ij} = \widetilde{D}_{ijkl}\dot{\varepsilon}_{kl} \tag{2.11}$$

Here, $\tilde{D}_{ijkl}$ contains a continuous and discontinuous contribution.

The direction of the crack propagation can be found by using a level-set method, which is briefly explained in Section 2.2.2. A typical algorithm that is used to find the correct crack path is based on checking the failure criterion at the neighbouring integration points and using their orientations.

In this method, no additional degrees of freedom are required. This makes this method easily incorporated in available standard FEM packages. This is an advantage compared to the XFEM method.

This method is able to capture both weak and strong discontinuities. This method is also intended to model structural discontinuities and is therefore less applicable to model material discontinuities.

2.3. Smeared finite element models

In the smeared crack model the material properties at an integration point are modified when a condition of crack initiation is reached; i.e. the normal stresses exceed the maximum tensile stress. When a crack forms it is sufficient to switch from the initial isotropic stress-strain law to an orthotropic law. This approach smears the crack out over the whole element in which this happens, therefore it is not sensible to use very coarse meshes in combination with a smeared model.

Both fixed smeared crack models and rotating smeared crack models exist. In a fixed smeared crack model the direction of the normal to the crack is fixed upon initiation of the crack, whereas the rotating smeared crack model allows the normal to the crack to rotate during the crack propagation. For a more detailed report on smeared crack models and a comparison with other crack modelling techniques, see Rots and Blaauwendraad (1989).

This research focusses on modelling a pile foundation in soil. In the case of a pile foundation the interaction between the pile and soil takes place at a discrete location, which is known beforehand. Furthermore, the idea of the embedded beam approach is to be able to use a coarse mesh. A smeared model in this case is not a sensible choice, therefore smeared models will not be elaborated in more detail in this report.

2.4. The embedded beam element

The embedded beam element is solely intended to model a beam surrounded by soil, which is, according to the definitions at the beginning of this chapter, a material discontinuity.

In the embedded beam approach the goal is to model the pile-soil interaction behaviour accurately without explicitly modelling interface elements. Still, the principle of interface elements is applied in the sense of a **virtual interface**. At the locations of the embedded beam nodes virtual nodes are created. The beam displacements in the embedded beam nodes and the soil displacements at the virtual nodes are evaluated separately, making it possible to take into account relative displacements between the two. A new constitutive relation is used to describe the relation between these relative displacements and the tractions along the pile. The resulting additional stiffness matrix and force vector are then added to the global stiffness matrix and force vector. This effectively models the interaction between the pile and soil without explicitly including interface elements.

In the formulation that is proposed in this report the pile-soil interaction will be modelled at the true pile circumference, instead of at the pile axis.

2.4.1. Relation to research field

The development of the embedded beam element has a different origin than previously mentioned methods. Whereas methods such as XFEM are intended to model crack propagation in a material, the embedded beam element is intended to model pile foundations alone. When looking at history, completely different methods were used to model either crack propagation or pile foundations in soil.

Methods to model pile foundations have existed for a long time; the Winkler hypothesis stems from the 19th century (Winkler, 1867). This method models the pile foundation as a beam element with independent springs distributed along the length to model the soil reactions. The stiffness of the springs is also referred to as coefficient of subgrade reaction (Appendix A.2.1), which is still used in current design standards. Until the introduction of the embedded beam element by Sadek and Shahrour (2004), the only numerical modelling technique based on finite elements that was used to model pile foundations was the volume pile approach including interface elements (Section 2.2.1).

In the introduction of this chapter it was mentioned that the numerical modelling of cracking in concrete emerged in the 1960's, based on the finite element method. However, during the first World War Griffith (1921) already developed a theory that explains the failure of brittle materials. Griffith explained that the fracture strength is lower than the theoretical strength of a material, because of flaws in the material which cause stress concentrations. An expression was developed that determines when a crack grows based on energy. Unfortunately, this work was ignored for a long time.

The two subjects of research meet each other with the introduction of the use of interface elements to model a discontinuity in FEM. Interface elements can be used for both structural and material discontinuities, making it applicable for both modelling cracking and pile foundations or any other kind of problem containing a discontinuity as long as the location can be predicted. The more recently proposed methods (XFEM, IGFEM, DE-FEM, CLED and the embedded beam element) are again only intended for one of the two purposes. However, more recent studies have shown that XFEM can be extended to be used for different applications as well, as long as the localised feature can be described by a suitable set of basis functions (Belytschko et al., 2009). The possibility to use XFEM or one of the extensions described in Sections 2.2.3 and 2.2.4 for modelling pile foundations can be studied in future research (see Chapter 10).

2.4.2. Possible applications of the embedded beam in other work fields

The ability to model an embedded beam element inside a three-dimensional solid element independent of the mesh size and direction, can be useful in more cases than just for modelling pile foundations. Some examples will be discussed in this section.

The first example is also mentioned by Engin et al. (2008) and is the most obvious application; soil reinforcement. Soil reinforcement is most often used to steepen slopes.

The second example is reinforced concrete. The interaction between concrete and its reinforcement is different than the interaction between a pile and the soil, as concrete has very different properties. Therefore, before using embedded beam elements to model reinforced concrete an investigation should be performed to gain insight in the interface properties.

The third example is the use of medical screws and nails. In the bio-mechanical sector finite element models are often used to model biological systems. Think for example of someone with scoliosis that gets a spinal fusion to prevent further curvature of the pine. A spinal fusion is when two or more adjacent vertebrae are connected (fused) with rods, screws, hooks and/or wires to prevent further curvature of the spine. To model this using finite element software, it might be possible to use embedded beam elements with adjusted properties. In order to make this possible, again research should be conducted to investigate the interaction between bone and screws.

In fact, embedded beam elements can be used to model any situation in which some element crosses another element at any arbitrary location with any arbitrary inclination. Adjusting the properties of the elements and the interface stiffness to model the specific situation and the interaction correctly are necessary, but not impossible.

3

Embedded beam element theory

This chapter presents the embedded beam theory as it was initially proposed by Sadek and Shahrour (2004). This theory, elaborated in Section 3.1, is still the basis for the embedded beam formulation that is currently implemented in PLAXIS 2D and 3D. Subsequently, a recently published paper by Turello et al. (2016b) is presented in Section 3.2. Their paper proposes an embedded beam element with explicit interaction surface, including two different methods to include an interface that takes into account lateral interaction behaviour between the pile and soil. Since the new embedded beam formulation that will be proposed in this report considers an interaction surface as well, it is relevant to be able to compare these two formulations (Appendix D.3).

3.1. Embedded beam formulation by Sadek and Shahrour

The embedded beam theory was first formulated by Sadek and Shahrour (2004). In this formulation an embedded beam element consists of a three-dimensional solid element and a beam element. The beam element can cross the solid volume elements at any arbitrary location with any arbitrary orientation. This is shown in Figure 3.1. The beam element has two nodes with both six DOFs; 3 translational and 3 rotational.

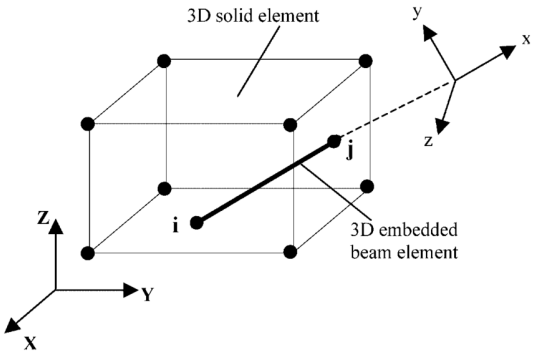

Figure 3.1: Embedded beam element, (Sadek and Shahrour, 2004)

Initially, a perfect bond between the beam and solid element is assumed. This makes it possible to determine the beam nodal displacements in terms of soil nodal displacements and soil shape functions. The beam nodes can be interpreted as virtual nodes inside the solid element and no explicit beam element needs to be modelled. The contribution of the beam element can now easily be added to the soil element stiffness matrix.

Subsequently, a formulation is presented in which relative displacements between the pile and soil are possible, which does require the modelling of an explicit beam element. The interaction between the beam element and the solid element is described using interface elements, taking into account the relative displacements. The relative displacement between the beam and solid element along the beam axis is given by:

$$\boldsymbol{u_{rel} = u_b - u_s} \tag{3.1}$$

The bonding force vector $\boldsymbol{f^{int}}$ is linked to relative displacement between the beam and soil by the following relation:

$$\boldsymbol{f^{int}} = \boldsymbol{D^e u_{rel}} \tag{3.2}$$

with

$$\boldsymbol{D^e} = \begin{bmatrix} K_s & 0 & 0 \\ 0 & K_t & 0 \\ 0 & 0 & K_n \end{bmatrix} \tag{3.3}$$

K_s is the material stiffness of the interface in the direction parallel to the beam axis, K_t and K_n are the material stiffnesses of the interface element in the directions perpendicular to the beam axis.

The contribution of the interface elements to the overall global stiffness matrix can be computed. Equation (3.2) can be transformed to

$$\boldsymbol{f^{int}} = \boldsymbol{K^e_{local} a^e} \tag{3.4}$$

The global nodal displacement vector ($\boldsymbol{a^e_{global}}$) is related to the local nodal displacement vector ($\boldsymbol{a^e}$) through a transformation matrix $\boldsymbol{T}$ as follows:

$$\boldsymbol{a^e} = \boldsymbol{T} \cdot \boldsymbol{a^e_{global}} \tag{3.5}$$

Thus, the global interface stiffness matrix is given by

$$\boldsymbol{K^e_{global}} = \boldsymbol{T}^T \boldsymbol{K^e_{local}} \boldsymbol{T} \tag{3.6}$$

It is convenient to express the displacement vectors $\boldsymbol{a^s_{i,global}}$ and $\boldsymbol{a^s_{j,global}}$ in the nodal displacements of the solid element. This is done via the interpolation matrix of the solid element $\boldsymbol{N^s}$ (shape functions), therefore:

$$\boldsymbol{a^e_{global}} = \begin{bmatrix} \boldsymbol{a^b_i} \\ \boldsymbol{a^b_j} \\ \boldsymbol{a^s_i} \\ \boldsymbol{a^s_j} \end{bmatrix}_{global} = \boldsymbol{N^{int}_s} \begin{bmatrix} \boldsymbol{a^b_i} \\ \boldsymbol{a^b_j} \\ \boldsymbol{a^s} \end{bmatrix}_{global} \tag{3.7}$$

with

$$\boldsymbol{N^{int}_s} = \begin{bmatrix} \boldsymbol{I} & \boldsymbol{0} & \boldsymbol{0} \\ \boldsymbol{0} & \boldsymbol{I} & \boldsymbol{0} \\ \boldsymbol{0} & \boldsymbol{0} & \boldsymbol{N^s(X_i)} \\ \boldsymbol{0} & \boldsymbol{0} & \boldsymbol{N^s(X_j)} \end{bmatrix} \tag{3.8}$$

The global interface stiffness matrix in terms of the nodal displacements of the solid element is then given by:

$$\boldsymbol{K^{e,s}_{global}} = \left(\boldsymbol{N^{int}_s}\right)^T \boldsymbol{K^e_{global}} \boldsymbol{N^{int}_s} \tag{3.9}$$

3.1.1. Advantages

With this embedded beam formulation Sadek and Shahrour were the first to introduce a method to model material discontinuities that uncouples the mesh of the soil domain and the beam element. As is evident in Chapter 2, most methods to model discontinuities focus on structural discontinuities. Until the introduction of embedded beam elements, the only method to model a material discontinuity using FEM was to use explicit interface elements. This embedded beam formulation makes it possible for a beam to cross any solid element at any arbitrary location with any arbitrary orientation, without explicitly modelling interface elements. No mesh alignment between soil domain and beam element is required and the nodes of the beam do not need to coincide with solid nodes.

As no explicit interface elements need to be modelled, the modelling and meshing of an embedded beam model is much more efficient than modelling a pile foundation using the, for example, volume pile approach. Furthermore, the resulting mesh will contain less elements, which also reduces the calculation time.

3.1.2. Limitations

Some problems arise with this formulation. In this formulation the beam is a line element without a volume. This can cause problems in case of a very small mesh size. It is possible that there are solid elements located inside the actual pile radius, causing local behaviour such as stress singularities. For this reason the embedded beam element behaves extremely mesh sensitive.

The fact that the pile-soil interaction is modelled at the beam axis, makes it impossible to take into account the soil behaviour around the pile circumference accurately. Also, the interaction between the pile and soil in lateral direction cannot be evaluated, since a line cannot distinguish between different normal and tangential directions along the pile surface.

Engin et al. (2007) showed that for very small mesh sizes numerical instability occurs, causing premature failure. The paper proposes to define a elastic region around the pile. All Gaussian points of the solid elements that are located inside this region are forced to remain elastic. The size of this region is determined by the pile radius. This method is adopted in the current PLAXIS 3D implementation of the embedded beam element and will be elaborated in more detail in Section 4.2.

3.2. Embedded beam with explicit interaction surface by Turello et al.

Turello et al. (2016a) proposed a three-dimensional embedded beam element with explicit interaction surface in order to overcome the problems of existing embedded beam elements concerning stress singularities and mesh sensitivity. In addition, Turello et al. (2016b) proposed two methods to model lateral deformation behaviour of the embedded beam element more accurate.

The model represents the force interactions at the pile surface; the interaction surface denoted with ω. The layout of the proposed model is shown in Figure 3.2.

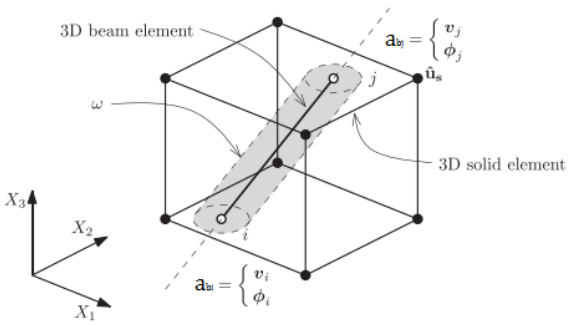

Figure 3.2: Layout of proposed embedded beam element, (Turello et al., 2016a)

The solid displacement vector $\boldsymbol{u_s}$ is discretised by means of standard interpolation functions $\boldsymbol{N^s}$ and nodal displacements $\boldsymbol{a_s}$:

$$\boldsymbol{u_s} = \boldsymbol{N^s}\ \boldsymbol{a^s} \tag{3.10}$$

The beam displacement vector field at the interaction surface $\boldsymbol{u_b}$ is expressed as a function of the beam nodal displacements $\boldsymbol{a^b}$, by means of a mapping matrix $\boldsymbol{H_u}$. This mapping matrix consists of an interpolation matrix $\boldsymbol{N_u}$ that defines the displacement field at the beam axis in terms of nodal displacements, and a matrix $\boldsymbol{M_u}$ that converts displacements and rotations at the beam axis into a vector displacement field at the interaction surface.

$$\boldsymbol{u_b} = \boldsymbol{H_u}\left(r,\varphi\right)\boldsymbol{a^b} = \boldsymbol{M_u}\left(\varphi\right)\boldsymbol{N_u}\left(r\right)\boldsymbol{a^b} \tag{3.11}$$

Here r is the local coordinate axis along the beam axis and φ is the local cylindrical coordinate. The mapping matrix $\boldsymbol{M_u}$ takes into account the standard Euler-Bernoulli hypothesis, where the beam cross-section remains planar, undeformed and perpendicular to the beam axis.

In the same way the interaction force field $\boldsymbol{f^{int}}$ at the interaction surface can be expressed as a function of nodal interaction forces $\boldsymbol{p^{int}}$. The layout of the mapping matrices are shown in Figure 3.3.

The explicit form of the interpolation matrix $\boldsymbol{N_u}$ for a 2-noded cylindrical pile in local coordinates is given by:

$$\boldsymbol{N_u}\left(r\right) = \boldsymbol{N_{ui}}\left(r\right)\boldsymbol{N_{uj}}\left(r\right) \tag{3.12}$$

with

$$\boldsymbol{N_{ui}}\left(r\right) = \begin{bmatrix} n_{1i}^H & 0 & 0 & 0 & n_{2i}^H & 0 \\ 0 & n_{1i}^H & 0 & n_{2i}^H & 0 & 0 \\ 0 & 0 & n_i^L & 0 & 0 & 0 \\ 0 & -n_{1i,r}^H & 0 & -_{2i,r}^H & 0 & 0 \\ n_{1i,r}^H & 0 & 0 & 0 & n_{2i,r}^H & 0 \\ 0 & 0 & 0 & 0 & 0 & n_i^L \end{bmatrix} \tag{3.13}$$

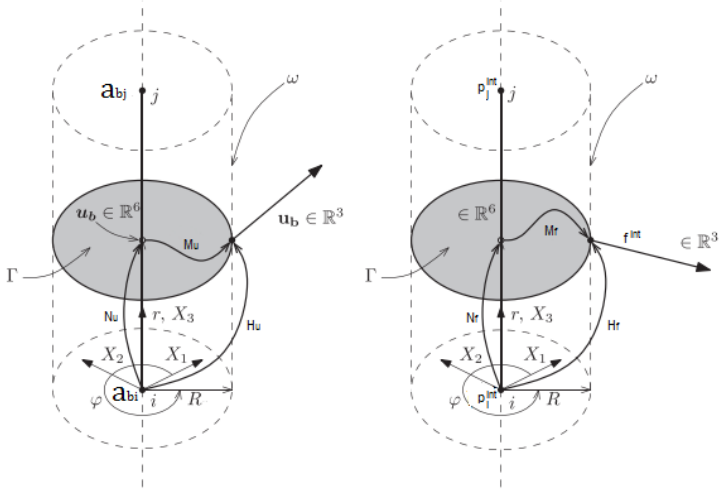

Figure 3.3: Layout of mapping matrices for respectively displacements and forces, (Turello et al., 2016a)

where n_1^H and n_2^H are the cubic Hermitian polynomial functions for interpolation of displacements in terms of nodal displacements and rotations respectively, n^L are the standard linear interpolation functions, and $(\,)_{,r}$ represents the partial derivative with respect to r. It is convenient to choose the same interpolation matrix for both $\boldsymbol{u_b}$ and $\boldsymbol{f^{int}}$, so $\boldsymbol{N_u} = \boldsymbol{N_f}$. The explicit form of the mapping functions are given by:

$$\boldsymbol{M_u}(\varphi) = \begin{bmatrix} 1 & 0 & 0 & 0 & 0 & -R\sin\varphi \\ 0 & 1 & 0 & 0 & 0 & R\cos\varphi \\ 0 & 0 & 1 & R\sin\varphi & -R\cos\varphi & 0 \end{bmatrix} \tag{3.14}$$

and

$$\boldsymbol{M_f}(\varphi) = \begin{bmatrix} \frac{1}{2\pi R} & 0 & 0 & 0 & 0 & -\frac{\sin\varphi}{2\pi R^2} \\ 0 & \frac{1}{2\pi R} & 0 & 0 & 0 & \frac{\cos\varphi}{2\pi R^2} \\ 0 & 0 & \frac{1}{2\pi R} & \frac{\sin\varphi}{\pi R^2} & -\frac{\cos\varphi}{\pi R^2} & 0 \end{bmatrix} \tag{3.15}$$

Compatibility of the pile and soil displacements is considered at the interaction surface ω. To define a fully rough elastic interaction it is imposed that the relative displacement between pile and soil produces no virtual work at the interaction surface with respect to any admissible system of virtual interaction forces $\delta\boldsymbol{f^{int}}$:

$$\begin{aligned} &\int_{\omega^e} \delta\left(\boldsymbol{f^{int}}\right)^T (\boldsymbol{u_b} - \boldsymbol{u_s})\, d\omega^e = \boldsymbol{0} \\ \Longrightarrow\ &\delta\left(\boldsymbol{p^{int}}\right)^T \underbrace{\int_{\omega^e} \boldsymbol{H_f}^T \boldsymbol{H_u}\, d\omega^e}_{\boldsymbol{A}^T} \boldsymbol{a^b} - \delta\left(\boldsymbol{p^{int}}\right)^T \underbrace{\int_{\omega^e} \boldsymbol{H_f}^T \boldsymbol{N^s}\, d\omega^e}_{\boldsymbol{S}^T} \boldsymbol{a^s} = \boldsymbol{0} \\ \Longrightarrow\ &\boldsymbol{A}^T \boldsymbol{a^b} - \boldsymbol{S}^T \boldsymbol{a^s} = \boldsymbol{0} \end{aligned} \tag{3.16}$$

where the capitals are the global equivalents of the local vectors. Now it becomes clear why it was convenient to choose $\boldsymbol{N_u} = \boldsymbol{N_f}$, as it turns out that the matrix $\boldsymbol{A}$ is invertible in this case. Therefore:

$$\boldsymbol{a^b} = \boldsymbol{A}^{-T} \boldsymbol{S}^T \boldsymbol{a^s} \tag{3.17}$$

In a similar way it is possible to express the nodal interaction forces in terms of beam DOFs $\boldsymbol{p_b}$ in terms of nodal interaction forces $\boldsymbol{p^{int}}$:

$$\begin{aligned} &\int_{\omega^e} \delta\boldsymbol{u_b}^T \boldsymbol{f^{int}}\, d\omega \Longrightarrow \delta\boldsymbol{a^b}^T \underbrace{\int_{\omega^e} \boldsymbol{H_u}^T \boldsymbol{H_f}\, d\omega^e}_{\boldsymbol{A}} \boldsymbol{p^{int}} = \delta\boldsymbol{a^b}^T \boldsymbol{p_b} \\ &\Longrightarrow\ \boldsymbol{p_b} = \boldsymbol{A}\, \boldsymbol{p^{int}} \end{aligned} \tag{3.18}$$

Similarly, the interaction load vector defined in terms of the solid DOFs $\boldsymbol{p_s}$ can be expressed in terms of the nodal interaction forces $\boldsymbol{p^{int}}$:

$$\begin{aligned} &\int_{\omega^e} \delta \boldsymbol{u_s}^T \, \boldsymbol{f^{int}} \, d\omega^e = \delta \boldsymbol{a^s}^T \underbrace{\int_{\omega^e} \boldsymbol{N^s}^T \, \boldsymbol{H_f} \, d\omega^e}_{\boldsymbol{S}} \boldsymbol{p^{int}} = \delta \boldsymbol{a^s}^T \boldsymbol{p_s} \\ &\implies \boldsymbol{p_s} = \boldsymbol{S} \, \boldsymbol{p^{int}} \end{aligned} \tag{3.19}$$

Using Equation (3.18), the beam equilibrium can be written as:

$$\boldsymbol{K_b} \, \boldsymbol{a^b} = \boldsymbol{p_b} = \boldsymbol{A} \, \boldsymbol{p^{int}} \tag{3.20}$$

As matrix $\boldsymbol{A}$ is invertible $\boldsymbol{p^{int}}$ can be expressed as:

$$\boldsymbol{p^{int}} = \boldsymbol{A}^{-1} \boldsymbol{K_b} \boldsymbol{a^b} \tag{3.21}$$

Using Equations (3.17), (3.19) and (3.21), the global beam stiffness matrix can be expressed in terms of solid DOFs as follows:

$$\begin{aligned} &\boldsymbol{p_s} = \boldsymbol{S} \, \boldsymbol{p^{int}} = \boldsymbol{S} \, \boldsymbol{A}^{-1} \, \boldsymbol{K_b} \, \boldsymbol{a^b} = \underbrace{\boldsymbol{S} \, \boldsymbol{A}^{-1} \, \boldsymbol{K_b} \, \boldsymbol{A}^{-T} \, \boldsymbol{S}^T}_{\boldsymbol{K_{bs}}} \, \boldsymbol{a^s} \\ &\boldsymbol{p_s} = \boldsymbol{K_{bs}} \, \boldsymbol{a^s} \end{aligned} \tag{3.22}$$

The global stiffness matrix $\boldsymbol{K_{bs}}$ is symmetric, because it inherits the symmetry of the standard beam stiffness matrix. In order to obtain the total stiffness matrix of the embedded pile, this stiffness matrix can be assembled to the solid stiffness matrix. The problem is solved in terms of solid DOFs and using a post-processing step (Equation (3.17)) it is possible to obtain the beam DOFs.

Using Equations (3.18) and (3.19) it is possible to transform $\boldsymbol{p_b}$ into an equivalent nodal solid load vector $\boldsymbol{p_{bs}}$:

$$\boldsymbol{p_{bs}} = \boldsymbol{S} \, \boldsymbol{A}^{-1} \, \boldsymbol{p_b} \tag{3.23}$$

The complete load vector in terms of solid DOFs is obtained by adding $\boldsymbol{p_s}$, $\boldsymbol{p_{bs}}$ and the load vector due to external forces.

3.2.1. Elasto-plastic interface

In Turello et al. (2016b) a new formulation of an elasto-plastic interface is presented. This elasto-plastic interface formulation represents the plasticity in the soil around the pile and can easily be coupled with the embedded beam element with interaction surface, as presented before in this section.

The hypothesis of perfect adherence of the pile and soil is now released and relative displacements between the pile and soil are introduced. It is assumed that the same mapping functions as presented before can be applied to the displacement jump and its corresponding interaction forces on the interaction surface. The compatibility requirement presented in (3.16) is now changed in order to include the possibility of relative displacements denoted by $\boldsymbol{\Delta u}$:

$$\begin{aligned} &\int_{\omega^e} \delta \left(\boldsymbol{f^{int}} \right)^T (\boldsymbol{u_b} - \boldsymbol{u_s} - \boldsymbol{\Delta u}) \, d\omega^e = \boldsymbol{0} \\ &\implies \delta \left(\boldsymbol{p^{int}} \right)^T \underbrace{\int_{\omega^e} \boldsymbol{H_f}^T \, \boldsymbol{H_u} \, d\omega^e}_{\boldsymbol{A}^T} \left(\boldsymbol{a^b} - \boldsymbol{\Delta a} \right) - \delta \left(\boldsymbol{p^{int}} \right)^T \underbrace{\int_{\omega^e} \boldsymbol{H_f}^T \, \boldsymbol{N^s} \, d\omega^e}_{\boldsymbol{S}^T} \boldsymbol{a^s} = \boldsymbol{0} \\ &\implies \boldsymbol{A}^T \left(\boldsymbol{a^b} - \boldsymbol{\Delta a} \right) - \boldsymbol{S}^T \boldsymbol{a^s} = \boldsymbol{0} \end{aligned} \tag{3.24}$$

Due to the inclusion of a possible displacement jump between the soil and the pile, an additional system of interaction forces arises at the interaction surface, denoted by $\boldsymbol{t^{int}}$. For this force vector a constitutive relation in terms of $\boldsymbol{\Delta u}$ is required. It must be noted that on the interaction surface two force vectors work now; $\boldsymbol{f^{int}}$, which is introduced to guarantee a kinematic compatibility requirement, and $\boldsymbol{t^{int}}$, which is introduced by plastic behaviour in the soil around the pile. The relation between these two forces is found by assuming

a balance of their corresponding virtual works under any admissible virtual displacement jump:

$$\begin{aligned} &\int_{\omega^e} \delta(\boldsymbol{\Delta u})^T \boldsymbol{f}^{\boldsymbol{int}}\, d\omega^e = \int_{\omega^e} \delta(\boldsymbol{\Delta u})^T \boldsymbol{t}^{\boldsymbol{int}}\, d\omega^e \\ \Longrightarrow\ &\delta(\boldsymbol{\Delta a})^T \underbrace{\int_{\omega^e} \boldsymbol{H_u^T H_f}\, d\omega^e}_{\boldsymbol{A}} \boldsymbol{p}^{\boldsymbol{int}} = \delta(\boldsymbol{\Delta a})^T \underbrace{\int_{\omega^e} \boldsymbol{H_u^T t}^{\boldsymbol{int}}\, d\omega^e}_{\boldsymbol{q}^{\boldsymbol{int}}} \\ \Longrightarrow\ &\boldsymbol{A p}^{\boldsymbol{int}} = \boldsymbol{q}^{\boldsymbol{int}} \end{aligned} \tag{3.25}$$

The interaction force vector $\boldsymbol{q}^{\boldsymbol{int}}$ can be expressed in either beam or solid kinematics, making it possible to add this contribution easily to both equilibrium equations.

Combining this result with Equation (3.18), the equivalent load vector of the complete pile (induced by the interaction forces) can be expressed as:

$$\boldsymbol{p_b} = \boldsymbol{A p}^{\boldsymbol{int}} = \boldsymbol{q}^{\boldsymbol{int}} \tag{3.26}$$

Now the equivalent nodal vector of the soil $\boldsymbol{p_s}$ can be expressed as:

$$\boldsymbol{p_s} = \boldsymbol{S p}^{\boldsymbol{int}} = \boldsymbol{S A^{-1} q}^{\boldsymbol{int}} \tag{3.27}$$

The complete system can be solved by the following system of equilibrium equations:

$$\begin{cases} \boldsymbol{K_s a^s} = \boldsymbol{p_s} + \boldsymbol{p_{es}} \\ \boldsymbol{K_b a^b} = \boldsymbol{p_b} + \boldsymbol{p_{eb}} \end{cases} \tag{3.28}$$

Where $\boldsymbol{p_{es}}$ and $\boldsymbol{p_{eb}}$ are nodal load vectors caused by external forces. This system of equations can be rewritten:

$$\begin{cases} \boldsymbol{K_s a^s} = \boldsymbol{S A^{-1} q}^{\boldsymbol{int}} + \boldsymbol{p_{es}} \\ \boldsymbol{K_b a^b} = \boldsymbol{q}^{\boldsymbol{int}} + \boldsymbol{p_{eb}} \end{cases} \tag{3.29}$$

Evidently, the coupling between the pile and soil takes place through the interaction forces $\boldsymbol{q}^{\boldsymbol{int}}$. The relative displacements can be written as:

$$\boldsymbol{\Delta a} = \boldsymbol{a^b} - \boldsymbol{A^{-T} S^T a^s} \tag{3.30}$$

This can be interpreted as the nodal beam displacements at the beam axis minus the nodal soil displacements evaluated at the interaction surface and mapped onto the beam axis.

It was mentioned before that the interaction forces $\boldsymbol{t}^{\boldsymbol{int}}$ require a constitutive model in terms of the displacement jump. This constitutive model can either be based on beam or solid kinematics. Both approaches will be explained shortly, in order to be able to compare them to the method proposed in this report.

Beam kinematics

In this case the displacement jump along the beam axis is obtained:

$$\boldsymbol{\Delta u} = \boldsymbol{u_b} - \boldsymbol{u_s^\omega} \tag{3.31}$$

where $\boldsymbol{u_s^\omega}$ is the solid displacement field evaluated over the interaction surface ω and mapped onto the beam axis. Subsequently, the distributed loads and moments along the beam axis, $\boldsymbol{t}^{\boldsymbol{int}}$, are calculated by means of the constitutive model. It must be noted that in this case the interaction between the pile and soil is added to the global problem at the beam axis, not at the real interaction surface.

The displacement jump consists of six components; three translational and three rotational. However, the constitutive model is only defined in terms of four components. The four components that are considered are the displacement along the π-axis; which is aligned with the resultant lateral displacement jump, the rotation along the ζ-axis; which is perpendicular to the π-axis and the beam axis, and the displacement and rotation along the beam axis. The equivalent displacement jump vector is now given by:

$$\boldsymbol{\Delta u}^* = \begin{bmatrix} \Delta v_\pi \\ \Delta v_3 \\ \Delta \theta_\zeta \\ \Delta \theta_3 \end{bmatrix} = \begin{bmatrix} \cos\phi_\pi & \sin\phi_\pi & 0 & 0 & 0 & 0 \\ 0 & 0 & 1 & 0 & 0 & 0 \\ 0 & 0 & 0 & \cos\phi_\zeta & \sin\phi_\zeta & 0 \\ 0 & 0 & 0 & 0 & 0 & 1 \end{bmatrix} \begin{bmatrix} \Delta v_1 \\ \Delta v_2 \\ \Delta v_3 \\ \Delta \theta_1 \\ \Delta \theta_2 \\ \Delta \theta_3 \end{bmatrix} \tag{3.32}$$

Here, ϕ_π and ϕ_ζ are the angles between the global axis 1 and the resultant lateral jump along the π-axis and resultant rotation jump along the ζ-axis. The same transformation can be applied to obtain $\boldsymbol{t}^{int*}$. The constitutive relation is now given by:

$$\boldsymbol{t}^{int*} = f\left(\boldsymbol{\Delta u}^*\right) \tag{3.33}$$

It is possible to insert any model to describe the relation between $\boldsymbol{t}^{int*}$ and $\boldsymbol{\Delta u}^*$. In the paper a bi-linear model with linear hardening and a model with exponential hardening are presented. Figure 3.4 shows an example of an one dimensional elasto-plastic model to describe the relation between t_π and Δv_π. The initial elastic interface stiffness is assumed fictionally large, as the elastic behaviour of the soil is already taken into account by the soil model.

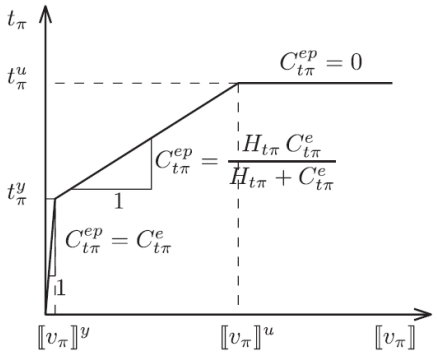

Figure 3.4: One dimensional elasto-plastic model to describe the relation between t_π and Δv_π. (Turello et al., 2016b)

In the paper a methodology is explained, with which the initial stiffness coefficients are determined. Subsequently, the well-known p-y method is used to calibrate the 1D elasto-plastic models. Key parameters of the p-y curves that are used to calibrate the 1D elasto-plastic models are the ultimate load, yield load and the ultimate relative displacements. A more elaborate explanation of these methods can be found in Turello et al. (2016b).

Solid kinematics

In this case a narrow domain around the pile is modelled with thickness h_i, that represents the interaction surface. The displacement jump develops within this narrow domain. This ring around the pile is modelled by means of a fully 3D elasto-plastic constitutive law. A section of this formulation of the interface is shown in Figure 3.5. The coordinate system (x_1', x_2', x_3') is used to define the normal and tangential components of the displacement jump. This coordinate system is obtained by means of a ordinary transformation matrix; $\boldsymbol{\Delta u}' = \boldsymbol{T}\boldsymbol{\Delta u}$.

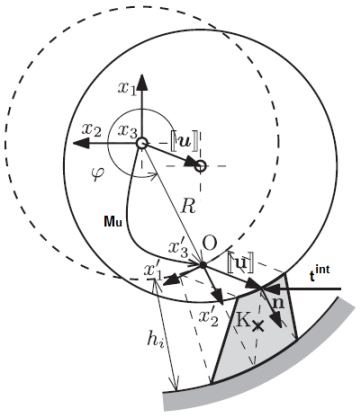

Figure 3.5: Top view of the interface expressed in solid kinematics. (Turello et al., 2016b)

In the paper it is assumed that the deformation gradient is constant along the normal direction in the

narrow domain around the pile. The strain tensor can now be defined as follows:

$$\boldsymbol{\varepsilon_i} = \frac{\boldsymbol{\Delta u'} \otimes^s \boldsymbol{n}}{h_i} \tag{3.34}$$

where $\otimes^s$ is the symmetric tensor product. The stress tensor at the interface can be obtained by adding the a stress increment to the previous stress state.

$$\boldsymbol{\sigma_i} = \boldsymbol{\sigma_i^t} + \Delta\boldsymbol{\sigma_i} = \boldsymbol{\sigma_i^t} + \boldsymbol{D^e} \cdot \Delta\boldsymbol{\varepsilon_i} \tag{3.35}$$

The interaction forces at point O on the interaction surface can be obtained by:

$$\boldsymbol{t^{int'}} = \boldsymbol{\sigma_i} \cdot \boldsymbol{n} \implies \boldsymbol{t^{int}} = \boldsymbol{T^T}\, \boldsymbol{t^{int'}} \tag{3.36}$$

3.2.2. Limitations

The $\boldsymbol{M_u}$ and $\boldsymbol{M_f}$ mapping matrices, as presented in the previous section, are not general. They can only be used for vertically oriented piles with a circular cross-section shape. As the authors themselves state (Turello et al., 2016a, p. 571): "While the procedure can be generalised for other cases, this is not a straightforward task, as a new generalised mapping operator needs to be defined."

Furthermore, the Euler-Bernoulli hypothesis is taken into account, neglecting shear deformations. For long and slender piles, this hypothesis produces accurate results, but for piles with a small L/D ratio shear deformations really make a difference.

4

Embedded beam element in PLAXIS 3D

The embedded beam elements that are currently available in PLAXIS 3D are based on the embedded beam approach by Sadek and Shahrour (2004), which is presented in the previous chapter. This chapter will describe the embedded beam formulation, as it is implemented in PLAXIS 3D, in more detail.

The beam and soil contributions are coupled by the virtual interface elements, which are described in Section 4.1. Subsequently, the elastic zone approach is explained in Section 4.2. The addition of this approach to the embedded beam formulation solves numerical problems that occurred in the model before. In Section 4.4 the existing limitations of the embedded beam element are described and shown by means of two test cases. A more detailed elaboration on the numerical implementation of the existing embedded beam element can be found in Appendix B.2.

4.1. Interface description

In PLAXIS 3D the beam elements are modelled as 3-noded line elements that can cross a three-dimensional, 10-noded tetrahedral element at any arbitrary location and with any arbitrary orientation (Figure 4.1). Every node of the beam element has 6 DOFs; 3 translational and 3 rotational. The interface elements describe the interaction between the pile and soil at the skin and at the foot of the pile.

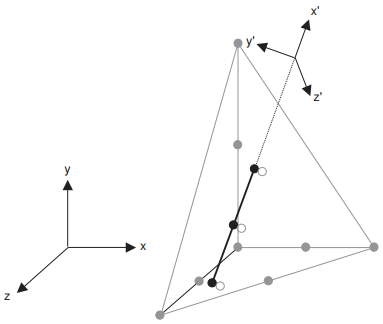

Figure 4.1: Embedded beam element in PLAXIS 3D with the virtual interface nodes. (Brinkgreve et al., 2015)

The skin interface elements are 3-noded line elements, containing pairs of nodes instead of single nodes. One node of every pair belongs to the beam element, the other is a virtual node on which the soil displacements are interpolated. The interaction between the pile and the soil at the skin of the pile is represented by a skin traction ($\boldsymbol{t}$) and the stiffness of the embedded interface elements, as presented in Equation (4.1).

$$\begin{bmatrix} t_s \\ t_n \\ t_t \end{bmatrix} = \begin{bmatrix} K_s & 0 & 0 \\ 0 & K_n & 0 \\ 0 & 0 & K_t \end{bmatrix} \begin{bmatrix} u_s^b - u_s^s \\ u_n^b - u_n^s \\ u_t^b - u_t^s \end{bmatrix} \tag{4.1}$$

The embedded interface stiffnesses describe the relation between the skin tractions [kN/m] and the relative displacements [m] and must therefore have the unit [kN/m^2], which is equal to the unit of the shear modulus.

The interface stiffness should be defined in such a way that the stiffness of the interface elements does not influence the total elastic behaviour of the pile-soil structure. This ensures that the pile displacements are governed by the stiffness of the surrounding soil and that the interface only influences the plastic slip along the pile. As long as the maximum skin friction is not reached yet, the relative displacements are only related to the interface stiffness K_s. To ensure the previously mentioned properties K_s must be chosen high compared to the shear modulus G_{soil} of the soil.

$$\begin{aligned} K_s &= 50 \cdot G_{soil} \\ G_{soil} &= \frac{E}{2(1+\nu)} \\ K_n = K_t &= \frac{2(1-\nu_i)}{1-2\nu_i} K_s \end{aligned} \tag{4.2}$$

Here ν_i is the Poisson's ratio of the interface, which has a default value of 0.45, ν is the soil Poisson's ratio, and E is the soil Young's modulus.

In the currently used embedded beam interface elements K_s is equal to the soil shear modulus times a large factor (50), but in standard interface elements the soil shear modulus is multiplied by the factor R_{inter}^2 / t_i (Equation (2.1)). The virtual thickness t_i is assumed to be very small, resulting in a large interface stiffness, having the same effect as the high factor of 50 in the embedded beam interface stiffness.

The orientation of the interface stiffnesses along the shaft of the pile are shown in Figure 4.2a.

The interaction at the foot of the pile is described by a linear elastic perfectly plastic interface element. Additionally, no tension forces are allowed and a limit can be set, F_{max}.

$$F_{foot} = K_{foot} \left(u_{foot}^b - u_{foot}^s \right) \leq F_{max} \tag{4.3}$$

The foot interface stiffness K_{foot} must have the unit [kN/m]:

$$K_{foot} = 50 \cdot G_{soil} \cdot R_{eq} \tag{4.4}$$

Figure 4.2b shows the stiffness of the embedded interface element at the foot of the pile.

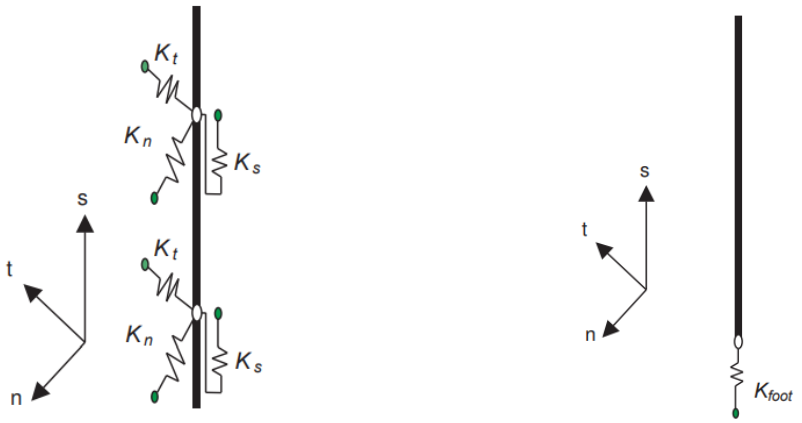

(a) Stiffness of the embedded interface elements at the skin of the pile

(b) Stiffness of the embedded interface element at the foot of the pile

Figure 4.2: Stiffness of the interface elements, (Brinkgreve et al., 2015)

As long as the shear stress along the beam axis is smaller than the maximum skin friction, elastic behaviour will occur. These relative displacements depend on the interface stiffness K_s. Only when the maximum skin resistance at an integration point is reached, can relative displacements between the pile and soil take place.

At the moment, three different options are available in PLAXIS 3D to define the ultimate skin resistance. The first one is used by entering two input values $T_{top,max}$ and $T_{bot,max}$. This results in a constant or linear

distribution of the ultimate skin resistance in terms of an integrated force per unit of pile length. The second option makes it possible to define values for the skin friction at certain depths. This results in a multi-linear distribution of the ultimate skin resistance in terms of an integrated force per unit of pile length. This option can for instance be used when the pile is located in a layered soil. The maximum skin friction is predefined in these two options, and therefore independent of the stress state in the soil. This results in the fact that bearing capacity of the pile is an input and not a result of the analysis.

The third option to define the skin resistance is the layer-dependent option. In this option the maximum shear stress $t_{s,max}$ of the embedded pile is linked to the strength parameters of the soil and the normal stress σ_n^{avg} along the interface. The shear force t_s will remain elastic as long as:

$$|t_s| < \left(c_i - \sigma_n^{avg} \tan\varphi_i\right) \cdot 2\pi R_{eq} < t_{s,max} \tag{4.5}$$

with

$$\sigma_n^{avg} = \frac{\sigma_t' + \sigma_n'}{2} \tag{4.6}$$

σ_t' and σ_n' are the effective stresses of the soil around the pile perpendicular to the pile. φ_i and c_i are the friction angle and cohesion of the interface element. R_{eq} is the equivalent radius, computed according to Equation (4.8). An input parameter for the layer-dependent option is R_{inter}. This value is the strength reduction factor for interfaces. The interface properties are calculated from the soil properties applying the following rules:

$$\begin{aligned} \tan\left(\varphi_i\right) &= R_{inter} \tan\left(\varphi_{soil}\right) \\ c_i &= R_{inter} c_{soil} \end{aligned} \tag{4.7}$$

Lateral displacements of the beam are allowed and a relative displacement between the beam and soil is accounted for, however there's no limit to the corresponding interaction tractions t_n and t_t. The normal stresses will therefore always remain elastic, resulting in the fact that slip in lateral direction does not occur. Changing the ultimate skin resistance or using the layer-dependent option and varying the R_{inter} factor won't have any effect on the lateral deformation behaviour or capacity, only on the axial deformation behaviour and capacity.

4.2. Elastic zone approach solving numerical problems

As was mentioned in Section 3.1.2, Engin et al. (2007) showed that the previously described embedded beam method is mesh sensitive. Figure 4.3 shows that for a very fine mesh and a fine mesh premature failure occurs. This is caused by numerical instability. The figure also shows that for finer meshes larger displacements at failure are found. This is to be expected in finite element analysis.

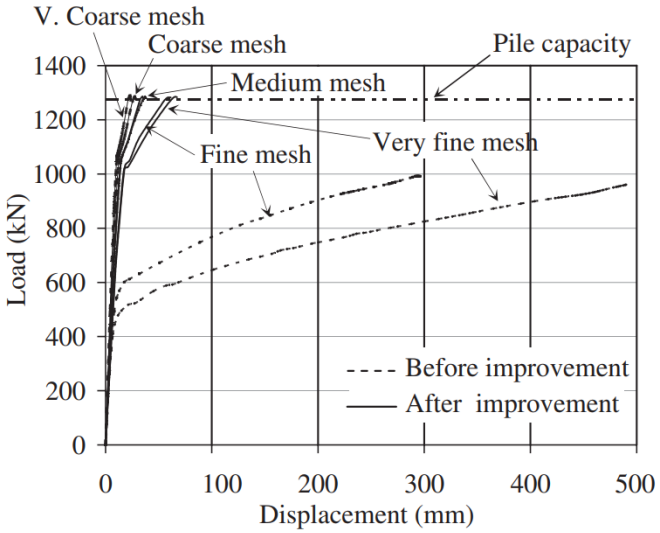

Figure 4.3: Load-displacement diagram with and without elastic zone approach, (Engin et al., 2007)

To solve the problem of numerical instability for fine meshes, an elastic zone is assumed around the pile. In this zone all Gaussian soil points are forced to remain elastic, as described in Engin et al. (2007). The size of this zone is determined by the equivalent pile radius, which is given by:

$$R_{eq} = \max\left\{\sqrt{\frac{A}{\pi}}, \sqrt{\frac{2I_{avg}}{A}}\right\} \tag{4.8}$$

where

$$I_{avg} = \frac{I_2 + I_3}{2} \tag{4.9}$$

4.3. Adjusting the interface stiffnesses

To study the influence of the interface stiffness, Tschuchnigg and Schweiger (2015) used a modified calculation kernel that allows the possibility to define the interface stiffnesses independently from the soil shear modulus. This definition also allows the possibility to define the axial and normal/tangential stiffnesses independently.

$$\begin{aligned} K_s &= 50 \cdot G_{soil} \cdot \Gamma_s + \Delta_s \\ K_n = K_t &= 50 \cdot G_{soil} \frac{2(1-\nu_i)}{1-2\nu_i} \cdot \Gamma_n + \Delta_n \\ K_{foot} &= 50 \cdot G_{soil} \cdot R_{eq} \cdot \Gamma_{foot} \end{aligned} \tag{4.10}$$

It was concluded that the interface stiffness K_{foot} should be increased by a factor of 5 to 10. A modification of K_s, K_n and K_t is not necessary. Increasing the interface stiffness K_{foot} has a big influence on the mobilisation of the base resistance by reducing the relative displacements necessary to mobilise the base resistance. This increased foot interface stiffness results in a better load-settlement behaviour.

However, the influence of the interface stiffnesses might be different when the interface is considered on a surface, instead of a line, as will be the case in the new formulation. Therefore, appropriate values for the interface stiffnesses have to be investigated again for the new formulation.

4.4. Limitations

Brinkgreve et al. (2015) states that, even though the elastic zone makes the embedded beam almost behave like a volume pile, installation effects of piles are not taken into account. This makes it impossible to capture the real soil behaviour around the pile circumference. Therefore, the embedded beam should primarily be used for some types of bored piles, but not for driven or soil displacement piles. It must be noted that the volume pile method doesn't take installation into account either.

It is possible in PLAXIS 3D to choose for a massive circular, circular tube or massive square cross-section shape. However, when using the square shape, it computes an equivalent radius, instead of taking the true cross-section shape into account.

The pile-soil interaction is evaluated at the beam axis, not at the real perimeter of the pile. This is the cause for several limitations in the existing embedded beam formulation, such as the inability to distinguish between the soil reactions working on the pile in normal or transversal direction.

The existing embedded beam implementation in PLAXIS 3D still behaves very mesh sensitive, despite the improvement of the elastic zone approach. This problem can easily be demonstrated by a simple test case of a vertically oriented pile with an axial load; see Section 4.4.1.

The existing formulation of the interface, doesn't allow for lateral slip between the soil and pile. Both the lateral shear component and normal stresses in the interface are unlimited. Therefore the interface will behave elastically in lateral direction for any loading. This behaviour is shown in Section 4.4.2, using a simple test case considering a disc that is pushed through the soil.

4.4.1. Alzey Bridge pile load test for axial loading

The Alzey Bridge pile load test is an axially loaded validation case, which is frequently used in previous studies to validate new methods. The Alzey Bridge pile load test was carried out near Frankfurt. During the test load cells were installed at the foot of the pile to measure the loads that are carried directly by the pile base, making it possible to differentiate between the pile base capacity and skin traction capacity. The test results and model parameters of the corresponding FE model are presented in Engin et al. (2007).

The Alzey Bridge pile load test considers an axially loaded pile with a diameter of 1.3 m and a length of 9.5 m. The ground water table is approximately 3.5 m below the ground surface. Figure 4.4 shows the geometry of the test case. The properties of the Hardening soil model that is used is shown in Appendix C.

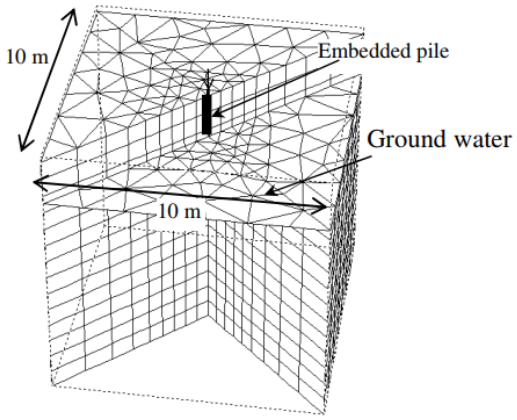

Figure 4.4: Alzey Bridge pile load test model. (Septanika et al., 2007)

The mesh sizes that are used for the models of the Alzey Bridge pile load test are shown in Table 4.1.

	Embedded beam		Volume pile	
	Elements	Nodes	Elements	Nodes
Mesh 1	129	234	974	1535
Mesh 2	231	384	3934	6078
Mesh 3	1063	1633	11796	17539
Mesh 4	6141	8721	31695	45893
mesh 5	46280	65215		

Table 4.1: Mesh sizes for Alzey Bridge pile load test

Volume pile method

In order to be able to compare and validate the embedded beam approach, the volume pile method will be used as a benchmark solution. In this method the pile is modelled by means of volume elements that are assigned a linear elastic, non-porous material type. Additionally, material properties that are suitable for piles can be entered. The interaction with the soil is modelled by interface elements along the skin. The interface elements make it possible to take relative displacements between the soil and the pile into account. A disadvantage of this method is that it needs more computation time.

Figure 4.5a shows results that have been obtained using the volume pile method in PLAXIS Foundation 3D Beta version versus measurement data. These results have been obtained years ago and since then PLAXIS 3D has seen many updates. Therefore, the Alzey Bridge pile load test has been modelled again using the volume pile method; the results are shown in Figure 4.5b.

In the paper by Engin et al. (2007) no indication of mesh size has been made, which makes it hard to compare the results in Figure 4.5a and Figure 4.5b. Nevertheless, the curves do seem to show the same behaviour, especially when the mesh is refined the results are very close.

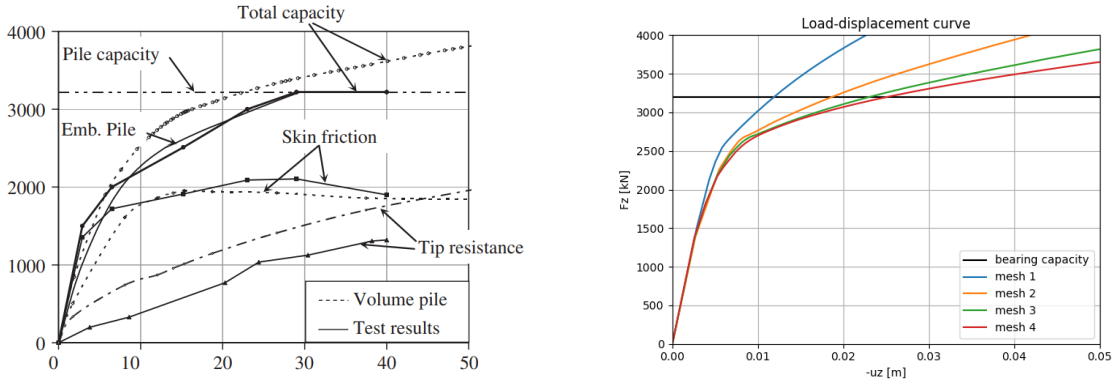

(a) Results from Engin et al. (2007)

(b) Volume pile method

Figure 4.5: Alzey Bridge pile load test data and volume pile results

Existing embedded beam method

Figure 4.6a shows the load displacement curves that have been obtained by measurements and modelling in PLAXIS Foundation 3D Beta version, see Engin et al. (2007). Since then, PLAXIS 3D has been updated, therefore it is necessary to check whether the embedded beam element still finds the same results. Results of the existing embedded beam element are shown in Figure 4.6b.

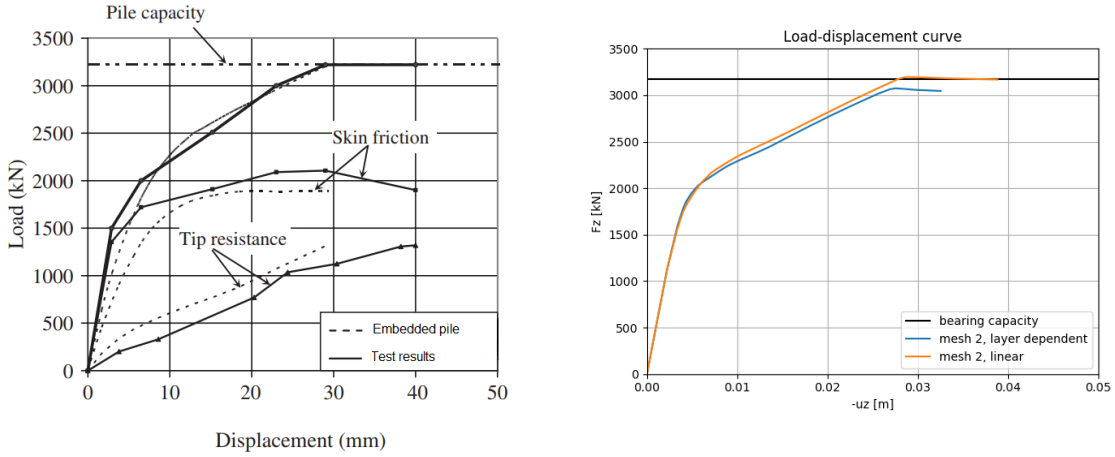

(a) Results from Engin et al. (2007)

(b) Results obtained with the existing embedded beam element in PLAXIS 3D

Figure 4.6: Alzey Bridge pile load test data and existing embedded beam results

For the linear traction model the base resistance is set equal to the maximum base resistance of the measurement data (1320 kN). The maximum skin tractions are determined by subtracting the base resistance from the ultimate failure load. A value of 201.37 kN/m for the maximum skin tractions yields the same failure load as the measurement data. The same input parameters are used by Tschuchnigg (2012). When the second mesh size (see Table 4.1) is used, the results are in very good agreement with the results that are obtained in Engin et al. (2007), who presumably uses the same input parameters for the linear traction model.

When the layer-dependent traction model is used, the failure load is slightly lower than the measurement data. The base resistance is still the same; 1320 kN. Therefore, the difference must be in the maximum skin tractions. In the layer-dependent traction model the maximum skin tractions are obtained using the strength and stresses from the surrounding soil. The simplified soil model that is used in PLAXIS 3D to model the test case doesn't match the real soil at the test site exactly, causing this slight difference in results.

The mesh sensitivity is shown in Figure 4.7a. When the mesh is refined in a finite element model, the results are expected to converge towards the exact solution. However, this is not what happens in the exist-

ing embedded beam formulation; Figure 4.7a clearly shows that for the first three mesh sizes the resulting displacements at failure keep on growing. For the fourth mesh size the results don't make sense at all any more; no failure is found when it is expected and the displacements that are found at failure don't have any recognizable relation with the results of the other mesh sizes.

Figure 4.7b shows the results of the Alzey Bridge pile load test modelled with the embedded beam element when the elastic zone approach is deactivated. In Section 4.2 it was described that the embedded beam formulation without elastic zone approach showed premature failure. In order to solve localised behaviour that causes mesh dependency, the elastic zone approach is implemented. Comparing Figure 4.7a and Figure 4.7b indeed shows that the inclusion of the elastic zone approach reduces the mesh sensitivity in the first part of loading.

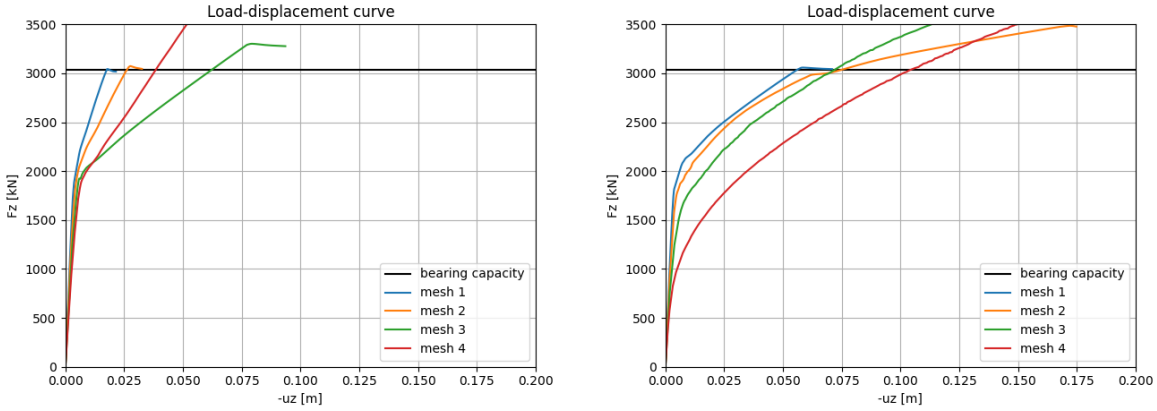

(a) Elastic zone activated

(b) Elastic zone deactivated

Figure 4.7: Alzey Bridge model calculated with existing embedded beam formulation for different mesh sizes and with and without elastic zone approach

4.4.2. Laterally loaded disc

A simple test case, as proposed by Dao (2011), that only models one meter of the soil and beam is used to validate lateral loading behaviour. An overview of the model is presented in Figure 4.8.

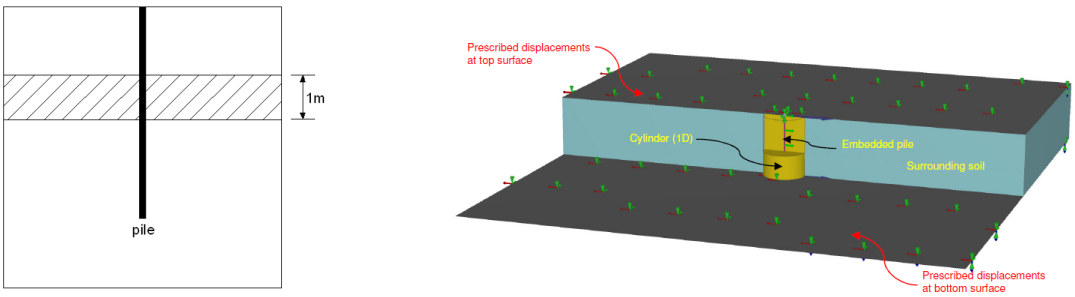

(a) 1 meter cross-section

(b) Model overview in PLAXIS 3D

Figure 4.8: Laterally loaded disc model. (Dao, 2011)

Around the embedded beam element a cylinder with a diameter equal to the diameter of the pile (0.7 m) is modelled. Inside this cylinder soil with the exact same properties as the surrounding soil is modelled. This cylinder is used to manipulate the mesh around the embedded beam. The incorporation of the cylinder ensures that there are element boundaries located at the pile perimeter. This makes the embedded beam model more comparable with the volume pile model, as the mesh of the volume pile model always has element boundaries at the interaction surface.

Dao used a prescribed displacement at the top and bottom of the embedded beam element of 0.2 m, but in the results presented in this report a load is prescribed at the top and bottom of the pile. The reason for this is explained in Section B.3.

The model dimensions are 8x8x1 m. The soil and embedded beam properties of the model are shown in Appendix C. It is important to note that a 'drained' soil type is used with a zero effective friction angle. This ensures that the drained shear strength of the soil is fully determined by the effective cohesion (Figure 4.9). In addition, the unit weight of the soil and beam are set to zero in order to neglect the initial stresses and increase of the drained shear strength with depth.

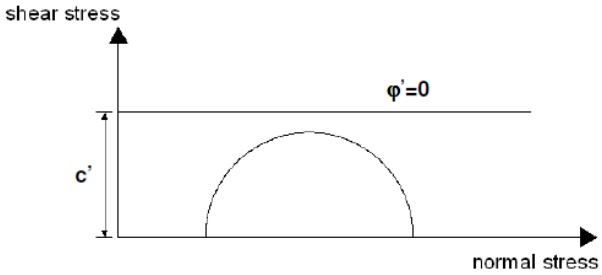

Figure 4.9: Drained shear strength c'. (Dao, 2011)

The volume pile method results are used as a benchmark solution, enabling a comparative analysis with the embedded beam models.

The mesh sizes that are used for the laterally loaded disc test case are shown in Table 4.2.

	Embedded beam				Volume pile	
	Manipulated mesh		No manipulated mesh			
	Elements	Nodes	Elements	Nodes	Elements	Nodes
Mesh 1	3593	4765	2996	4008	4064	5448
Mesh 2	7578	10 000	7799	10276	7282	9646
Mesh 3	10 062	13 370	10 012	13 314	10710	14151
Mesh 4	28 214	37 292	26 593	35 303	29863	39399

Table 4.2: Mesh sizes for laterally loaded disc test case

Volume pile method

Figure 4.10 shows the results for the volume pile method. The results show that there is still some mesh sensitivity left, even when the volume pile method is used (Figure 4.10a). The mesh sensitivity is reduced considerably when an interface is modelled around the beam (Figure 4.10b). The usage of the interface also reduces the failure load of the model, because slip of the soil around the pile is captured. This is more realistic.

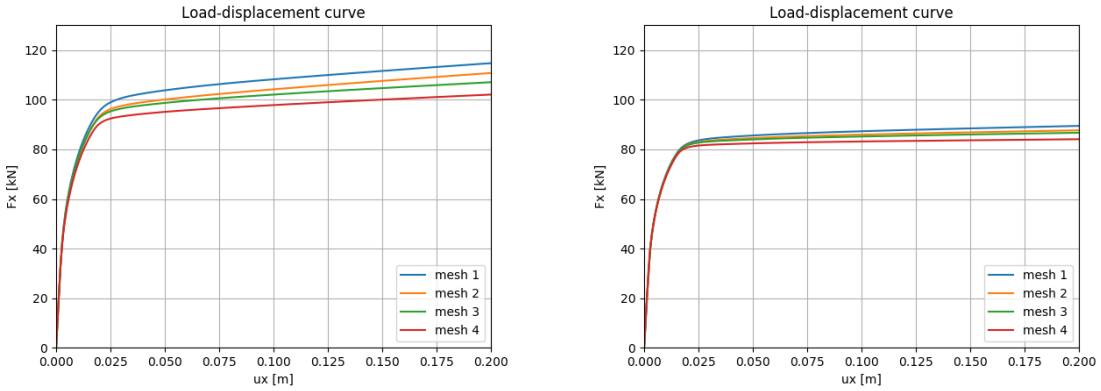

(a) Volume pile without interface

(b) Volume pile with interface

Figure 4.10: Laterally loaded disc modelled with the volume pile method

Existing embedded beam

Figure 4.11 shows the results for the existing embedded beam formulation. Either with and without a manipulated mesh that ensures element boundaries at the pile perimeter. Figure 4.11a shows that the existing formulation is very good at capturing the same behaviour as the volume pile method without an interface.

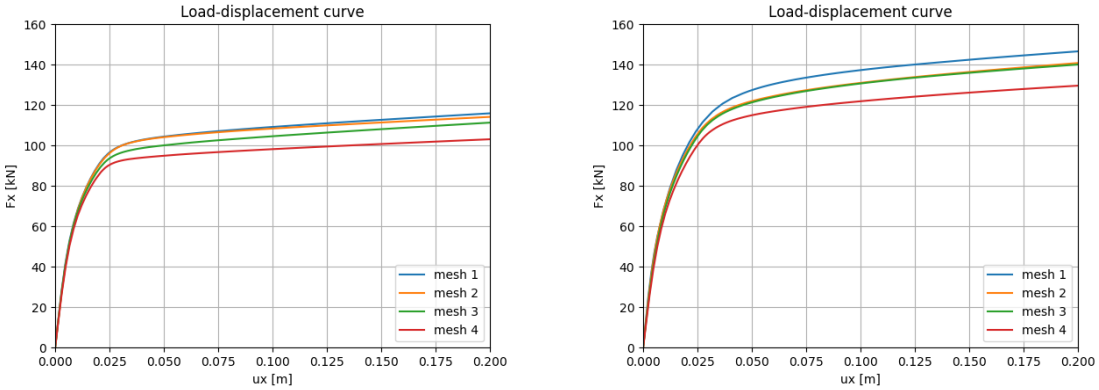

(a) Existing embedded beam formulation with manipulated mesh

(b) Existing embedded beam formulation without manipulated mesh

Figure 4.11: Laterally loaded disc modelled with existing embedded beam element. Layer-dependent traction model

The influence of the elastic zone approach is visualised in Figure 4.12. Clearly, the elastic zone influences the results of the existing embedded beam model significantly. When the elastic zone is deactivated, the failure load that is obtained is unrealistically low and the mesh sensitivity is increased.

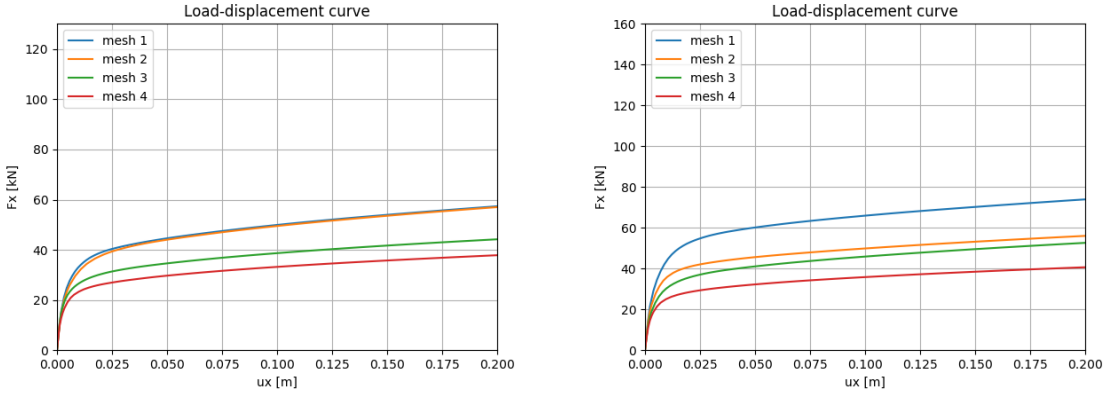

(a) Existing embedded beam model with manipulated mesh

(b) Existing embedded beam model without manipulated mesh

Figure 4.12: Laterally loaded disc model with deactivated elastic zone

II

Model Development

5

Embedded beam element with explicit interaction surface

This chapter presents a new method to model an embedded beam element with an explicit interaction surface on which the interaction between the pile and soil is described (Figure 5.1). This formulation is formulated in such a way that the possible inclination of a pile is taken into account. The beam element in PLAXIS 3D is based on the Timoshenko beam theory, explained in Section 5.1.

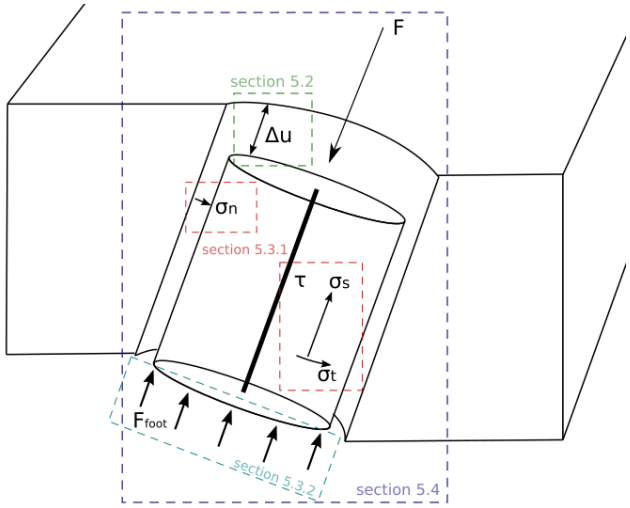

Figure 5.1: Outline of Chapter 5

At first, the discretised kinematic equations are derived (Section 5.2), starting with the determination of the beam displacements at the interaction surface (Section 5.2.1). Next, three different methods to obtain the soil displacements at the interaction surface are described in Section 5.2.2. The difference between the beam and soil displacements at the interaction surface is fundamental for the kinematics of the virtual interface elements around the embedded beam element.

Second, the constitutive model for the new embedded beam elements is presented (Section 5.3), distinguishing between the shaft and foot interface. In addition to the modifications that are necessary for the transformation from beam axis to explicit interaction surface, three different methods to include a correction for lateral plasticity along the shaft are proposed.

At last the equilibrium equations for the model are derived in Section 5.4. The kinematic, constitutive and equilibrium equations together form the full description of the new embedded beam formulation.

5.1. Three-dimensional Timoshenko beam theory

Whereas the Euler-Bernoulli beam theory assumes that a plane that is initially normal to the longitudinal axis remains plane and normal to the longitudinal axis, in Timoshenko beam theory planes must remain plane, but not necessarily normal to the longitudinal axis. This allows for shear deformations to be taken into account. The rotation of a plane is given by:

$$\theta_x = \frac{dw}{dx} - \gamma \tag{5.1}$$

where γ is the rotation due to shear deformations. This is graphically shown in Figure 5.2.

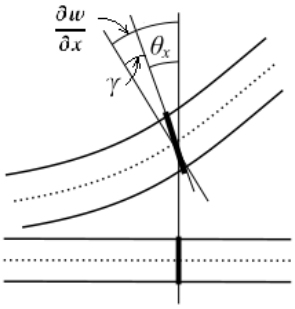

Figure 5.2: Deformation of a Timoshenko beam

5.2. Kinematic equations

A new embedded beam element with an explicit interaction surface is proposed, based on the ideas of Turello et al. (2016a,b). The starting point is the existing embedded beam implementation in PLAXIS 3D. In this method the beam is modelled as a line element with three nodes. The transformation to the explicit interaction surface takes place at the height of these three nodes (Figure 5.3).

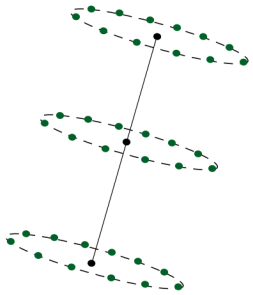

Figure 5.3: Considered points on the interaction surface, depending on nCirDiv[1]

This section first explains how the beam displacements at the interaction surface are obtained and subsequently three different methods to obtain the soil displacements at the interaction surface are presented. The beam and soil displacements at the interaction surface are necessary to compute the relative displacements in the virtual interface. After discretisation this should result in an expression of the form: $\boldsymbol{\Delta u} = \boldsymbol{B a^e}$. The deformation matrix ($\boldsymbol{B}$) is necessary to compute both the element stiffness matrices and force vectors (Section 5.4). The vector $\boldsymbol{a^e}$ contains the nodal displacement components of the considered beam and soil element.

5.2.1. Beam displacements at interaction surface

The finite element formulation of the three-dimensional curved beam element as is currently implemented in PLAXIS 3D, is based on the theory in Bathe (2014). In this section the same philosophy will be used to find the beam displacements at the interaction surface for a circular cross-section. The result provides a method

[1] nCirDiv is the number of points on the interaction surface

that takes into account the beam curvature and is generalised for possibly inclined piles. This is an extension of the method proposed by Turello et al. (2016a).

In addition, the cross-section shape of the pile doesn't necessarily have to be circular. Therefore, a similar formulation for rectangular cross-section shapes is presented in Appendix D.1.

Figure 5.4 shows the geometry of a circular beam element. In this figure (x, y, z) is the global coordinate system and $\boldsymbol{V_1}$, $\boldsymbol{V_2}$, $\boldsymbol{V_3}$ are local unit vectors.

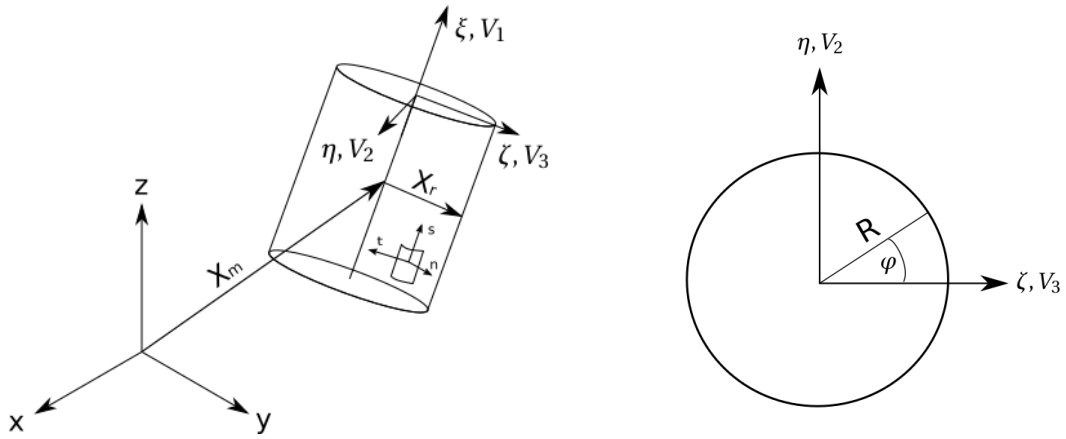

(a) 3D view

(b) Topview

Figure 5.4: Geometry of an embedded beam element

To describe the location of a point on the interaction surface two steps have to be taken; first the location on the beam axis needs to be determined ($\boldsymbol{X_m}$), then this point can be mapped to the explicit interaction surface ($\boldsymbol{X_r}$). The location on the interaction surface in the undeformed state is then given by:

$$\boldsymbol{X^0} = \boldsymbol{X_m^0} + \boldsymbol{X_r^0} \tag{5.2}$$

The superscript 0 denotes the undeformed state, 1 denotes the deformed state. The vector $\boldsymbol{X_r}$ can be described using the radius of the pile R and the angle φ (Figure 5.4b), according to:

$$\boldsymbol{X_r} = R\cos\varphi \cdot \boldsymbol{V_3} + R\sin\varphi \cdot \boldsymbol{V_2} \tag{5.3}$$

The beam displacement at the interaction surface at a certain location is the difference between the deformed and undeformed state. This displacement can be calculated by combination of Equations (5.2) and (5.3):

$$\boldsymbol{u_b} = \boldsymbol{X^1} - \boldsymbol{X^0} = \underbrace{\left(\boldsymbol{X_m^1} - \boldsymbol{X_m^0}\right)}_{\boldsymbol{u_m}} + R\cos\varphi \cdot \left(\boldsymbol{V_3^1} - \boldsymbol{V_3^0}\right) + R\sin\varphi \cdot \left(\boldsymbol{V_2^1} - \boldsymbol{V_2^0}\right) \tag{5.4}$$

Substitution of the relation $\boldsymbol{V_3^1} - \boldsymbol{V_3^0} = \boldsymbol{\theta} \times \boldsymbol{V_3^0}$ gives:

$$\boldsymbol{u_b} = \boldsymbol{u_m} + R\cos\varphi \cdot \left(\boldsymbol{\theta} \times \boldsymbol{V_3^0}\right) + R\sin\varphi \cdot \left(\boldsymbol{\theta} \times \boldsymbol{V_2^0}\right) \tag{5.5}$$

The cross product $\boldsymbol{\theta} \times \boldsymbol{V_3^0}$ can be transformed to a dot product of a matrix $\boldsymbol{W_3}$ and $\boldsymbol{\theta}$, according to:

$$\boldsymbol{W_3} \cdot \boldsymbol{\theta} = \begin{bmatrix} 0 & V_{3z}^0 & -V_{3y}^0 \\ -V_{3z}^0 & 0 & V_{3x}^0 \\ V_{3y}^0 & -V_{3x}^0 & 0 \end{bmatrix} \begin{bmatrix} \theta_x \\ \theta_y \\ \theta_z \end{bmatrix} \tag{5.6}$$

The same can be done for the cross product between $\boldsymbol{\theta} \times \boldsymbol{V_2^0}$ by replacing subscript 3 with 2 in the above equation.

The beam displacements at the interaction surface can be discretised, using the standard finite element discretisations for $\boldsymbol{u_b} = \boldsymbol{N^b u_b^e}$ and $\boldsymbol{\theta} = \boldsymbol{N^b \theta^e}$. Combining all equations gives the following discretisation:

$$\begin{aligned}\boldsymbol{u_b} = &\begin{bmatrix} N_1^b & 0 & 0 & \cdots & N_3^b & 0 & 0 \\ 0 & N_1^b & 0 & \cdots & 0 & N_3^b & 0 \\ 0 & 0 & N_1^b & \cdots & 0 & 0 & N_3^b \end{bmatrix} \begin{bmatrix} u_{1x}^b \\ \vdots \\ u_{3z}^b \end{bmatrix} \\ &+ R \cdot \cos\varphi \cdot \begin{bmatrix} 0 & V_{3z}^0 & -V_{3y}^0 \\ -V_{3z}^0 & 0 & V_{3x}^0 \\ V_{3y}^0 & -V_{3x}^0 & 0 \end{bmatrix} \begin{bmatrix} N_1^b & 0 & 0 & \cdots & N_3^b & 0 & 0 \\ 0 & N_1^b & 0 & \cdots & 0 & N_3^b & 0 \\ 0 & 0 & N_1^b & \cdots & 0 & 0 & N_3^b \end{bmatrix} \begin{bmatrix} \theta_{1x} \\ \vdots \\ \theta_{3z} \end{bmatrix} \\ &+ R \cdot \sin\varphi \cdot \begin{bmatrix} 0 & V_{2z}^0 & -V_{2y}^0 \\ -V_{2z}^0 & 0 & V_{2x}^0 \\ V_{2y}^0 & -V_{2x}^0 & 0 \end{bmatrix} \begin{bmatrix} N_1^b & 0 & 0 & \cdots & N_3^b & 0 & 0 \\ 0 & N_1^b & 0 & \cdots & 0 & N_3^b & 0 \\ 0 & 0 & N_1^b & \cdots & 0 & 0 & N_3^b \end{bmatrix} \begin{bmatrix} \theta_{1x} \\ \vdots \\ \theta_{3z} \end{bmatrix}\end{aligned} \tag{5.7}$$

The translational and rotational nodal degrees of freedom can be combined in one vector; $\boldsymbol{a^b}$. In order to write the discretisation in the form $\boldsymbol{u_b} = \boldsymbol{H} \cdot \boldsymbol{a^b}$, the matrix $\boldsymbol{H}$ is defined as:

$$\begin{aligned}\boldsymbol{H} = &\begin{bmatrix} N_1^b & 0 & 0 & \cdots & N_3^b & 0 & 0 & \cdots \\ 0 & N_1^b & 0 & \cdots & 0 & N_3^b & 0 & \\ 0 & 0 & N_1^b & \cdots & 0 & 0 & N_3^b & \end{bmatrix} \\ &\begin{bmatrix} 0 & G(1,z) & -G(1,y) & \cdots & 0 & G(3,z) & -G(3,y) \\ -G(1,z) & 0 & G(1,x) & \cdots & -G(3,z) & 0 & G(3,x) \\ G(1,y) & -G(1,x) & 0 & \cdots & G(3,y) & -G(3,x) & 0 \end{bmatrix}_{(3\times 18)}\end{aligned} \tag{5.8}$$

with

$$G(\alpha,\beta) = R N_\alpha^b \left(\cos\varphi \cdot V_{3\beta}^0 + \sin\varphi \cdot V_{2\beta}^0 \right) \tag{5.9}$$

5.2.2. Soil displacements at interaction surface

To find the soil displacements at the interaction surface three different methods are formulated. Instead of acquiring the exact soil displacements at the interaction surface, the first two methods approximate the soil displacements. The first of these methods obtains the soil displacements at the interaction surface by extrapolation from the soil element at the beam axis (method A). Extrapolation is more inaccurate than interpolation, therefore the second method that is considered obtains the soil displacements at the interaction surface by correcting the soil displacements at the beam axis (interpolation) with a first order Taylor approximation (method B). Higher order Taylor approximations can be used as well, but the implementation of them is not straightforward, and therefore they are not considered during this research. Approximating the soil displacements would reduce the computational effort tremendously compared to calculating the exact soil displacements at the interaction surface. Therefore, they are interesting to evaluate.

The third method that is considered determines the soil displacements at the interaction surface in the most accurate way possible (method C). Interpolation inside the soil elements at the interaction surface is used. This method has a drawback; it requires more computational effort. Alternative approximation methods are not evaluated during this research due to time constraints. The goal of this research is to provide an indication of the capability of the proposed embedded beam formulation. If the new method doesn't work with method C, evaluation of more approximation methods would have been superfluous.

All three methods are described in more detail in this section.

Method A

This method uses extrapolation to obtain the soil displacements at the interaction surface. The soil displacements at the interaction surface are obtained using the interpolation functions (shape functions) of the soil element in which the beam axis is located. For piles with large diameters or when a fine mesh is used in the model, the interaction surface might lie outside this soil element (Figure 5.5). In this case, inserting the local coordinates of the points on the interaction surface into the shape functions of this central soil element results in extrapolation.

Implementation of this method is straightforward. The existing embedded beam model uses the same soil elements, hence the connectivity of the beam elements to these soil elements is already present. The only

thing that needs to be modified is the computation of the global coordinates of the points on the interaction surface. When the global coordinates are known, the local soil coordinates can readily be computed based on the shape functions of the soil element in which the beam axis is located.

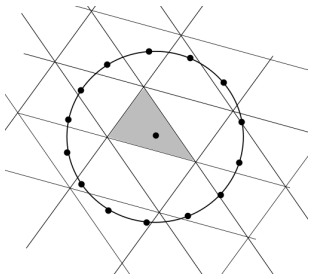

Figure 5.5: Graphical representation of method A

The soil displacements at the interaction surface can be discretised by $\boldsymbol{u_s} = \boldsymbol{N^s} \cdot \boldsymbol{a^s}$. The relative displacement between the pile and soil at the interaction surface can now be computed:

$$\boldsymbol{u_{rel}} = \boldsymbol{u_b} - \boldsymbol{u_s} = \boldsymbol{H} \cdot \boldsymbol{a^b} - \boldsymbol{N^s} \cdot \boldsymbol{a^s} \tag{5.10}$$

This can be written as:

$$\boldsymbol{u_{rel}} = \underbrace{\begin{bmatrix} \boldsymbol{H} & -\boldsymbol{N^s} \end{bmatrix}}_{\boldsymbol{B}_{(3\times 48)}} \cdot \underbrace{\begin{bmatrix} \boldsymbol{a^b} \\ \boldsymbol{a^s} \end{bmatrix}}_{\boldsymbol{a^e}_{(48\times 1)}} \tag{5.11}$$

Method B

This method uses interpolation in combination with a first order Taylor correction to obtain the soil displacements at the interaction surface. First, the soil displacements at the beam axis are computed using interpolation, similar as in the existing formulation. Subsequently, a correction in the form of a first order Taylor approximation is applied. The first order Taylor correction is based on the radius of the pile and the gradient of the soil displacements at the pile axis in the direction towards the considered point on the interaction surface. Figure 5.6 shows a graphical representation of this method.

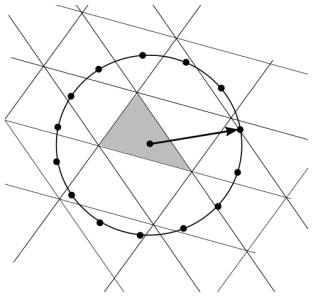

Figure 5.6: Graphical representation of method B

In order to apply this method the B-matrix, as determined in the previous section, needs to be modified. The soil displacements at the interaction surface are now given by:

$$\boldsymbol{u_s} = \boldsymbol{u_{s,axis}} + \frac{\partial \boldsymbol{u_{s,axis}}}{\partial x}\delta x + \frac{\partial \boldsymbol{u_{s,axis}}}{\partial y}\delta y + \frac{\partial \boldsymbol{u_{s,axis}}}{\partial z}\delta z + O(h^2) \tag{5.12}$$

Substituting the discretisation $\left(\boldsymbol{u_{s,axis}} = \boldsymbol{N^s a_s}\right)$ gives:

$$\begin{aligned}\boldsymbol{u_s} &= \boldsymbol{N^s a_s} + \frac{\partial \boldsymbol{N^s}}{\partial x}\boldsymbol{a_s}\delta x + \frac{\partial \boldsymbol{N^s}}{\partial y}\boldsymbol{a_s}\delta y + \frac{\partial \boldsymbol{N^s}}{\partial z}\boldsymbol{a_s}\delta z + O(h^2)\\ &= \boldsymbol{N^s a_s} + \left(\frac{\partial \boldsymbol{N^s}}{\partial \xi}\frac{\partial \xi}{\partial x} + \frac{\partial \boldsymbol{N^s}}{\partial \eta}\frac{\partial \eta}{\partial x} + \frac{\partial \boldsymbol{N^s}}{\partial \zeta}\frac{\partial \zeta}{\partial x}\right)\boldsymbol{a_s}\delta x\\ &\quad + \left(\frac{\partial \boldsymbol{N^s}}{\partial \xi}\frac{\partial \xi}{\partial y} + \frac{\partial \boldsymbol{N^s}}{\partial \eta}\frac{\partial \eta}{\partial y} + \frac{\partial \boldsymbol{N^s}}{\partial \zeta}\frac{\partial \zeta}{\partial y}\right)\boldsymbol{a_s}\delta y\\ &\quad + \left(\frac{\partial \boldsymbol{N^s}}{\partial \xi}\frac{\partial \xi}{\partial z} + \frac{\partial \boldsymbol{N^s}}{\partial \eta}\frac{\partial \eta}{\partial z} + \frac{\partial \boldsymbol{N^s}}{\partial \zeta}\frac{\partial \zeta}{\partial z}\right)\boldsymbol{a_s}\delta z + O(h^2)\end{aligned} \tag{5.13}$$

In the PLAXIS 3D source code the derivatives of the shape functions are already determined and a subroutine exists that computes the inverse of the Jacobian. In order to apply this method the B-matrix now looks as follows:

$$\boldsymbol{B} = \begin{bmatrix} & & -N_1^s - \left(\boldsymbol{dN_1^s}\right)^T \boldsymbol{J^{-1}X_r} & 0 & 0 & \cdots \\ \boldsymbol{H} & \cdots & 0 & -N_1^s - \left(\boldsymbol{dN_1^s}\right)^T \boldsymbol{J^{-1}X_r} & 0 & \cdots \\ & & 0 & 0 & -N_1^s - \left(\boldsymbol{dN_1^s}\right)^T \boldsymbol{J^{-1}X_r} & \cdots \\ & & -N_{10}^s - \left(\boldsymbol{dN_{10}^s}\right)^T \boldsymbol{J^{-1}X_r} & & & \\ & & 0 & -N_{10}^s - \left(\boldsymbol{dN_{10}^s}\right)^T \boldsymbol{J^{-1}X_r} & 0 & \\ & & 0 & 0 & -N_{10}^s - \left(\boldsymbol{dN_{10}^s}\right)^T \boldsymbol{J^{-1}X_r} & \end{bmatrix} \tag{5.14}$$

Here $\boldsymbol{X_r}$ is the vector containing δx, δy and δz, which are the components of the distance between the pile axis and the point on the circumference. The Jacobian matrix ($\boldsymbol{J}$) and the derivative of the shape function $\boldsymbol{dN_i^s}$ are given by:

$$\boldsymbol{J} = \begin{bmatrix} \frac{\partial x}{\partial \xi} & \frac{\partial y}{\partial \xi} & \frac{\partial z}{\partial \xi} \\ \frac{\partial x}{\partial \eta} & \frac{\partial y}{\partial \eta} & \frac{\partial z}{\partial \eta} \\ \frac{\partial x}{\partial \zeta} & \frac{\partial y}{\partial \zeta} & \frac{\partial z}{\partial \zeta} \end{bmatrix}, \quad \boldsymbol{dN_i^s} = \begin{bmatrix} \frac{\partial N_i^s}{\partial \xi} \\ \frac{\partial N_i^s}{\partial \eta} \\ \frac{\partial N_i^s}{\partial \zeta} \end{bmatrix} \tag{5.15}$$

This B-matrix can be substituted in Equation (5.11).

Method C

This method obtains the soil displacements at the interaction using the soil elements at the interaction surface (Figure 5.7). Interpolation can be used again to obtain the displacements in the exact point on the circumference. This is the most accurate way to find the soil displacements at the interaction surface, and therefore the most accurate way to make use of this explicit interaction surface.

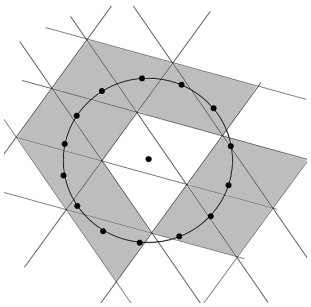

Figure 5.7: Graphical representation of method C

However, the implementation of this method is a little more difficult than for method A and B. If, for example, 10 points are considered at the interaction surface for every integration point of the beam element. This means $10 \cdot 3 = 30$ points that need to be considered, which might all lie in a different soil element. Every soil element has 10 nodes, so this means that the total element stiffness matrix might become a 918 x 918 matrix[2]. Besides, the size of the stiffness matrix might be different for every embedded beam element. This

[2] 3 beam nodes with 6 DOF's and $10 \cdot 30$ soil nodes with 3 DOF's: $6 \cdot 3 + 10 \cdot 30 \cdot 3 = 918$

means very large stiffness matrices and a very difficult assembly procedure. A solution for this problem is to assemble the contributions of every point on the interaction surface separately to the global stiffness matrix. The same method can be used to assemble the force vector.

This method makes sure that the B-matrix looks the same as for method A (Equation (5.11)). Only, now the local coordinates of the points on the interaction surface are different. The search for and storage of the correct soil elements and the local coordinates of the points on the interaction surface is done only once at the beginning of the calculation.

5.3. Constitutive model

To compute the stresses at the interaction surface, the relative displacements at the local (s,n,t) level (Figure 5.4a) are necessary. These can be computed by transforming Equation (5.11) to the local coordinate system:

$$\boldsymbol{u_{rel}} = \boldsymbol{B} \cdot \boldsymbol{a^e} = \boldsymbol{B R_\varphi T} \cdot \boldsymbol{a^e_{global}} \tag{5.16}$$

First a transformation from the global (x,y,z) coordinate system to the local beam (ξ,η,ζ) coordinate system is done, described by transformation matrix $\boldsymbol{T}$. Subsequently, a transformation from the local beam (ξ,η,ζ) coordinate system to the local coordinate system at the pile circumference (s,n,t) is done, described by $\boldsymbol{R_\varphi}$. The different coordinate systems are shown in Figure 5.4a.

Transformation matrix $\boldsymbol{T}$ is already present in the existing implementation of the embedded beam element in PLAXIS 3D. It makes sure that the ξ axis is aligned with the beam axis (Appendix B.2). The transformation matrix $\boldsymbol{R_\varphi}$ is given by:

$$\boldsymbol{R_\varphi} = \begin{bmatrix} 1 & 0 & 0 \\ 0 & \cos(\varphi) & \sin(\varphi) \\ 0 & -\sin(\varphi) & \cos(\varphi) \end{bmatrix} \tag{5.17}$$

5.3.1. Shaft interface

Since the interaction between the pile and soil is now described on a surface, instead of at a line, the incremental traction update of the existing embedded beam formulation transforms to an incremental stress update.

$$\boldsymbol{\sigma_i} = \boldsymbol{\sigma_i^t} + \Delta\boldsymbol{\sigma_i} \tag{5.18}$$

with:

$$\Delta\boldsymbol{\sigma_i} = \boldsymbol{D^e} \cdot \Delta\boldsymbol{u_{rel}} \tag{5.19}$$

It must be noted that this material stiffness matrix $\boldsymbol{D^e}$ with the material stiffnesses K_n, K_s and K_t is not the same as the one in Equation (4.1). The existing embedded beam formulation considers the interface element as a line element with tractions in [kN/m]. The new embedded beam formulation considers the interface as a surface with stresses in [kN/m^2]. In order to find stresses, the units of the interface stiffnesses are defined in [kN/m^3] instead of [kN/m^2].

In the existing formulation the interface element is a line with a certain length. In the new formulation the interface element is a surface with the same length as in the existing formulation and with a width of $2\pi R$/nCirDiv. Therefore, in the new formulation the total interface stiffness matrix and force vector are computed by taking double integrals; an integral over the length (same as before) and an integral over the circumference over the pile. That's where the difference comes in compared to the existing formulation.

$$\begin{aligned} \int_0^L \boldsymbol{D^e u_{rel}}\, dl &= \int_0^L \int_0^{2\pi} \boldsymbol{D^e_{new} u_{rel}}\, dl\, R d\varphi \\ \boldsymbol{D^e u_{rel}} &= \int_0^{2\pi} \boldsymbol{D^e_{new} u_{rel}}\, R d\varphi \\ \boldsymbol{D^e_{new}} &= \frac{\boldsymbol{D^e}}{2\pi R} \end{aligned} \tag{5.20}$$

So, the new interface stiffnesses are the existing ones divided by the circumference $2\pi R$.

In the objective of this research it was mentioned that, on top of implementing a new embedded beam formulation that describes the interaction between the pile and the soil on an explicit interaction surface, the possibility of a lateral interface shall be investigated. In order to achieve this goal three methods to incorporate a correction for lateral plasticity along the shaft are proposed.

To allow for slip of the soil along the pile, maximum allowable stresses at the interaction surface have to be defined. In Section 4.1 three methods are described that are currently available in PLAXIS 3D to define the ultimate skin resistance. The linear and multi-linear options have the disadvantage that the bearing capacity of the pile needs to be defined by the user; it is an input variable. However, it is more realistic to have the bearing capacity of the pile as a result from the analysis. This is the case in the third option; the layer-dependent option. This option links the ultimate skin resistance of the pile to the strength parameters of the surrounding soil and to the stress state in the soil.

Equation (4.5) defines the maximum allowable axial shear traction in the interface for the layer-dependent option. To allow not only for axial slip, but also slip in lateral direction, a different expression is necessary that limits σ_t as well. Slip in axial and transversal direction can easily be combined:

$$\sqrt{\sigma_s^2 + \sigma_t^2} \leq c_i - \sigma_n \tan\varphi_i \tag{5.21}$$

The multiplication by $2\pi R$ can be omitted, since stresses are considered instead of tractions. The standard interface elements in PLAXIS 3D do not limit the normal stresses in the interface. The compression limit in soil is not determined by a limit in compressive normal stresses, but by the fact that it finds planes for which the shear limit is reached. When this happens the soil starts sliding along that plane. When the interaction between the interface and soil is modelled correctly, growing normal stresses in the interface should induce failure planes in the surrounding soil. For this reason, no limit for the normal stresses in the interface is required.

The normal stress in Equation (5.21) can either be taken from the soil ($\sigma_{n,soil}$) or from the interface ($\sigma_{n,int}$). This results in two possible methods to incorporate a correction for lateral plasticity:

- **Method 1**: Including correction for lateral plasticity by Equation (5.21), using the normal stresses from the soil.
- **Method 2**: Including correction for lateral plasticity by Equation (5.21), using the normal stresses from the interface.

When $\sqrt{\sigma_s^2 + \sigma_t^2} - \left(c_i - \sigma_n \cdot \tan\varphi\right) > 0$ the shear stresses are updated as follows:

$$\begin{aligned} Fac &= \frac{\left(c_i - \sigma_n \cdot \tan\varphi\right) - \sqrt{\sigma_s^2 + \sigma_t^2}}{\sqrt{\sigma_s^2 + \sigma_t^2}} \\ \sigma_s &= \sigma_s + \sigma_s \cdot Fac \\ \sigma_t &= \sigma_t + \sigma_t \cdot Fac \end{aligned} \tag{5.22}$$

The stress update method in Equation (5.22) is not conform the return mapping procedure as described in Van Langen (1991). Van Langen used a plastic potential function to derive the rate of plastic slip, which he incorporated in the return mapping method in order to return the plastic stresses to the yield surface more accurately. However, the correct return mapping algorithm can only be used when the normal stresses from the interface are used in Equation (5.21). Also, a similar method as described in Equation (5.22) is applied in the existing embedded beam model. Therefore, application of this method makes the new methods in better correspondence with the existing embedded beam formulation.

The third method to include lateral plasticity uses the normal stresses from the interface in combination with the correct return mapping algorithm (Van Langen (1991), Appendix D.2). The return mapping is done in a separate subroutine.

- **Method 3**: Including correction for lateral plasticity by calling the correct return mapping scheme (Appendix D.2), using the normal stresses from the interface in Equation (5.21).

So, method 3 is the only method that takes into account the correct return mapping of plastic stresses to the yield surface according to plasticity theory.

5.3.2. Foot interface

In the existing formulation the foot interface is working on one point (the beam axis) at the base of the foot. This introduces a stress singularity, which causes problems with mesh refinements. In order to solve this

(a) Current foot resistance on one point (b) Foot resistance spread over more points

Figure 5.8: Visualisation of the foot resistance

problem an improved foot interface is formulated. The foot interface is now considered as a surface, distributing the foot resistance over multiple points on this surface, not just one (Figure 5.8b).

The choice to use points on the circumference (Figure 5.8b) is not incidental. PLAXIS considers sparse storage of the global stiffness matrix, requiring that the connectivity between DOF's is known beforehand in order to add components to the global stiffness matrix. If a stiffness contribution is added to a location in the stiffness matrix that is expected to remain zero, the contribution will not be added and the calculation will break. The points on the circumference are already used to describe the pile-soil interaction at the pile shaft, therefore using these points is the easiest way to effectively improve the foot interface.

However, it must be noted that this doesn't result in an uniform distribution of points over the cross-section area. In fact, this distribution looks more like a circular line load than a circular distributed surface load. The distribution of the considered points on the foot interface can therefore be improved, but optimisation lies outside the scope of this research. For now, the focus is on evaluating the potential of the new embedded beam formulation.

In the existing embedded beam formulation the relation between the foot resistance and the relative displacements in the interface is described by Equation (4.3). Now the foot resistance is spread over the cross-section area; πR^2, changing the base resistance in kN on one point to a stress [kN/m^2] over an area. In order to achieve this, Equation (4.3) is changed to:

$$\sigma_{foot} = \frac{K_{foot}}{\pi R^2} \cdot u_{rel,s} \leq \frac{F_{max}}{\pi R^2} \tag{5.23}$$

This gives a foot interface stiffness of:

$$K_{foot,new} = \frac{50 \cdot G_{soil} \cdot R}{\pi R^2} = \frac{50 \cdot G_{soil}}{\pi R} \tag{5.24}$$

5.4. Equilibrium equations

The principle of virtual work states that the equilibrium of the considered volume requires that for any compatible small virtual displacement imposed on it, the total internal virtual work is equal to the total external virtual work. This is generally determined as:

$$\underbrace{\int_V \delta\boldsymbol{\varepsilon}^T \boldsymbol{\sigma}\, dV}_{\text{Internal virtual work}} = \underbrace{\int_V \delta\boldsymbol{u}^T \boldsymbol{f} dV}_{\text{External virtual work}} \tag{5.25}$$

Here, the internal stresses $\boldsymbol{\sigma}$ are in equilibrium with the applied loads $\boldsymbol{f}$.

Usually, Hooke's law is used to describe the relation between the stresses and strains in the constitutive model. However, in case of the virtual interface elements considered in this chapter, the constitutive model describes the relation between the stresses and the relative displacements. In addition, Equation (5.25) is

based on equilibrium of a volume, but in the proposed embedded beam model a surface is considered. Therefore, the principle of virtual work is applied to the virtual interface elements in the following way:

$$\begin{aligned} &\int_A \delta\left(\boldsymbol{u_{rel}}\right)^T \boldsymbol{\sigma_i}\, dA = \int_A \delta \boldsymbol{u}^T \boldsymbol{f}\, dA \\ \Longrightarrow \qquad &\int_A \boldsymbol{B}^T \boldsymbol{\sigma_i}\, dA = \boldsymbol{f_{ex}^{local}} \end{aligned} \tag{5.26}$$

Substitution of Equation (5.18) and (5.19) leads to the following expression for the internal virtual work:

$$\underbrace{\int_A \boldsymbol{B}^T \boldsymbol{\sigma}_i^t\, dA}_{\boldsymbol{f}_{in}^t} + \underbrace{\int_A \boldsymbol{B}^T \boldsymbol{D}^e \boldsymbol{B}\, dA}_{\boldsymbol{K}_{local}^e} \cdot \Delta \boldsymbol{a}^e \tag{5.27}$$

The integral over the interaction surface A of an interface element is taken over the length of the element and around the entire circumference. Taking into account the iso-parametric coordinates, it is found that:

$$\boldsymbol{K}_{local}^e = \int_0^L \int_0^{2\pi} \boldsymbol{B}^T \boldsymbol{D}^e \boldsymbol{B}\, d\varphi dl \Longrightarrow \int_{-1}^1 \int_0^{2\pi} \boldsymbol{B}^T \boldsymbol{D}^e \boldsymbol{B}\, \frac{dl}{d\xi} d\varphi d\xi \tag{5.28}$$

Numerical integration over the length of the interface is done using the Newton-Cotes integration scheme, described in Section B.2.1. The integration over the circumference is taken into account by multiplying the existing weight factor with $2\pi R/\text{nCirDiv}$.

The element stiffness matrix and internal force vector in global coordinates are computed by:

$$\begin{aligned} \boldsymbol{K}_{global}^e &= \boldsymbol{T}^T \boldsymbol{R}_{\varphi}^T \boldsymbol{K}_{local}^e \boldsymbol{R}_{\varphi} \boldsymbol{T} \\ \boldsymbol{f}_{in}^t &= \boldsymbol{T}^T \boldsymbol{R}_{\varphi}^T \boldsymbol{f}_{in}^{local,t} \end{aligned} \tag{5.29}$$

When a embedded beam element is located at the foot of the pile the foot interface stiffness matrix and force vector can be computed in a similar fashion. The foot interface stiffness matrix and force vector can then easily be added to the element stiffness matrix and force vector.

Subsequently, the global interface element stiffness matrices can readily be assembled to the global stiffness matrix of the model ($\boldsymbol{K}$) in order to solve the global equilibrium equation:

$$\boldsymbol{K} \Delta \boldsymbol{a} = \boldsymbol{f}_{ex}^{t+\Delta t} - \boldsymbol{f}_{in}^t \tag{5.30}$$

where $\boldsymbol{f}_{ex}^{t+\Delta t}$ is the external force vector that is applied at the current step and $\boldsymbol{f}_{in}^t$ is the internal reaction force vector that is obtained from the previous step.

It must be noted that this procedure is only used for method A and B. When method C is applied, the stiffness matrix and force vector contribution of every point on the interaction surface is assembled separately to the global stiffness matrix of the model. So, no element stiffness matrices and force vectors are computed nor the addition of the foot contribution to the shaft interface will take place.

III

Parametric Study

6

Axially loaded models

The results in this chapter are obtained using a simple test case; the Alzey Bridge pile load test as described in Section 4.4.1. This test case considers a vertically oriented pile with axial loading. The measurement data of this field test are available and the existing embedded beam has already been proven to obtain a coinciding load-displacement curve in case of mesh size 2. Both the measurement data and results of the existing embedded beam are used as benchmark solution, to which the newly proposed method can be compared. The new formulation should at least be able to capture similar results as the existing embedded beam formulation. Otherwise, the new formulation would reduce the reliability of the embedded beam formulation in PLAXIS 3D, instead of improving it.

The influences of the proposed modifications and methods are evaluated separately first. Section 6.1 investigates which method to obtain the soil displacements at the interaction surface performs best. Next, the influence of the improved foot interface (Section 6.2) and incorporation of lateral plasticity (Section 6.3) on an axially loaded model are evaluated separately. In Section 6.4 the final new embedded beam element is compared to the existing embedded beam formulation and the available measurement data in case of an axially loaded situation.

The performance of the different methods is checked and compared on their ability to

- capture the results of the existing formulation,
- solve the mesh sensitivity problem, and
- reduce the influence of the elastic zone approach.

The last item comes from the fact that with the new formulation the pile-soil interaction is modelled at the interaction surface, hopefully making the elastic zone approach redundant.

The results in this chapter are obtained using the layer-dependent traction model, unless mentioned otherwise.

6.1. Investigation of the soil displacement methods

In the proposed embedded beam formulation, the soil displacements and stresses can be obtained by three different methods (Section 5.2.2). The proposed embedded beam element should at least be able to capture similar results as the existing embedded beam element for axially loaded piles. Additional goals are to reduce the mesh sensitivity and the influence of the elastic zone approach on the results.

In order to verify that the new methods are able to achieve the same results as the existing embedded beam formulation, the response obtained with mesh size 2 should be compared. The reason for this is the fact that the existing embedded beam element matches the measurement data almost exactly for this mesh configuration. In order to evaluate whether a mesh sensitivity reduction is obtained, the model is calculated with four different mesh sizes (Table 4.1). At last, the influence of the elastic zone is investigated by switching the elastic zone approach off.

6.1.1. Agreement with existing embedded beam and mesh sensitivity

Looking at the results obtained with the second mesh size, it is notable that method A (Figure 6.1b) and B (Figure 6.1c) both obtain a slightly lower failure load than the existing embedded beam formulation (Figure 6.1a). Even more remarkable is the fact that the calculation of method A continues after the kink at a displacement of approximately 0.03 m and overshoots the bearing capacity of the pile.

At last, method C calculated with mesh size 2 shows results (Figure 6.1d) that are in very good agreement with the existing embedded beam formulation. Both in terms of ultimate failure load and displacements at failure. For this criterion method C clearly preforms best.

Next, the mesh sensitivity of the different methods is evaluated. The transformation from pile-soil interface at the beam axis to an explicit interaction surface is proposed with the aim to reduce this mesh sensitivity. Figure 6.1b, 6.1c and 6.1d can readily be compared with Figure 6.1a. It is evident that none of the proposed methods is able to solve the mesh sensitivity problem completely.

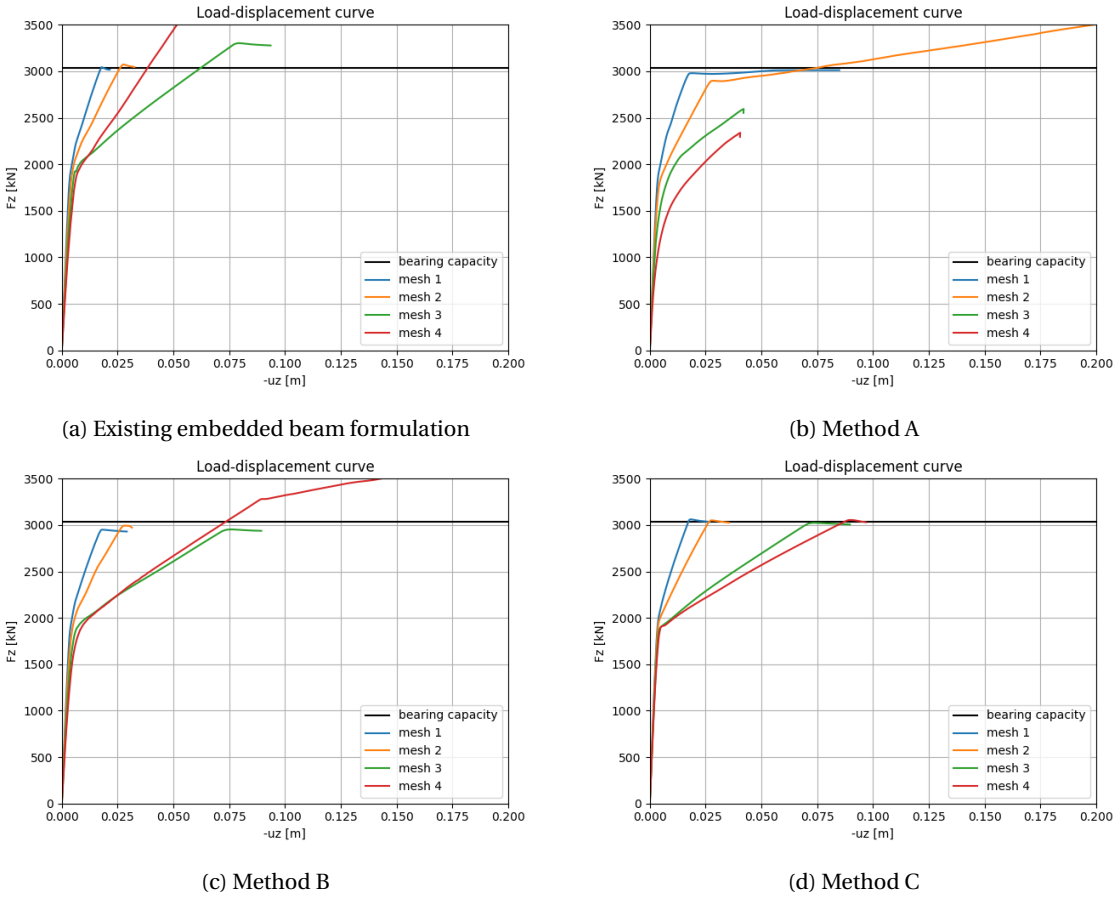

(a) Existing embedded beam formulation

(b) Method A

(c) Method B

(d) Method C

Figure 6.1: Alzey Bridge model calculated with different soil displacement methods and mesh sizes

Method A shows even less predictable behaviour than the existing embedded beam implementation. Already for the second mesh size the failure load is over predicted and for the third and fourth mesh sizes the failure load is not even reached. The calculation of the third mesh fails, because the soil body collapses and the fourth mesh fails for numerical reasons.

Method B shows equally unpredictable behaviour as the existing embedded beam formulation. The obtained failure load is not constant and the finer mesh sizes show much larger displacements at failure and even severe over-prediction of the failure load.

It is very clear that the mesh sensitivity is not solved by method C, but the results do show a perfectly predictable behaviour when the mesh is refined. For increasing mesh refinement, the calculation finds larger displacements at failure. This is a common phenomenon for stress singularities in the finite element method. The failure load that is obtained with the different mesh sizes is constant and no over-prediction occurs any more for the finer mesh sizes.

It is possible to compare the convergence behaviour of the models by looking at the required number of load steps for the calculation. More load steps means that it has more trouble finding convergence for larger load steps, indicating that the calculation takes longer. Since the embedded beam element in PLAXIS 3D is aimed to provide a fast method to model pile foundations, it is important that the calculation time doesn't increase drastically compared to the existing embedded beam formulation. In addition, convergence problems also indicate that inaccuracies develop during the calculation. The number of load steps are shown in Table 6.1 for the different mesh sizes (Table 4.1) and the different soil displacement methods.

	Existing EB	Method A	Method B	Method C
mesh 1	27	59	38	28
mesh 2	37	129	51	29
mesh 3	47	74	83	51
mesh 4	57	133	616	73

Table 6.1: Rate of convergence in terms of number of load steps

The table shows that the convergence behaviour of method A and B is far worse than the convergence behaviour of the existing embedded beam formulation. The convergence behaviour of method C is comparable to the existing embedded beam formulation.

6.1.2. Influence elastic zone approach

At last, the influence of the elastic zone approach is evaluated. Results of each method with the elastic zone deactivated are shown in Figure 6.2. The different methods can now easily be compared to each other and to their response with elastic zone approach.

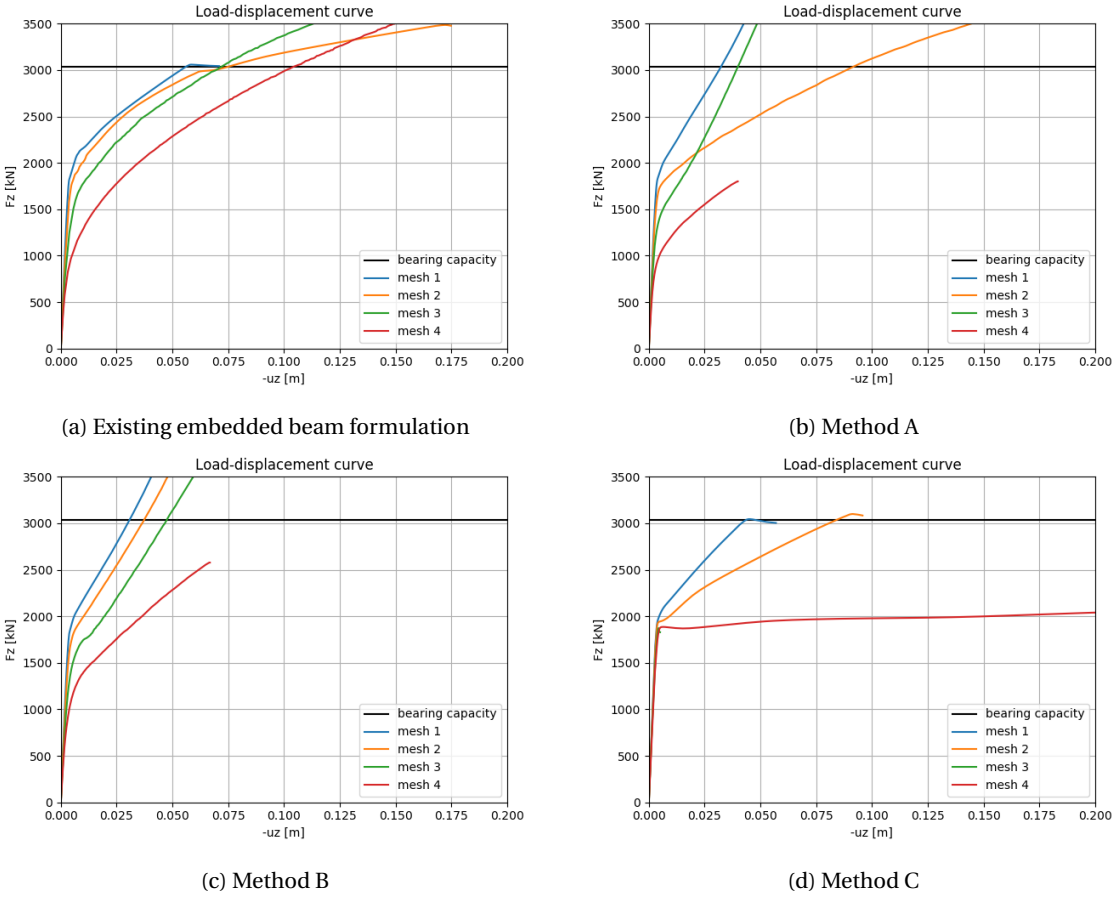

(a) Existing embedded beam formulation

(b) Method A

(c) Method B

(d) Method C

Figure 6.2: Alzey Bridge model calculated with different soil displacement methods and deactivated elastic zone approach

When the elastic zone is deactivated in the existing embedded beam formulation (Figure 6.2a), the results

show a higher mesh sensitivity and the failure load is over-predicted for coarser mesh sizes as well. This is behaviour is also visible for method A and B (Figure 6.2b, 6.2c).

Method A (Figure 6.2b) shows an even higher unpredictability than the existing embedded beam formulation and already over-predicts the failure load for the coarsest mesh size. The calculation of mesh size 4 breaks due to numerical problems.

Method B (Figure 6.2c) shows a slightly more predictable behaviour than the existing embedded beam formulation, but over-predicts the failure load already for the coarsest mesh size. Here the calculation of the fourth mesh size breaks as well due to numerical problems.

When method C is used, the mesh size doesn't influence the response until a load level of approximately 1900 kN (Figure 6.1d). The mesh sensitivity problem only starts to develop at load levels beyond that. When the elastic zone approach is deactivated, only method C (Figure 6.2d) is able to capture the same constant behaviour at load levels below 1900 kN. In addition, this is also the only method that doesn't show severe over-prediction of the failure load. However, the results of mesh size 3 (failure due to soil body collapse) and 4 are not very useful. Therefore, the elastic zone approach is still essential.

The models that are compared in this section do not include the improved foot interface. Therefore, in order to specifically evaluate the improvements of the shaft interface at the explicit interaction surface, the influence of the behaviour at the foot should be excluded.

It was already mentioned that method C is the only method that is able to capture the same constant behaviour until a load level of approximately 1900 kN when the elastic zone approach is deactivated. When the embedded beam is loaded the friction along the shaft of the pile is mobilised first. The base resistance is mobilised after the skin traction capacity is reached. This means that the behaviour until a load level of 1900 kN is mainly determined by the shaft interface.

When the foot resistance of the pile is set to zero, the foot interface is completely skipped in the calculation. The results of the Alzey Bridge pile load test with zero foot resistance for the existing embedded beam model and method C are shown in Figure 6.3. The results of method A and B are presented in Appendix E.1, but previous results have already shown that both methods do not obtain the desired improvements.

When the influence at the foot is omitted, the results of method C shows a reduction in mesh sensitivity compared to the existing embedded beam formulation (Figure 6.3b). In addition the influence of the elastic zone approach appears to have almost completely been erased (Figure 6.3c).

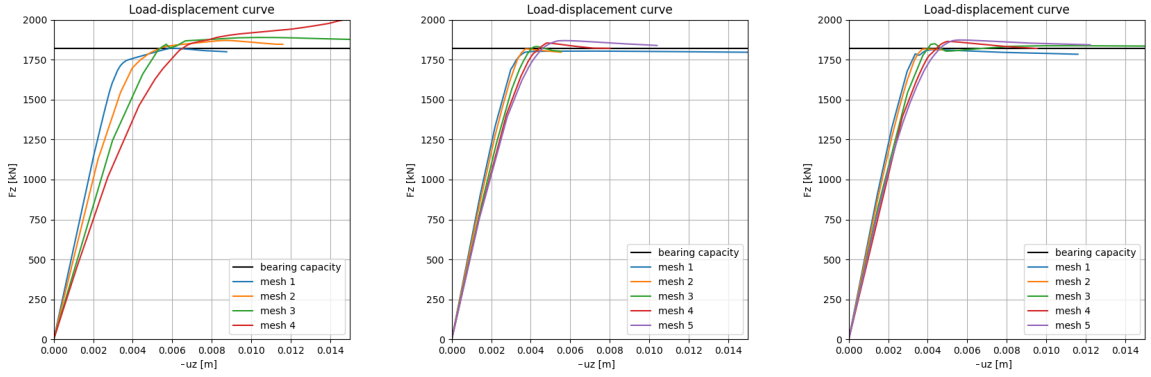

(a) Existing embedded beam (b) Method C, elastic zone activated (c) Method C, elastic zone deactivated

Figure 6.3: Alzey Bridge model with zero base resistance

Concluding, the remaining mesh sensitivity and influence of the elastic zone in method C must mainly be located at the base of the pile, since the model without base resistance shows very good results.

6.1.3. Explanation of results

The results in the previous sections show that methods A and B yield no improved behaviour compared to the existing embedded beam formulation in terms of mesh sensitivity or necessity of the elastic zone approach. Especially method A shows even more unpredictable and inconsistent results than the existing formulation. For the results to be so unpredictable when the mesh is refined, inaccuracies have to enter the calculation

somewhere. The most logical place for this to happen is in the calculation of the soil displacements at the interaction surface, because both methods include an approximation here. This is also where the only difference between the two methods enters the calculation.

This theory can be tested by excluding plasticity in the soil. Plasticity in the soil can cause extrapolation to be more inaccurate. Also, the gradient of the soil displacements, which is used in method B, can be affected by local plastic behavioiur in the soil. Figure 6.4 shows the results of the Alzey Bridge pile load test modelled with method A and B. The cohesion of the soil is increased to 200 to keep the soil behave elastically and the interface strength is reduced with a factor of 0.2. The latter is done to ensure that failure happens in the interface and not in the soil.

Both methods show a much more predictable behaviour now; no failure load over- or under-prediction and a monotonic increase of displacements at failure for an increase in number of elements. This confirms the theory that the unpredictable results in the previous sections are caused by plastic behaviour in the soil. The failure load that is found for both models is slightly lower than in the previous sections. This is caused by the changed soil properties and interface strength.

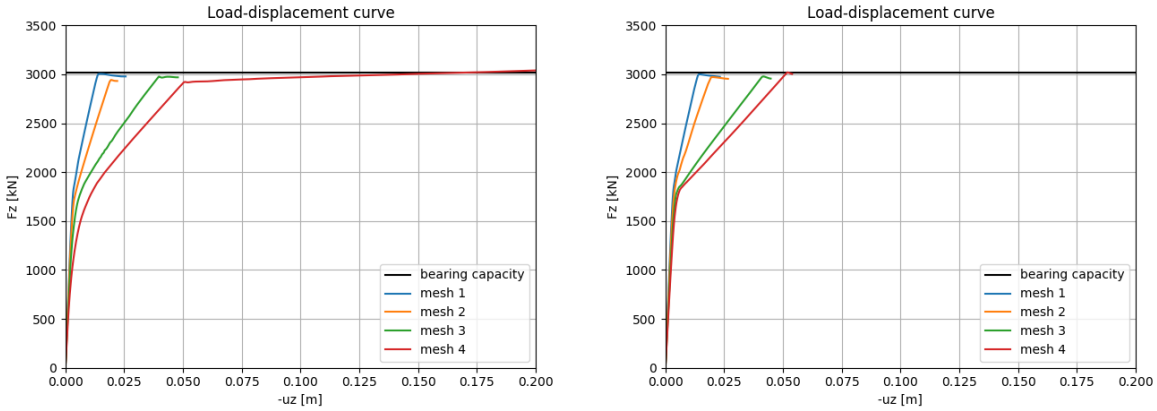

(a) Method A

(b) Method B

Figure 6.4: Alzey Bridge model with increased soil strength and reduced interface strength

The embedded beam element aims to model pile-soil interaction realistically, also in case of plasticity in the soil. Therefore, methods that are not able to capture this behaviour accurately are not suitable to be used in the new embedded beam formulation. The first two methods that are proposed to obtain the soil displacements at the interaction surface (A and B) are intended to reduce the computational effort compared to the method that obtains the exact soil displacements at the interaction surface (C). However, this advantage is insignificant compared to the reliability of the results. Thus, method A and B should not be used.

6.1.4. Conclusion

The previous section already advises against the use of method A and B to obtain the soil displacements at the interaction surface. However, it is still interesting to compare the results of the different methods, which is visualised in Table 6.2 based on the results that are presented in Section 6.1.

	Agreement with existing formulation	Ability to solve mesh sensitivity	Ability to reduce the influence of the elastic zone
Method A	0	–	– –
Method B	+	0	0
Method C	++	+	0

Table 6.2: Overview of the performance of the different methods to determine the soil stresses and displacements

The table confirms the fact that method A and B are not able to solve the mesh sensitivity nor are they able to reduce the influence of the elastic zone approach. In fact, they do not even show perfect agreement with the existing embedded beam element in case of mesh size 2. A quick verification test in which the influence

of soil plasticity is excluded, gives reason to believe that the strange and unpredictable results are caused by inaccuracies in the obtained soil displacements and stresses at the interaction surface.

Method C is the only method that shows an improvement in the obtained results. When the mesh sensitivity is evaluated the behaviour with this method is clearly less unpredictable than the existing embedded beam model, but the mesh sensitivity is not solved entirely. The results lead to the conclusion that method C is the preferred method to obtain the displacements at the interaction surface. Therefore, this method is used during the remainder of this research.

Even though a conclusion can already be drawn by comparing the three soil displacement methods, the decision to use method C is substantiated by the results of the model without base resistance. Nearly perfect results are found when method C without base resistance is used; the mesh sensitivity is reduced tremendously and the influence of the elastic zone approach is almost entirely imperceptible. This is not true for the other two methods. However, users should be able to use piles with base resistances, so this case is just meant to help proof that the behaviour along the shaft of the pile is improved tremendously with the new formulation. In addition, it shows that the only remaining mesh sensitivity and necessity for the elastic zone approach is due to the pile-soil behaviour at the foot.

The next subsections describe the scale and determination of the ratings that are presented in Table 6.2.

Agreement with existing embedded beam

For this criterion the scale shown in Table 6.3 is used.

– –	No similarities with the existing EB formulation and no recognizable relationship
–	Large deviations from the existing EB formulation
0	Comparable results, but showing some deviations
+	Reasonable agreement with the existing EB formulation
++	Very good agreement, no noteworthy deviations from the existing EB formulation

Table 6.3: Scale for the first criterion

The mesh 2 results of method A in Figure 6.1b show reasonable agreement with the existing embedded beam formulation. However, at a displacement of approximately 0.03 m the obtained failure load is slightly lower and the calculation doesn't break there but continues to overshoot the bearing capacity of the pile (0).

The mesh 2 results of method B in Figure 6.1c shows reasonable agreement with the existing embedded beam formulation, although the obtained failure load is slightly lower (+).

Method C shows very good agreement with the existing embedded beam formulation in case of mesh size 2 (Figure 6.1d) (++).

Ability to solve mesh sensitivity

For this criterion the scale shown in Table 6.4 is used.

– –	Completely mesh dependent, no recognizable relation and utterly unpredictable results
–	More mesh dependency than the existing EB formulation
0	Same amount of mesh dependency as existing EB formulation
+	Improved mesh dependency compared to the existing EB, but still mesh dependency present
++	Mesh sensitivity is completely solved

Table 6.4: Scale for the second criterion

The results of method A in Figure 6.1b show less predictable behaviour than the existing embedded beam implementation. In addition, the calculation of the third and fourth mesh fail prematurely, which makes these results very unreliable. (–)

The results of method B in Figure 6.1c show that the mesh sensitivity is not solved. The results in Figure 6.1c are comparable to the results in Figure 6.1a. (0)

The results of method C in Figure 6.1d show that the mesh sensitivity is not solved, but the behaviour has become more predictable than the results of the existing embedded beam formulation. (+)

– –	Completely useless and unreliable results when elastic zone approach deactivated
–	Increased influence of the elastic zone approach compared to the existing EB formulation
0	Influence of the elastic zone approach is similar to the existing EB formulation
+	Influence of the elastic zone is reduced
++	Influence of the elastic zone approach is imperceptible

Table 6.5: Scale for the third criterion

Ability to reduce influence elastic zone approach

For this criterion the scale shown in Table 6.5 is used.

The results of method A in Figure 6.2b show worse behaviour than the results of the existing formulation without elastic zone approach; even for coarse meshes the failure load is not captured and premature failure is found for the fourth mesh size. The results of method A are therefore not useful. (– –)

The results of method B in Figure 6.2c show the mesh sensitivity is not solved. The results in Figure 6.2c show that the model is not able to capture the failure load, even for the coarsest mesh size. However, the behaviour of the model with the first three mesh sizes is more predictable than the results of the existing embedded beam formulation in Figure 6.2a; the softening behaviour increases monotonically. (0)

The results of method C in Figure 6.2d show that the influence of the elastic zone approach is reduced for the first two mesh sizes. However, the results of the third and fourth mesh size of the new formulation with real interaction surface are very unreliable (0). Therefore, the elastic zone approach will still be applied.

6.2. Influence of improved foot interface

The influence of the improved foot interface is evaluated separately from the improved shaft interface in this section. The same criteria that are used to compare the soil displacement methods are used to evaluate the performance of the improved foot interface.

When the improved foot interface is included in the new embedded beam implementation, the mesh sensitivity is reduced tremendously (Figure 6.5b). However, the model behaves stiffer than the measurement data would suggest is correct. It is possible to modify the obtained displacements at failure by adjusting the foot interface stiffness. Section 6.2.1 will elaborate on this.

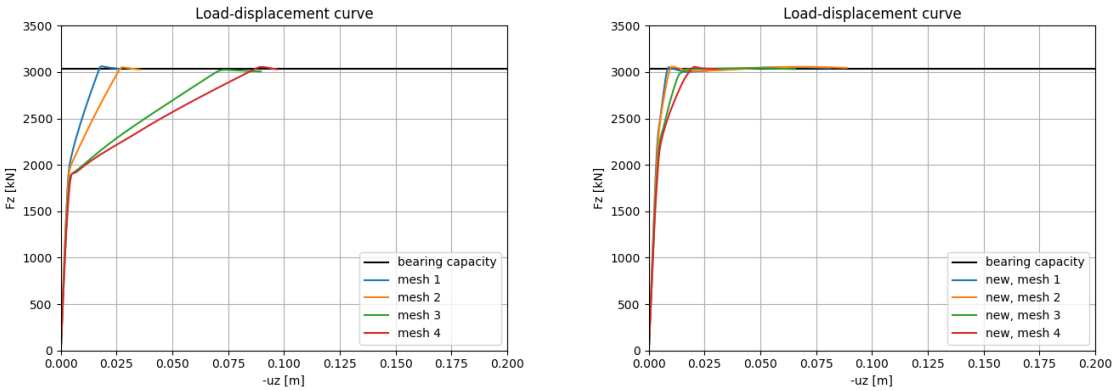

(a) Without improved foot interface

(b) With improved foot interface

Figure 6.5: Alzey Bridge model calculated with new embedded beam formulation and different mesh sizes

6.2.1. Reduction of the foot interface stiffness

The results in Figure 6.5 show that the incorporation of the improved foot interface makes the embedded beam model behave stiffer. Dividing the foot stiffness by the cross-section area of the pile should make the existing and new embedded beam formulation equivalent in stiffness response. However, this clearly is not the case, which requires an explanation.

In the existing embedded beam formulation the foot stiffness is based on the expression for the vertical displacements at the centre of a loaded circular area (distributed load). This expression is presented in

Verruijt (2012) as:

$$u_z = \frac{2f \cdot R\left(1-\nu^2\right)}{E} \tag{6.1}$$

Here, f is the distributed load in [kN/m^2], R is the pile radius, E is the Young's Modulus and ν is the Poisson's ratio. Rewriting this expression to the form $f = D_f \cdot u_z$ and considering that $G_{soil} = \frac{E}{2(1+\nu)}$, this gives a stiffness of:

$$D_f = \frac{G_{soil}}{R\,(1-\nu)} \tag{6.2}$$

The stiffness $\left(D_f\right)$ describes the relation between a distributed load [kN/m^2] and the displacement [m]. However, in the existing embedded beam formulation the foot stiffness describes the relation between a force [kN] and the relative displacement [m]. In order to obtain this, the distributed load must be multiplied by the loading area (the pile cross-section):

$$D_F = \frac{G_{soil} \cdot \pi R}{(1-\nu)} \approx 5 \cdot G_{soil} \cdot R \tag{6.3}$$

When the elastic stiffness of the interface is too small, the interface introduces unrealistic additional displacements to the elastic behaviour of the pile-soil model. This is not desired, therefore the foot stiffness should be increased. Instead of a factor of 5, a factor of 50 is used, which is based on the research conducted by Tschuchnigg (2012). It must be noted that this research was conducted using PLAXIS 3D Foundation and a factor of 25 to 50 was proposed, but the choice for 50 was not further motivated.

In the existing embedded beam formulation the pile-soil interaction is considered along the beam axis, inducing a point load onto the soil at the foot of the pile. A point load introduces locally very high stress concentrations in the soil, causing plastic behaviour in the soil, which results in large soil deformations. The improved foot interface spreads the foot resistance over a number of points on the perimeter of the pile, in other words the base resistance works as a circular line load on the soil. This reduces the effect of the stress singularity introduced by a point load significantly, resulting in relatively smaller soil deformations than the existing embedded beam model. The expected displacement profiles in the soil and the relative displacements between beam and soil are presented in Figure 6.6.

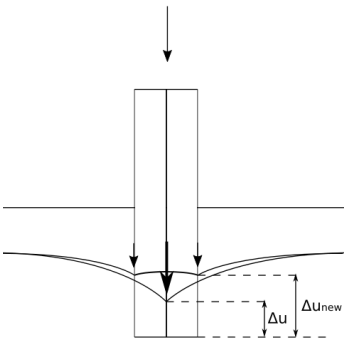

Figure 6.6: Relative displacements between pile and soil

This expected behaviour is confirmed by the output results from PLAXIS 3D, depicted in Figure 6.7. When the existing foot formulation is used (Figure 6.7a) locally large soil deformations occur near the foot of the pile. Figure 6.7b shows that the new foot still induces slightly larger deformations at the pile perimeter near the foot, but the effect is reduced tremendously compared to the existing foot formulation.

The local deformation behaviour in the soil near the foot of the pile has an influence on the relative displacements between pile and soil (Figure 6.6). When the improved foot is applied, the relative displacements develop faster. This leads to a faster mobilisation of the base resistance in the new embedded beam formulation, resulting in a stiffer response. Therefore, in order to obtain an equivalent stiffness response between the existing and new embedded beam model, the foot stiffness needs to be reduced.

In this section a parameter study will be done based on the measurement data from the Alzey Bridge pile load test. This will give a rough estimation of the magnitude of the foot stiffness reduction. In order to perform this parameter study, a reduction factor (Γ_{foot}) is introduced in the expression for the new foot interface stiffness, in a similar way as in Equation (4.10). This factor can easily be varied.

$$K_{foot} = \frac{50 \cdot G_{soil}}{\pi R} \cdot \Gamma_{foot} \tag{6.4}$$

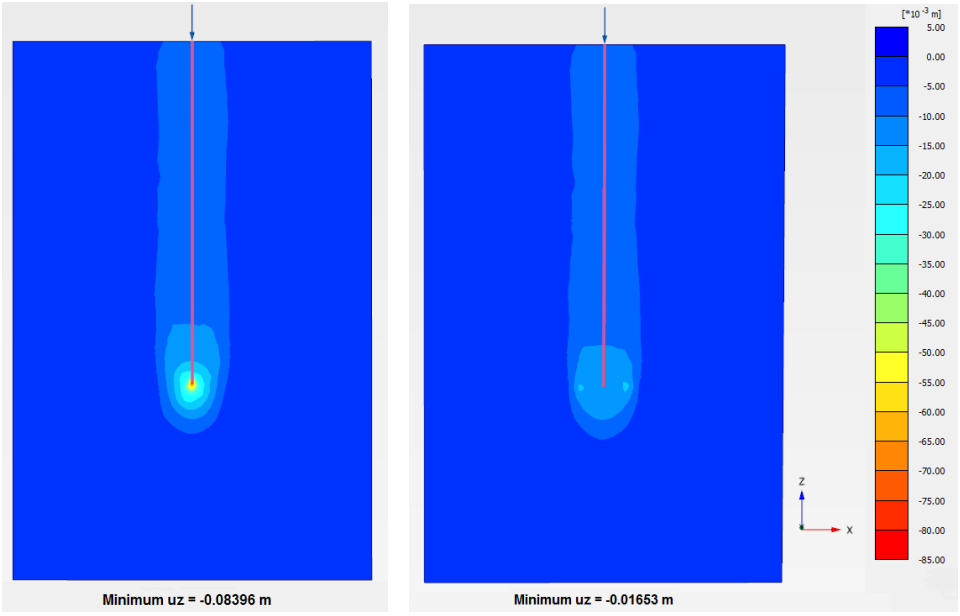

(a) Without improved foot (b) With improved foot

Figure 6.7: Contour plot of displacement in z-direction

For a layer-dependent traction model the required foot reduction factors are shown in Table 6.6 for different mesh sizes. The layer-dependent traction model requires slightly higher reduction factors than the linear traction model (Section E.2).

When the layer-dependent traction model is used, a slightly lower failure load is obtained (Figure 6.8). This is caused by the fact that the soil that is used in the PLAXIS 3D model doesn't exactly match the soil at the test site. A non-layered simplification is used, as was proposed by Engin et al. (2007). However, since the new embedded beam formulation is supposed to replace the existing formulation, it is interesting to be able to compare the new one to the existing one. The existing embedded beam formulation has proven to be mesh sensitive, and only mesh size 2 rendered results that are comparable with the measurement data. Therefore, the results of the existing embedded beam formulation with mesh size 2 are considered as reference for the new formulation as well.

Mesh size	Foot stiffness reduction factor
1	0.065
2	0.07
3	0.08
4	0.14
average	0.08875

Table 6.6: Foot stiffness reduction factors for model with layer-dependent traction model

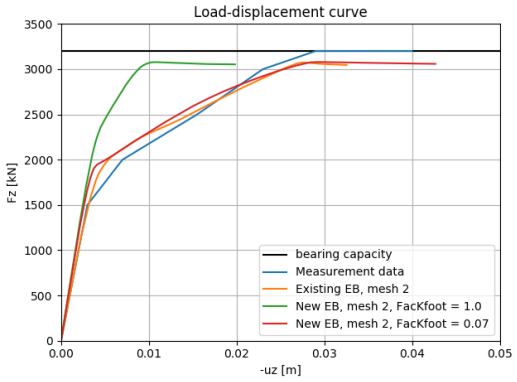

Figure 6.8: New embedded beam formulation with improved foot for different values of Γ_{foot}

A reduction factor of 0.07 for mesh size 2 results in exactly the same displacements at failure as the existing embedded beam model that is used as benchmark. A multiplication factor of 0.07 shall be used for the Alzey Bridge test case from now on when the Hardening soil model is used and the layer-dependent traction model. However, it is important to note that this value is obtained based on one model only and is not generally applicable.

The influence of several parameters on the required foot stiffness reduction factor is investigated shortly. The following conclusions are drawn based on the results presented in Appendix E.2. However, a more thorough investigation is still necessary to be able to draw final conclusions. Due to lack of measurement data to serve as benchmark solution, the new embedded beam formulation is compared to the existing formulation with mesh size 2.

- Reducing or increasing the Young's modulus of the soil doesn't change the required foot stiffness reduction factor for the new formulation, when compared to the existing embedded beam formulation with mesh size 2. This is true for both a linear and layer-dependent traction model and for both Hardening Soil and Mohr-Coulomb soil models.
- The used soil model influences the required foot interface reduction factor to match the new embedded beam formulation to the existing one. This has only been verified by comparing a Hardening soil model to a Mohr-Coulomb soil model. A Hardening Soil model includes stress dependency of stiffness, a Mohr-Coulomb soil model has a constant stiffness. The soil model influences the interface stiffness via the shear modulus, therefore it is not unexpected that the change in soil model influences the required foot stiffness reduction. Compared to a Hardening soil model, the Mohr-Coulomb model requires a smaller reduction.
- The Poisson's ratio influences the required foot stiffness reduction for the new formulation to match the existing formulation. An increase in Poisson's ratio results in a smaller necessary reduction. The existing foot stiffness definition is based on Equation (6.3), which clearly shows that instead of 50 a factor of $10 \cdot \frac{\pi}{1-\nu}$ would be more realistic, taking the influence of the Poisson's ratio into account.
- The radius of the pile has influence on the required foot stiffness reduction. A reduction of the pile radius results in the necessity of a smaller reduction. The radius appears in the definition of the foot stiffness (Equation (6.4)), but it seems that not the entire influence of the radius is taken into account correctly.

Based on the results presented in this chapter and Appendix E.2 it is expected that the required foot stiffness for the new embedded beam formulation is one order of magnitude lower than the foot stiffness of the existing embedded beam formulation. To come to a specific and generally applicable reduction factor a more thorough parameter study is required.

Influence of the foot interface stiffness on base resistance and skin traction mobilisation

The reduction of the foot interface stiffness is expected to influence the base resistance and skin traction evolution along the pile during loading. This is evaluated by comparing the results of the new formulation with and without foot stiffness reduction. Figure 6.9 shows the total load-displacement curve of the model in addition to the foot resistance and skin traction mobilisation.

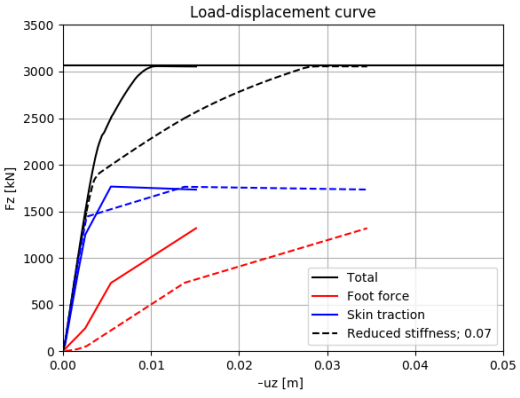

Figure 6.9: Foot force and skin traction mobilisation in new embedded beam model with and without reduced foot stiffness

In compliance with expectations, the foot resistance develops too fast when the foot stiffness is not reduced. This results in a stiff response of the model, obtaining too small displacements at failure. The results for $\Gamma_{foot} = 0.07$ can be compared to the measurement data (Figure 4.6a). The base resistance evolution when the foot stiffness is reduced seems to be in very good agreement with the measurement data.

The skin tractions at different load levels during the calculation are shown in Figure 6.10. Figure 6.10b can easily be compared to Figure 6.10a. Increasing the stiffness of the foot interface results in smaller peak values of the skin tractions near the foot of the pile. This is in agreement with the observations in Tschuchnigg (2012). An increase in foot stiffness results in a reduction of relative displacements at the foot. The reduction of the relative displacements is larger than the increase in stiffness, resulting in a reduction of the obtained tractions near the foot of the pile $(\sigma_{foot} = K_{foot} \cdot \Delta u)$. The skin tractions in the lower half of the pile evolve a little bit slower, creating a less pronounced bottom to top evolution.

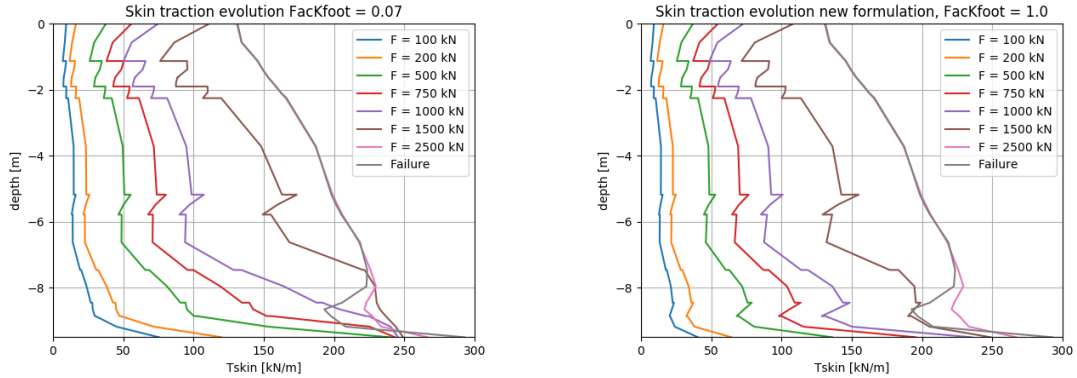

(a) Skin traction evolution for$\Gamma_{foot} = 0.07$

(b) Skin traction evolution for $\Gamma_{foot} = 1.0$

Figure 6.10: Influence of foot interface stiffness on skin traction evolution

The results show that reducing the foot interface stiffness doesn't influence the skin traction evolution significantly. The effect is mainly limited to the skin tractions at the foot of the pile.

6.2.2. Mesh sensitivity and influence elastic zone approach

Figure 6.5b shows a tremendous reduction in the mesh sensitivity of the response of the new embedded beam model when the improved foot interface is incorporated. It should be verified that the foot interface reduction doesn't influence this result in a negative way. In addition, the influence of the elastic zone along the shaft was already proven to be negligible (Section 6.1.2), but the influence is still significant at the foot of the pile. It is expected that the improved foot interface reduces the influence at the foot as well.

Figure 6.11 shows the results for the new embedded beam formulation with improved foot interface for different mesh sizes and with and without elastic zone activated. The foot stiffness is reduced with a reduction factor of 0.07 for all mesh sizes and the layer-dependent traction model is used.

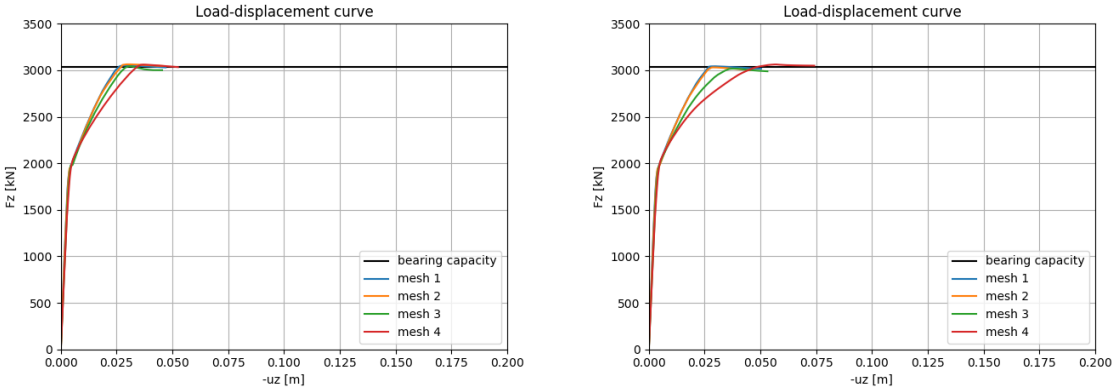

(a) Elastic zone activated

(b) Elastic zone deactivated

Figure 6.11: Alzey Bridge model calculated with new embedded beam formulation including improved foot interface. $\Gamma_{foot} = 0.07$

Figure 6.11a doesn't show an increased mesh sensitivity compared to Figure 6.5b. The stiffness of the model is now in better agreement with the measurement data. So, it is safe to conclude that the foot stiffness

reduction doesn't influence the mesh sensitivity in a negative way.

When Figure 6.11b is compared to Figure 6.11a the influence of the elastic zone is still visible, but much improved compared to models without this improved foot interface (Figure 6.2d). In addition, the mesh sensitivity of the new embedded beam formulation with improved foot interface without elastic zone approach is even reduced compared to the results of the new embedded beam formulation without improved foot interface and activated elastic zone approach or the existing embedded beam formulation with activated elastic zone.

6.2.3. Conclusion

The implementation of the improved foot interface results in a huge improvement to the new embedded beam formulation. The results in Figure 6.5b show that the mesh sensitivity is reduced tremendously. Furthermore, the improved foot interface reduces the influence of the elastic zone enormously as well. The new embedded beam formulation without elastic zone now returns better results than the existing embedded beam with elastic zone. The huge improvement in terms of mesh sensitivity is the foremost reason to include the improved foot interface to the new embedded beam formulation with explicit interaction surface.

However, the improved foot interface without stiffness reduction yields a stiffer response than the existing formulation and measurement data. Section 6.2.1 presents an explanation for this phenomena and a parameter study in order to determine an appropriate foot stiffness reduction factor. This parameter study is based on the available measurement data of the Alzey Bridge pile load test and the existing embedded beam formulation. Due to the mesh sensitivity of the existing formulation, only mesh size 2 is used as benchmark, since for this mesh the existing embedded beam resembles the measurement data best.

Due to lack of more field data and time constraints, it is not possible to draw a decisive conclusion on an exact reduction factor that is applicable to every situation. In the remainder of this report a foot stiffness reduction factor of 0.07 is used when the improved foot interface is incorporated. The decision to use 0.07 is based on the fact that

- the layer-dependent traction model is used for all models in this report and
- this reduction factor matches mesh size 2 of the new formulation with mesh size 2 of the existing formulation (Table 6.6), which matches the field data best.

The influence of the foot stiffness reduction shall be evaluated in every test case, by comparing the results of the reduced stiffness to the unreduced stiffness.

Furthermore, the obtained reduction factors provide an estimation of magnitude for a generally applicable foot stiffness reduction; the required foot stiffness in the new formulation is one order of magnitude lower than the foot stiffness in the existing embedded beam formulation divided by the cross-section area.

6.3. Influence of lateral plasticity on axially loaded models

In this section the new formulation is upgraded by the addition of correction for lateral plasticity. When correction for lateral plasticity is included in the implementation, the results of an axially loaded vertically oriented pile shouldn't change. Therefore, it is imperative to evaluate the influence of the three different lateral plasticity methods (Section 5.3.1) on an axially loaded model. The Alzey Bridge model is used and the results of the new embedded beam formulation without lateral plasticity are used as comparison.

The application of these methods is only sensible for the layer-dependent traction model. For the linear and multi-linear no input options are available to set a lateral bearing capacity.

Figure 6.12 enables an efficient comparison of the different lateral plasticity methods to the new embedded beam formulation without lateral plasticity and without improved foot interface (Figure 6.12a). Method 1 to include lateral plasticity (Figure 6.12b) doesn't influence the results of an axially loaded, vertically oriented pile. On the contrary, method 2 (Figure 6.12c) and 3 (Figure 6.12d) do influence the results in terms of ultimate failure load.

When the normal stresses in the interface are used (method 2 and 3), the model fails at a lower failure load. Figure 6.12c and 6.12d show that the kink in the curves happen at a load of approximately 1500 kN. When the normal stresses in the soil are used, this kink happens at a loading of approximately 2000 kN (Figure 6.12b). During the loading of the Alzey Bridge pile load test, first the skin tractions are mobilised. The foot resistance is mainly mobilised when the skin traction capacity is already reached (Figure 6.9). Therefore, the difference in failure load is caused by a change of shaft friction capacity (first part of graphs).

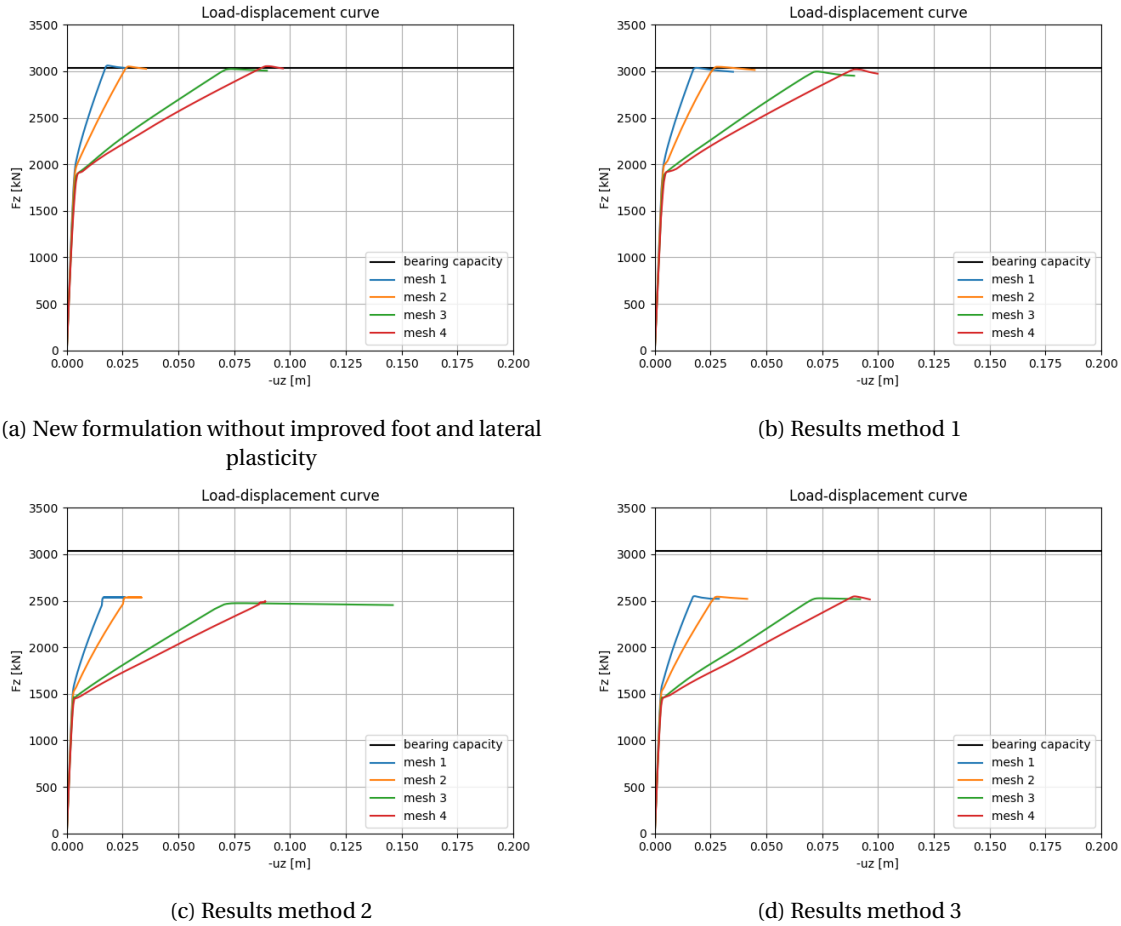

(a) New formulation without improved foot and lateral plasticity

(b) Results method 1

(c) Results method 2

(d) Results method 3

Figure 6.12: Alzey Bridge model. Influence of the lateral plasticity methods in the new embedded beam formulation in case of a layer-dependent traction model

In the layer-dependent traction model the maximum shaft friction is given by $\left(c_i - \sigma_n \tan\varphi\right) \cdot R_{inter}$. The cohesion, friction angle and strength reduction factor are input parameters and can therefore not be the cause for the change in capacity. The difference must come from the normal stresses.

6.3.1. Explanation of results

In the previous section is argued that the obtained lower failure load for methods 2 and 3 is caused by the maximum allowed friction along the shaft of the pile. In addition, based on the expression for the maximum friction is explained that the only variable that can cause the change is the normal stress in the interface. This also makes sense when observing that the normal stress is the only difference between method 1 and method 2 and 3, whereas method 1 doesn't find a lower failure load.

The lower failure load that is obtained in Figure 6.12c and 6.12d is caused by a reduction in the maximum shaft friction. For this expression to reduce, the normal stresses must have a higher value; considering soil only takes up compressive stresses, the absolute value reduces $|\sigma_n| \downarrow$.

Apparently, the absolute normal stresses in the interface are lower than the normal stresses in the soil. However, equilibrium is obtained. Therefore, a part of the normal stresses in the soil must go elsewhere. Looking at the equilibrium situation at the virtual interface (Figure 6.13), it is evident what happens.

When an embedded beam model in PLAXIS 3D is initialised, the soil inside the pile region is taken into account. This leads to initial stresses in the soil inside the pile region which are in equilibrium with the initial stresses in the soil around the pile region. Subsequently, the embedded beam is loaded, resulting in additional stresses in the soil around the pile region. These additional stresses make equilibrium with the interaction stresses in the interface. Total equilibrium is now provided by the sum of the stresses in the soil inside the pile radius, the soil around the pile and the interaction stresses in the interface. When the normal

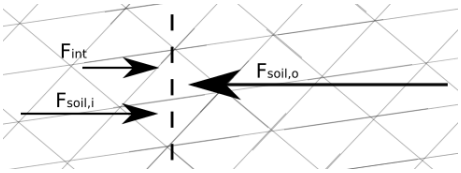

Figure 6.13: Equilibrium situation at virtual interface

stresses from the interface are used in the correction for plasticity only the additional stresses are taken into account, not the total stresses that work on the beam.

It is possible to compute and store both components of the interface stresses in order to be able to use the combined value for the correction of plasticity. However, for now it suffices to use the normal stresses from the soil. When the normal stresses from the soil are used (method 1), the stresses on the right side of the virtual interface in Figure 6.13 is inserted in the shear limit. This is the correct value of the normal stresses that should be taken into account here.

It must be noted that only the additional interaction stresses need to be added to the total force vector. The stresses that occur in the soil inside the pile region are already present in the force vector. They shouldn't be taken into account twice (both in the interface and in the soil).

6.3.2. Conclusion

The results of the first lateral plasticity method show very good agreement with the results of the new embedded beam element without lateral plasticity. The latter has already been proven to be an improvement compared to the existing embedded beam formulation in terms of mesh sensitivity.

Using the normal stresses from the interface (method 2 and 3) results in a lower failure load. This is an undesired effect of the incorporation of lateral plasticity, because it shouldn't have an significant influence on an axially loaded pile. An explanation of this phenomena is provided, which leads to the conclusion that the use of the normal stresses in the interface is incorrect. Therefore, method 1 is the only method that requires further validation, which is done in Section 7.1 for a purely laterally loaded model.

6.4. Axially loaded Alzey Bridge model

The improved foot interface is now added to the new embedded beam formulation, including a foot interface stiffness reduction factor of 0.07. Lateral plasticity method 1 is applied as well and the elastic zone approach is still used.

Figure 6.14b shows the resulting load displacement curves for different mesh sizes. As comparison, the results of the existing embedded beam formulation are shown on the left.

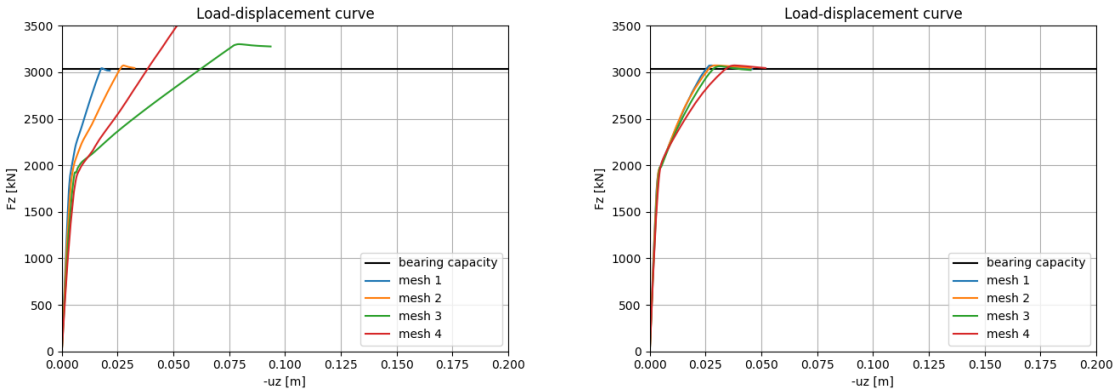

(a) Existing formulation

(b) New formulation including improved foot and lateral plasticity method 1

Figure 6.14: Alzey Bridge model. Comparing existing embedded beam with new formulation including all improvements

The difference in mesh sensitivity is huge, showing how big of an improvement the new embedded beam

formulation is. No unpredictable behaviour is found any more; no over-prediction of the failure load for some mesh sizes and no fluctuation in stiffness response when the mesh is refined.

6.4.1. Skin traction evolution

Previous research (Tschuchnigg, 2012; Lebeau, 2008) has focussed on the foot force and skin traction mobilisation of the embedded beam element in PLAXIS. Several conclusions have been drawn, such as:

- Mesh coarseness influences base resistance mobilisation (coarse meshes perform better)
- Foot interface stiffness influences base resistance mobilisation
- Change in shaft interface stiffness has less influence than change in foot interface stiffness
- Stress dependency of stiffness (HS) influences skin resistance mobilisation (inclined profile), which is better than constant stiffness along length of the pile (MC).

In this section the skin traction evolution that is obtained with the new embedded beam formulation will be compared to the existing formulation. In addition, Appendix E.3 elaborates in more detail on the influence of the mesh size, foot stiffness, shaft interface, soil model and traction model on the skin traction evolution.

Figure 6.15 shows the axial skin traction evolution for the Alzey Bridge pile load test modelled with the existing and new embedded beam formulation. Mesh 2 is evaluated, because the foot interface stiffness was set to match those results best, making these results best comparable. A Hardening soil model is used, which takes into account stress dependency in the soil stiffness, and therefore also in the interface stiffness. This feature results in a soil and interface stiffness that increase with depth.

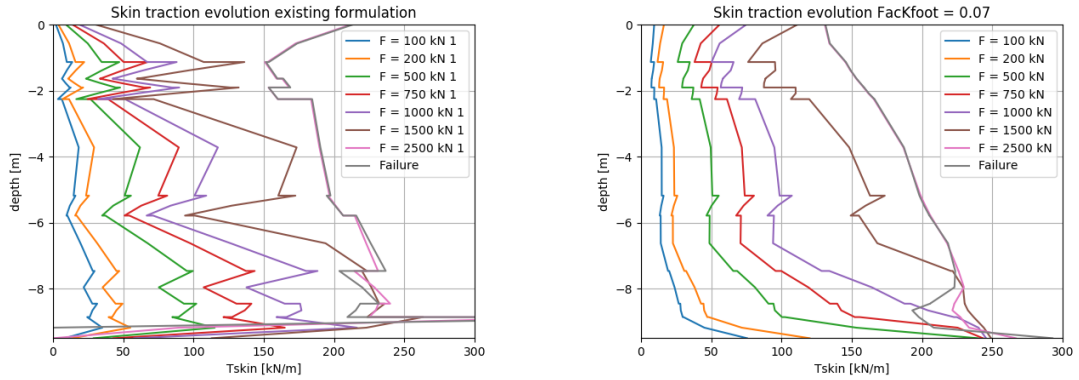

(a) Existing formulation

(b) New formulation

Figure 6.15: Skin traction evolution for layer-dependent traction model at different load levels

The new embedded beam formulation (Figure 6.15b) shows much smoother skin traction profiles than the existing embedded beam formulation (Figure 6.15a). This can easily be explained; the pile-soil interaction in the existing formulation is evaluated at one point only in the cross-section, hence local effects can influence the results substantially. In the new embedded beam formulation the curves are obtained by integrating over the whole pile perimeter, resulting in a limited influence of local effects.

At the foot of the pile the existing formulation finds unrealistic low values of the skin traction, and even zero skin tractions at failure. These unrealistic low values near the foot of the pile require an explanation. Before failure of the model the skin tractions are determined by the interface stiffness and the relative displacements between the pile and soil. The relative low skin traction values are explained by the small relative displacements that are obtained near the foot (Figure E.9). These small relative displacements can be explained; in the existing embedded beam formulation two contributions work on the last node of the pile; the foot resistance and shaft friction. The resistance and stiffness is therefore locally higher here, causing smaller relative displacements.

At failure the skin tractions are determined by the maximum allowed skin tractions along the pile. Zero values at failure are only found for the layer-dependent traction model, not for the linear traction model (Figure E.10a). This gives reason to believe that the cause can be found in the maximum skin traction limit of

the layer-dependent model; $\left(c_i - \sigma_{n,soil} \cdot \tan\varphi\right) \cdot 2\pi R$. The cohesion, friction angle and radius are fixed input parameters, so the only variable that can cause this expression to become lower than or equal to zero is the normal stress that is obtained from the soil. This variable is verified and indeed turns out to have a positive value near the foot of the pile at the two highest load levels. Although tension cut-off is selected, positive soil stresses can be obtained in the nodes by extrapolation from the integration points. Due to the plasticity near the foot of the pile (Section 6.2.1), extrapolation is more likely to return more inaccurate results.

Instead of unrealistically low values near the foot of the pile, the new formulation finds relative large values. This corresponds with the high relative displacements that are found near the foot of the pile (Figure E.9). The elastic response of the soil is already modelled in the soil, therefore the interface should actually have an infinitely large elastic stiffness at the foot. However, this causes numerical problems and an overly stiff response of the embedded beam model. Section 6.2.1 elaborates in more detail on the required foot stiffness for the new embedded beam model. The relative low foot stiffness allows for large relative displacements at the foot of the pile. Increasing the foot stiffness would reduce the relative displacements and skin tractions near the foot.

Figure 6.16 can readily be compared to Figure 4.6a. The mobilisation of the foot force and skin tractions of the existing and new formulation show very similar behaviour. The failure load is slightly under-predicted compared to the test results, but this is caused by simplified soil model that doesn't exactly match the real soil properties. The final base resistance is an input variable, which is set equal to the final base resistance of the test data. Clearly, the new embedded beam formulation is very capable to capture a skin traction evolution and foot force mobilisation that is in very good agreement with field data and the existing embedded beam formulation.

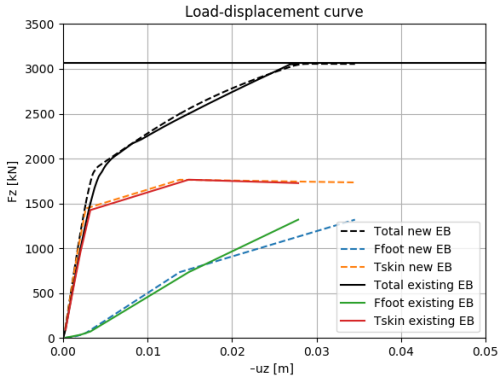

Figure 6.16: Mobilisation of foot force and skin tractions

Based on the results in Appendix E.3 the following remarks can be made:

- The skin traction evolution of the new embedded beam formulation is not influenced significantly by the mesh size. This is an improvement compared to the existing embedded beam formulation. (Appendix E.3.1)
- The difference between a Hardening Soil model and a Mohr-Coulomb soil model is not very pronounced. Both the existing and new embedded beam models find an inclined skin traction profile for the Mohr-Coulomb soil model, in contradiction with the observations made by Tschuchnigg (2012). (Appendix E.3.2)
- The new embedded beam formulation reduces inaccuracies in the obtained normal stresses from the soil. (Appendix E.3.4).
- Reducing the shaft stiffnesses influences the load-displacement curve in a negative manner; resembles the measurement data less accurately. The skin tractions evolve slower. (Appendix E.3.5)
- In the new formulation K_n and K_t are interchanged compared to the existing formulation, because the existing formulation is not able to distinguish between the two. The new formulation has a less pronounced bottom to top evolution because of it. (Appendix E.3.5)

6.4.2. Influence of the interface strength reduction factor R_{inter}

Figure 6.17 shows the results for the Alzey Bridge pile load test computed with the existing and new embedded beam formulation for varying values of R_{inter}. Mesh size 2 is used and the layer-dependent traction model. The load-displacement curves show that the new embedded beam formulation is equally able to capture the interface strength reduction as the existing embedded beam formulation. The strength reduction of the interface only works for axially loaded piles.

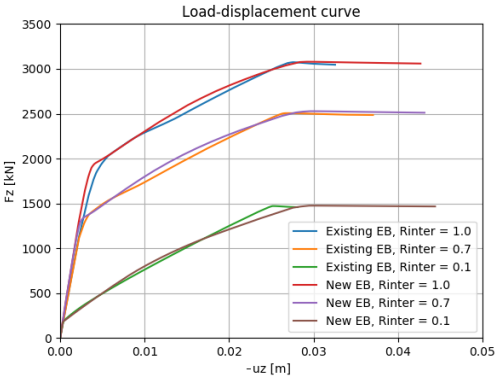

Figure 6.17: Alzey Bridge model, varying R_{inter}

6.4.3. Influence of the number of points on the interaction surface

Figure 6.18 shows that the number of points on the interaction surface that are used to compute the pile-soil interaction can be relatively low. The difference between 200 points or 4 points is negligible for a vertically oriented and axially loaded pile.

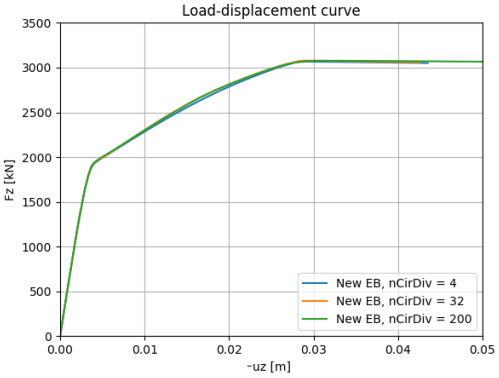

Figure 6.18: Alzey Bridge model, varying nCirDiv

However, it is expected that the influence of the number of points on the interaction surface for laterally loaded piles is higher. For a purely axially loaded pile the stress state around the pile is fairly constant. For a laterally loaded case the stress state around the pile will be compressive at the front of the pile and tensile at the back. To take this into account accurately, it is expected that more points need to be considered at the interaction surface.

6.5. Summary

In Section 6.1 three different methods to obtain the soil displacements at the interaction surface are compared. The first two methods are unable to calculate the soil displacements accurate enough to be useful. Both methods use an approximation to obtain the soil displacements (extrapolation and Taylor approximation), causing inaccuracies to enter the calculation. Excellent results are obtained with the third method, which considers the true soil elements at the interaction surface. Therefore, the latter method is chosen to

be implemented and used in the remainder of this study. When the base resistance is set to zero, the mesh sensitivity is reduced tremendously and the influence of the elastic zone is almost entirely removed. This suggests that the remaining problems are induced by the pile-soil behaviour at the foot of the pile.

The improved foot interface introduces a significant improvement in terms of mesh sensitivity. However, the new foot description makes the model behave stiffer. Reduction of the foot interface stiffness is applied in order to make the model behave less stiff. Unfortunately, no decisive and unique reduction factor is obtained due to a lack of enough field data to serve as benchmark solution. In Section 6.2.3 it is decided to use a foot stiffness reduction factor of 0.07 in the remainder of this research. However, the influence of the foot stiffness reduction is verified for every test case.

The three lateral plasticity methods are compared in Section 6.3. The lateral plasticity methods should not affect the results of a purely axially loaded model, but method 2 and 3 show a significant reduction in failure load. This is caused by the fact that the interface only considers the additional stresses caused by relative displacements, neglecting the initial stresses. This leads to the use of a too low value of the normal stresses in the expression for the maximum skin friction, leading to a reduction in the failure load. This is an incorrect result, leading to the conclusion that method 2 and 3 should not be used. Therefore, it is decided that only method 1 is evaluated further in Section 7.1 for a laterally loaded test case.

In case of an axially loaded pile the new embedded beam element reduces the mesh sensitivity significantly. In addition, the remaining influence of the elastic zone approach is very slight. However, the elastic zone will still be used in the next chapters, because the influence of the elastic zone approach is expected to be larger for piles with a lateral loading component.

The new embedded beam formulation reduces the influence of local effects on the skin traction profile, resulting in a smoother distribution. The existing embedded beam model finds unrealistic low skin traction values near the foot of the pile, but this problem is solved with the implementation of the new embedded beam formulation. However, the new embedded beam model now finds peak values near the top, which is caused by the relative low elastic foot stiffness.

For a purely axially loaded model no discernible differences are obtained in the response when 4 or 200 points on the interaction surface are considered. This is very fortunate, since the more points need to be considered, the longer the calculation will take. It is expected that more points are required for laterally loaded models.

7

Laterally loaded models

Apart from reducing the mesh sensitivity of the existing embedded beam model, the proposed new embedded beam element formulation is intended to improve the behaviour of a laterally loaded pile. The introduction of an explicit interaction surface on which the pile-soil interaction is considered is the first step towards the ability to model the lateral interaction more accurate. The interaction surface reduces the localised influence of the embedded beam, by spreading its contribution over a larger area. Besides, the interaction surface makes it possible to distinguish between normal and transversal directions along the shaft of the pile.

On top of these expected improvements, three methods to include a correction for lateral plasticity are proposed in Section 5.3.1. The results in Section 6.3 have already led to the conclusion that method 2 and 3 are not sensible choices, because they do not take the total stresses that work on the pile into account when correcting for plasticity. Incorporation of a correction for lateral plasticity is expected to make it possible to capture slippage of the soil around the pile in lateral direction and gap forming at the back of the pile. Section 7.1 presents the results of method 1 for a laterally loaded disc in order to evaluate the lateral response.

Subsequently, the Alzey Bridge pile load test is modified by removing the axial load and adding a lateral load. This model is used to compare the existing embedded beam, new embedded beam and volume pile method (Section 7.2). A parametric variation of the L/D ratio of the pile is performed in Section 7.3, in order to verify that an improvement is obtained for both relative short and slender piles. At last, a laterally loaded inclined pile is evaluated, in order to verify that the generalisation for inclined piles does indeed work (Section 7.4).

The results that are obtained in this chapter with the new embedded beam formulation consider 32 points on the interaction surface. The layer-dependent traction model is used, unless explicitly mentioned otherwise.

7.1. Influence of lateral plasticity on laterally loaded models

In case of a pile with a lateral loading component, the lateral interface should reduce the mesh sensitivity and enable a reduction in failure load when the interface strength is reduced by the strength reduction factor R_{inter}. In Section 6.3 it turned out that using the normal stresses in the interface is incorrect (method 2 and 3). Therefore, only method 1 requires additional validation.

7.1.1. Mesh sensitivity

The load-displacement curves that are obtained for the laterally loaded disc model for different mesh sizes are shown in Figure 7.1. The results are obtained using a manipulated mesh; forcing element boundaries at the interaction surface.

Method 1 obtains very similar results as the new embedded beam formulation without lateral plasticity (Figure 7.1a). These curves are in turn in almost the same as the curves obtained with the existing embedded beam formulation (Figure 4.11a) or the volume pile method without interface (Figure 4.10a).

It is interesting to compare the convergence behaviour of the new embedded beam formulation with method 1 to the existing embedded beam formulation, since this influences the calculation time significantly. Table 7.1 shows the number of load steps that are necessary for the calculation of the laterally loaded disc model.

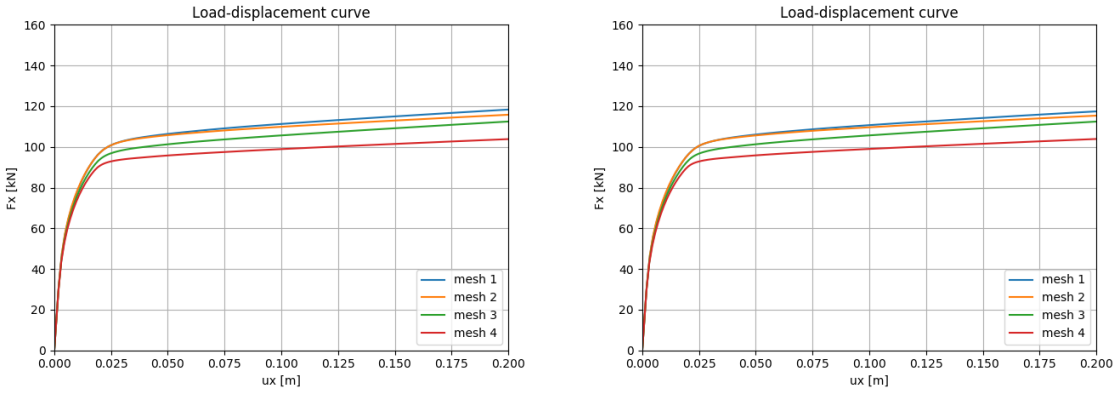

(a) New formulation without lateral plasticity (b) Method 1

Figure 7.1: Laterally loaded disc model with manipulated mesh

Clearly, the convergence behaviour of the new embedded beam model with lateral plasticity method 1 is very comparable to the convergence behaviour of the existing embedded beam method.

	Existing EB	Method 1
mesh 1	63	65
mesh 2	61	64
mesh 3	68	70
mesh 4	74	74

Table 7.1: Rate of convergence in terms of number of load steps

Mesh manipulation, as has been applied so far, shouldn't be necessary to obtain the good results for the embedded beam model. The purpose of the embedded beam in PLAXIS is to simplify modelling of foundation piles. For this purpose, requiring mesh manipulation for every embedded beam is not sensible. Therefore, it is important to evaluate the results of the embedded beam model without mesh manipulation as well; Figure 7.2.

The first thing that is important to note is that the new embedded beam formulation without lateral plasticity shows an increase in mesh sensitivity and failure load compared to the existing embedded beam formulation (Figure 4.11b). Lateral plasticity method 1 shows an improvement with respect to this, but the obtained failure load and mesh sensitivity are still higher than in the existing embedded beam model.

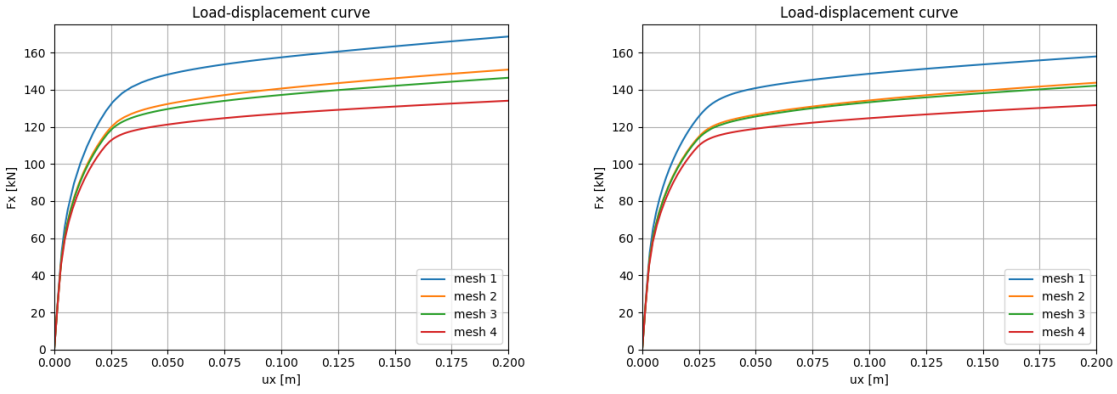

(a) New formulation without lateral plasticity (b) Method 1

Figure 7.2: Laterally loaded disc model without manipulated mesh

Furthermore, the results of the model without manipulated mesh all show an over-prediction of the failure load and a higher mesh sensitivity than the model with manipulated mesh and the volume pile method. This,

in combination with the lack of improvement for when a manipulated mesh is used compared to the existing embedded beam, suggests that the proposed method to incorporate lateral plasticity is not able to capture the interface in the desired way.

7.1.2. Influence of the elastic zone approach

For axially loaded models the elastic zone approach was proven to be redundant when the base resistance was set to zero. The laterally loaded disc model doesn't include a base resistance either, therefore this model is suitable to check the influence of the elastic zone along the shaft of the pile for a purely laterally loaded case.

The failure load that is obtained with a deactivated elastic zone approach is lower than with elastic zone approach, both in case of a model with and without manipulated mesh (Figure 7.3). So, the influence of the elastic zone is still evident in the new embedded beam formulation for a laterally loaded case, but has much reduced compared to the existing embedded beam formulation (Figure 4.12a, 4.12b).

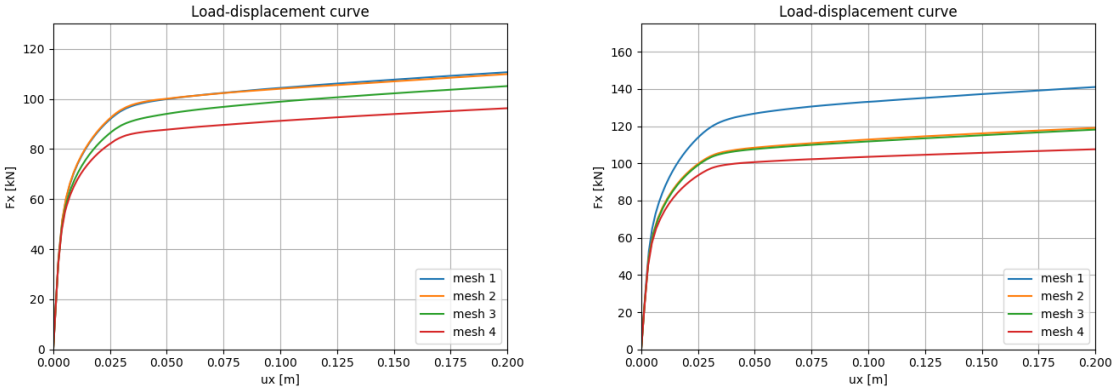

(a) New embedded beam model with manipulated mesh

(b) New embedded beam model without manipulated mesh

Figure 7.3: Laterally loaded disc model with deactivated elastic zone and lateral plasticity method 1

Even though the effect of a reduction in failure load is actually desired, the influence of the elastic zone is undesired. This is evident in Figure 7.4; the soil inside the pile region deforms completely with a deactivated elastic zone. By modelling the pile-soil interaction at the interaction surface, the behaviour of the soil inside the pile region should follow the beam element.

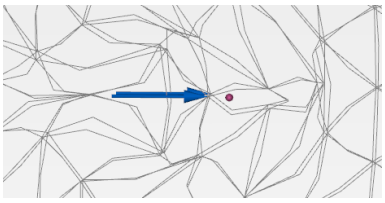

Figure 7.4: Deformed mesh configuration when elastic zone approach is deactivated

The reduction of the failure load by deactivation of the elastic zone approach can easily be explained, because the elastic zone influences the stress state in the soil. Forcing the integration points inside the pile region to remain elastic, enables the stresses in that region to grow unlimited. This provides an additional resistance to the beam-soil response.

It is not surprising that the influence of the elastic zone is larger for a laterally loaded model than for an axially loaded one. In case of a laterally loaded model the entire soil volume inside the pile region must follow the movement of the pile, because the interaction surface encloses it. So, the whole soil body inside the pile region is affected. In the case of axial loading the soil inside the pile region doesn't necessarily have to follow the beam element, because the interaction surface is like an open tube. Therefore, only the soil near the interaction surface is affected.

7.1.3. Influence of the interface strength reduction factor R_{inter}

When the volume pile method is used to model a pile foundation, it is possible to reduce the interface strength by a factor R_{inter}. When R_{inter} is defined as a value below 1, this results in a softer behaviour in the elastic phase and a lower ultimate failure load. Now that lateral plasticity is also applied to the embedded beam method, the influence of the interface strength reduction should also be visible for this method as well. Figure 7.5 shows the results for two different values of R_{inter}. Clearly, a significant reduction of the interface strength does not result in a lower failure load.

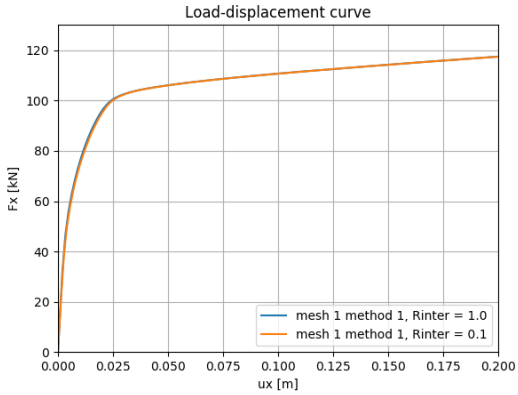

Figure 7.5: Laterally loaded disc model with manipulated mesh and lateral plasticity method 1, varying R_{inter}

The failure mechanism that is captured with the existing embedded beam model is soil failure, because the interface is only able to capture elastic behaviour in lateral direction and the soil inside the pile radius is forced to remain elastic. Only when the elastic soil around the pile axis pushes the soil around the pile region enough, is failure obtained. Since, the same failure load is obtained with the new embedded beam formulation including lateral plasticity, it is believed that soil failure around the pile region is still the dominant failure mechanism, not interface failure.

7.1.4. Reason ineffective interface plasticity

The unsatisfying results that are obtained with the proposed method to include lateral plasticity require an explanation. Why doesn't the proposed lateral plasticity method capture the desired interface behaviour? Therefore, an extensive investigation is conducted in order to identify why the model doesn't behave as expected. Several steps are taken to reduce the complexity of the problem and to return to a formulation that does yield predictable results. Starting from this point, small steps can be taken to determine where and what causes the problem (Figure 7.6).

First, the simple laterally loaded disc model is even more simplified (Appendix F.1.1), in order to reduce the number of parameters that influence the results. For this reason a Mohr-Coulomb soil model is adopted (no stress-dependency of stiffness) and the friction angle is set to zero (no normal stress influence in layer-dependent shear limit of the interface). After verification that this doesn't solve the problem, the first test is done with a zero interface capacity. This is done in order to make sure that the only coupling between beam and soil takes place through the interface. This is confirmed, since the results in Appendix F.1.2 show the beam moves without applied force.

Subsequently, it is discovered that when only the shear capacity of the interface is used (no normal stress capacity), the load-displacement curves do show a different failure load for different values of R_{inter}. However, when the unlimited normal stress capacity is included, the influence of R_{inter} diminishes.

On account of this result, the influence of the normal stresses in the interface on the interface behaviour is investigated (Appendix F.1.3). Several ways to limit the normal stresses in the interface based on the normal stresses in the soil are evaluated, but unfortunately no acceptable results are obtained. During the investigation of these methods, it is discovered that an incorrect mechanism occurs when the interface capacity is reached.

In this section, the cause of the ineffective lateral interface plasticity is explained and substantiated.

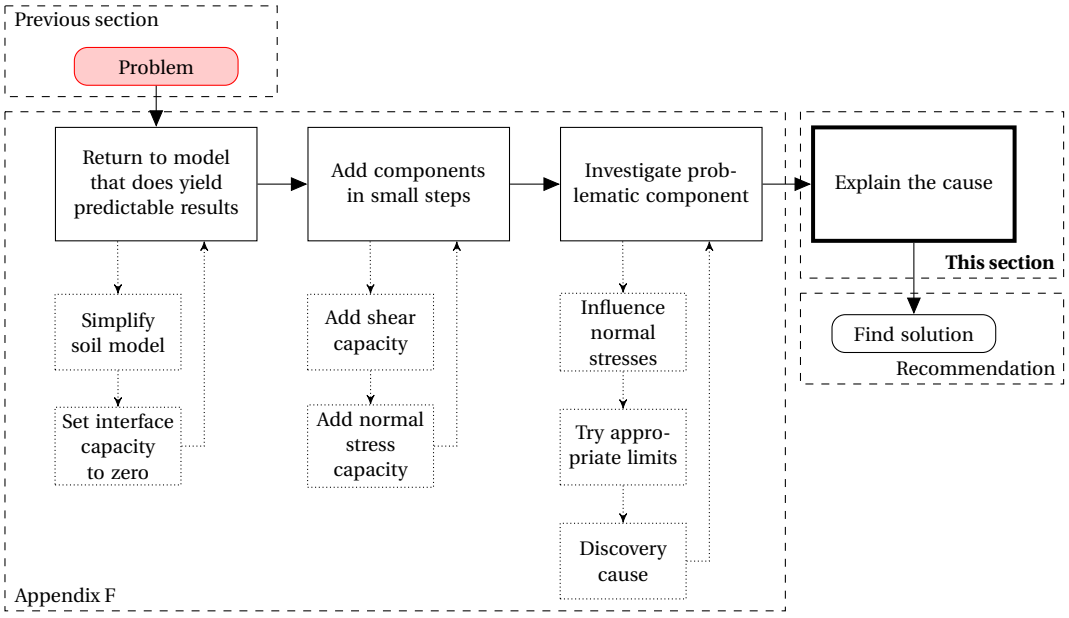

Figure 7.6: Systematic procedure to identify problem

When the interface capacity is described by a limit for both the shear and normal stresses, variation of R_{inter} does influence the ultimate failure load. However, the reduction of R_{inter} doesn't result in the same reduction of the failure load as in the volume pile method. Therefore, a closer look is taken at what happens at failure. The first thing that stands out in the deformed configuration, is that the beam element moves away from the centre of the pile region (Figure 7.7). Apparently, the beam doesn't pull the soil inside the pile region along. This is in contradiction with the desired behaviour, because when R_{inter} is reduced (smoother pile surface) the soil around the pile should start slipping more easily around the pile, causing larger displacements of the entire pile region.

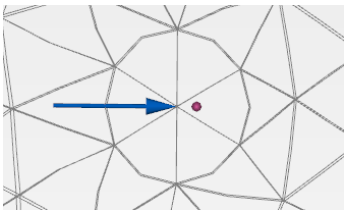

Figure 7.7: Deformed mesh of model with simplified soil and zero normal stress capacity (R_{inter} = 1.0)

The notion that the beam element moves relative to the interaction surface, instead of the soil, is investigated in more detail. For two different values of R_{inter} the beam and soil displacements are tracked (Figure 7.8a). An important observation can be made; the soil displacements for R_{inter} = 1.0 or 0.1 are almost exactly the same, the only (small) difference is in the beam displacements. This means that a change in interface strength doesn't influence the soil behaviour around the pile.

The last statement is verified by looking at the normal stresses in the soil around the pile (Figure 7.8b). The normal stresses around the pile region are almost exactly the same for R_{inter} = 1.0 and 0.1 at failure. Even though the interface capacity is reduced, no difference in soil loading is found around the pile. Clearly, R_{inter} has no influence on the way that the soil around the beam is loaded or when this soil fails. The influence of the limited interface capacity must therefore be diverted to the other side of the interface; the displacements of the beam element. Figure 7.8b shows two peaks with positive normal stress values even though tension cut-off is selected. This is caused by extrapolation of the stresses in the integration points to the nodes.

The fact that the same ultimate failure load is obtained for R_{inter} = 1.0 and 0.1 is caused by the normal stresses in the interface. The relative displacements grow faster when the shear capacity of the interface is reached, causing the normal stresses in the interface to grow as well. The normal stresses take over the inter-

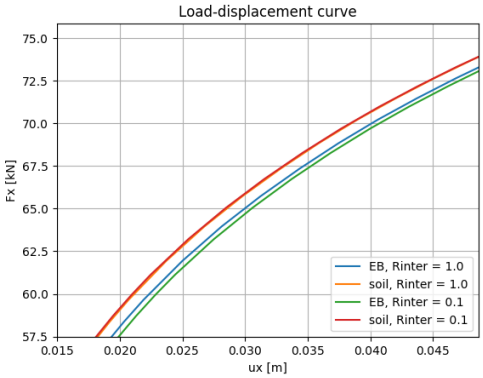

(a) Beam and soil displacements

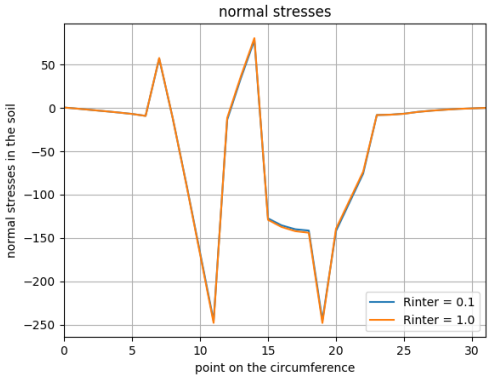

(b) Normal stresses in the soil at the interaction surface

Figure 7.8: Laterally loaded disc model with simplified soil, lateral plasticity method 1

face capacity, pulling the pile region along again. In Appendix F.1.3 it is indeed confirmed that the additional normal stresses almost exactly compensate for the loss in shear capacity when R_{inter} is reduced from 1.0 to 0.1.

The ultimate failure load that is found at the end, is completely dominated by soil failure around the pile region. The pile region, which cannot fail because of the elastic zone approach, pushes against the surrounding soil until this fails. This happens for both R_{inter} = 1.0 and 0.1 at the same failure load, because the displacements of this region are exactly the same. R_{inter} doesn't influence this failure mechanism. The only difference is in the beam displacements found at failure, which are slightly larger for R_{inter} = 0.1 than 1.0.

Looking back at the way that the interface is defined, this behaviour is not very surprising at all. The interface describes the connection between the beam element and the soil elements at the interaction surface. The soil elements are in turn connected to their neighbouring elements, but the beam element is not connected to anything else. When the connection between the beam and soil elements is severed, it is logical that the 'free' beam starts moving more easily than the soil elements, which are still interconnected with other soil elements.

In conclusion, the method that is proposed to incorporate lateral plasticity in the interface between the pile and soil result in an incorrect failure mechanism. Instead of modelling slip of the soil around the pile, the beam element moves relative to the pile region without affecting the ultimate failure load. Even when appropriate limits for the normal stresses in the interface are adopted, no realistic behaviour is obtained.

In order to model lateral plasticity along the shaft of the embedded beam, it is recommended to think of and investigate entirely different methods than proposed in this research. For instance, possibilities of XFEM related methods can be investigated or perhaps it is possible to weaken the soil around the pile locally, to cause failure to occur sooner. Unfortunately, due to time constraints this research falls outside the scope of this research.

7.1.5. Conclusion

The investigation into the behaviour of the pile-soil model with the inclusion of the proposed lateral plasticity method has proven that this way of incorporating lateral plasticity doesn't result in a physically realistic failure mechanism. Instead of influencing the slippage of the soil around the pile circumference, the movement of the beam axis through the soil inside the pile region is influenced.

An overview of the performance of the different lateral plasticity methods is presented in Table 7.2. Method 2 and 3 influenced the results for an axially loaded model (Section 6.3), which is a negative result (– –). It is for this reason that these two methods are not evaluated in case of a laterally loaded model (X). Method 1 didn't show an influence for an axially loaded model (++).

In case of a laterally loaded model method 1 is not able to capture the desired interface behaviour. The mesh sensitivity is still very similar to the mesh sensitivity in the existing embedded beam formulation (0) and the method is not able to capture the effect of R_{inter} (– –). However, the new formulation does show an significant improvement when the elastic zone approach is deactivated compared to the existing embedded

	Axially loaded	Laterally loaded		
	No influence	Mesh sensitivity	Influence elastic zone approach	Ability to capture effect of R_{inter}
method 1	++	0	+	– –
method 2	– –	X	X	X
method 3	– –	X	X	X

Table 7.2: Overview performance of lateral plasticity methods

beam formulation (+). The influence of the elastic zone approach is not entirely diminished yet, leading to the conclusion that the elastic zone approach remains incorporated in the new embedded beam formulation.

Despite the disappointing outcome that the correct interface behaviour is not captured, lateral plasticity method 1 is still applied to the new embedded beam formulation. This decision is made for several reasons:

- The new embedded beam element without lateral plasticity shows an increased mesh sensitive behaviour compared to the existing embedded beam formulation for the laterally loaded disc model with no manipulated mesh. This is an undesired effect of the new embedded beam formulation, which is largely solved by incorporating method 1 (Figure 7.2).
- From a physical point of view it is more realistic to combine the two shear components in the interface ($\tau = \sqrt{\sigma_s^2 + \sigma_t^2}$). The shear strength as is used in Equation (5.21) is the well-known Mohr-Coulomb failure criterion (Verruijt, 2012), in which the shear stress is considered as τ as well.

7.2. Laterally loaded Alzey Bridge model

The proposed embedded beam model with explicit interaction surface, including the improved foot interface and lateral plasticity method 1 is evaluated in this section, especially focussing on the lateral deformation behaviour. The influence of the foot interface reduction is assessed again, since no conclusive value has been obtained. The embedded beam models, both the existing and new one, should be compared to the volume pile method without interface, since the embedded beam elements don't have an interface in lateral direction.

The Alzey Bridge model is used, only now with a load of 1000 kN in x-direction. No load in z-direction is applied. It is not only relevant to verify the deformations at the head of the pile, but also at the foot. In previous research and validation studies (Sluis, 2012; Hermans, 2014) it was noted that the obtained displacements at the foot of a laterally loaded embedded pile in PLAXIS 2D are too large. Although this problem was mainly noted in PLAXIS 2D, it is still relevant to check the performance of the embedded beam at the foot in PLAXIS 3D. The load-displacement curves at the head and foot of the pile computed with different models are presented in Figure 7.9.

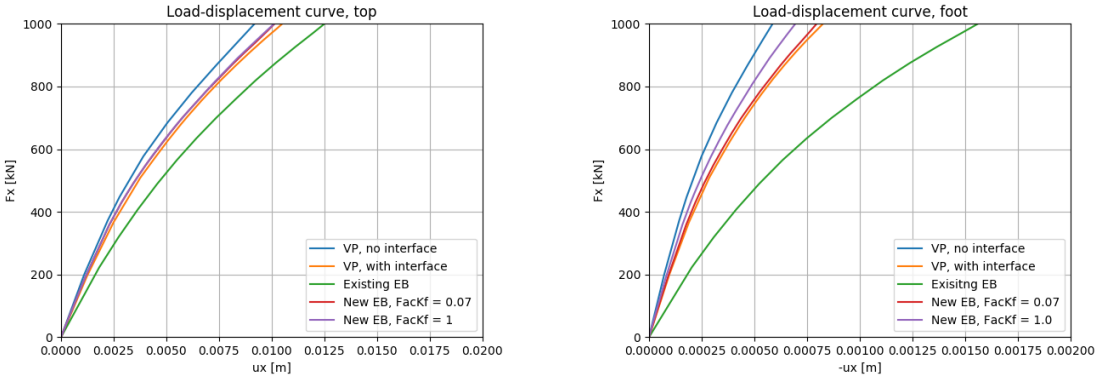

(a) Head of the pile

(b) Foot of the pile

Figure 7.9: Laterally loaded Alzey Bridge model

The new embedded beam formulation seems to be in very good agreement with the volume pile method with interface. This is assumed to be coincidence for this test case. Both the displacements at the head and foot of the pile show that the existing embedded beam formulation behaves too flexible. The new embedded beam formulation behaves stiffer, even when the foot interface stiffness is reduced, resulting in a much better agreement with the volume pile method. The influence of the foot interface stiffness reduction is merely visible in the behaviour at the foot of the pile. This is in confirmation with the conclusion that was already drawn in Section 6.4.1.

7.2.1. Influence of the interface strength reduction factor R_{inter}

In the volume pile method the strength reduction of the interface results in a lower interface stiffness and a lower plastic limit. The former is clearly visible in Figure 7.10a. The results for $R_{inter} = 0.1$ are not very realistic, since a physical equivalent doesn't exist.

The existing embedded beam formulation doesn't have a limit for the interface stress components in lateral direction, only in axial direction. This is confirmed by the results in Figure 7.10b, where the variation of R_{inter} doesn't influence the results. In the new embedded beam formulation R_{inter} doesn't influence the interface stiffness as in the volume pile method, only the plastic limit for the shear stresses is influenced by R_{inter}. Since the shear components (axial and lateral) are combined in the new formulation, R_{inter} has an influence on the results of a laterally loaded pile (Figure 7.10c). The influence of R_{inter} in the new embedded beam formulation is smaller than in the volume pile method, which is according to expectations.

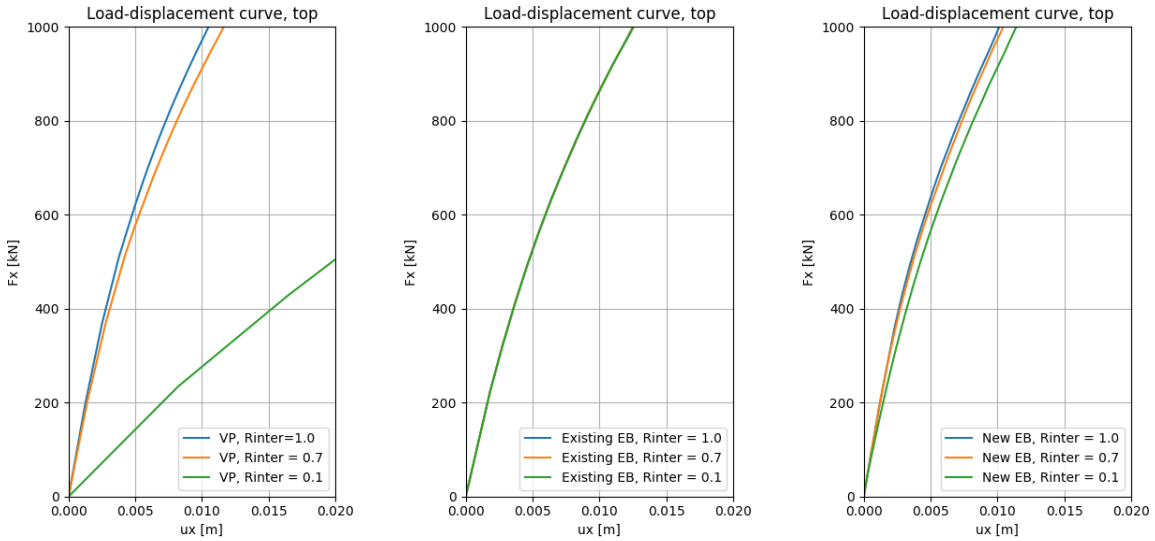

(a) Volume pile

(b) Existing embedded beam formulation

(c) New embedded beam formulation

Figure 7.10: Laterally loaded Alzey Bridge model, influence of R_{inter}

7.2.2. Influence of the number of points on the interaction surface

In Section 6.4.3 it was concluded that the number of points that are considered on the interaction surface can be chosen relatively low, since no difference in results was found between a number of 4 and 200 points. Whereas the interaction surface is straight in axial direction, it is curved in lateral direction, which might cause the necessity for more points to consider on the interaction surface.

Figure 7.11 shows the results for varying values of nCirDiv. The curve for nCirDiv = 4 clearly deviates from the curves for higher nCirDiv's. From values of nCirDiv = 8 onward the results show negligible differences again. Therefore, it is recommended to consider at least 8 points on the interaction surface.

However, it must be noted that the influence of, for example, the diameter or mesh size on the required number of points on the interaction surface is not evaluated. Therefore, in all test cases that are presented in Chapters 6 and 7 nCirDiv values of 16 (axial) and 32 (lateral) and higher are used.

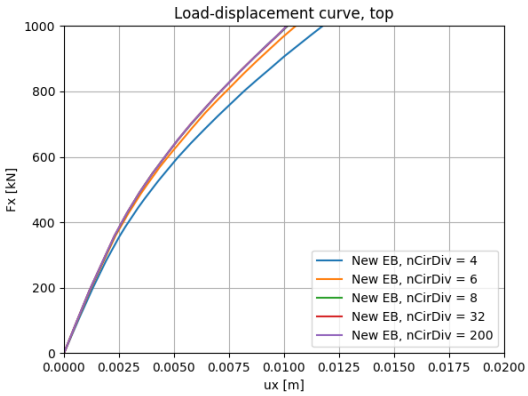

Figure 7.11: Laterally loaded Alzey Bridge model calculated with new embedded beam, varying nCirDiv

7.3. Influence on the response for different L/D ratio's

The deformation behaviour of piles with small L/D ratio's (relative short piles) is different than of piles with large L/D ratio's. A different failure mechanism occurs (Fleming et al. (2009), Appendix A). Figure 7.12 shows the configuration of the piles with different L/D ratio's at the end of the calculation. The existing embedded beam element seems to be better in capturing the lateral deformation behaviour for relatively long piles, and less so for relatively short piles. Chapter 8 will explain this further.

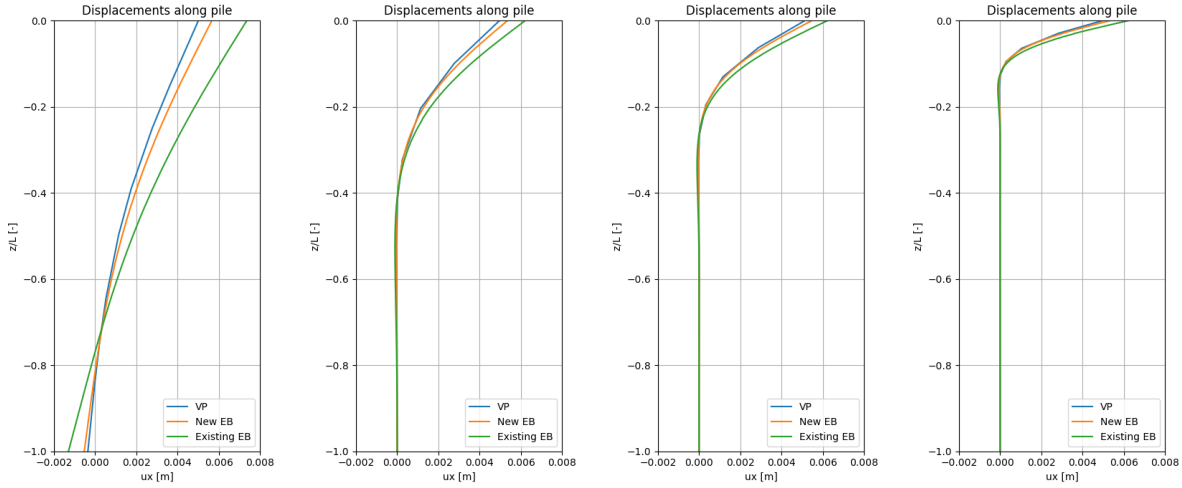

(a) L/D = 5 (b) L/D = 12 (c) L/D = 19 (d) L/D = 40

Figure 7.12: Displacement profiles for piles with different L/D ratio's

It is interesting to evaluate how much of an improvement is achieved with the new embedded beam formulation compared to the existing one in terms of stiffness. However, there are many parameters and settings that might influence this, such as the mesh size, radius of the pile and load level. Therefore, the relative improvement is computed for six different L/D ratio's (5, 12, 19, 26, 33, 40), two different diameters and two different mesh sizes (Figure 7.13). The relative improvement here is defined by:

$$\left(1 - \frac{VP - EB_{new}}{VP - EB_{ex}}\right) \cdot 100 \tag{7.1}$$

So, when the difference between the results of the new embedded beam model and the volume pile model is smaller than the difference between the existing embedded beam model and the volume pile model an improvement is obtained. The volume pile without interfaces is considered, because the embedded beam models are not able to capture lateral interface behaviour. The red dot in Figure 7.13b indicates the relative improvement that is obtained with the model that is evaluated in Section 7.2.

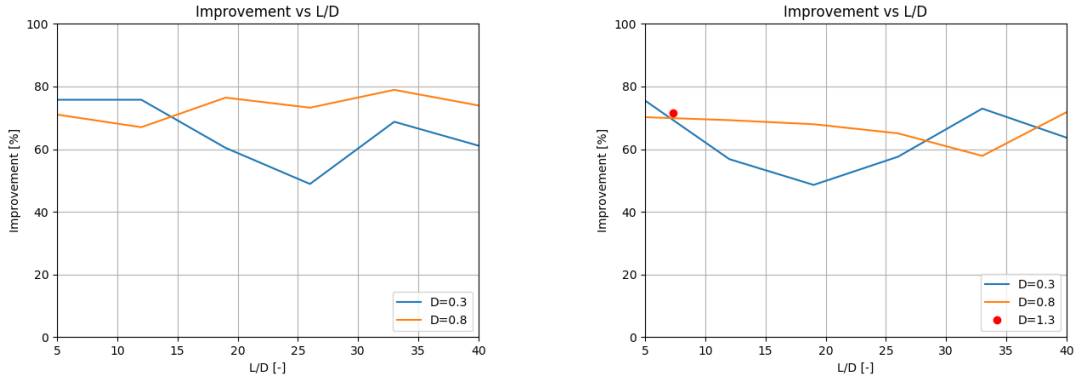

(a) Very coarse mesh (b) Medium mesh

Figure 7.13: Relative improvement at the head of the pile

Evaluation of Figures 7.13a and 7.13b doesn't show a clear trend that depends on the L/D ratio. For both long and short piles an improvement is obtained, even though the existing embedded beam element already shows reasonable behaviour for long piles. A feature worth mentioning is that for all L/D ratio's and both mesh sizes the volume pile model always behaves stiffest and the existing embedded beam model always behaves too flexible. The obtained relative improvements at the head of the pile seem to be bounded between 50% and 80% with an average of 67 %, which is excellent.

The results at the foot show a completely different behaviour (Figure 7.14). For large L/D ratio's the displacements near the foot of the pile are approximately zero (Figure 7.12). When values near zero are obtained, the numerical error is relatively large. Therefore, the results near the foot of relative long piles are not accurate and should not be taken into account. This fact is confirmed by the irregular results that are shown in Figure 7.14 for large L/D ratio's.

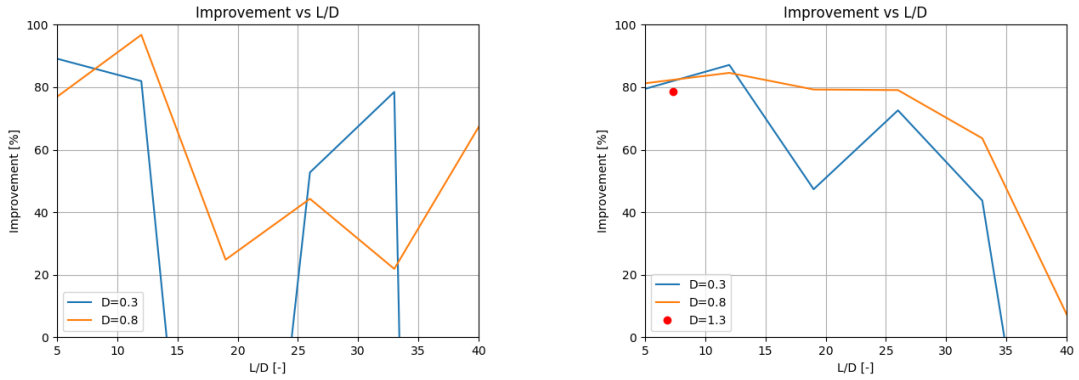

(a) Very coarse mesh (b) Medium mesh

Figure 7.14: Relative improvement at the foot of the pile

Looking at the results for small L/D ratio's (5, 12 and 7.3) an average relative improvement of approximately 84% is obtained. In this case the existing embedded beam model behaves too flexible, which is largely solved by the implementation of the new embedded beam model.

7.4. Inclined pile

The method proposed in Section 5.2.1 is generalised for piles with arbitrary inclinations. The performance of this generalisation is validated in this section. The model that is described in Sadek and Shahrour (2004) is used (Figure 7.15). The soil is modelled as a linear elastic material with a Young's Modulus of 100 MPa. The pile has a diameter of 0.25 m and a Young's Modulus of 200 GPa.

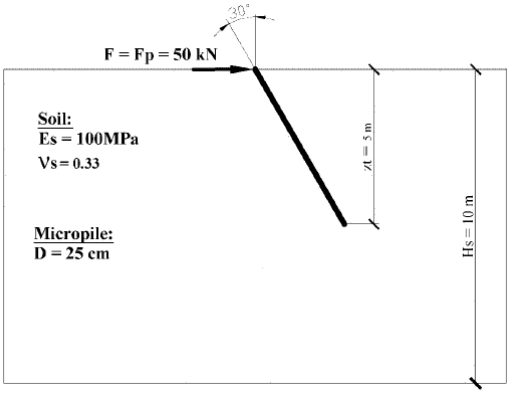

Figure 7.15: Example used to verify an inclined pile. (Sadek and Shahrour, 2004)

This model is calculated with the volume pile method, existing embedded beam formulation and new embedded beam formulation. The lateral displacements along the length of the pile are shown in Figure 7.16a. The plot with normalised displacements over depth presented in Sadek and Shahrour (2004) (Figure 7.16b) shows much larger displacements for both the conventional and embedded beam formulation. The embedded beam element has seen many changes since the initially proposed embedded beam element by Sadek and Shahrour (2004). One of the major modifications is the elastic zone approach, which made the embedded beam element behave significantly stiffer (Engin et al., 2007). Therefore the obtained differences with the results from Sadek and Shahrour (2004) are not unexpected.

When the existing embedded beam element is compared to the volume pile method, it is obvious that the existing embedded beam element behaves too flexible (Figure 7.16a). The new embedded beam formulation behaves very close to the volume pile without interface.

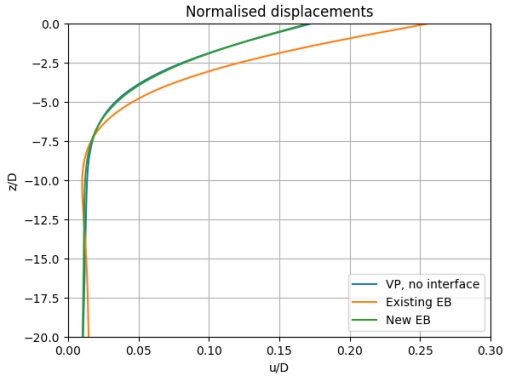

(a) New results

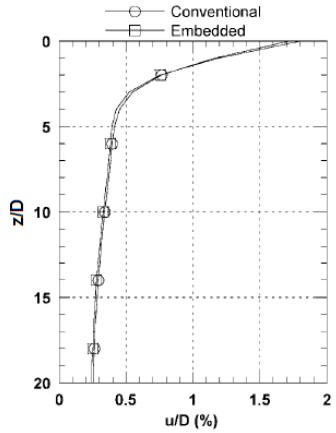

(b) Results from Sadek and Shahrour (2004)

Figure 7.16: Normalised displacements vs normalised depth

Figure 7.17 shows the different force distributions along the length of the pile obtained with the different methods. Unfortunately, it is not possible to extract the normal force distribution for the volume pile method from the PLAXIS output accurately, so it's not possible to compare the embedded beam models to the volume pile model in this case. The embedded beam models show very good agreement with the normal force distribution presented in Sadek and Shahrour (2004) for the same example.

The shear and moment distributions of all methods show a different behaviour than the results presented by Sadek and Shahrour (2004). Both the shear and moment force distributions presented by Sadek and Shahrour (2004) approach zero at a smaller depth than the other models. Especially in the moment force distribution the Sadek and Shahrour (2004) result shows a smaller peak value. For both the shear and moment force distributions the new embedded beam formulation seems to behave in better agreement with the volume pile model than the existing embedded beam model.

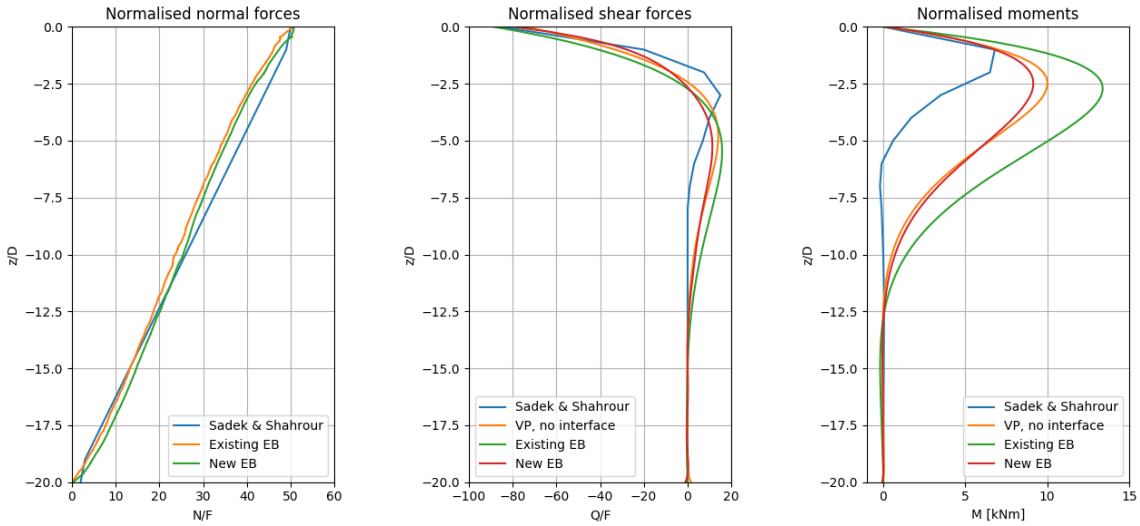

(a) Normal forces (b) Shear forces (c) Moment forces

Figure 7.17: Force distributions over depth

7.5. Summary

The results presented in Section 7.1 and the corresponding explanation for the obtained results lead to the conclusion that the proposed method to incorporate lateral plasticity doesn't result in a physically realistic failure mechanism. Instead of influencing the slippage of the soil around the pile perimeter, the movement of the beam axis through the soil inside the pile region is influenced. Therefore, the method is not able to capture the desired interface behaviour.

Nevertheless, it is decided that method 1 will be applied to the new embedded beam model. This decision is made for several reasons, including the fact that it does result in a small improvement compared to the new formulation without lateral plasticity methods and it makes sense from a physical point of view to combine the two shear stress components.

The results of the new embedded beam model for a laterally loaded model (Section 7.2) clearly show that the new embedded beam formulation is a significant improvement of the new embedded beam formulation. The existing embedded beam element behaves too flexible when loaded laterally, the new embedded beam element results are much closer to the volume pile without interfaces.

The influence of the foot stiffness reduction is confirmed to be limited to the behaviour near the foot of the pile, in accordance with the results from Chapter 6.

Variation of R_{inter} does influence the response of the new embedded beam element slightly. This is caused by the combination of the two shear components in the correction for plasticity. However, the influence of R_{inter} is not similar as for the volume pile method. Therefore, it is recommended not to use this option for laterally loaded piles. When results of laterally loaded piles are evaluated, it should be kept in mind that no lateral interface is modelled.

For the considered model it is observed that for values of nCirDiv of 8 and higher no significant difference in response is obtained. Therefore, it is concluded that at least 8 points on the interaction surface should be considered. Since, the conducted parameter study has not investigated the influence of different model dimensions or input parameters, higher values of nCirDiv are used in this report.

For different L/D ratio's (Section 7.3) the average relative improvement in stiffness that is obtained with the new embedded beam formulation is 67% at the head of the pile. It also proofs that the new embedded beam model is applicable to a wide range of pile dimensions. For small L/D ratio's the behaviour at the foot is improved considerably as well with an average improvement of 84%. Likewise, it is proven (Section 7.4) that the generalisation for arbitrarily inclined piles is successful.

IV

Application

8

Case study: Offshore monopile foundation

In this chapter the proposed embedded beam element is applied in a case study. In this case study the proposed embedded beam element is evaluated considering a realistic case of a monopile foundation. Monopile foundations are used, for example, for offshore wind turbines structures, which are subjected to lateral wind and wave loading. These monopile foundations have a very large diameter and therefore small L/D ratio's.

The ability to model monopile foundations is relevant, because a recent study (PISA) has shown that significant cost reductions can be obtained in this field. Until now, the method that is used in the offshore design codes to analyse laterally loaded piles is based on the Winkler model, also known as the p-y approach (Appendix A). This method was initially designed for long and slender piles with a relatively large L/D ratio, but the diameters of the monopiles that are used for offshore wind turbine structures are significantly larger than the diameters on which the p-y curves are based.

The PISA (PIle Soil Analysis) project is a joint industry research project led by DONG Energy and run through the Carbon Trust's Offshore Wind Accelerator programme. The project focussed on the use of numerical modelling with 3D finite element analysis to develop a new 1D design method to model monopile foundations, which is validated and calibrated using field tests. During the project it turned out that when all components of the soil reactions (Figure 8.1b) are taken into account, the obtained bearing capacity of the pile is higher than in the traditional methods (Appendix G.1). This results in the possibility to reduce the pile dimensions, resulting in a reduction in the amount of steel and, therefore, in fabrication, transportation and installation costs.

The proposed design method in the PISA project is based on an extension of the existing p-y curves. Whereas in the traditional p-y curves the pile-soil interaction is only based on distributed lateral forces that develop between the pile and soil, the proposed design method includes three other components; distributed moments, base shear and base moments. Figure 8.1a and 8.1b show the differences between the current method and the new method. The results from the 3D finite element models are used to extract the soil reaction curves that are used in the proposed 1D model (Figure 8.1c). The vertical shear stresses around the pile perimeter lead to a distributed moment in the 1D model.

Especially the influence of the shear stresses that lead to a distributed moment in the 1D model has proven to be important for piles with small L/D ratio's. Taking into account this contribution leads to a stiffer response of the pile foundation, which is favourable for pile dimensioning. It is expected that the existing embedded beam is not able to take into account this contribution, because the shear is modelled along the beam axis making it impossible to take downward shear at the back and upward shear at the front of the pile into account. This expectation is confirmed by previous results in Chapter 7, which show that the existing embedded beam model behaves too flexible. Since the proposed embedded beam model is able to take into account the shear stresses at the true pile perimeter, it is expected that the new model is better able to capture the contribution of this component.

Furthermore, Plaxis recently developed a monopile design tool (PLAXIS MoDeTo, Appendix G.2) that applies the PISA 1D design tool. Before the 1D design tool can be used 3D calculations need to be done to calibrate the soil reactions working on the pile. Now the question arises if the proposed embedded beam is able to model large diameter monopiles, because it is expected that this would reduce the calculation time of the 3D calculations significantly.

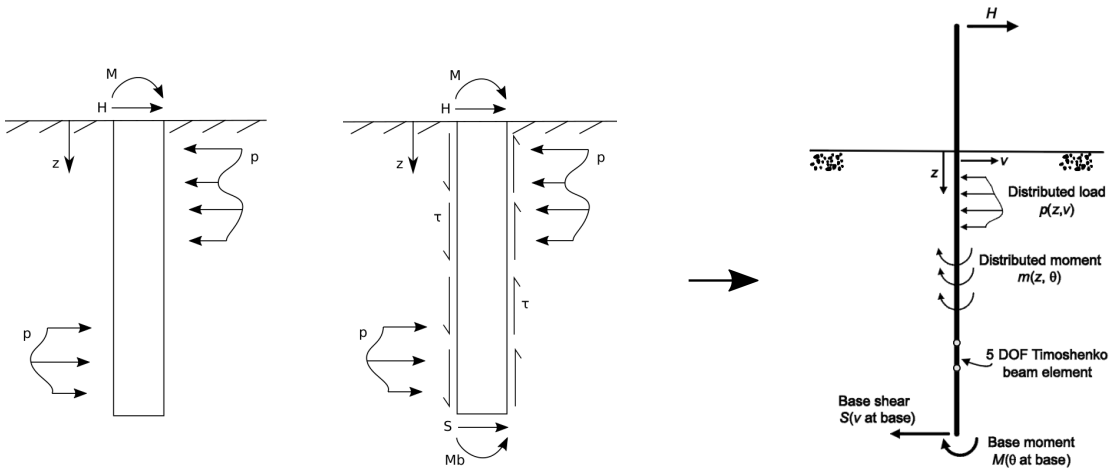

(a) Current method (b) New method (c) Proposed 1D model. (Byrne et al., 2015)

Figure 8.1: PISA design method

8.1. The model

Monopile foundations are generally circular steel tubes with a very large diameter. The considered pile (Figure 8.2a) has a diameter of 10 meter, thickness of 0.091 m and a total length of 110 m, of which 60 m is embedded in the soil. This gives a L/D ratio of only 6, which is a relatively 'short' pile. The model is easily constructed using PLAXIS MoDeTo.

The symmetry in the model makes it possible to model only half of the full 3D model; this is automatically done in PLAXIS MoDeTo. The model dimensions are 100 by 40 by 150 meter. The pile is modelled using plate elements with steel properties; Young's Modulus of 200 GPa and a Poisson's ratio of 0.3. The model on the left (Figure 8.2a) has proven to be in good agreement with field data from the PISA project.

The model consists of 13 soil layers, accurately describing the real soil. However, this detailed soil profile yields a relatively fine mesh and a rather lengthy calculation. The focus of this research is not on the soil but on the structural element. Hence, it is not necessary to take such detailed soil behaviour into account. So, in order to obtain the embedded beam results and to compare them to a full 3D model, a model is developed (Figure 8.2b) consisting of only three soil layers. The simplified soil layers are based on the detailed soil model in such a way that the final results are comparable. The input parameters for the simplified soil and monopile are presented in Appendix G.3. In addition, embedded beam elements are not able to calculate a bisected model. Therefore, the model dimensions are 100 by 80 by 150 m, considering the full 3D situation.

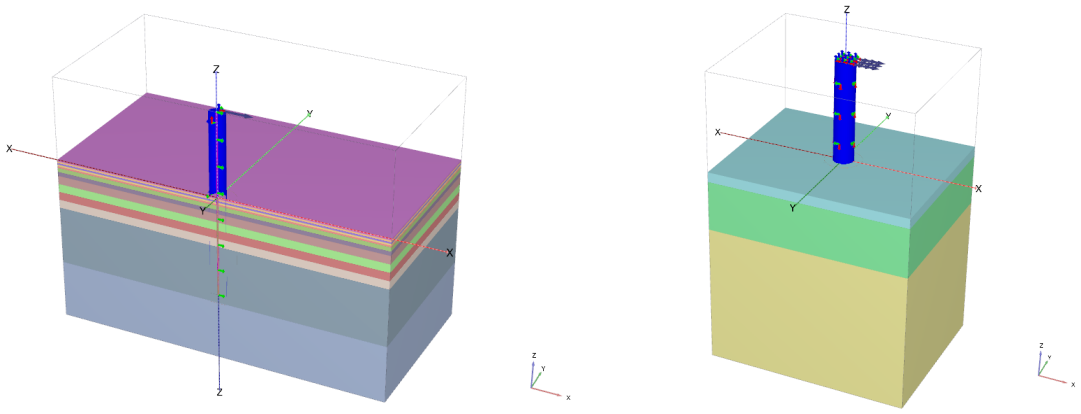

(a) Detailed model (b) Full and simplified 3D model

Figure 8.2: Case study model

It is better to use the same mesh for the full 3D model and the embedded beam model, in order to be able

to make a proper comparison. At the centre of the pile in Figure 8.2b an embedded beam element is located, which is deactivated to obtain the results in Figure 8.3. When the plate elements and interface elements are deactivated and the embedded beam element activated, the same model (and mesh) can be used to calculate the embedded beam models.

Figure 8.3 shows load-displacement curves that are obtained with the detailed and full 3D models with and without interfaces. The curves that are obtained with the simplified model show reasonable agreement with the detailed model. The differences that are obtained are largely caused by the differences in mesh. The mesh of the simplified model can be refined, which yields results that are in better agreement with the detailed model (Figure G.2).

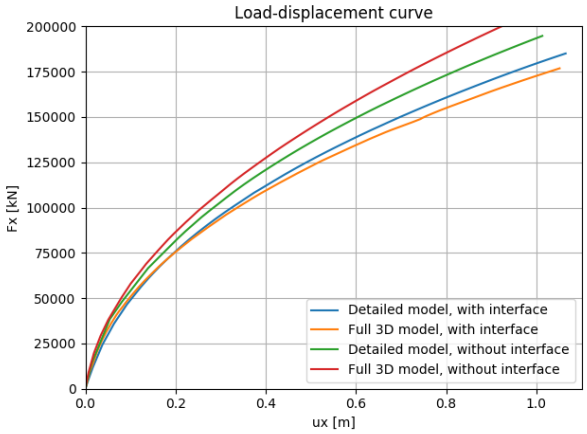

Figure 8.3: Results of case study; detailed and simplified full 3D model

When the interface is switched off, both models show a stiffer response. This is according to expectations. Without the interface elements the plate elements are rigidly connected to the soil. No slippage of soil around the pile can occur now. This results in an additional resistance compared to the model where the interface elements would have caused slippage.

8.2. Analysis of results

With the models presented in the previous section, the new embedded beam model can be compared to the existing embedded beam model and the results of a full 3D model with and without interface. First the response in terms of load-displacement curves shall be evaluated. Subsequently, the force distribution in the pile, mesh sensitivity of the models and computation time are evaluated. These results lead to a conclusion on the possibility to use the proposed embedded beam element to replace 3D calculations in the future.

8.2.1. Deformation behaviour

The load-displacement curves at the head and foot of the pile computed with different models are presented in Figure 8.4a. The head of the pile is considered to be at ground level. The new embedded beam formulation shows a response that is in very good agreement with the full 3D model without interface. The existing embedded beam model shows a slightly more flexible response than the new embedded beam formulation.

Looking at the response at the foot of the pile, the new embedded beam model doesn't resemble the full 3D model without interface exactly (Figure 8.4b). The response of the new embedded beam model deviates from the full 3D response at a load level of approximately 150 000 kN, behaving too flexible. Until then, the response of the full 3D model without interface and the new embedded beam model are in very good agreement. Even though this result is not perfect, the improvement that is obtained with the new embedded beam model compared to the existing one is significant. The foot of the existing embedded beam model initially behaves too stiff, but around a load level of 125 000 it starts behaving extremely flexible.

Clearly, the influence of the foot stiffness is limited to the response at the foot of the pile. The load-displacement curve of the head of the pile (Figure 8.4a) doesn't show a perceptible difference between the results of the new embedded beam formulation with reduced and full foot stiffness. When the foot stiffness is increased, the load-displacement curve at the foot of the new embedded beam model (Figure 8.4b)

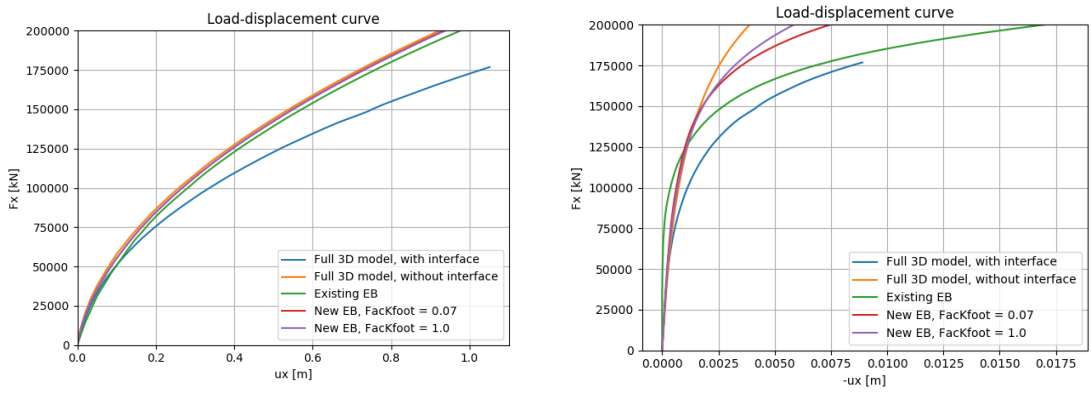

(a) Head of the pile

(b) Foot of the pile

Figure 8.4: Load-displacement curves of full 3D and embedded beam models

approaches the curve of the full 3D model without interface. Even when the full foot stiffness is used, the behaviour at the foot is still less stiff than the full 3D model without interface.

The obtained results in both axial and lateral loaded models (Chapters 6, 7) suggest that the foot stiffness in axial direction requires reduction, but that the foot stiffness in lateral direction doesn't necessarily require reduction. Therefore, it is suggested to investigate the possibility to decouple the axial and lateral foot stiffness and find appropriate values for both.

In addition, in the current PLAXIS 3D input it is not possible to define a maximum foot resistance in lateral direction. At the moment the lateral foot force is obtained by an elastic calculation, based on the same stiffness as the foot stiffness in axial direction. Especially for large diameter piles, the influence of the lateral foot force is significant. This is also came out of the PISA research (Figure 8.1b). Therefore, it is recommended to study an appropriate limit for the lateral foot force and incorporate it, either based on input or on soil properties. This research lies outside the scope of this research.

Looking at the deformed mesh configurations of the different models (Figure 8.5), the full 3D model with interfaces stands out from the others. The interface elements are able to model gap forming at the back of the pile, creating a space between the pile and surrounding soil. The influence of gap forming in the full 3D model with interfaces is investigated in more detail in Appendix G.5, but no decisive conclusion can be deduced from the obtained results.

The other deformed mesh configurations show very similar behaviour, though different than the full 3D model with interfaces. The soil elements at the back of the pile are stretched and the soil elements at the front are compressed. In all models the stretch and compression are of equal amounts.

The deformed mesh of the existing embedded beam models shows that the centre of the pile region moves slightly more than the rest of the pile region. This is caused by the connection of the beam to the soil element at the beam axis, which causes locally high stresses and deformations. When the soil element at the beam axis starts to deform, it pushes and pulls the surrounding soil elements, taking them along. But the largest deformation still occurs in the soil element at the beam axis.

In the new embedded beam model this doesn't happen any more, because the connection between the beam and soil is modelled at the interaction surface. However, the new embedded beam formulation shows a small shape distortion of the pile region, elongating it slightly in the x-direction. This is caused by the incorporation of lateral plasticity method 1, because deactivation of the lateral plasticity method eliminates this behaviour (Figure G.3). The lateral shear capacity in the interface is limited, but the normal stress capacity not. When the shear capacity is reached at the sides of the beam, the resistance is dominated by the normal compressive stresses at the front of the pile. So the beam element pushes more against the front of the interaction surface, causing the front to deform slightly more than the rest of the interaction surface. The slight distortion is deemed negligible and is assumed to have no significant effect on the results.

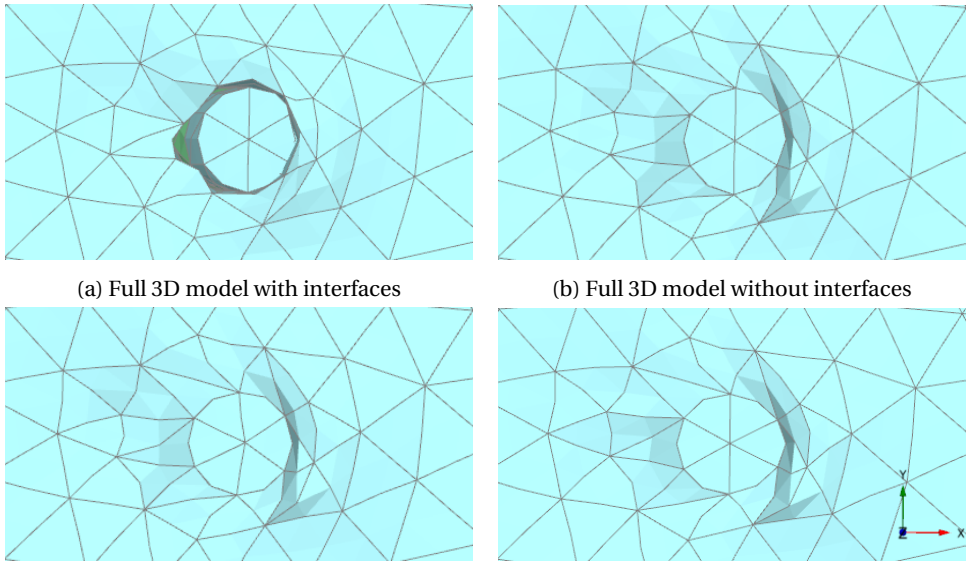

(a) Full 3D model with interfaces

(b) Full 3D model without interfaces

(c) Existing embedded beam model

(d) New embedded beam model ($\Gamma_{foot} = 0.07$)

Figure 8.5: Deformed mesh configurations

8.2.2. Force distribution

The force distributions along the length of the pile as obtained with the embedded beam models are shown in Figure 8.6.

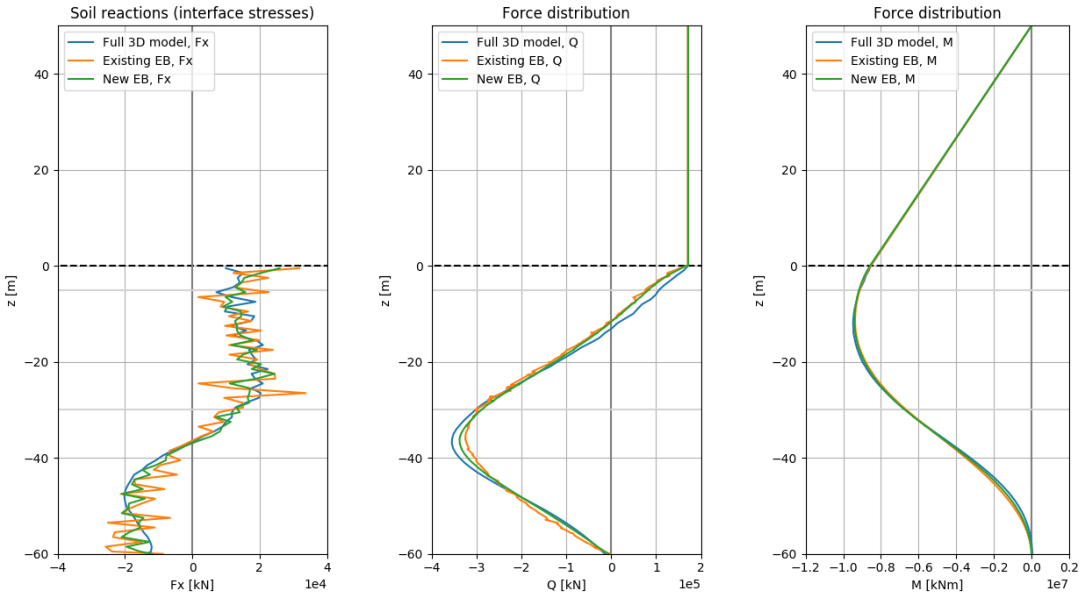

(a) Soil reactions

(b) Shear force

(c) Moment force

Figure 8.6: Force distributions along the length of the pile

First, it is confirmed that the sum of the soil reactions is in equilibrium with the force at the top of the pile for every model. The distribution of the soil reactions along the pile (Figure 8.6a) for all models are in very good agreement. However, the curve of the full 3D model is much smoother than the curves obtained with the embedded beam models. Especially the existing embedded beam model shows large fluctuations.

It must be noted that the interface elements in the full 3D model are triangular elements with six pairs of nodes. They are integrated using six-point Gauss integration. These elements are relatively small and one beam element might be surrounded by multiple interface elements. In the embedded beam the virtual

interface is cylindrical, for which the integration in the length is done with a 3-noded Newton-Cotes scheme and the integration along the perimeter is done by division by the number of points and multiplication with the perimeter. Only one interface element per beam element is considered. The method used in the standard interface elements is more accurate than the method for the virtual interface elements in the embedded beam models. The method that is applied for the virtual interface elements along the embedded beams causes inaccurate integration and therefore a less accurate spread of the results along the pile. The new embedded beam model shows slightly less fluctuations than the existing one. This is a result of the higher number of points on the interface that is used to obtain the nodal values.

The output results of the soil reactions along the pile can be optimised to obtain smoother curves. For example, averaging could be applied.

A smoother shear force distribution is found for the new embedded beam model compared to the existing embedded beam model (Figure 8.6b). This in accordance with the larger fluctuations that are obtained in the soil reaction distribution of the existing embedded beam model. In the existing embedded beam formulation localised behaviour in the soil can affect the results more severely than in the new embedded beam formulation, because the response is calculated at a very limited number of points.

The shear and moment force distributions show very good agreement with the expected response of the beam under the considered loading conditions. The moment force (Figure 8.6c) in the beam increases linearly until the pile enters the soil. Inside the soil the moment force distribution shows two parabolic shapes, corresponding with the distributed loading conditions along the pile caused by the soil reactions. The shear force distribution (Figure 8.6b) corresponds with the gradient of the moment force distribution; the maximum moment corresponds with a zero shear force. The maximum slope in the moment force distribution corresponds with the maximum shear force in the beam. In the pile above the soil a constant shear force of approximately 171 000 kN is found. This corresponds with the force that is working at the top of the pile.

8.2.3. Mesh sensitivity

The case study model considers a laterally loaded model. In Chapter 7 it was already shown that the mesh sensitivity of the volume pile method without interface, the existing and new embedded beam models are very similar for a purely laterally loaded model. However, in that case only a slice of a pile was considered that was loaded equally at the top and bottom, not taking into account the foot of the embedded beam models. Therefore, it is still interesting to evaluate the results for the case study model.

The mesh sizes that are considered in the mesh sensitivity study are shown in Table 8.1. A coarse, medium and fine mesh are used.

	Elements	Nodes
mesh 1	4981	7773
mesh 2	7853	12064
mesh 3	10197	15504

Table 8.1: Mesh sizes for the case study

The mesh sensitivity in the response at the head and foot of the pile is considered. The mesh sensitivity at the head of the pile (Figure 8.7) confirms the obtained results and conclusions of the simple laterally loaded disc test case; the mesh sensitivity in the full 3D model, existing and new embedded beam model are very similar. The full 3D model without interfaces and the new embedded beam model almost show no perceptible differences at all. The existing embedded beam model shows a slightly less stiff response, but the mesh sensitivity seems to be similar.

At the foot of the pile the mesh sensitivity shows larger differences (Figure 8.8). The full 3D model without interfaces shows a very small mesh sensitivity, the new embedded beam model slightly more and the existing embedded beam significantly more. Clearly, the new embedded beam model already shows a large improvement compared to the existing embedded beam model in terms of stiffness and mesh sensitivity. However, there is still some room for improvement at the foot. It is expected that optimising the foot stiffness and its relation with the shaft stiffness might yield an improvement of the behaviour at the foot of the pile.

The increase in foot stiffness only influences the mesh sensitivity at the foot of the pile (Figure 8.8d). Compared to the new embedded beam formulation with reduced foot stiffness (Figure 8.8c) the mesh sensitivity is reduced. The results are not exactly the same as the full 3D model without interface (Figure 8.8a), but they are in reasonable agreement.

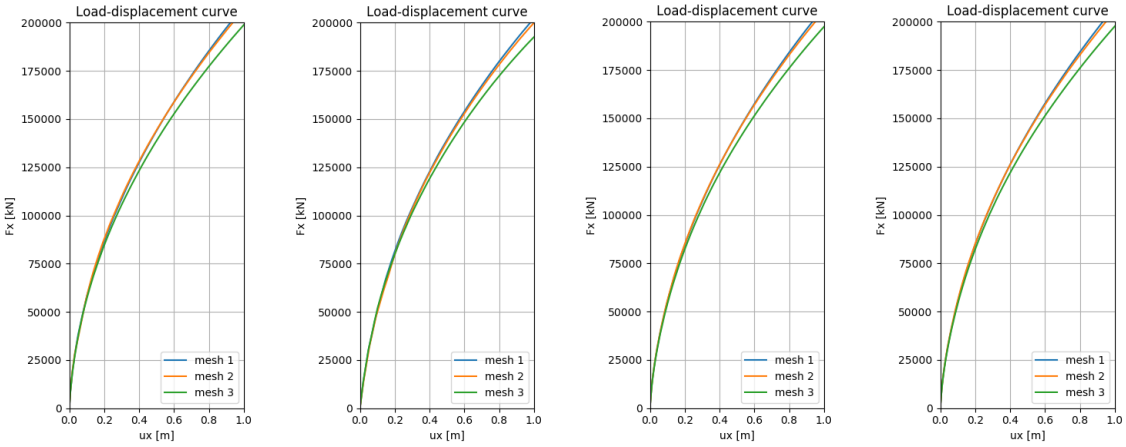

(a) Full 3D model without interface (b) Existing embedded beam model (c) New embedded beam with $\Gamma_{foot} = 0.07$ (d) New embedded beam with $\Gamma_{foot} = 1.0$

Figure 8.7: Mesh sensitivity at head of the pile

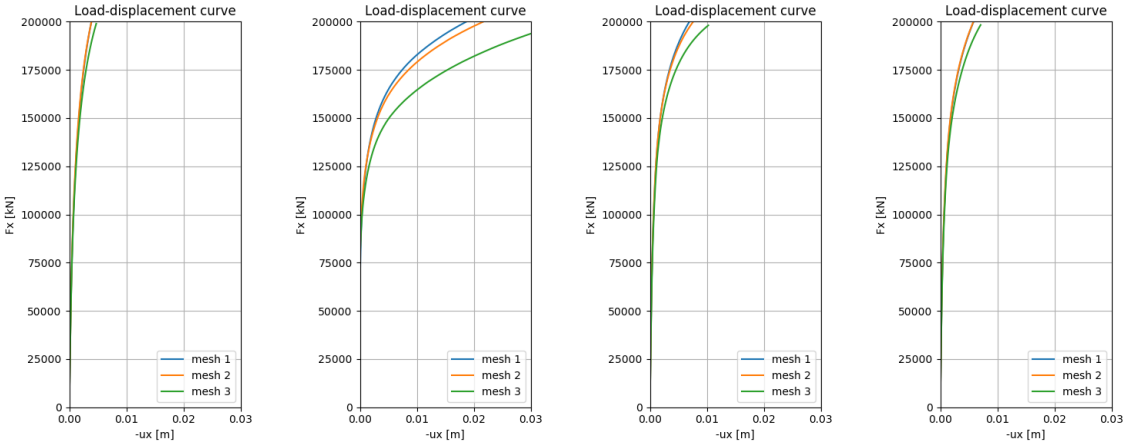

(a) Full 3D model without interface (b) Existing embedded beam model (c) New embedded beam with $\Gamma_{foot} = 0.07$ (d) New embedded beam with $\Gamma_{foot} = 1.0$

Figure 8.8: Mesh sensitivity at foot of the pile

Notable in both figures (Figure 8.7 and 8.8) is that the third mesh size shows a larger deviation from the other two mesh sizes. Although, Table 8.1 shows that the third mesh is not significantly finer than the other two. For the mesh generation in PLAXIS 3D the option of enhanced mesh refinements is applied, which might result in local mesh refinements. It is suspected that in the third mesh size this option has resulted in a more significant mesh refinement near the embedded beam than for the first two mesh sizes. The number of elements is not significantly higher because a coarser mesh might be applied to the soil farther away from the embedded beam.

8.2.4. Computation time

The embedded beam model in PLAXIS 3D is intended to simplify the modelling of pile foundations and reduce the calculation time compared to a full 3D model or the volume pile method. Therefore, it is interesting to compare the computation time for the different models (Table 8.2).

The existing embedded beam model indeed needs significantly less time to compute the results than the full 3D model with interfaces. However, it is very interesting to note that the full 3D model without interfaces requires even less time. The full 3D model without interfaces doesn't take into account interface behaviour, so it doesn't have to obtain the interface stiffness matrix and force vector contributions. This saves time. In the

	Full 3D with interface	Full 3D without interface	Existing EB	New EB
Initial phase	5	4	5	5
Installation phase	3.4	4.61	4.66	55.11
Loading phase	400.83	140.99	170.83	335.17
Total	409.23	149.6	180.49	395.17

Table 8.2: Computation time of the different models

existing embedded beam the stiffness matrix and force vector contributions are calculated. Although no limit for the lateral shear stress and normal stress in the interface is defined, the existing embedded beam model does take into account the elastic behaviour of the interface. This probably causes the longer calculation time for the existing embedded beam model.

The new embedded beam model requires more time to calculate than the existing embedded beam model. In fact, the computation time is almost double. This is not very surprising, because the new embedded beam model takes (in this case) 32 points into account for every beam integration point. So, whereas the existing embedded beam model calculates 3 points, the new embedded beam model calculates 96 points.

The calculation time of the new embedded beam model is slightly lower than the calculation time of the full 3D model with interfaces, but not much. However, it must be noted that the calculation procedure of the new embedded beam model can be improved significantly. During this research the focus was on making the model work, not on optimising the code. It is expected that significant computation time reductions can still be obtained. Two major improvements would be to optimise the search for the soil elements at the interaction surface and to take into account the plastic potential when correcting the stresses in case of plasticity.

8.3. Conclusion

The PISA research has proven that all of four soil reaction terms (lateral resistance and vertical shear along the shaft and base shear and moment) should be taken into account to model the response of a large diameter pile foundation accurate. The new embedded beam element models the pile-soil interaction at the true pile perimeter, making it possible to take into account the components along the shaft much better than the existing embedded beam formulation. For this reason a stiffer response is obtained with the proposed embedded beam model, which is in better agreement with a full 3D model without interfaces.

However, the full 3D model with interfaces behaves more flexible. The use of interfaces and a strength reduction (R_{inter}) of approximately 0.7 is recommended when modelling pile foundations in PLAXIS. The results clearly show that the proposed embedded beam element is not able to capture the desired interface behaviour in lateral direction.

In addition, spreading the pile-soil interaction over a surface reduces the stress singularity that is induced in the soil by the embedded beam. This leads to a considerable mesh sensitivity reduction compared to the existing embedded beam model near the foot of the pile.

Furthermore, the desired computation time reduction is not obtained with the current prototype. For this reason and the lack of lateral interface makes the proposed model not suitable to replace full 3D calculations yet. Nevertheless, the proposed embedded beam element is already more robust than the existing implementation and has features that open up many possibilities to improve the model in the future. A selection of the possibilities is elaborated in Chapter 10.

V

Conclusions and Recommendations

9 Conclusions

In Chapter 1 the research objective is formulated. The aim of this research is to develop a new embedded beam element in PLAXIS 3D that improves the response of the existing embedded beam element. In order to achieve this, the research is divided in smaller steps by formulation of a number of sub-questions. The answers to these sub-questions lead to the answer on the main research question.

Literature review

- *Which numerical modelling techniques to model discontinuities exist and how does the embedded beam element relate to them?*
  A pile foundation in soil can be considered as a discontinuity in the soil domain. Current state-of-the-art in finite element modelling of discrete structural discontinuities is mainly intended to model structural discontinuities. The discontinuity between the soil and beam of a pile foundation is considered a material discontinuity. Historically, these two discontinuity types have a different modelling origin. The two research fields met with the introduction of interface elements.

- *What are the fundamentals and current state-of-the-art in embedded beam elements?*
  The embedded beam element was introduced by Sadek and Shahrour (2004). The extension of the elastic zone approach is proposed by Engin et al. (2007), solving occurring numerical problems and reducing the mesh sensitivity. Turello et al. (2016a,b) proposed an embedded beam element with explicit interaction surface. This latter method describes the pile-soil interaction at the true pile perimeter, leading to promising results concerning mesh sensitivity and lateral deformation behaviour.

- *How is the existing three-dimensional embedded beam element modelled in PLAXIS 3D and what are its limitations?*
  The existing embedded beam element in PLAXIS 3D is modelled as a 3-noded line element inside a 10-noded tetrahedral solid element.The elastic zone approach proposed by Engin et al. (2007) is incorporated. An interface in axial direction along the pile is taken into account. The two most important limitations of the existing embedded beam formulation in PLAXIS 3D are its mesh sensitivity and the impossibility to capture lateral interface behaviour.

The main conclusion that can be drawn from the literature review is that the idea of an embedded beam element with explicit interaction surface (Turello et al., 2016a,b) can be used to improve the existing embedded beam formulation in PLAXIS 3D.

Model development

- *How can the pile-soil interaction be modelled on the explicit interaction surface in a generalised manner?*
  In order to model the pile-soil interaction on the explicit interaction surface, the beam and soil displacements on this surface need to be computed.

  – The beam displacements at the interaction surface are obtained using the method described in Bathe (2014). The proposed approach is generalised for arbitrarily inclined piles and can easily be

extended for rectangular cross-section shapes (Appendix D.1). The mapping takes into account the beam displacements at the pile axis and the beam curvature according to Timoshenko beam theory.

– To obtain the soil displacements at the interaction surface three methods are proposed. Two of these methods are formulated in order to limit the calculation time; one uses extrapolation from the soil element at the beam axis (A) and the other corrects the soil displacements at the beam axis with a first order Taylor approximation (B). The third method obtains the soil displacements at the interaction surface more accurately by using the soil elements at the interaction surface (C). The last method considers a point-wise assembly of the interface contributions to the total stiffness matrix and force vector.

When both displacement components at the interaction surface (beam and soil) are known the interaction between the beam and soil can be described using appropriate constitutive relations.

- *How can the stress singularity at the foot of the pile be solved?*
  An improved foot interface is proposed, in which the base resistance is spread over a number of points on the pile perimeter. This induces a circular line load on the soil, rather than a point load as in the existing implementation. A significant reduction in the plastic behaviour in the soil near the foot of the pile is obtained, leading to a tremendous reduction in mesh sensitivity.

- *How can lateral plasticity (slippage) be modelled at the interaction surface and what are appropriate limits for the stress components in the interface?*
  Three methods to incorporate lateral plasticity are proposed. All methods are based on the Mohr-Coulomb failure criterion; $\tau \leq c - \sigma_n \tan\varphi$. The first method obtains the normal stresses from the soil and the second method obtains the normal stresses from the interface. The first two methods use an inaccurate method to correct the stresses in case of plasticity. The third method solves this by using the return mapping algorithm that is used for the standard interface elements in combination with the normal stresses from the interface. No compressive limit for the normal stresses is defined, but tension cut-off is taken into account.

Parametric study

- *What is the best method to calculate the soil displacements and stresses on the interaction surface in terms of accuracy?*
  Method C yields the best results in terms of comparability with available measurement data, mesh sensitivity reduction and reduction of the elastic zone approach. This conclusion is based on results from an axially loaded pile model.

- *Which of the proposed lateral plasticity methods performs best?*
  None of the proposed lateral plasticity methods are able to capture the desired interface behaviour. The reason for this is that a wrong failure mechanism is modelled instead. Nonetheless, it is decided to apply method 1 to the new embedded beam formulation. This decision is made because method 1 solves the slight increase in mesh sensitivity and obtained failure load of the new embedded beam formulation without lateral plasticity method. In addition, the applied Mohr-Coulomb failure criterion $\left(\tau \leq c - \sigma_n - \tan\varphi\right)$ considers the shear stress as the total of the two components; $\tau = \sqrt{\sigma_s^2 + \sigma_t^2}$, therefore it is not sensible to leave one component out.

- *What are appropriate values for the interface stiffnesses in the new model?*
  The shaft and foot interfaces are evaluated separately:

  – For the interface stiffnesses along the shaft of the pile the existing stiffness definitions are divided by the pile perimeter. This returns stiffness behaviour that is equivalent to the existing embedded beam model, which is in good agreement with measurement data. Therefore, no additional modifications to these stiffnesses are required.

  – However, the foot interface stiffness does require an additional reduction. Dividing the existing foot stiffness by the cross-section area of the pile yields a too stiff response. A short parameter study has indicated that the new foot stiffness requires an additional reduction of approximately 90% compared to the existing foot stiffness divided by the cross-section area.

- *To what extend is the proposed model an improvement compared to existing FE models?*
  A distinction is made between axially and laterally loaded models:
  - In case of an axially loaded model the mesh sensitivity is reduced tremendously and the influence of the elastic zone approach is almost entirely gone; the response with and without elastic zone are in very good agreement. Especially, the improved foot interface resulted in a great reduction of the mesh sensitivity.
  - In case of laterally loaded models a significant improvement in overall response is obtained, even though lateral interface behaviour is not taken into account. The existing embedded beam element behaves too flexible, considering that it doesn't have an interface in lateral direction. The new embedded beam formulation behaves stiffer, matching volume pile results without interface much better. This also holds true for inclined piles.

    Varying the L/D ratio of a fictional pile, the new embedded beam element obtains an average improvement in stiffness of 67% at the head of the pile compared to the existing formulation, when the volume pile method without interface is considered as benchmark solution. At the foot for small L/D ratio's a relative improvement in terms of stiffness of 84% is observed. This is a huge improvement.

Application

- *How well does the proposed model perform compared to the real behaviour (case study)?*
  Even though no real measurement data are presented for the case study due to confidentiality reasons, the results of the new embedded beam model again proof to be in very good agreement with full 3D models without interfaces. The inability of the new embedded beam model to capture the same behaviour as the full 3D model with interfaces demonstrates the necessity for a lateral interface.

  The embedded beam element is supposed to be a more efficient alternative to modelling pile foundations with full 3D models. However, the current prototype takes almost as long as a full 3D model to calculate. For this reason and the lack of lateral interface the proposed embedded beam element is not suitable to replace full 3D calculations yet.

Main research question

The main research question is formulated as:

How can the original embedded beam element be improved and generalised in order to overcome its limitations and drawbacks?

Summarizing, the following conclusions can be drawn with respect to the main research question:

- The proposed embedded beam element model consists of the following components:
  - An explicit interaction surface along the pile shaft
  - An improved foot interface
  - Lateral plasticity method 1
  - Elastic zone approach
- The proposed model is an improvement of the existing embedded beam element in terms of:
  - Mesh sensitivity in axially loaded models
  - Overall response in laterally loaded models
- The proposed embedded beam element is not able to capture the correct interface behaviour in lateral direction, such as full 3D finite element models.
- The proposed model is an extension and generalisation of the embedded beam element proposed by Turello et al. (2016a,b) with respect to:
  - The use of Timoshenko beam theory
  - Ability to model inclined piles
  - Interaction surface at the foot of the pile
  - A more practical formulation of the constitutive model of the interface

10

Recommendations

This chapter gives an overview of some recommendations for future research.

- The implementation of the embedded beam element in the PLAXIS 3D source code that is developed during this research is focussed on making the new model work. It is not focussed on optimising the code in order to achieve better numerical performance. For example, improvements can be achieved by:
  - Optimising the search for the soil elements at the interaction surface. The search for the soil elements at the interaction surface is performed using a loop that runs from zero to the maximum soil element number. However, when one soil element is found, it is more efficient to check the neighbouring elements first.
  - Applying the correct return mapping algorithm to correct the stresses in case of plasticity. This requires the use of the interface normal stresses in the Mohr-Coulomb failure criterion. Currently, only the additional stresses caused by relative displacements between beam and soil are stored in the interface. The initial stresses are stored in the soil inside the pile region. In order to apply the preferred return mapping algorithm both components need to be taken into account and corrected appropriately.
- Before application of the new embedded beam element in PLAXIS 3D more validation should be performed. Complex case studies often lead to discoveries of unnoticed bugs or limitations of a new implementation. In addition, comparison with more field data cases can offer a more solid confirmation about the performance of the new embedded beam formulation. During this research the validation was limited to cases with active loading, neglecting passive lateral loading or cyclic loading. Also, behaviour of pile groups is not evaluated.
- No final reduction factor for the foot stiffness is obtained during this research. It is advised to define a foot stiffness that is generally applicable. More validation with real test data should be performed in order to come to a conclusion about the required foot stiffness reduction. Three topics that are recommended to give special attention are:
  - The influence of certain model dimensions and soil properties should be investigated more thoroughly and if necessary they should be taken into account appropriately.
  - Decoupling of lateral and axial foot stiffness might enable an optimisation of the response in both directions. The results presented in this report suggest that in axial direction a relatively lower foot stiffness is required than in lateral direction.
  - A parameter study to examine the relation between the shaft and foot stiffness is recommended. An optimisation for the skin traction mobilisation could be achieved.
- The proposed methods to incorporate lateral plasticity along the shaft of the embedded beam have proven to be unable to capture the desired interface behaviour. The proposed methods influence the movement of the beam axis relative to the interaction surface, not the soil movement around the pile.

Therefore, in order to model a lateral interface that is able to capture the desired behaviour a fundamentally different method is necessary. Suggestions are:

- **Ring model**: In this model the beam element is rigidly connected to the interaction surface. Instead of limiting the connection between beam and interaction surface, a ring with a certain thickness (h_i) is defined around the interaction surface in which the soil strength can be manipulated (Figure 10.1). Similar as the elastic zone approach, the integration points that lie inside this region

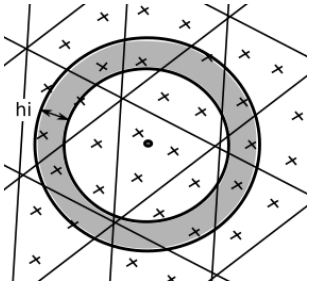

Figure 10.1: Ring model

  can be found and the soil properties at these points can be modified. For example, the soil properties can be modified by a strength reduction factor R_{inter}. When the soil in a thin region around the beam is slightly weaker than the rest of the soil, failure is expected to happen sooner at this location than in the rest of the soil. This would effectively model slip of the soil around the beam. However, it must be noted that this method is hypothetical. No efforts have been made to verify the feasibility of this approach.
- **XFEM related methods**: The soil elements in which the interface is located can be enriched according to one of the XFEM related methods in order to capture the displacement jump between the pile and soil. Future research might look into the formulation of an appropriate relation between the discontinuity in the soil elements at the interaction surface and the relative displacements between the beam and soil. Especially DE-FEM looks promising, because of its easier implementation and capability to model both weak and strong discontinuities.

- The new embedded beam formulation with an explicit interaction surface opens up many possibilities:
  - The true cross-section shape can now be taken into account. In Appendix D.1 the formulation for a rectangular cross-section is already presented, but this has not been implemented and validated yet.
  - A distinction between massive and tube cross-section types can now be made. For example, it might be more realistic to use the elastic zone approach for massive cross-section types only and not for tube cross-section types. Also, the foot interface now considers the pile cross-section area computed according to πR^2, but for tube cross-section types the perimeter length might be used instead.
  - Gap forming at the back of a laterally loaded pile could not be taken into account in the existing embedded beam formulation. However, the new embedded beam formulation might be able to model this behaviour correctly.
  - It became evident during the case study that the embedded beam elements are not capable of being used in a bisected model, in which the symmetry of the model is taken into account. However, this would reduce the computational effort significantly. Future research might look into the possibility of the new embedded beam formulation to be used in bisected models.

Bibliography

API RP 2A-WSD (2002). *Recommended practice for planning, designing and constructing fixed offshore platforms - working stress design*. American Petroleum Institute.

Aragón, A. M. and Simone, A. (2017). The discontinuity-enriched finite element method. *International journal for numerical methods in engineering*, 112:1589–1613.

Babuška, I., Caloz, G., and Osborn, J. E. (1994). Special finite element methods for a class of second order elliptic problems with rough coefficients. *SIAM Journal on Numerical Analysis*, 31(4):945–981.

Barton, Y. O. (1982). *Laterally loaded model piles in sand: Centrifuge tests and finite element analyses*. University of Cambridge. Dissertation.

Bathe, K.-J. (2014). *Finite Element Procedures*. Prentice Hall, Pearson Education, Inc., second edition.

Belytschko, T., Gracie, R., and Ventura, G. (2009). A review of extended/generalized finite element methods for material modelling. *Modelling and simulation in materials science and engineering*, 17(4):1–31.

Blaauwendraad, J. and Grootenboer, H. J. (1981). Essentials for discrete crack analysis. *IABSE Reports, Coll. Advanced Mech. of Reinforced Cocnrete*, 34:263–272.

Brinkgreve, R. B. J., Engin, E., and Swolfs, W. M. (2015). Plaxis 3d 2015 manual. *Plaxis bv, the Netherlands*.

Broms, B. B. (1964a). Lateral resistance of piles in cohesionless soils. *Journal of Soil Mechanics and Foundations Div., ASCE*, 90:123–156.

Broms, B. B. (1964b). Lateral resistance of piles in cohesive soils. *Journal of Soil Mechanics and Foundations Div., ASCE*, 90:27–63.

Byrne, B. W., McAdam, R., Burd, H. J., Houlsby, G. T., Martin, C. M., Zdravkovic, L., Taborda, D. M. G., Potts, D. M., Jardine, R. J., Sideri, M., Schroeder, F. C., Gavin, K., Doherty, P., Igoe, D., Muir Wood, A., Kallehave, D., and Skov Gretlund, J. (2015). New design methods for large diameter piles under lateral loading for offshore wind applications. *Conference paper, Third International Symposium on Frontiers in Offshore Geotechnics*.

Carter, J. P. and Kulhawy, F. H. (1988). Analysis and design of drilled shaft foundations socketed into rock. Report to Electric Power Research Institute, California.

Courant, R. (1943). Variational methods for the solution of problems of equilibrium and vibrations. *Bulletin of the American Mathematical Society*, 49:1–23.

Courant, R., Friedrichs, K. O., and Lewy, H. (1928). über die partiellen differenzengleichungen der mathematischen physik. *Mathematische Annalen*, 100:32–74.

Cundall, P. A. and Strack, O. D. L. (1979). A discrete numerical model for granular assemblies. *Géotechnique*, 29(1):47–65.

Dao, T. P. T. (2011). Validation of plaxis embedded piles for lateral loading. Master's thesis, Delft University of Technology.

Davisson, M. T. (1970). Lateral load capacity of piles. *Highway Research Board*, 333:104–112.

Davisson, M. T. and Prakash, S. (1963). A review of soil-pole behavior. *Highway Research Record*, 39:25–48.

De Borst, R. and Sluys, L. J. (2015). *Computational methods in non-linear solid mechanics*. Technical University Delft.

Duarte, C. A., Babuška, I., and Oden, J. T. (1998). Generalized finite element methods for three dimensional structural mechanics problems. *Computers & Structures*, 77:215–232.

Engin, H. K., Septanika, E. G., and Brinkgreve, R. B. J. (2007). Improved embedded beam elements for the modelling of piles. *Numerical models in geomechanics - NUMOG X*.

Engin, H. K., Septanika, E. G., and Brinkgreve, R. B. J. (2008). Estimation of pile group behavior using embedded piles. *International Association for Computer Methods and Advances in Geomechanics (IACMAG)*, pages 3231–3238.

Eymard, R., Gallouët, T., and Herbin, R. (2000). Finite volume methods. *Handbook of Numerical Analysis, P. G. Ciarlet, J. L. Lions eds*, 7:713–1020.

Fleming, K., Weltman, A., Randolph, M., and Elson, K. (2009). *Piling Engineering*. Taylor & Francis, third edition.

Fries, T. (2013). The extended finite element method. rwth aachen university. `http://www.xfem.rwth-aachen.de/Background/Introduction/XFEM_Introduction.php`. Accessed: 14/2/2018.

Griffith, A. A. (1921). The phenomena of rupture and flow in solids. *Philosophical Transactions of the Royal Society of London, A*, 221:163–198.

Hermans, J. J. (2014). Lateral loaded piles, validation of the embedded pile row in plaxis 2d for passive lateral loading. Master's thesis, Delft University of Technology.

Ingraffea, A. R. and Saouma, V. (1985). *Fracture Mechanics of Concrete*. Martinus Nijhoff, Dordrecht.

Lebeau, J.-S. (2008). Fe-analysis of piled and piled raft foundations. Master's thesis, Graz University of Technology.

Melenk, J. M. and Babuška, I. (1996). The partition of unity finite element method: Basic theory and applications. *Computer Methods in Applied Mechanics and Engineering*, 139:289–314.

Moës, N., Dolbow, J., and Belytschko, T. (1999). A finite element method for crack growth without remeshing. *International journal for numerical methods in engineering*, 46:131–150.

NEN 9997-1 (2016). *Geotechnisch ontwerp van constructies - Deel 1: Algemene regels*. Nederlands Normalisatie-instituut.

Ngo, D. and Scordelis, A. C. (1967). Finite element analysis of reinforced concrete beams. *ACI*, 64:152–163.

Offshore Standard DNV-OS-J101 (2010). *Appendix F - Pile resistance and load-displacement relationships*. DNV GL.

Peck, R. B. and Davisson, M. T. (1962). Discussion: Design and stability considerations for unique pier. *ASCE*, 127:413–424.

Pietruszczak, S. and Haghighat, E. (2014). Modeling of fracture propagation in concrete structures using a constitutive relation with embedded discontinuity. *Studia Geotechnica et Mechanica*, 36(4):27–33.

Poulos, H. G. and Davis, E. H. (1980). *Pile foundation analysis and design*.

Randolph, M. F. (1981). The response of flexible piles to lateral loading. *Geotechnique*, 31(2):247–259.

Randolph, M. F. and Houlsby, G. T. (1984). The limiting pressure on a circular pile loaded laterally in cohesive soil. *Geotechnique*, 34:613–623.

Rashid, Y. R. (1968). Analysis of prestressed concrete pressure vessels. *Nuclear Eng. Des.*, 7, 51:45–59.

Reese, L. C. and Matlock, H. (1956). Non-dimensional solutions for laterally loaded piles with soil modulus assumed proportional to depth. *Proc. of 8th Texas Conference on Soil Mechanics and Foundation Engineering. Austin, Texas*, pages 1–41. Special Publication 29.

Rots, J. G. (1991). Smeared and discrete representations of localized fracture. *Int. Journal of Fracture*, 51:45–59.

Rots, J. G. and Blaauwendraad, J. (1989). Crack models for concrete: discrete or smeared? fixed, multi-directional or rotating? *Heron journal*, 34, 1.

Sadek, M. and Shahrour, I. (2004). A three dimensional embedded beam element for reinforced geomaterials. *International journal for numerical and analytical methods in geomechanics*, 28:931–946.

Schultz, R. A. and Fossen, H. (2008). Terminology for structural discontinuities. *AAPG Bulletin*, 97, no. 7:853–867.

Septanika, E. G., Bonnier, P. G., Brinkgreve, R. B. J., and Bakker, K. J. (2007). An efficient 3d modeling of (multi) pile-soil interaction. *International Geomechanics Converence, Nessebar*.

Skempton, A. W. (1951). The bearing capacity of clays. *Building Research Congress, London Institution of Civil Engineers*, 1:180–189.

Sluis, J. (2012). Validation of embedded pile row in plaxis 2d. Master's thesis, Delft University of Technology.

Soghrati, S., Aragón, A. M., Duarte, C. A., and Geubelle, P. H. (2010). An interface-enriched generalized finite element method for problems with discontinuous gradient fields. *International journal for numerical methods in engineering*, 00:1–19.

Strouboulis, T., Babuška, I., and Copps, K. (2000). The design and analysis of the generalized finite element method. *Computer methods in applied mechanics and engineering*, 181:43–69.

Sulsky, D., Chen, Z., and Schreyer, H. L. (1994). A particle method for history-dependent materials. *Computer methods in applied mechanics and engineering*, 118:179–196.

Tschuchnigg, F. (2012). *3D Finite Element Modelling of Deep Foundations Employing an Embedded Pile Formulation*. PhD thesis, Technische Universitat Graz.

Tschuchnigg, F. and Schweiger, H. F. (2015). The embedded pile concept - verification of an efficient tool for modelling complex deep foundations. *Elsevier, Computers and Geotechnics*, 63:244–254.

Turello, D. F., Pinto, F., and Sánchez, P. J. (2016a). Embedded beam element with interaction surface for lateral loading of piles. *International journal for numerical and analytical methods in geomechanics*, 40:568–582.

Turello, D. F., Pinto, F., and Sánchez, P. J. (2016b). Three dimensional elasto-plastic interface for embedded beam elements with interaction surface for the analysis of lateral loading of piles. *International journal for numerical and analytical methods in geomechanics*, 41:859–879.

Van Langen, H. (1991). *Numerical analysis of soil-structure interaction*. PhD thesis, Technische Universiteit Delft.

Van Langen, H. and Vermeer, P. A. (1991). Interface elements for singular plasticity points. *International Journal for Numerical and Analytical Methods in Geomechanics*, 15(5):301–315.

Verruijt, A. (2012). *Soil Mechanics*. VSSD.

Wilson, S. D. and Hilts, D. E. (1967). How to determine lateral load capacity of piles. *Pile-Foundation Know-How*, pages 41–45.

Winkler, E. (1867). Die lehre von der elastizität und festigkeit (the theory of elasticity and stiffness). H. Dominicus Prague: Czechoslovakia.

Appendices

A

Design standards for laterally loaded pile foundations

The current design standards for laterally loaded pile foundations are based on modelling a beam on which the soil reactions are modelled by distributed springs. The behvaiour of the springs is described by non-linear p-y curves. This method yields a conservative response.

This chapter describes the basics and current design standards on how to design laterally loaded piles. NEN 9997-1 (2016) doesn't contain methods for laterally loaded piles, only for axially loaded piles. Therefore, alternative sources are found that present methods on how to obtain the lateral bearing capacity of laterally loaded piles (Section A.1). The API method is presented (Section A.1.3). In addition, results from a simple model in PLAXIS 3D are compared to the API method (Section A.1.4). Subsequently, different methods to obtain the deformation behaviour of a laterally loaded pile are described (Section A.2).

A.1. Lateral bearing capacity

Fleming et al. (2009) gives an overview of proposed formulas to determine the lateral bearing capacity of single piles. Furthermore, the American Petroleum Institute (API) has a standard containing recommendations on planning, designing and constructing fixed offshore platforms (API RP 2A-WSD, 2002). This standard contains a method to determine the bearing capacity of laterally loaded piles. This method will be explained in Section A.1.3.

Lateral loading of a pile may be caused by an external load or by movement of the soil surrounding the pile. The first type of lateral loading is called 'active' loading, with the soil resisting the load and the second one is called 'passive' loading, with the soil movements causing stresses in the pile. In this research the focus will be on the first type of lateral loading.

When a pile is loaded laterally, normal stresses increase in front of the pile (compression) and decrease behind the pile. At some stage a gap will open up between the soil and the pile at the ground surface behind the pile. In front of the pile the soil will be failing in a wedge type of mechanism, shown in Figure A.1. At a greater depth the soil will eventually fail by flowing around the pile, without creating a gap. This is a different failure mechanism.

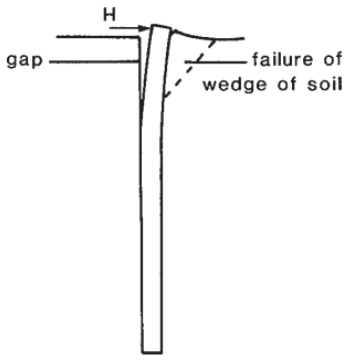

Figure A.1: Deformation of a pile under lateral load, (Fleming et al., 2009)

Short piles or very stiff piles will rotate as a rigid body when failing. This failure mode and the resulting soil resistance is shown in Figure A.2a. When a long pile is failing, a plastic hinge will develop at some depth and only the part above this plastic hinge will deform significantly. This failure mode and the resulting soil resistance above the plastic hinge is shown in Figure A.2b. Below the plastic hinge there will be soil pressure present as well, but they are not relevant for calculating the failure load.

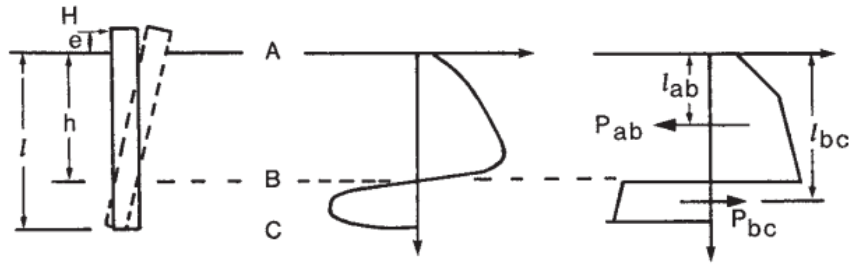

(a) Short pile

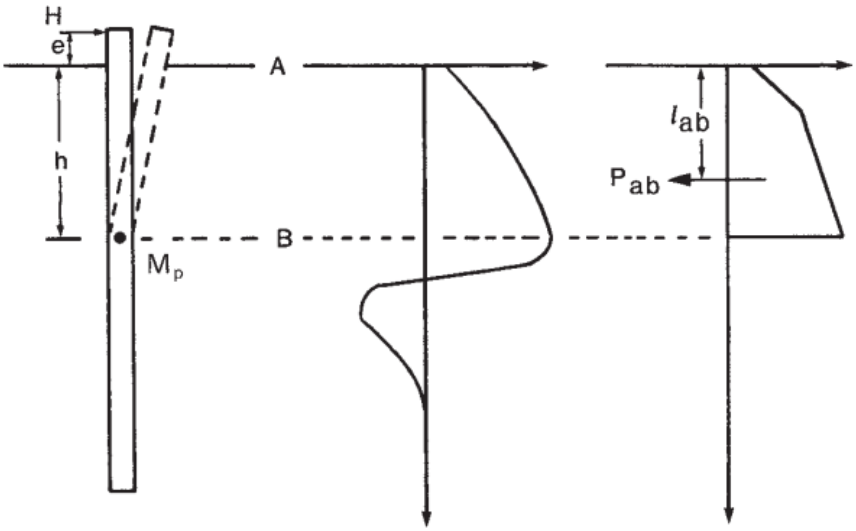

(b) Long pile

Figure A.2: Variation of soil resistance along laterally loaded piles, (Fleming et al., 2009)

For short piles, the equilibrium of horizontal forces gives:

$$H = P_{ab} - P_{bc} \tag{A.1}$$

and bending moment equilibrium at level B is given by:

$$H \cdot (e+h) = P_{ab} \cdot (h - l_{ab}) + P_{bc} \cdot (l_{bc} - h) \tag{A.2}$$

For long piles, a plastic hinge forms at the point of the maximum bending moment, which is at the location of zero shear force. Zero shear force occurs at level B when H is equal to P_{ab}. Calculating the bending moment at level B then gives:

$$H \cdot (e+h) - H \cdot (h - l_{ab}) = H \cdot (e + l_{ab}) = M_p \tag{A.3}$$

A.1.1. Cohesionless soil

To determine the total bearing resistance of a pile subjected to lateral loading, the ultimate soil pressure per unit length P_u is necessary. Several formulas have been proposed to calculate this value. Two formulas that are often used are proposed by Broms (1964a) and Barton (1982) respectively:

$$P_u = 3K_p \sigma'_v D \tag{A.4}$$

$$P_u = K_p^2 \sigma'_v D \tag{A.5}$$

with

$$K_p = \frac{1+\sin\varphi}{1-\sin\varphi} \tag{A.6}$$

σ'_v is the effective vertical stress, φ is the friction angle and D is the diameter of the pile. Equation (A.4) underestimates the bearing capacity by about 30%, when compared to field test results. As K_p is generally greater than 3, so Equation (A.5) gives a better approximation.

Both Equations (A.4) and (A.5) are specific cases of the more general case where the soil resistance is assumed to vary along the depth according to:

$$P_u = nDz \tag{A.7}$$

where n is the gradient of the average ultimate pressure across the width of the pile. So, for Equations (A.4) and (A.5) n is equal to $3K_p\gamma'$ and $K_p^2\gamma'$ respectively. Here γ' is the dry unit weight of the soil.

A.1.2. Cohesive soil

Fleming et al. (2009) describes an idealised variation of the ultimate soil pressure along the depth. This profile is shown in Figure A.3. For piles in cohesive soil, the ultimate soil pressure near the ground surface may

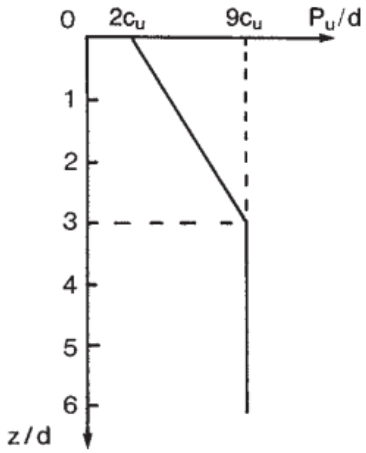

Figure A.3: Idealised variation of ultimate soil pressure with depth, (Fleming et al., 2009)

be taken as $2c_u$, where c_u is the undrained shear strength of the soil. The ultimate soil pressure increases linearly up to a value of about $9c_uD$ at a depth of $3D$. This limit of the ultimate soil pressure is a conservative assumption. The following expression describes this profile:

$$\begin{aligned} P_u &= 2c_uD + \frac{7c_uD}{3D} \cdot z \qquad \text{For } z < 3D \\ P_u &= 9c_uD \qquad\qquad\qquad\quad \text{For } z \geq 3D \end{aligned} \tag{A.8}$$

A.1.3. API method

API RP 2A-WSD (2002) describes a method to determine the lateral bearing capacity for soft and stiff clays and for sand.

Cohesive soils

For static lateral loading the lateral bearing capacity ($p_u = P_u/D$) of soft and stiff clays varies between $8c_u$ and $12c_u$, except at very shallow depths where a different failure mode occurs, as mentioned before. Cyclic loads cause a decrease in lateral bearing capacity.

API RP 2A-WSD (2002) recommends to use a profile for the lateral bearing capacity p_u that increases from $3c_u$ to $9c_u$ according to:

$$\begin{aligned} p_u &= 3c_u + \gamma' z + J\frac{c_u z}{D} && \text{For } 0 \le z < Z_R \\ p_u &= 9c_u && \text{For } z \ge Z_R \end{aligned} \tag{A.9}$$

where γ' is the effective unit weight of soil, J is a dimensionless empirical constant with values ranging from 0.25 to 0.5 and z is the depth below the ground surface in mm.

Cohesionless soil

The lateral bearing capacity of sand varies between

$$p_u = (C_1 \cdot z + C_2 \cdot D) \cdot \gamma' z \tag{A.10}$$

at shallow depth and

$$p_u = C_3 \cdot D\gamma' z \tag{A.11}$$

where z is the depth in m and C_1, C_2 and C_3 are coefficients that are determined using Figure A.4.

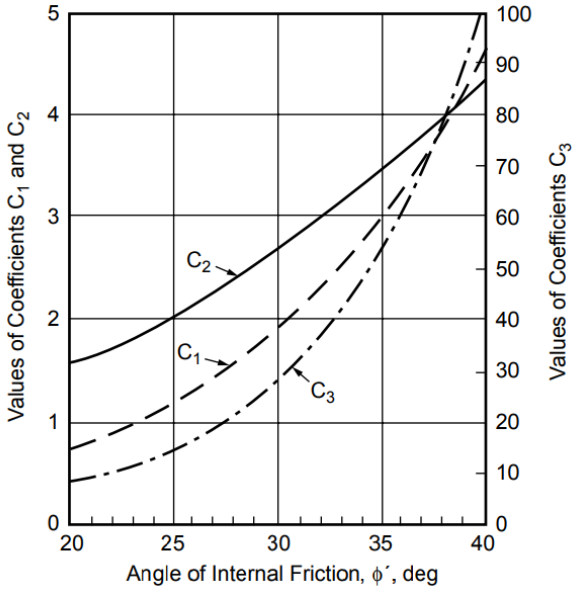

Figure A.4: Coefficients C_1, C_2 and C_3 as function of ϕ', (API RP 2A-WSD, 2002)

A.1.4. Results from PLAXIS 3D

Looking at the lateral bearing capacity as is defined in the API method in Section A.1.3 for cohesive soils we find that from a certain depth on the ultimate lateral bearing capacity is defined by:

$$P_u = 9c_u D \tag{A.12}$$

However, Randolph and Houlsby (1984) found an analytical expression for the lateral bearing capacity. This expression is given by:

$$\frac{P_u}{c_u D} = \pi + 2\Delta + 2\cos\Delta + 4\left[\cos\frac{\Delta}{2} + \sin\frac{\Delta}{2}\right] \tag{A.13}$$

with

$$\sin\Delta = R_{inter} \tag{A.14}$$

For R_{inter} = 1.0 this formula results in a factor of 11.94 and for R_{inter} = 0.0 it results in a factor of 9.142.

This has been verified in PLAXIS 3D for the volume pile method. A model with all dimensions set to one is modelled in PLAXIS 3D; D = 1 m, cohesion = 1, φ = 0, L= 1 m. Figure A.5 shows the resulting load-displacement curves. The results of PLAXIS 3D appear to be in good agreement with the analytical solution as proposed by

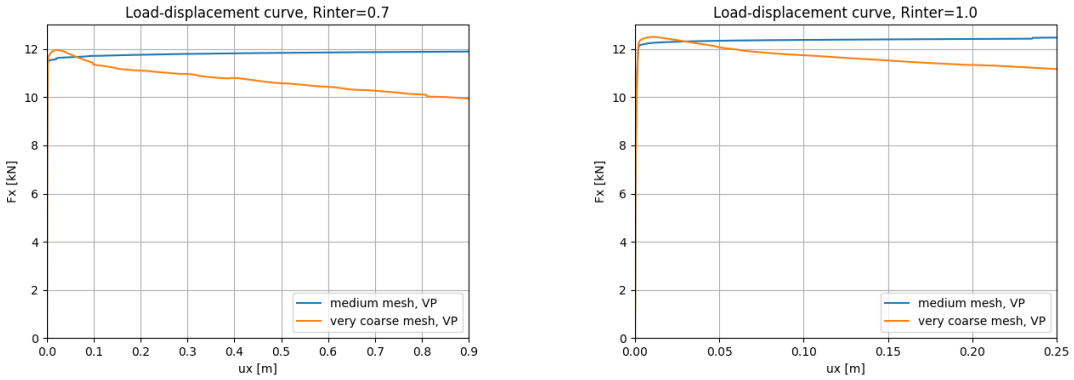

(a) Load-displacement curve for R_{inter} = 0.7.

(b) Load-displacement curve for R_{inter} = 1.0.

Figure A.5: Check for the factor of the lateral bearing capacity

Randolph and Houlsby (1984). It's not necessary to set a maximum for the normal stresses at the interface. The way the soil is modelled in PLAXIS 3D will make sure that the correct failure mechanism will be modelled.

A.2. Deformation behaviour of laterally loaded piles

The Eurocode doesn't contain an explicit way to determine the lateral deformation behaviour of laterally loaded piles. However, Fleming et al. (2009) describes two methods to determine the deformation of single piles under lateral loading; the subgrade reaction approach and the elastic continuum approach.

A.2.1. Subgrade reaction approach

This approach is based on the Winkler idealisation of soil, where the soil is modelled as a series of springs down the length of the pile (Figure A.6). The spring stiffness, k, is referred to as the coefficient of subgrade reaction.

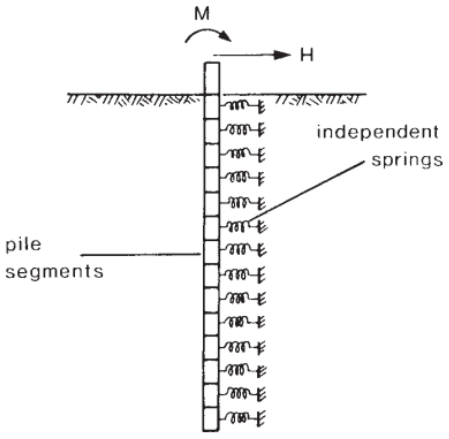

Figure A.6: Subgrade reaction model of soil around pile, (Fleming et al., 2009)

For a constant k along the length of the pile, analytical solutions are available to determine the deflected shape of the pile, shear force and bending moment distribution along the pile. There is a critical length of the

pile, for which the pile behaves as if it were infinitely long. This means that at a certain depth, the effects of the load at the top is negligible. This critical length can be computed by:

$$L_c = 4 \cdot \left(\frac{EI_p}{k} \right)^{0.25} \tag{A.15}$$

where EI_p is the bending rigidity of the pile. For piles longer than the critical length, the deflection and rotation at ground level due to an applied load H and bending moment M can be determined by:

$$\begin{aligned} u &= \sqrt{2} \frac{H}{kD} \left(\frac{L_c}{4} \right)^{-1} + \frac{M}{kD} \left(\frac{L_c}{4} \right)^{-2} \\ \theta &= \frac{H}{kD} \left(\frac{L_c}{kD} \right)^{-2} + \sqrt{2} \frac{M}{kD} \left(\frac{L_c}{4} \right)^{-3} \end{aligned} \tag{A.16}$$

For a varying kD with the depth according to $kD = nz$, the critical length can be determined by:

$$L_c = 4 \left(\frac{EI_p}{n} \right)^{0.2} \tag{A.17}$$

and the deflection and rotation at ground level due to an applied load H and bending moment M can be determined by:

$$\begin{aligned} u &= 2.43 \frac{H}{n} \left(\frac{L_c}{4} \right)^{-2} + 1.62 \frac{M}{n} \left(\frac{L_c}{4} \right)^{-3} \\ \theta &= 1.62 \frac{H}{n} \left(\frac{L_c}{4} \right)^{-3} + 1.73 \frac{M}{n} \left(\frac{L_c}{4} \right)^{-4} \end{aligned} \tag{A.18}$$

Nowadays, it is possible to include non-linear springs to describe the soil in computer programs. A complete load transfer (p-y) curve can be specified, instead of a coefficient of subgrade reaction. That is in fact done in the elasto-plastic interface for the embedded beam element with explicit interaction surface proposed by Turello et al. (2016b), mentioned in Section 3.2.1.

Coefficient of subgrade reaction

A limitation of the subgrade reaction approach is the determination of appropriate values of the subgrade reaction coefficient k. Methods used to determine k are full scale lateral loading tests on a pile, plate loading tests and empirical correlations with other soil properties. The first method is very time consuming. A problem with the second method is the extrapolation of the results for a plate to a pile.

A number of empirical correlations for k are available. In the case of stiff over-consolidated clays a constant k with depth is assumed. Broms (1964b) has related k to the secant modulus E_{50}:

$$k = 1.67 \, \frac{E_{50}}{D} \tag{A.19}$$

Skempton (1951) used a value of E_{50} equal to 50 to 200 times the undrained shear strength c_u, giving:

$$k = (80 \text{ to } 320) \, \frac{c_u}{D} \tag{A.20}$$

Davisson (1970) suggested a more conservative approach:

$$k = 67 \frac{c_u}{D} \tag{A.21}$$

For softer cohesive soils, it is assumed that k increases linearly with the depth;

$$k = n \cdot z / D \tag{A.22}$$

Typical values of n for these sort of soils are collected by Poulos and Davis (1980) and shown in Table A.1.

For piles in sand (cohesionless soil), typical values of n are shown in Table A.2.

Soil type	n in kN/m^3	Reference
Soft NC clay	163-3447	Reese and Matlock (1956)
	271-543	Davisson and Prakash (1963)
NC organic clay	179-271	Peck and Davisson (1962)
	179-814	Davisson (1970)
Peat	54	Davisson (1970)
	27-109	Wilson and Hilts (1967)

Table A.1: Typical values of n for cohesive soils, (Poulos and Davis, 1980)

Soil type	Relative density		
	Loose	Medium	Dense
Dry or moist sand	2425	7275	19400
Sand under water	1386	4850	11779

Table A.2: Typical values of n for cohesionless soils, (Poulos and Davis, 1980)

A.2.2. Elastic continuum approach

In order to express the solution independent of the Poisson's ratio, Randolph (1981) introduced G^*:

$$G^* = G_{soil}\frac{1+3\nu}{4} \tag{A.23}$$

The characteristic modulus G_c is the average value of G^* over the critical length of the pile and ρ_c reflects the degree of homogeneity in the soil stiffness:

$$\rho_c = \frac{G^*_{Lc/4}}{G_c} \tag{A.24}$$

where $G^*_{Lc/4}$ is the value of G^* at a depth of $L_c/4$.

It is convenient to cast the solution in terms of an equivalent solid pile that has the same cross-sectional area and bending rigidity as the real pile. The appropriate Young's modulus can be calculated by:

$$E_p = \frac{EI_p}{\pi D^4/64} \tag{A.25}$$

The critical pile length can now be determined using:

$$L_c = D\left(\frac{E_p}{G_c}\right)^{\frac{2}{7}} \tag{A.26}$$

It is noted that G_c depends on the critical length L_c and vice versa. Therefore, some iterations might be necessary to find correct values.

The lateral deflection and rotation at ground level can now be determined by:

$$\begin{aligned} u &= \frac{\left(E_p/G_c\right)^{1/7}}{\rho_c G_c}\cdot\left[0.27\frac{H}{L_c/2}+0.30\frac{M}{(L_c/2)^2}\right] \\ \theta &= \frac{\left(E_p/G_c\right)^{1/7}}{\rho_c G_c}\cdot\left[0.30\frac{H}{(L_c/2)^2}+0.80\sqrt{\rho_c}\frac{M}{(L_c/2)^3}\right] \end{aligned} \tag{A.27}$$

These expressions have been derived by synthesizing a number of finite element analyses.

A.2.3. Short piles

For piles that are shorter than the critical length, the lateral deformation at ground level will be larger than for piles that are longer than the critical length. The increase in deformation is small as the piles are still longer than $0.8L_c$, but when the pile is shorter than $0.8L_c$, the increase in deformation becomes significant.

For piles with

$$\frac{L}{D} \leq 0.05\left(\frac{E_p}{G_c}\right)^{1/2} \tag{A.28}$$

Carter and Kulhawy (1988) presented the following solution:

$$\begin{aligned} u &= 0.32 \frac{H}{DG_c} \left(\frac{L}{D}\right)^{-1/3} + 0.16 \frac{M}{D^2 G_c} \left(\frac{L}{D}\right)^{-7/8} \\ \theta &= 0.16 \frac{H}{D^2 G_c} \left(\frac{L}{D}\right)^{-7/8} + 0.25 \frac{M}{D^3 G_c} \left(\frac{L}{D}\right)^{-5/3} \end{aligned} \tag{A.29}$$

This solution is valid for rigid piles in homogeneous soil ($\rho_c = 1$).

For very short piles, a failure mode might occur in which the entire pile translates laterally. In that case the failure load may be calculated by integrating the ultimate soil pressure over the length of the pile.

A.2.4. API method

API RP 2A-WSD (2002) recommends the use of p-y curves that describe the non-linear relation between load (p) and displacement (y).

Cohesive soils

For clays in API RP 2A-WSD (2002) Table A.3 is given from which the p-y curve can be generated.

p/p_u	y/y_c
0.00	0.0
0.50	1.0
0.72	3.0
1.00	8.0
1.00	∞

Table A.3: Table from API RP 2A-WSD (2002) to generate p-y curve for cohesive soils

In Offshore Standard DNV-OS-J101 (2010) the following formula is proposed:

$$\frac{p}{p_u} = \begin{cases} \frac{1}{2} \cdot \left(\frac{y}{y_c}\right)^{1/3} & \text{For } y \leq 8y_c \\ 1.00 & \text{For } y > 8y_c \end{cases} \tag{A.30}$$

with

$$y_c = 2.5\varepsilon_c \cdot D \tag{A.31}$$

where ε_c is the strain in a triaxial test for 50% of the maximum shear stress. Both p-y curves are graphically presented in Figure A.7 Figure A.7 shows that the two standards are in very good agreement. The API method

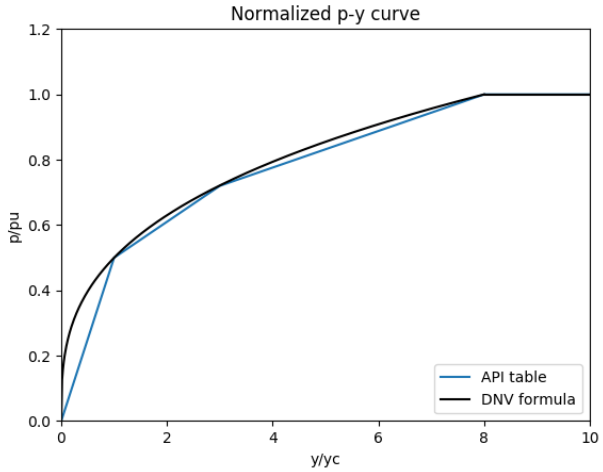

Figure A.7: Normalised p-y curve for clays

seems to be a discretised variation of the DNV formula.

Cohesionless soil

For sands the p-y curve can be approximated by:

$$P = A \cdot p_u \cdot \tanh\left(\frac{k \cdot H}{A \cdot p_u} \cdot y\right) \tag{A.32}$$

where A is a factor that accounts for the loading condition, given by

$$\begin{aligned} A &= 0.9 && \text{For cyclic loading} \\ A &= 3 - 0.5\frac{H}{D} \geq 0.9 && \text{For static loading} \end{aligned} \tag{A.33}$$

and k is the initial modulus of subgrade reaction that can be determined using Figure A.8.

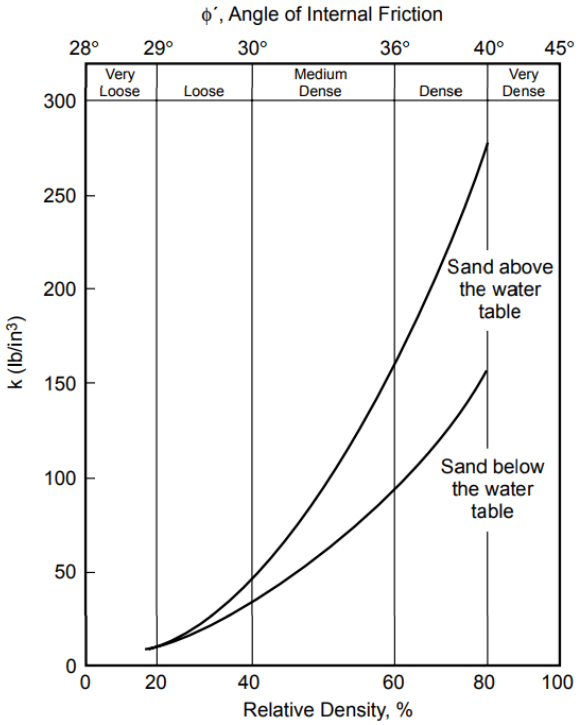

Figure A.8: k as function of ϕ' and relative density, (API RP 2A-WSD, 2002)

B

Existing PLAXIS 3D embedded beam implementation

B.1. Structure of the PLAXIS source code

The new embedded beam formulation needs to be applied in the PLAXIS 3D calculation kernel without breaking the existing embedded beam formulation. For this purpose several switches are created; 'isNewFormulation' and 'impfoot' are set to zero when the existing formulation is used and set to one when the new formulation is used.

The number of points that are considered on the interaction surface is defined by 'nCirDiv' and 'Latplas' defines what lateral plasticity method is used. All the new switches and variables are called upon from a "cheat file".

Understanding the structure of the source code of PLAXIS 3D is an important step in order to make the relevant changes. The flow charts in the following sections show the relevant parts of the structure of the Plaxis calculation kernel. In addition, the flow charts indicate in which parts of the calculation process modifications need to be made to incorporate the new embedded beam formulation.

No more details are provided about the PLAXIS calculation kernel for confidentiality reasons.

B.1.1. Main structure

Figure B.1 gives a very rough visualisation of the main program of PLAXIS 3D. The relevant subroutines for the new embedded beam element are highlighted.

The first highlighted box is relevant for the new implementation of the embedded beam element, because many vectors and matrices need to be increased in size. All tractions and displacements along the embedded beam element are now evaluated on multiple points at the pile perimeter instead of only at the beam axis. This leads to the necessity to store a lot more information. The soil elements at the pile perimeter need to be found and stored, including the local coordinates of the points on the perimeter inside this soil element. All new variables need to be allocated and initialised correctly, even as the use of the new switches ('isNewFormulation', 'nCirDiv', 'impfoot' and 'latplas') need to be read from the cheat file.

The second box that is highlighted is relevant because of the sparse storage of the global stiffness matrix. The profile of the global stiffness matrix is determined there, based on the element connectivities. When it finds two elements that are connected, the global DOF numbers corresponding to the element nodes need to be added to the global stiffness matrix as optional locations where non-zero values may occur. The new embedded beam implementation connects the beam element to different soil elements than the existing embedded beam element. Therefore, this needs to be modified.

The third highlighted box is the part where the global stiffness is build. The subroutine **Setup_newmatrix** sets up the global stiffness matrix, includes the boundary conditions and decomposes the stiffness matrix. In setting up the global stiffness matrix it calls upon the subroutine **Formmatrix**. This subroutine forms the global stiffness matrix by combining the stiffness matrices of the soil elements, interface elements, beam and plate elements, geotextile elements, anchors and viscous boundary elements. If embedded beam elements

are present in the model, subroutine **Add_EpilStiff_new** is called, which loops over all embedded piles and adds the element stiffness matrices for the interfaces around the embedded piles to the global stiffness matrix.

The stiffness matrix of the interface elements of the embedded beam is changed a lot. The assembly procedure, for instance, is not done element wise, but point wise. Instead of assembling the complete element stiffness matrix first and adding that to the global stiffness matrix, the stiffness contribution of every point on the pile circumference is now added to the global stiffness matrix separately. This is done, because one embedded beam element can be connected to multiple soil elements, whereas before an embedded beam element was only connected to one soil element. Also, the changes concerning the interface stiffness, weight factors and additional rotation matrix are included.

The change in assembly procedure in combination with the fact that now multiple points on the pile perimeter are considered for every beam integration points, results in the fact that many loops were included and existing loops had to be moved to a different location in the code. This causes problems with the existing formulations in some cases, making it necessary to duplicate some parts of code. The focus of this research is on the possibility and analysis of the new embedded beam formulation, not writing proper code. Optimisation is certainly still necessary if this new implementation of the embedded beam element is to be used in the future.

The calculation of initial forces and the calculation of the stresses (fourth and fifth highlighted boxes) both call upon the same subroutine if embedded beam elements are present in the model; **GetEpilSigs**. This subroutine loops over all embedded piles and determines the skin tractions and foot forces. Similar changes are applied in this subroutine as to **Add_EpilStiff_new**; interface stiffnesses, weight factors, additional rotation matrix and assembly procedure. In addition, this subroutine uses the switches 'impfoot' and 'latplas', based on which different methods are used to compute and assemble the foot resistance and correct the skin tractions for lateral plasticity.

B.1.2. Interface stiffness matrix

Figure B.2 gives a rough visualisation of the subroutine **Add_EpilStiff_new**. Again, the elements that need to modifications in order to implement the new embedded beam element are highlighted.

The first highlighted box is about the maximum resistance of the pile. The maximum foot force and skin tractions are either read from input (linear and multi linear traction models) or obtained using the interface properties and the normal stresses in the soil. In the existing embedded beam formulation the obtained value was always multiplied with $2\pi R$, but this is now not necessary any more. The maximum allowed foot force and skin tractions is not necessary for the computation of the interface stiffness matrix, but they are necessary to determine whether this embedded beam element has a bearing resistance. If not, the element can be skipped.

The second highlighted box indicates that the interface stiffnesses need to be modified, as explained in Section 5.3.

The third highlighted box indicates the calculation of the interface element stiffness matrix; $\boldsymbol{SE}$. Here, the B-matrix needs to be changed to the new one, where the additional rotation matrix needs to be applied as well. The correct soil elements (at the perimeter, not at the beam axis) are taken into account. The interface stiffnesses and the weight factors are modified.

The foot interface stiffness is changed in case of 'impfoot'=1, which means that the improved foot interface is applied. The calculation of the foot interface stiffness matrix is modified. In case of 'impfoot'=0, the foot interface stiffness matrix needs to be compatible with the skin interface stiffness matrix. This means that the dimensions need to be increased from 39x39 to 48x48 by including 9 zero rows and columns at the location of the beam rotational DOF's. In case of 'impfoot'=1, the weight factors are modified and the new B-matrix is used including the additional rotation matrix.

When the improved foot interface is used, the foot interface stiffness matrix is not added to the shaft interface stiffness matrix any more. Both are then added separately to the global stiffness matrix. In addition, the assembly procedure now also needs to take the beam rotational DOF's into account.

B.1.3. Force vector

Figure B.3 gives a visualisation of the **GetEpilSigs** subroutine.

The first highlighted box needs the same changes as described in the previous section for the maximum foot force and skin tractions. The shaft interface stiffnesses need to be modified in the same way as described

before.

When the pile resistance is zero, the tractions need to be reset and the routine can be left. The resetting, and initialisation for that matter, of tractions now needs to be done for all points on the pile circumference.

In the calculation of the force vector the beam rotational DOF's need to be included. The modified interface stiffness and weight factors are used, even as the new B-matrix and the additional rotation matrix. The tractions and displacements are now calculated in every point on the pile circumference, not just at the beam axis.

In addition, the correction for plasticity takes place here. The existing embedded beam formulation didn't take lateral plasticity into account, so this whole possibility needs to be included. When 'latplas'=0 the existing correction for plasticity is used, which means only correction of the axial tractions along the beam. When 'latplas'=1 both shear traction components are corrected in case of plasticity using lateral plasticity method 1 (Section 5.3.1). 'Latplas'=2 is only applicable for the layer-dependent traction model and uses the normal stresses from the interface and updates the stresses using the return mapping scheme as described in Section D.2.

The foot interface stiffness and maximum foot force need to be divided by πR^2 in case of 'impfoot'=1. The initialisation of the displacements and tractions at the foot need to be modified in case of 'impfoot'=1 as well, since more data points need to be stored.

The calculation of the foot force vector in case of 'impfoot'=1 needs to take into account the beam rotational DOF's, the modified foot interface stiffness and weight factors. The new B-matrix needs to be used, including the additional rotation matrix. When 'impfoot'=0 the existing calculation of the foot force vector is used, but now including 9 zero's at the locations of the beam rotational DOF's. The assembly of the shaft force vector and foot force vector to the global force vector is done separately now.

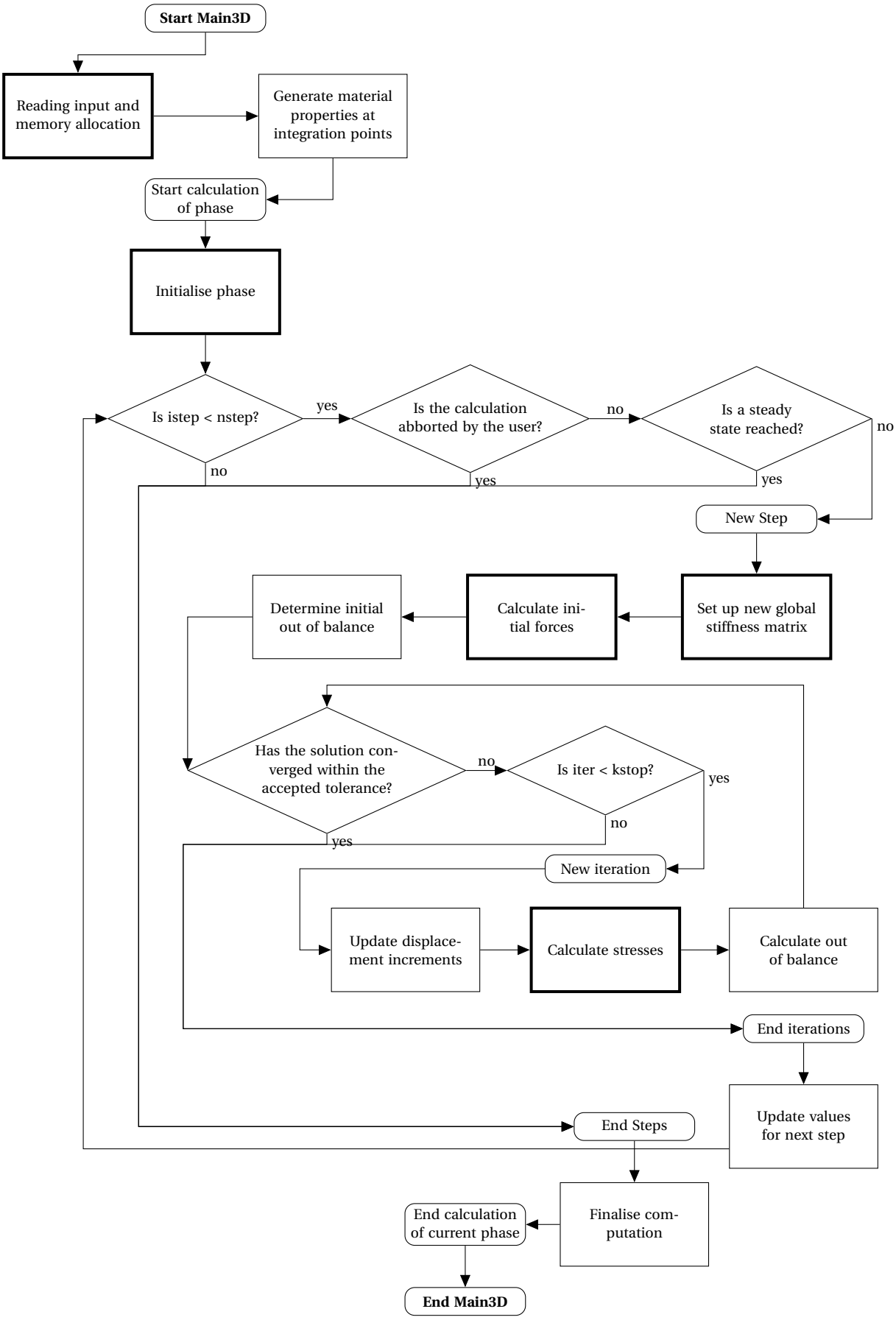

Figure B.1: Flow Chart of main program of PLAXIS 3D

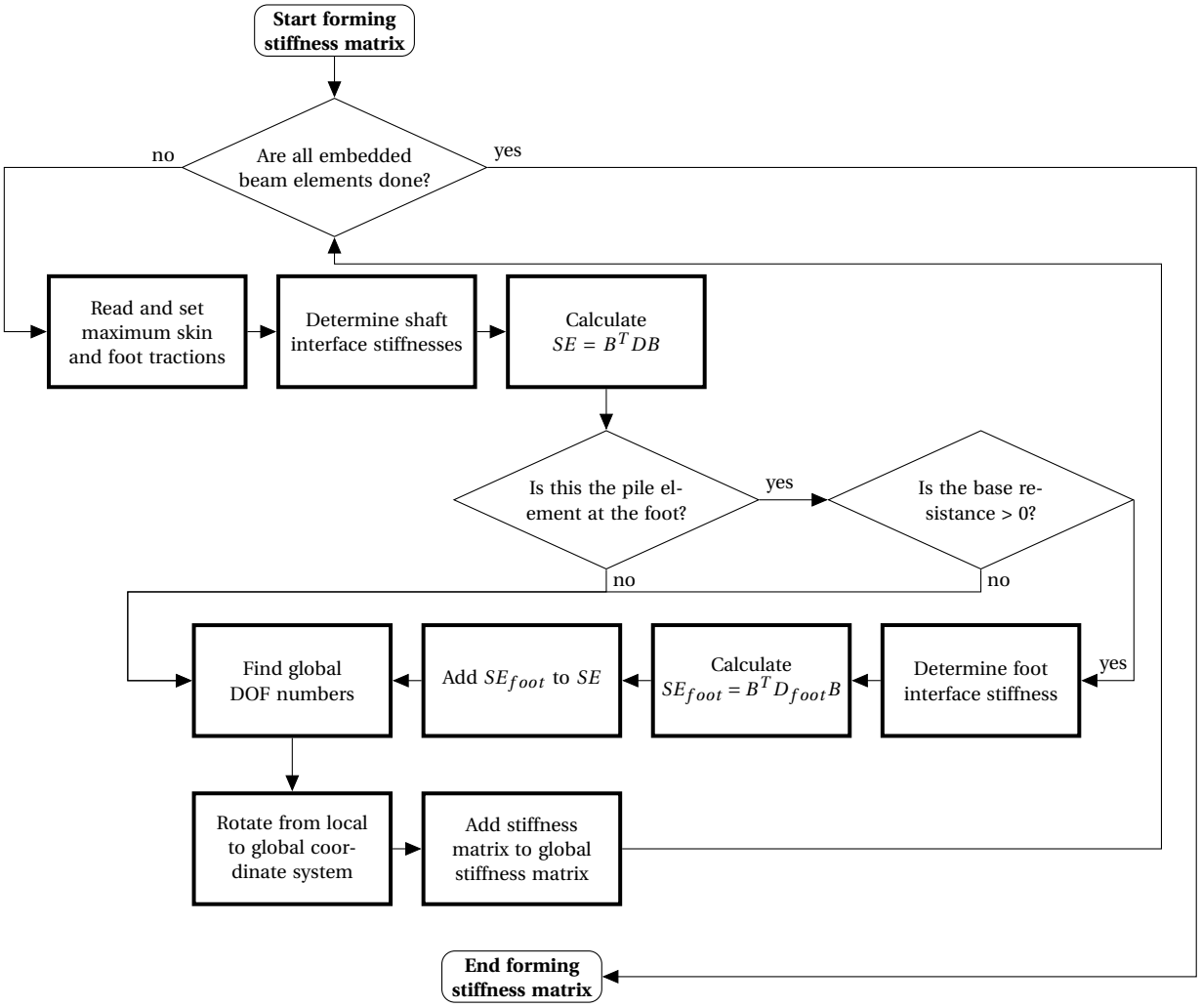

Figure B.2: Flow Chart of the procedure to calculate and assemble the interface stiffness matrix

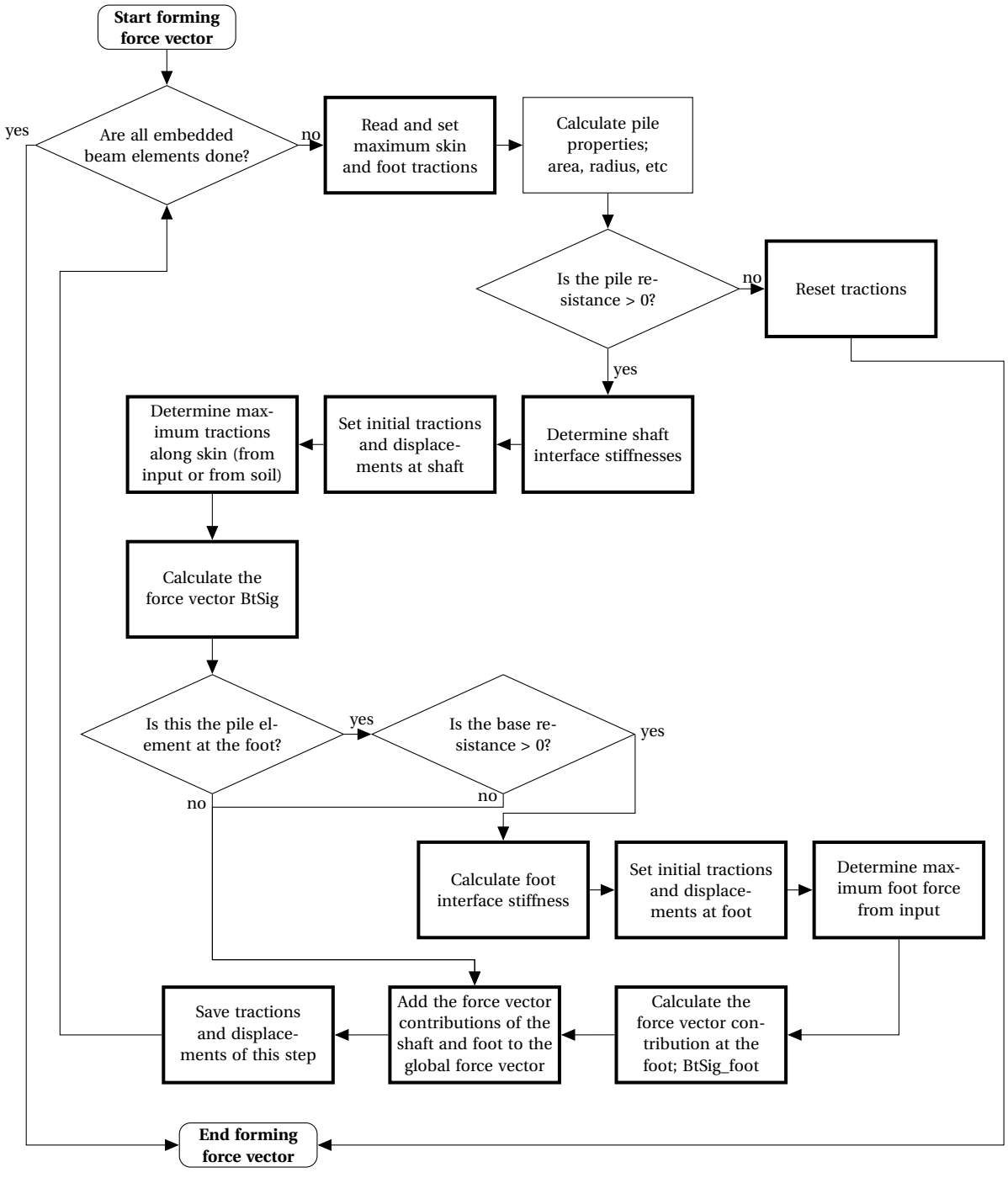

Figure B.3: Flow Chart of the procedure to calculate and assemble the force vector

B.2. Numerical implementation of the embedded beam element

The numerical implementation of the existing embedded beam element in PLAXIS 3D is described in more detail in this section.

The displacements of the beam and soil can be discretised, expressing them in terms of the nodal beam and soil displacements:

$$\begin{aligned}
\boldsymbol{u^b} = \boldsymbol{N^b}\ \boldsymbol{a^b} &= \begin{bmatrix} N_1^b & 0 & 0 & \cdots & N_3^b & 0 & 0 \\ 0 & N_1^b & 0 & \cdots & 0 & N_3^b & 0 \\ 0 & 0 & N_1^b & \cdots & 0 & 0 & N_3^b \end{bmatrix} \begin{bmatrix} a_{1x}^b \\ a_{1y}^b \\ a_{1z}^b \\ \vdots \\ a_{3x}^b \\ a_{3y}^b \\ a_{3z}^b \end{bmatrix} \\
\boldsymbol{u^s} = \boldsymbol{N^s}\ \boldsymbol{a^s} &= \begin{bmatrix} N_1^s & 0 & 0 & \cdots & N_{10}^s & 0 & 0 \\ 0 & N_1^s & 0 & \cdots & 0 & N_{10}^s & 0 \\ 0 & 0 & N_1^s & \cdots & 0 & 0 & N_{10}^s \end{bmatrix} \begin{bmatrix} a_{1x}^s \\ a_{1y}^s \\ a_{1z}^s \\ \vdots \\ a_{10x}^s \\ a_{10y}^s \\ a_{10z}^s \end{bmatrix}
\end{aligned} \tag{B.1}$$

Equation (3.1) can now be rewritten such that:

$$\boldsymbol{u_{rel}} = \boldsymbol{N^b}\ \boldsymbol{a^b} - \boldsymbol{N^s}\ \boldsymbol{a^s} = \underbrace{\begin{bmatrix} \boldsymbol{N^b} & -\boldsymbol{N^s} \end{bmatrix}_{(3x39)}}_{\boldsymbol{B}} \underbrace{\begin{bmatrix} \boldsymbol{a^b} \\ \boldsymbol{a^s} \end{bmatrix}_{(39x1)}}_{\boldsymbol{a^e}} \tag{B.2}$$

The shape functions N_i^s are the interpolation functions of an 10-noded tetrahedral element and the shape functions N_i^b are the interpolation functions for a 3-noded line element, given by:

$$\begin{aligned}
N_1^b &= -\frac{1}{2}(1-\xi)\,\xi \\
N_2^b &= (1+\xi)(1-\xi) \\
N_3^b &= \frac{1}{2}(1+\xi)\,\xi
\end{aligned} \tag{B.3}$$

and

$$\begin{aligned}
N_1^s &= (1-\xi-\eta-\zeta)(1-2\xi-2\eta-2\zeta) & N_6^s &= 4\xi\zeta \\
N_2^s &= \zeta(2\zeta-1) & N_7^s &= 4\xi(1-\xi-\eta-\zeta) \\
N_3^s &= \xi(2\xi-1) & N_8^s &= 4\eta(1-\xi-\eta-\zeta) \\
N_4^s &= \eta(2\eta-1) & N_9^s &= 4\eta\zeta \\
N_5^s &= 4\zeta(1-\xi-\eta-\zeta) & N_{10}^s &= 4\xi\eta
\end{aligned} \tag{B.4}$$

Both are expressed in terms of the iso-parametric coordinates (ξ,η,ζ). The local numbering of the nodes of a tetrahedral element and the locations of the integration points are shown in Figure B.4. To determine the coordinates of the integration points along the beam in terms of local soil coordinates, it is necessary to find the global coordinates of the integration points first.

The constitutive relation is given by Equation (B.11), where the matrix containing the interface stiffnesses is called $\boldsymbol{D^e}$. The local interface stiffness matrix can be derived, using the principle of virtual work (Equation (5.25):

$$\int_s \delta\,(\boldsymbol{u_{rel}})^T \cdot \boldsymbol{t}\ ds = \delta\boldsymbol{a^e}^T \underbrace{\int_s \boldsymbol{B}^T \boldsymbol{D^e} \boldsymbol{B}\ ds}_{\boldsymbol{K_{local}^e}} \cdot \boldsymbol{a^e} \tag{B.5}$$

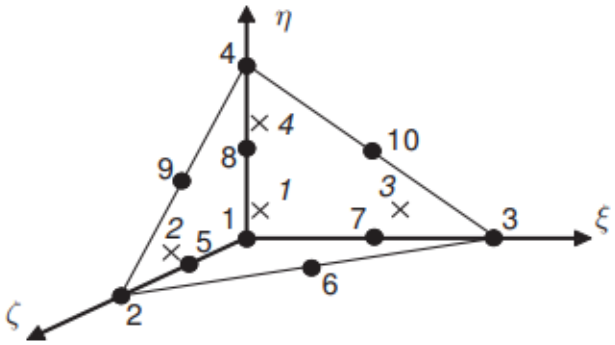

Figure B.4: Local numbering and positioning of nodes and integration points of a tetrahedral element, (Brinkgreve et al., 2015)

As the shape functions are functions of the iso-parametric coordinates (ξ, η, ζ), it is more convenient to calculate the local interface stiffness matrix in the iso-parametric coordinate system. To be able to do this, the change of variables theorem can be applied:

$$\boldsymbol{K}^{\boldsymbol{e}}_{\boldsymbol{local}} = \int_{-1}^{1} \boldsymbol{B}^T \boldsymbol{D}^{\boldsymbol{e}} \boldsymbol{B} \frac{ds}{d\xi}\, d\xi \tag{B.6}$$

In order to be able to assemble all element stiffness matrices into a total global stiffness matrix, it is necessary to transform the local element displacements to the global coordinate system. This is done using the following expression:

$$\boldsymbol{u}^{\boldsymbol{local}}_{\boldsymbol{rel}} = \boldsymbol{T} \cdot \boldsymbol{u}^{\boldsymbol{global}}_{\boldsymbol{rel}} \tag{B.7}$$

where $\boldsymbol{T}$ is a transformation matrix describing the transformation from the global x,y,z-coordinate system to the local beam ξ,η,ζ-coordinate system. The first row of $\boldsymbol{T}$ is given by a unit vector parallel to the beam axis ($\boldsymbol{V_1}$). Subsequently, the second and third row of $\boldsymbol{T}$ are computed by taking cross products of $\boldsymbol{V_1}$ and a random vector (= $\boldsymbol{V_3}$) and $\boldsymbol{V_1}$ and $\boldsymbol{V_3}$ (= $\boldsymbol{V_2}$). The global element stiffness matrix is computed by:

$$\boldsymbol{K}^{\boldsymbol{e}}_{\boldsymbol{global}} = \boldsymbol{T}^{\boldsymbol{T}} \boldsymbol{K}^{\boldsymbol{e}}_{\boldsymbol{local}} \boldsymbol{T} \tag{B.8}$$

B.2.1. Numerical integration

The integral is solved numerically using Newton-Cotes integration, given by:

$$\int_{-1}^{1} F(\xi)\, d\xi \approx \sum_{i=1}^{n} F(\xi_i)\, w_i \tag{B.9}$$

	ξ_i	w_i
2 nodes	± 1	1
3 nodes	± 1, 0	1/3, 4/3

Table B.1: Newton-Cotes integration

The use of Newton-Cotes integration means that the integration points are at the same location as the nodes, resulting in the fact that the shape functions at these points have either a value of one or zero.

B.2.2. Assembly of the total stiffness matrix

Finally, the global stiffness matrix for the entire problem has to be assembled. This total global stiffness matrix contains the contributions of all the solid, beam and interface elements. The contributions of the interface elements to the total global stiffness matrix couples the behaviour of the solid and beam elements, otherwise they would be uncoupled and behave completely independent from each other.

The solid elements have 10-nodes, each 3 DOFs, so the stiffness matrix of a solid element is a (30×30) matrix. The beam elements have 3 nodes, each with 6 DOFs, so the stiffness matrix is a (18×18) matrix. The stiffness matrix of an interface element is a (39×39) matrix, taking into account the solid and beam translational DOFs, excluding the beam rotational DOFs.

B.2.3. Iterative method

The development of the skin traction is implemented as an incremental process, using an iteration scheme. The skin traction is updated with an increment:

$$\boldsymbol{t} = \boldsymbol{t_0} + \Delta \boldsymbol{t} \tag{B.10}$$

Here $\boldsymbol{t_0}$ is the initial stress, which is obtained from the previous load step. The constitutive relation between the traction increment and the relative displacement increment is:

$$\Delta \boldsymbol{t} = \boldsymbol{D^e}\ \Delta \boldsymbol{u_{rel}} \tag{B.11}$$

Similar to Equation (B.2) $\Delta \boldsymbol{u_{rel}}$ can be expressed as $\Delta \boldsymbol{u_{rel}} = \boldsymbol{B}\Delta \boldsymbol{a^e}$. Combining Equations (B.10) and (B.11) and using the principle of virtual work, the following can be derived:

$$\begin{aligned}\int_S \delta\left(\boldsymbol{u_{rel}}\right)^T \boldsymbol{t}^t\ dS + \int_S \delta\left(\boldsymbol{u_{rel}}\right)^T \boldsymbol{D^e} \Delta \boldsymbol{u_{rel}}\ dS \\ \Longrightarrow \delta\left(\boldsymbol{a^e}\right)^T \underbrace{\int_S \boldsymbol{B}^T \boldsymbol{t}^t dS}_{\boldsymbol{f_{in}^{local,t}}} + \delta\left(\boldsymbol{a^e}\right)^T \underbrace{\int_S \boldsymbol{B}^T \boldsymbol{D^e} \boldsymbol{B}\ dS}_{\boldsymbol{K^e_{local}}} \cdot \Delta \boldsymbol{a^e}\end{aligned} \tag{B.12}$$

The local interface element stiffness matrix and local internal force vector can be transformed to the global coordinate system. Subsequently, they can be assembled into a total global stiffness matrix.

The total global equilibrium equation that has to be solved, is given by:

$$\boldsymbol{K}\Delta \boldsymbol{a} = \boldsymbol{f_{ex}^{t+\Delta t}} - \boldsymbol{f_{in}^t} \tag{B.13}$$

where $\boldsymbol{f_{ex}^{t+\Delta t}}$ is the external force vector that is applied at the current step and $\boldsymbol{f_{in}^t}$ is the internal reaction force vector that is obtained from the previous step.

In a full Newton-Raphson iteration method the stiffness matrix $\boldsymbol{K}$ is updated in every iteration, for the modified Newton-Raphson method the stiffness matrix is updated at the beginning of each load step and the calculation method based on the elastic stiffness matrix only calculated the stiffness matrix at the beginning of the calculation process.

The calculation process based on the elastic stiffness matrix is as follows (Brinkgreve et al., 2015):

Read input data	
Form stiffness matrix	$\boldsymbol{K}$
New step	i → i+1
Form new load vector	$\boldsymbol{f_{ex}^{i+1}} = \boldsymbol{f_{ex}^i} + \Delta \boldsymbol{f_{ex}}$
Form reaction force vector	$\boldsymbol{f_{in}^i}$
Calculate unbalance	$\Delta \boldsymbol{f} = \boldsymbol{f_{ex}^{i+1}} - \boldsymbol{f_{in}^i}$
Reset displacement increment	$\Delta \boldsymbol{a} = 0$
New iteration	j → j+1
Solve displacements	$\delta \boldsymbol{a} = \boldsymbol{K}^{-1} \Delta \boldsymbol{f}$
Update displacement increments	$\Delta \boldsymbol{a^{j+1}} = \Delta \boldsymbol{a^j} + \delta \boldsymbol{a}$
Calculate tractions	$\boldsymbol{t^{i,j+1}}$
Form reaction force vector	$\boldsymbol{f_{in}^{i,j+1}}$
Calculate unbalance	$\Delta \boldsymbol{f} = \boldsymbol{f_{ex}^{i+1}} - \boldsymbol{f_{in}^{i,j+1}}$
Calculate error	$e = \frac{\lvert \Delta \boldsymbol{f} \rvert}{\lvert \boldsymbol{f_{ex}^{i+1}} \rvert}$
Accuracy check	if $e >$ tolerance → new iteration
Update displacements	$\boldsymbol{a^{i+1}} = \boldsymbol{a^i} + \Delta \boldsymbol{a^{j+1}}$
Write output data (results)	
If not finished → new step	
Finish	

B.3. Prescribed loads vs. displacements

In PLAXIS a load or displacement can be prescribed to work on a point or surface. Contrary to expectations, they do not result in the same load-displacement curve in case of an embedded beam model.

Figure B.5 shows the beam and soil displacements at the top and bottom of the pile of the laterally loaded disc model with prescribed displacements. In this model a simplified soil is used, for which the parameters are given in Table C.3 in Appendix C.2. This simplified soil model excludes any stress dependencies that might influence the soil and interface stiffness. In addition, the interface capacity is set to zero, so the beam should behave as if connected to nothing. However, this is not what happens which suggests that the beam is connected to the soil in another way as well. When the soil and beam displacements at the top and bottom of the pile are compared they appear to be perfectly equal. In Figure B.5 this is shown by the fact that all the curves fall exactly on top of each other.

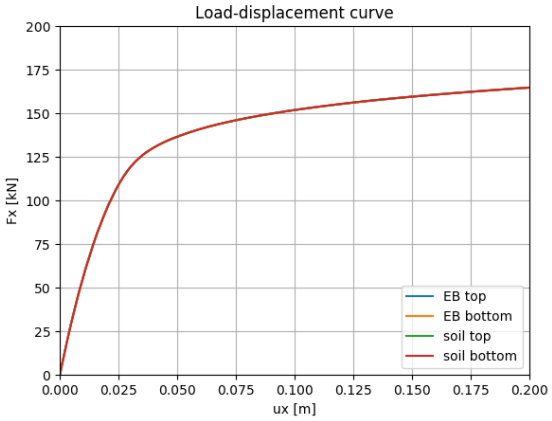

Figure B.5: Laterally loaded disc model with prescribed displacement and simplified soil, zero interface capacity

This result suggests that the top and bottom node of the embedded beam are connected to the soil nodes that are located at the same location. To verify this, a closer look is taken at what happens at these points. When a prescribed displacement is set on a node, the prescribed displacement is assigned to the soil node at that location. In order to transfer this prescribed displacement to embedded beam, the displacement is **copied** to the beam node. Both the soil node and the beam node now experience the same prescribed displacement, effectively making them rigidly connected.

It is possible to circumvent this by using a prescribed load or letting the embedded beam protrude from the soil. When a load is used, PLAXIS still puts this load on the soil node. During the calculation this load is now **moved** to the beam node at the same location, not copied. This way, the soil is not loaded any more and the beam and soil node are not connected.

C

Model input parameters

C.1. Alzey Bridge model

The soil and embedded beam properties are shown in Tables C.1 and C.2. The Hardening soil model shall be used in the report. The Mohr-Coulomb soil model is only used in Appendix E.

	Symbol	Mohr-Coulomb	Hardening soil	Unit
Drainage type	-	Drained	Drained	-
Unit weight	$\gamma_{unsat}/\gamma_{sat}$	20	20	kN/m^3
Young's modulus	E	33 185	-	kN/m^2
Secant stiffness	E_{50}^{ref}	-	4.5e4	kN/m^2
Oedometer stiffness	E_{oed}^{ref}	-	2.715e4	kN/m^2
Unloading-reloading stiffness	E_{ur}^{ref}	-	9.0e4	kN/m^2
Poisson's ratio	ν	0.3	0.2	-
Cohesion	c	20	20	kN/m^2
Friction angle	φ	20	20	°
Dilatancy angle	ψ	0	0	°
Stress dependency power	m	-	1	-
$K_{0,NC}$	-	-	0.658	
POP	-	-	50	kN/m^2
Tension cut-off	-	selected	selected	-

Table C.1: Soil parameters for Alzey Bridge pile load test models

Parameter	Symbol	Embedded beam	Unit
Unit weight	γ	5	[kN/m^3]
Young's modulus	E	$1 \cdot 10^7$	[kN/m^2]
Diameter	-	1.3	[m]
Axial skin resistance	$T_{skin,max}$	201.37	[kN/m]
Base resistance	F_{max}	1320	[kN]

Table C.2: Embedded beam parameters for Alzey Bridge pile load test models

The axial skin resistance is constant along the length of the beam in case of a linear traction model. However, the layer-dependent traction model shall be used often as well.

C.2. Laterally loaded disc model

The soil and embedded beam properties are shown in Tables C.3 and C.4. The simplified Mohr-Coulomb soil model is only used in Appendix F.1.

Parameter	Symbol	Mohr-Coulomb	Simplified Mohr-Coulomb	Unit
Drainage type	-	Drained	Drained	-
Unit weight above phreatic level	γ_{unsat}	0	0	[kN/m^3]
Unit weight below phreatic level	γ_{sat}	0	0	[kN/m^3]
Young's modulus	E	$1 \cdot 10^4$	$1 \cdot 10^4$	[kN/m^2]
Poisson's ratio	ν'	0.3	0.3	-
Cohesion	c'	10	$10 + 1 \cdot z$	[kN/m^2]
Friction angle	φ'	10	0	[°]
Dilatancy angle	ψ	0	0	[°]
Tension cut-off	-	Deselected	Selected	-
Strength reduction factor	R_{inter}	Varying	Varying	-

Table C.3: Soil parameters for laterally loaded disc models

Parameter	Symbol	Embedded beam	Unit
Unit weight	γ	0	[kN/m^3]
Young's modulus	E	$3 \cdot 10^7$	[kN/m^2]
Diameter	-	0.7	[m]
Axial skin resistance	$T_{bot,max}, T_{top,max}$	layer-dependent	[kN/m]
Base resistance	F_{max}	0	[kN]

Table C.4: Embedded beam parameters for laterally loaded disc models

D

New embedded beam formulation

D.1. Rectangular cross-section

The three-dimensional curved beam element as is described in Bathe (2014) is based on a rectangular cross-section. Therefore, this theory can easily be applied for an embedded beam element with a rectangular cross-section. Figure D.1 shows the topview for this type of cross-section with relevant parameters.

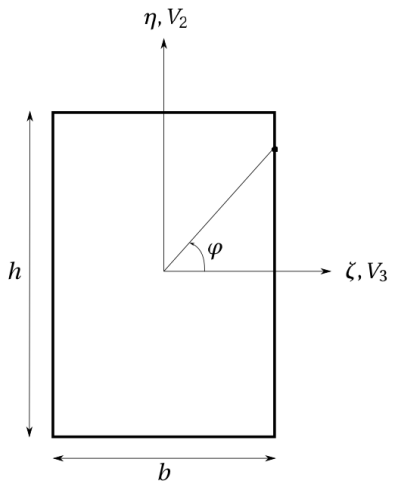

Figure D.1: Topview rectangular cross-section

According to the formulation in Bathe (2014), the Cartesian coordinates of a point in the element for a 3-noded three-dimensional beam element are given by:

$$\boldsymbol{X^0} = \boldsymbol{X_m^0} + \boldsymbol{X_p^0} \tag{D.1}$$

This equation is very closely related to Equation (5.2) in Section 5.2.1. The vector $\boldsymbol{X_m^0}$ is the same and $\boldsymbol{X_p^0}$ and $\boldsymbol{X_r^0}$ map the coordinate from the beam axis to the interaction surface. However, this mapping is different for a rectangular cross-section shape than for a circular cross-sectoin. The superscript 0 indicates the undeformed state. $\boldsymbol{X_p}$ is given by:

$$\boldsymbol{X_p} = \frac{\eta}{2} \cdot h \cdot \boldsymbol{V_2} + \frac{\zeta}{2} \cdot b \cdot \boldsymbol{V_3} \tag{D.2}$$

Here, h and b are the height and width of the cross-section, $\boldsymbol{V_2}$ and $\boldsymbol{V_3}$ denote unit vectors in the η and ζ directions. η and ζ can only vary from -1 to 1.

The beam displacements can be found by:

$$\boldsymbol{u^b} = \boldsymbol{X^1} - \boldsymbol{X^0} = \left(\boldsymbol{X_m^1} - \boldsymbol{X_m^0}\right) + \frac{\eta}{2} \cdot h \cdot \left(\boldsymbol{V_2^1} - \boldsymbol{V_2^0}\right) + \frac{\zeta}{2} \cdot b \cdot \left(\boldsymbol{V_3^1} - \boldsymbol{V_3^0}\right) \tag{D.3}$$

The relation $\boldsymbol{V_3^1} - \boldsymbol{V_3^0} = \boldsymbol{\theta} \times \boldsymbol{V_3^0}$ can be used again, as well as the equivalent dot product $\boldsymbol{W_3} \cdot \boldsymbol{\theta}$, to obtain:

$$\boldsymbol{u^b} = \boldsymbol{u_m} + \frac{\eta}{2} \cdot h \cdot (\boldsymbol{W_2} \cdot \boldsymbol{\theta}) + \frac{\zeta}{2} \cdot b \cdot (\boldsymbol{W_3} \cdot \boldsymbol{\theta}) \tag{D.4}$$

The beam displacements can be discretised, using $\boldsymbol{u^b} = \boldsymbol{N^b u_b^e}$ and $\boldsymbol{\theta} = \boldsymbol{N^b \theta^e}$:

$$\begin{aligned}
\begin{bmatrix} u^b \\ v^b \\ w^b \end{bmatrix} = &\begin{bmatrix} N_1^b & 0 & 0 & \cdots & N_3^b & 0 & 0 \\ 0 & N_1^b & 0 & \cdots & 0 & N_3^b & 0 \\ 0 & 0 & N_1^b & \cdots & 0 & 0 & N_3^b \end{bmatrix} \begin{bmatrix} u_{1x}^b \\ \vdots \\ u_{3z}^b \end{bmatrix} \\
&+ \frac{\eta}{2} \cdot h \cdot \begin{bmatrix} 0 & V_{2z}^0 & -V_{2y}^0 \\ -V_{2z}^0 & 0 & V_{2x}^0 \\ V_{2y}^0 & -V_{2x}^0 & 0 \end{bmatrix} \begin{bmatrix} N_1^b & 0 & 0 & \cdots & N_3^b & 0 & 0 \\ 0 & N_1^b & 0 & \cdots & 0 & N_3^b & 0 \\ 0 & 0 & N_1^b & \cdots & 0 & 0 & N_3^b \end{bmatrix} \begin{bmatrix} \theta_{1x} \\ \vdots \\ \theta_{3z} \end{bmatrix} \\
&+ \frac{\zeta}{2} \cdot b \cdot \begin{bmatrix} 0 & V_{3z}^0 & -V_{3y}^0 \\ -V_{3z}^0 & 0 & V_{3x}^0 \\ V_{3y}^0 & -V_{3x}^0 & 0 \end{bmatrix} \begin{bmatrix} N_1^b & 0 & 0 & \cdots & N_3^b & 0 & 0 \\ 0 & N_1^b & 0 & \cdots & 0 & N_3^b & 0 \\ 0 & 0 & N_1^b & \cdots & 0 & 0 & N_3^b \end{bmatrix} \begin{bmatrix} \theta_{1x} \\ \vdots \\ \theta_{3z} \end{bmatrix}
\end{aligned} \tag{D.5}$$

In order to write the discretisation in the form $\boldsymbol{u^b} = \boldsymbol{H} \cdot \boldsymbol{a^b}$, the matrix $\boldsymbol{H}$ is defined as:

$$\begin{aligned}
\boldsymbol{H} = &\begin{bmatrix} N_1^b & 0 & 0 & \cdots & N_3^b & 0 & 0 & \\ 0 & N_1^b & 0 & \cdots & 0 & N_3^b & 0 & \cdots \\ 0 & 0 & N_1^b & \cdots & 0 & 0 & N_3^b & \end{bmatrix} \\
&\begin{bmatrix} 0 & G(1,z) & -G(1,y) & \cdots & 0 & G(3,z) & -G(3,y) \\ -G(1,z) & 0 & G(1,x) & \cdots & -G(3,z) & 0 & G(3,x) \\ G(1,y) & -G(1,x) & 0 & \cdots & G(3,y) & -G(3,x) & 0 \end{bmatrix}_{(3\times 18)}
\end{aligned} \tag{D.6}$$

with

$$G(\alpha,\beta) = \frac{1}{2} N_\alpha^b \left(\eta \cdot h \cdot V_{2\beta}^0 + \zeta \cdot b \cdot V_{3\beta}^0 \right) \tag{D.7}$$

In this expression $\boldsymbol{a^b}$ contains both the local translational and rotational nodal displacement of an embedded beam element.

For a square cross-section ($h = b$), the values of η and ζ can be expressed as functions of φ.

$$\eta, \zeta = \begin{cases} \eta = \tan\varphi,\ \zeta = 1 & \text{for } 0 \le \varphi < \varphi_1 \\ \eta = 1,\ \zeta = \tan\left(90 - \varphi\right) & \text{for } \varphi_1 \le \varphi < 90 \\ \eta = 1,\ \zeta = -\tan\left(\varphi - 90\right) & \text{for } 90 \le \varphi < (180 - \varphi_1) \\ \eta = \tan\left(180 - \varphi\right),\ \zeta = -1 & \text{for } (180 - \varphi_1) \le \varphi < 180 \\ \eta = -\tan\left(\varphi - 180\right),\ \zeta = -1 & \text{for } 180 \le \varphi < (180 + \varphi_1) \\ \eta = -1,\ \zeta = -\tan\left(270 - \varphi\right) & \text{for } (180 + \varphi_1) \le \varphi < 270 \\ \eta = -1,\ \zeta = \tan\left(\varphi - 270\right) & \text{for } 270 \le \varphi < (360 - \varphi_1) \\ \eta = -\tan\left(360 - \varphi\right),\ \zeta = 1 & \text{for } (360 - \varphi_1) \le \varphi < 360 \end{cases} \tag{D.8}$$

with

$$\varphi_1 = \arctan\left(\frac{h}{b}\right) \tag{D.9}$$

For the circular cross-section the orientation of the η and ζ axes is not important, as long as they are orthogonal to each other and the beam axis. This is because the behaviour in any direction is the same. However, this is different in case of a rectangular cross-section shape. So, in order to implement this formulation for rectangular cross-section shapes this should be taken into account. Moreover, the implementation is very straightforward. However, due to the failure to model a lateral interface correctly, implementation of the extension to a rectangular cross-section shape is omitted.

D.2. Return mapping scheme

For standard interface elements a return mapping algorithm is applied to correct the stresses in case of plasticity. This algorithm updates the stresses differently than the simple method that is used for the virtual interface elements in the existing embedded beam model. Even when both stress update methods return the stresses to the same yield surface.

The simple method returns the stress point first to the boundary defined by FF1 and subsequently checks whether the tension cut-off criterion is met (Figure D.2a). The return mapping algorithm (Figure D.2b) first determines in which region (1, 2 or 3) the trial stress point is located. Whether or not a stress state is located in one of these regions can be checked by the following criteria:

- **1**: FF1 > 0 and HF4 < 0
- **2**: HF4 ≥ 0 and HF3 ≥ 0
- **3**: FF2 > 0 and HF3 < 0

When a stress state in region 1 is found, the stress state is returned to the FF1 boundary with a certain angle. This angle is defined by HF4. When a stress state in region 2 is found, the stress state is returned to the corner point and when a stress state in region 3 is found, the stress state is horizontally returned to the FF2 boundary.

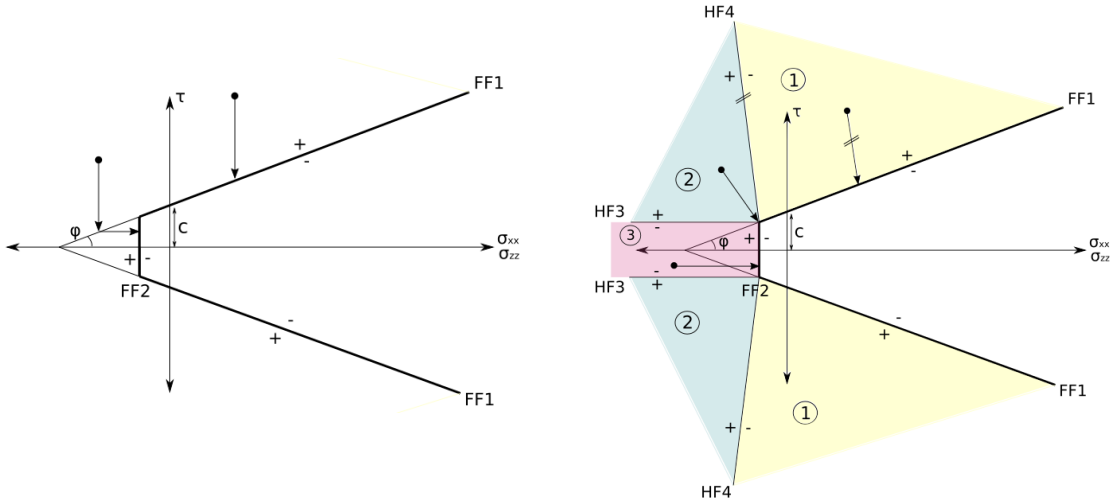

(a) Simple stress update

(b) Return mapping

Figure D.2: Stress update methods for a Mohr-Coulomb stress envelope with a tension cut-off criterion

D.3. Comparison with Turello et al. method

In Section 3.2 the method, proposed in Turello et al. (2016a) and Turello et al. (2016b), to model an embedded beam element with explicit interaction surface is explained, including the possibility of an elasto-plastic interface. Although, the idea for this research originates from their three-dimensional embedded beam element with explicit interaction surface, the methods are not entirely the same. This section will explain the differences between the two methods.

The first difference can be found in the mapping functions that are defined in both methods. For a vertically oriented pile the mapping functions are similar. Turello et al. (2016b) mention that the generalisation of the mapping functions is not a straightforward task, but this problem has been solved in the mapping functions that are defined in this report. Where the mapping functions presented in Turello et al. (2016a) are only applicable for vertical oriented piles, the mapping functions presented in Section 5.2.1 can be applied to beams with any arbitrary orientation.

Another thing that is worth mentioning, is that the mapping functions in the Turello et al. (2016a) paper are based on the hypothesis that the beam cross-section remains planar, undeformed and perpendicular to the beam axis. The rotations that are used in the mapping functions in this report take into account shear deformations (Section 5.1).

The second difference is in the interpolation matrix. In the Turello et al. (2016b) paper they use 2-noded beam elements and quadrilateral soil elements, which require different interpolation functions than the 3-noded beam elements and tetrahedral soil elements that are used in PLAXIS 3D. Turello et al. (2016a) use a combination of cubic Hermite polynomial interpolation functions and standard linear interpolation functions and their interpolation matrix is a square matrix. PLAXIS 3D uses Lagrangian shape functions. Comparing their expression for $\boldsymbol{N_u}$ and the $\boldsymbol{N^b}$ matrix in this report, shows that they are very different.

The Turello et al. (2016a,b) formulation the interaction surface is only defined around the shaft of the pile. No interaction surface at the foot of the pile is considered.

In the Turello et al. (2016a) paper, the only coupling between the beam and soil is present in the contribution of the interaction forces, $\boldsymbol{q^{int}}$, in the right hand side vector. When the elasto-plastic interface in Turello et al. (2016b) is proposed, they apply rather complex methods to describe the constitutive behaviour in the interface. In the method proposed in this report, a simple interface stiffness contribution is added to the global stiffness matrix. And three methods to correct for plasticity are proposed.

The validation that is presented in Turello et al. (2016b) doesn't consider an ultimate limit state failure. Therefore, it is not possible to verify whether or not their method is able to capture the same failure load as, for example, the volume pile method with an interface. In addition, the interface strength is not adjustable by one parameter, such as R_{inter}, to distinguish between rough and smooth pile surfaces.

Interface based on beam kinematics

The interface based on beam kinematics presented in Turello et al. (2016b) evaluates the beam and soil displacements at the interactions surface, integrates everything over the whole interaction surface and then maps it back to the beam axis.

Subsequently, in Turello et al. (2016b) they define a π-axis which is aligned with the resultant lateral displacement jump. When this direction is known, they are able to compute Δv_π and t_π at the beam axis. Subsequently, they define a constitutive model in which t_π is limited. This implies a limit for the integral over all stress components in the π-direction along the interaction surface . At some points at the interaction surface, the stress component in this direction is a shear stress, on other points at the interaction surface this is a normal stress.

In the methods to include a correction for lateral plasticity proposed in this report, only a limit is defined for the shear stresses in every point at the interaction surface. The normal stresses in every point on the interaction surface are unlimited, making an integral over all stress components in any direction along the interaction surface unlimited as well. However, the correct behaviour of the soil is supposed to be taken into account through the coupling of the interface with the surrounding soil. When the pressure in the soil in a certain direction increases, it will find a failure surface in another direction depending on the internal friction angle.

Interface based on solid kinematics

This method considers the displacement jump at the explicit interaction surface and not on the beam axis. The interface based on solid kinematics defines a second local coordinate system in order to define the normal and tangential components of the displacement jump, similar as in the method proposed in this report.

The difference comes in at the point that in Turello et al. (2016b) a fictional thickness h_i is defined. The displacement jump develops between the interaction surface and the fictitious surface at an offset of h_i. The domain between these two surfaces is modelled using a full 3D elasto-plastic constitutive law. Two different 3D laws are proposed: a Modified Cam Clay law and a J2 plasticity model to be applied in the narrow domain around the pile.

In the embedded beam formulation proposed in this report, the displacement jump develops between the beam and soil displacements at the same interaction surface. No fictional thickness is introduced. The soil around the pile should already be able to take plasticity into account (except of course when the linear elastic soil model is used), therefore a separate soil model to model a ring around the pile is not necessary.

Furthermore, the methods seem to work similar. When plasticity in the interface is reached, the stresses in the interface are limited. This means that in the right hand side vector of the equilibrium equations the coupling through $\boldsymbol{q^{int}}$ is limited, making a plastic displacement jump possible.

E

Validation details axially loaded models

E.1. Performance soil displacement methods without base resistance

The results of the Alzey Bridge pile load test without base resistance of the new embedded beam formulation with the two approximation methods to obtain the soil displacements at the interaction surface are shown in Figure E.1. Method A (Figure E.1a) shows an even higher mesh sensitivity than the existing embedded beam formulation.

Comparing method B (Figure E.1b) to the existing embedded beam formulation (Figure 6.3a) shows us that not much has changed with the application of the new formulation. Still, mesh sensitivity is present and the failure load is over predicted, especially for fine meshes. The mesh sensitivity is even slightly increased. The behaviour shows the same unreliability for fine meshes and the convergence behaviour is very bad.

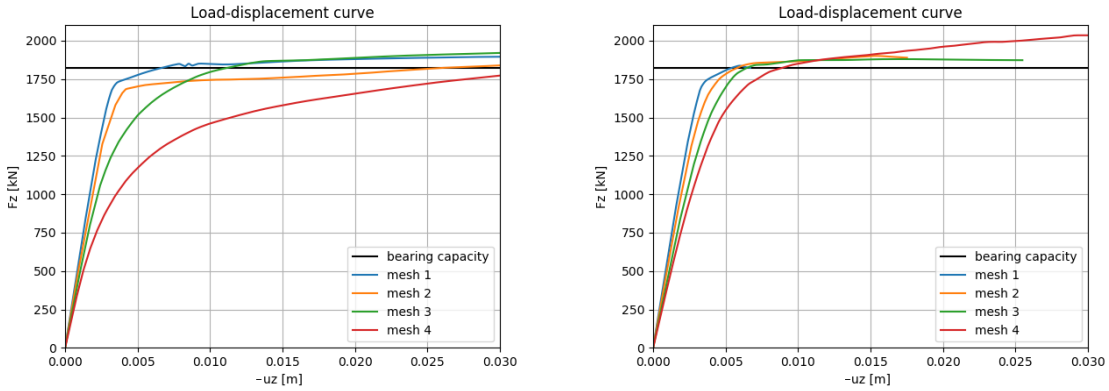

(a) Method A

(b) Method B

Figure E.1: Alzey Bridge pile load test modelled with the new embedded beam model without base resistance

Figure E.1 provides additional substantiation that the two approximation methods (A & B) to obtain the soil displacements at the interaction surface do not yield good results; no improvement in terms of mesh sensitivity is obtained compared to the existing embedded beam formulation.

E.2. Investigation of reduced foot stiffness

The stiffness of the model can be manipulated by adjusting the foot interface stiffness. This section presents load-displacement curves that are obtained with the Alzey Bridge pile load test modelled with the embedded beam elements. Several model dimensions and soil parameters are varied in order to evaluate their influence on the required foot stiffness reduction. The foot stiffness currently depends on the pile radius and the shear modulus of the soil. When variation of a certain parameter results in a different required foot stiffness, this suggests that this parameter is not taken into account appropriately in the definition of the foot stiffness. For all the results in this section the linear traction model and mesh size 2 are used.

First, Table E.1 shows the required foot stiffness reduction factors for different mesh sizes. This table can easily be compared to Table 6.6 in which the same is done for the layer-dependent traction model. Clearly, the linear traction model results in slightly smaller required foot stiffness reduction factors. The new embedded beam formulation still is slightly mesh sensitive, requiring different reduction factors for different mesh sizes to match the calculation results to the measurement data. The reduction factors are iteratively obtained, as is shown in Figure E.2 for mesh size 2. A reduction factor of 0.065 for mesh size 2 results in exactly the same displacements at failure as the measurement data.

Mesh size	Foot stiffness reduction factor
1	0.06
2	0.065
3	0.075
4	0.11
average	0.0775

Table E.1: Foot stiffness reduction factors for model with linear traction model

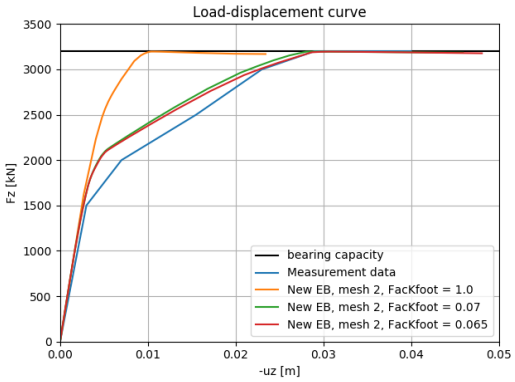

Figure E.2: New embedded beam with improved foot interface for different values of Γ_{foot}

First, the influence of the Young's Modulus (E) and Poisson's ratio (ν) on the foot stiffness reduction factor in a Hardening Soil model is investigated (Figure E.3).

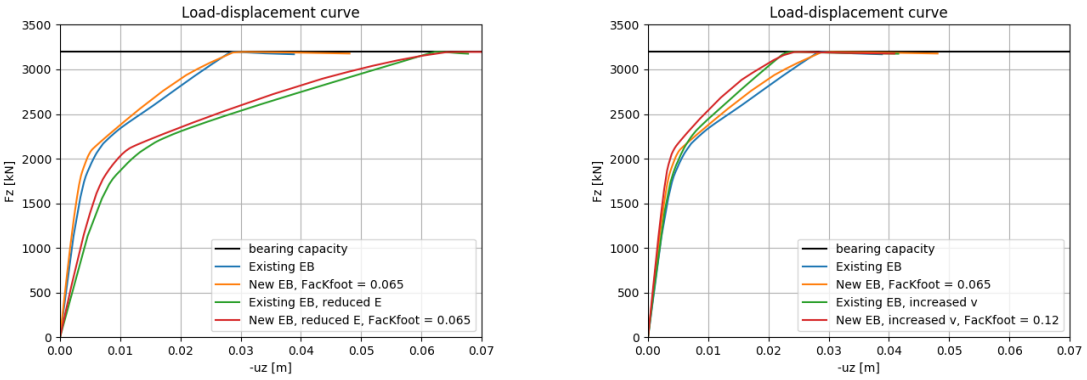

(a) Influence of Young's modulus

(b) Influence of Poisson's ratio

Figure E.3: Influence of E and ν on foot stiffness, Hardening Soil model

For a certain foot stiffness reduction factor (0.065) and mesh size the new formulation matches the existing embedded beam formulation. When the Young's Modulus is reduced (44% of E_{50}^{ref}, E_{oed}^{ref}, E_{ur}^{ref} in Table C.1), the same mesh and reduction factor still yield matching results for the new and existing embedded beam formulation. This suggests that the Young's Modulus has no influence on the required foot stiffness reduction factor.

When the Poisson's ratio is increased a different foot stiffness reduction factor is required to match the existing and embedded beam models. An increase from 0.2 to 0.4 of ν yields an increase in reduction factor from 0.065 to 0.12, which is significant. This suggests that the Poisson's ratio is not taken into account correctly in the definition of the foot stiffness.

Next, the influence of the radius of the embedded beam is evaluated in Figure E.4. Whereas a foot stiffness reduction factor of 0.065 was required in Figure E.3a (Radius = 0.65 m) to match the displacements at failure of the new and existing embedded beam formulation, a foot stiffness reduction factor of 0.13 is required

when the radius is reduced to 0.35 m. This leads to the conclusion that the radius of the pile is not taken into account correctly in the definition of the foot stiffness. In addition, Figure E.4 shows that when the resistance of the pile is reduced (linear traction model) this doesn't influence the required foot stiffness reduction factor.

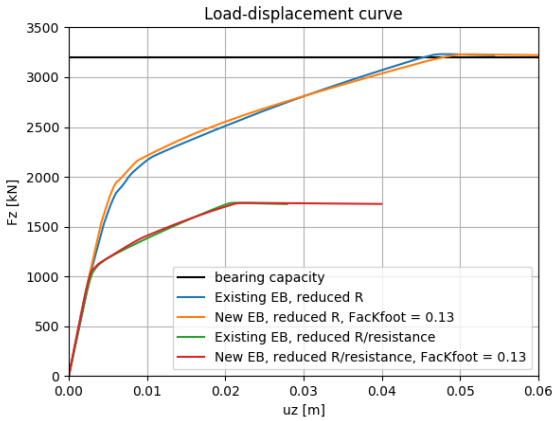

Figure E.4: Influence of pile radius on foot stiffness, Hardening Soil model

Subsequently, the influence of the Young's Modulus (E) and Poisson's ratio (ν) are investigated for a Mohr-Coulomb soil model (Figure E.5). The use of a different soil model makes it possible to evaluate the influence of the soil model. Comparing Figure E.3a to Figure E.5 shows that the Mohr-Coulomb soil model requires a higher foot stiffness reduction factor (0.09) than the Hardening Soil model (0.065).

The same conclusion can be drawn with respect to the influence of the Young's Modulus as for the Hardening Soil model; a change in Young's Modulus doesn't result in a different foot stiffness reduction factor to match the existing and new embedded beam models. Figure E.5a shows that when the Young's Modulus is increased from 33 185 to 50 000 kN/m^2 still the same foot stiffness reduction factor can be used.

The influence of the Poisson's ratio is evaluated in Figure E.5b. The results in Figure E.5 clearly show that a reduction factor of 0.09 matches the new embedded beam formulation to the existing one. However, when the Poisson's ratio in Figure E.5b is increased from 0.2 to 0.4, a reduction factor of 0.11 is required to match the new formulation to the existing one. Apparently, the Poisson's ratio has an influence on the required foot stiffness reduction factor, which suggests that this parameter is not taken into account appropriately in the definition of the foot stiffness.

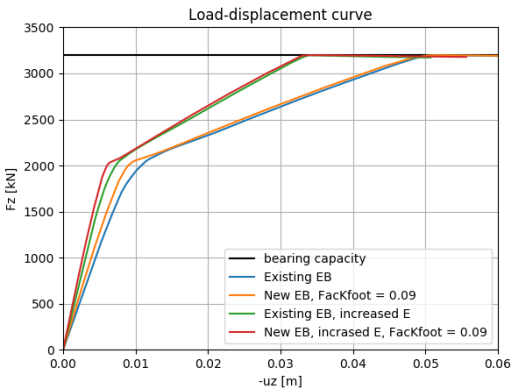

(a) Mohr-Coulomb soil model, influence of Young's modulus

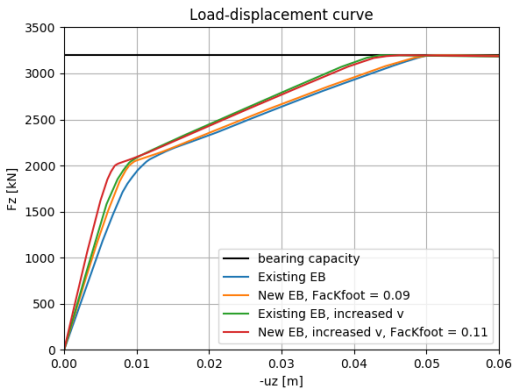

(b) Mohr-Coulomb soil model, influence of Poisson's ratio

Figure E.5: Influence of soil model, Young's Modulus and Poisson's ratio on foot stiffness

E.3. Skin traction mobilisation

This section contains additional results of the skin traction mobilisation in order to analyse the behaviour in more detail.

E.3.1. Mesh sensitivity

Several proposals were done to solve the mesh sensitivity in the existing embedded beam formulation, such as increasing the stiffness of the soil inside the pile region or reducing the shaft interface stiffness. The current implementation of the embedded beam element in PLAXIS 3D still shows a highly mesh sensitive response in the skin traction evolution along the pile (Figure E.6a). For a fine mesh extreme peaks near the top and foot of the pile occur and the overall skin traction profile is not smooth. The skin traction evolution of mesh size 2 shows much smaller peaks near the top and foot and the behaviour is significantly smoother (Figure 6.15a).

However, Figure E.6b shows that the new embedded beam formulation doesn't show a high mesh sensitivity in the skin traction evolution. The skin traction profiles computed with mesh size 4 show almost exactly the same behaviour as the results presented in Figure 6.15b with mesh size 2. The last two load steps show a fluctuating profile near the foot of the pile for mesh size 4. This is not entirely unexpected, since the foot resistance still introduces localised high stresses. For finer meshes, this can cause more extreme localised behaviour.

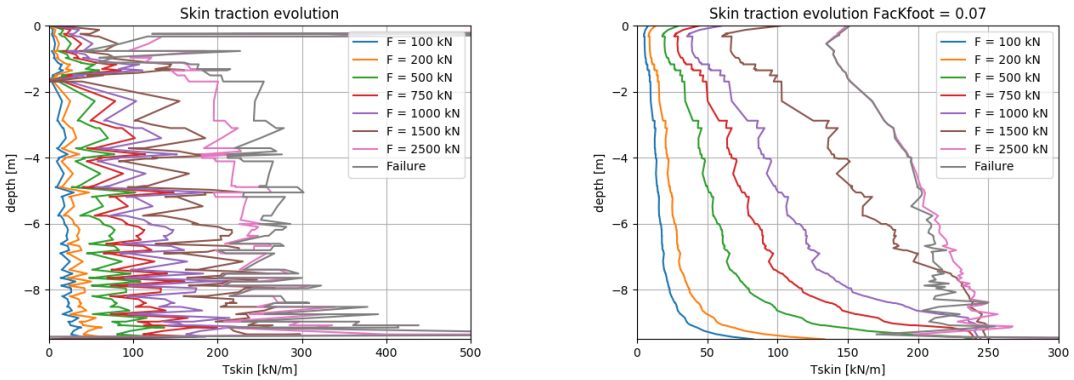

(a) Existing embedded beam

(b) New embedded beam

Figure E.6: Skin traction evolution with mesh size 4

E.3.2. Hardening soil vs. Mohr-Coulomb

The Hardening soil model that is used in the model takes stress-dependency of stiffness into account, both in the soil and in the interface. Tschuchnigg (2012) concluded that the skin friction mobilisation is mainly related to the interface stiffness and not to the soil stiffness. Also, he concluded that a stress-dependent interface stiffness is required.

Figure E.7 shows the skin traction evolution of the Alzey Bridge test case with a Mohr-Coulomb soil model. In contradiction with the results presented in Tschuchnigg (2012) and expectations, the skin traction mobilisations do show an inclination from low load levels on.

Figure E.8 shows linear fitted curves to the skin traction profiles for both the existing and new embedded beam formulation for the two different soil models. The fits do show that the Hardening soil model results in a skin traction profile with a larger inclination. In addition, the new embedded beam formulation seems to result in a slightly larger inclination for both Hardening soil and Mohr-Coulomb models compared to the existing embedded beam formulation.

A cause for the inclined skin traction profile can be in the use of the layer-dependent traction model. However, in Appendix E.3 the results for the linear traction model are shown, displaying the same behaviour for the linear traction model.

A quick check has confirmed that for the Mohr-Coulomb soil model the interface stiffness indeed is constant along the pile length. Therefore, the only cause for the inclined skin traction profiles can be caused by growing relative displacements along the pile. Figure E.9 shows the relative displacements along the length of the pile for both Mohr-Coulomb and Hardening soil models.

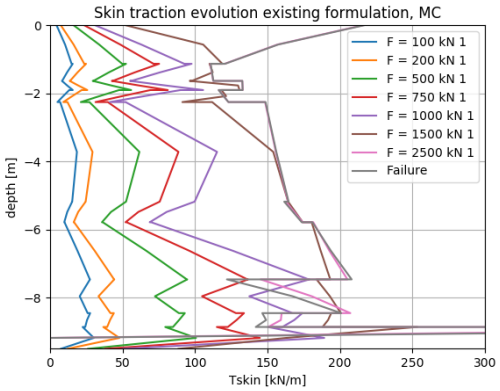

(a) Existing embedded beam

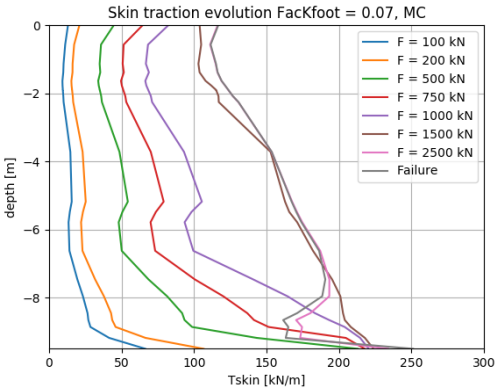

(b) New embedded beam

Figure E.7: Skin traction evolution for Mohr-Coulomb soil model

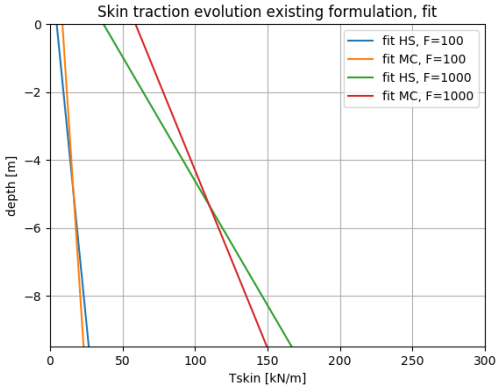

(a) Existing formulation

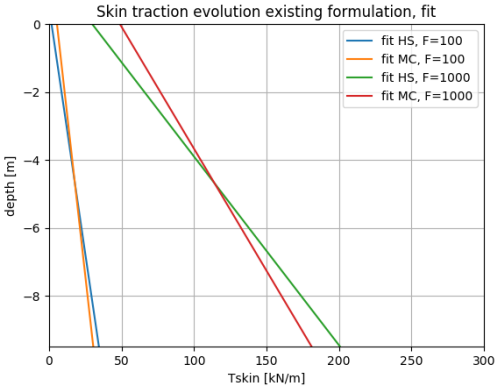

(b) New formulation

Figure E.8: Linear fitted curves of the skin traction profiles

For a Mohr-Coulomb soil model the relative displacements grow more with depth than for the Hardening soil model, this is more visible when looking at the existing embedded beam formulation.

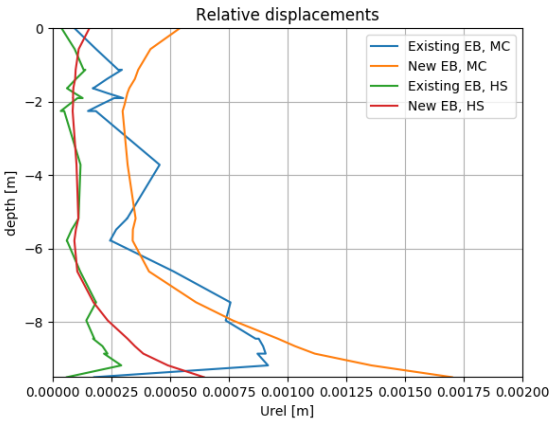

Figure E.9: Relative displacements along the beam at F = 1500 kN

In previous research the relative displacements along the length of the pile showed a constant profile for a Mohr-Coulomb soil. However, the results that are presented in the reports of the older research are outdated.

The results presented in Tschuchnigg (2012), for example, are obtained using PLAXIS 3D Foundation. Since then, many changes have been made to the PLAXIS 3D kernel. Therefore, it is not possible to determine what causes the difference in results.

Nonetheless, the analysis of the new results still lead to the conclusion that the skin traction profile that is obtained using the Hardening soil model is better than for the Mohr-Coulomb soil model. The Hardening soil model still finds a larger inclination in the skin traction profile, which is desired.

E.3.3. Linear traction model

Figure E.10 shows the skin traction evolution for the Alzey Bridge test case for both the existing and new formulation. Mesh 2 is evaluated, because the foot interface stiffness was set to match those results best, making these results best comparable. Only the axial component of the skin tractions are shown and the linear traction model is used. A Mohr-Coulomb soil model is used with a Young's Modulus of 33185 kN/m^2.

Similar as in the results for the layer-dependent traction model, Figure E.10a doesn't show a very smooth skin traction profile. The skin traction profile of the existing formulation is clearly very mesh sensitive.

The skin traction evolution in the existing formulation clearly starts developing from bottom to top; first the skin tractions at the lower halve of the pile increase and then the skin tractions at the top. At the foot of the pile the existing formulation finds an unrealistic low value of the skin traction, which is even zero at failure.

The new formulation shows the the bottom to top evolution less clearly. It is still a little visible, but the behaviour is less outspoken. Instead of unrealistically low values near the foot of the pile, the new formulation finds unrealistically large values. Tschuchnigg (2012) found that when the foot interface stiffness is increased, smaller tractions at the base of the pile are found. This is in agreement with the results that are shown in Figure E.10, since in the new formulation the foot interface stiffness is reduced and the reversed effect is found. This influence of the foot interface stiffness can easily be explained. A higher foot interface stiffness limits the relative displacements at the foot, resulting in lower interface stresses.

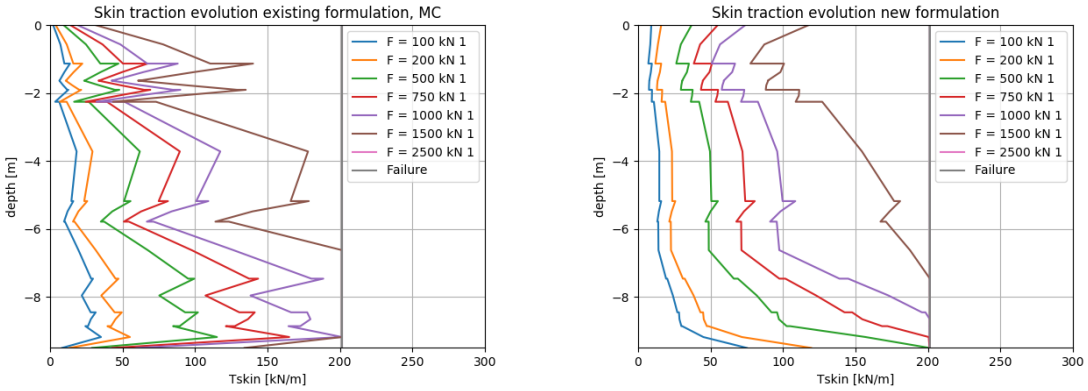

(a) Existing formulation

(b) New formulation

Figure E.10: Skin traction evolution for linear traction model

E.3.4. Influence foot formulation and stiffness

The question arises whether the foot interface stiffness or new foot interface influences the skin traction mobilisation at the foot. Figure E.11a shows that when the foot interface stiffness is reduced in the existing embedded beam formulation, the low skin traction values at the lower load levels increase, but that at failure the skin traction at the foot still goes to zero. In addition, Figure E.11b shows that using the old foot (resistance working only at beam axis) in the new embedded beam formulation doesn't result in unrealistic low skin traction values near the foot. This suggests that the problem is not caused by the way that the foot interface is implemented or a too high foot stiffness. The values of the normal stresses in the soil at the interaction surface are more accurate than the value of the normal stress at the beam axis, resulting in a more realistic skin traction profile near the foot of the pile.

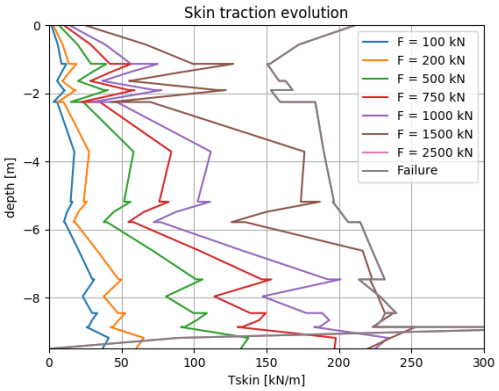

(a) Existing embedded beam with $\Gamma_{foot} = 0.01$

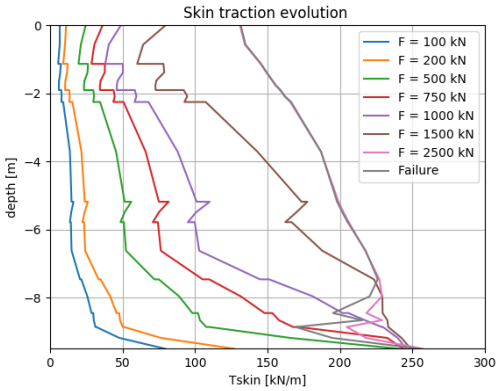

(b) New embedded beam with the old foot

Figure E.11: Skin traction evolution of embedded beam models with old foot

E.3.5. Influence of the shaft interface stiffness

Furthermore, varying the normal and shear stiffnesses along the shaft of the pile is expected to have an influence on the skin traction evolution. Figure E.12 consists of two figures that present the influence of a reduced shaft interface stiffness. The layer-dependent traction model is now used.

Reducing the interface stiffness along the shaft of the pile mainly results in the fact that the skin tractions evolve slower along the whole length of the pile, this is visible in both Figure E.12a and E.12b. The way that the foot force develops is not influenced that much. The slope in the elastic phase of the total load-displacement curve is reduced a lot, making this curve not in very good agreement with the measurement data any more.

The reduced shaft interface stiffness results in the fact that the skin traction evolution curve deviates from the total load displacement curve. This happens in the measurement data in Figure 4.6a as well. Nevertheless, the results for a reduced shaft interface stiffness deviate too much from the measurement data and therefore it is concluded that the original shaft interface stiffnesses are preserved.

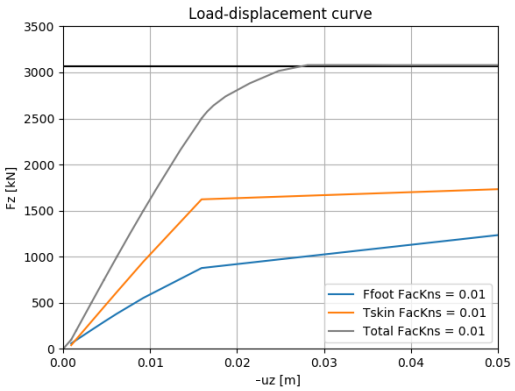

(a) Foot force and skin traction mobilisation for reduced shaft interface stiffness

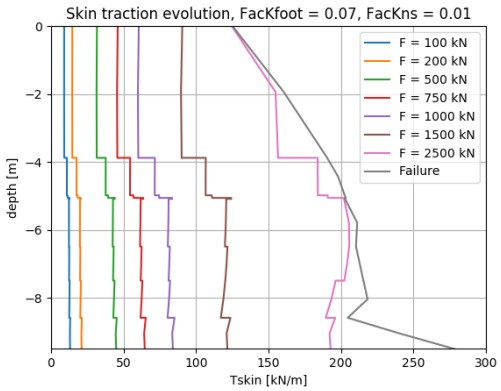

(b) Skin traction evolution for reduced shaft interface stiffness

Figure E.12: Influence of reduced interface stiffness along the shaft on skin traction and foot force evolution

In the existing formulation, the normal and tangential direction at the pile circumference couldn't be distinguished. Therefore, the normal and tangential stiffness were equal. In the new embedded beam formulation the normal and tangential direction are known, making it possible to set the tangential stiffness equal to the shear stiffness (equal to K_s), and the normal stiffness normal to the normal stiffness.

The influence of this change in tangential interface stiffness is studied and the relevant figures are shown in Figure E.13. Looking at the load-displacement curves in Figure E.13a the influence of this change is imperceptible.

When the skin traction evolution is studied in more detail in Figure E.13b, it is evident that the bottom to top evolution is a little bit more pronounced in case of $K_t = K_n$ than for $K_t = K_n$ (Figure 6.15b). The difference is only visible near the head of the pile.

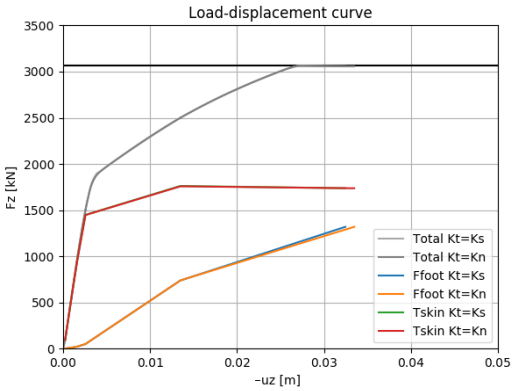

(a) Foot force and skin traction mobilisation for $K_t = K_n$

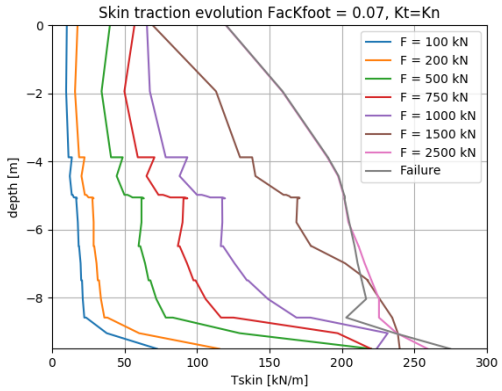

(b) Skin traction evolution for $K_t = K_n$

Figure E.13: Influence of change of tangential interface stiffness on foot force and skin traction mobilisation

F

Validation details laterally loaded models

F.1. Investigation of lateral plasticity

This section explains the steps that are taken to investigate the lateral interface behaviour. This investigation is performed in order to explain why the proposed lateral plasticity method is not able to capture the desired interface behaviour.

F.1.1. Simplified soil model

During the investigation of this problem a simplified soil model is used in the laterally loaded disc model. This way, the number of parameters that influence the results is reduced. A model in which the stress dependency is excluded is used, by using a Mohr-Coulomb soil with a zero friction angle (Table C.3). The cohesion is 10 kN/m^2 at the top and 11 kN/m^2 at the bottom of the model. Figure F.1 shows the results of the laterally loaded disc model with this simplified soil.

The volume pile model is modelled with and without an interface, which clearly gives very different results. The new EB formulation again seems to be close to the VP without interface results in terms of failure load. When the mesh is refined in the volume pile model, the failure load decreases as is expected. The mesh sensitivity of the embedded beam model is smaller.

When no lateral plasticity is applied in the embedded beam model (Figure F.1b) the obtained behaviour is very similar to the behaviour when method 1 is applied. This suggests that plasticity in lateral direction is not taken into account correctly with method 1.

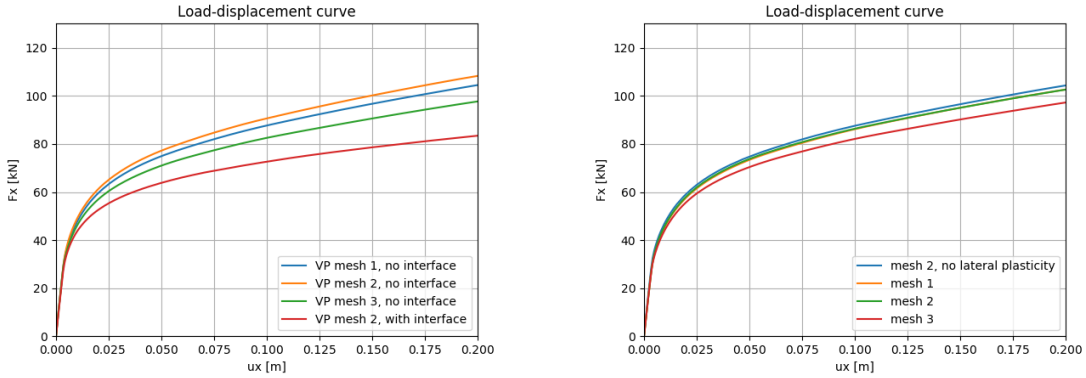

(a) Volume pile method

(b) Method 1

Figure F.1: Laterally loaded disc model with manipulated mesh and simplified soil model

All results together suggest that the failure that is found in the embedded beam model is soil failure. Plasticity in the interface in lateral direction doesn't have any influence on the failure load.

F.1.2. Interface capacity

In the first calculation shown in Figure F.2 the interface capacity was set to zero, in order to check if indeed the beam and soil are disconnected in this case. Clearly, this holds true, as the embedded beam moves without force and the calculation fails almost immediately. The embedded beam finds no resistance in horizontal direction as no force can be transferred from the pile to the soil.

In the next calculations the interface is set to only have shear capacity. The normal stresses in the interface are set to zero, both compressive and tensile stresses. As there is no other force transfer between the pile and soil any more, the reduction of R_{inter} does have the desired effect on the results now.

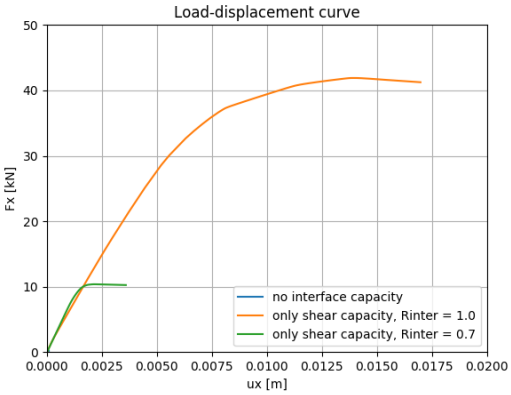

Figure F.2: Laterally loaded disc model with simplified soil, influence of the interface capacity

F.1.3. Influence normal stresses

When the normal stress capacity is unlimited in the interface and only the shear capacity is limited, the response of the new embedded beam model with lateral plasticity method 1 is almost exactly the same as when no lateral plasticity is taken into account at all (Figure F.1). Apparantly, the normal stress capacity in the interface takes over the reduced shear capacity in lateral direction.

This leads to the suspicion that the final failure of the model is not caused by the interface, but is happening somewhere else. That the interface doesn't fail, can only be caused by the unlimited normal stresses in the interface.

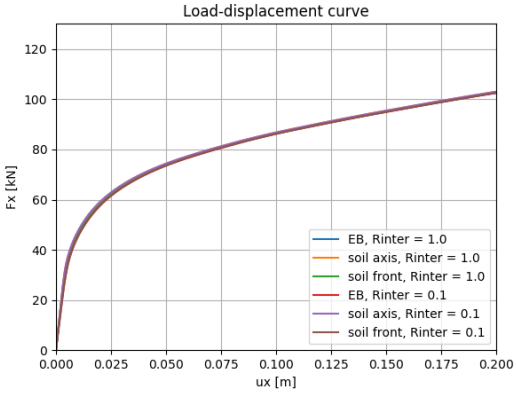

Figure F.3: Laterally loaded disc model with simplified soil model, lateral plasticity method 1

The suspicion that the normal stresses take over is confirmed when a closer look is taken at the total sums of the stresses in the interface. Table F.1 shows the total stresses in the interface at the last step in the calculation for different values of R_{inter}. The differences clearly show that the reduction in horizontal shear are compensated by an increase in normal stresses. Thus, the normal stresses in the interface indeed seem to take over the interface capacity.

	Sum σ_t	Sum σ_n
$R_{inter} = 1.0$	920.027	-5159.626
$R_{inter} = 0.1$	88.017	-5904.097
Difference	832.01	744.471

Table F.1: Evaluation of total stresses in the interface at the last step in the calculation

F.1.4. Limit for the normal stresses

The previous section shows that the normal stresses take over the interface capacity when the shear capacity in lateral direction is limited. This results in the fact that no lower failure load is found than when no lateral plasticity occurs.

The idea is now to set a limit for the normal stresses in the interface, such that the behaviour of the new embedded beam formulation resembles the volume pile method behaviour.

Method I

The first limit for the normal stresses that is tried is the compression that is present in the soill. If the compressive normal stresses in the interface exceed the compressive normal stresses in the soil, the normal stresses in the interface are adjusted to be equal to the normal stresses in the soil. The results of this implementation are shown in Figure F.4b.

Comparing these results to the results of the volume pile method (Figure F.4a) shows that the failure load obtained with the embedded beam model is far lower.

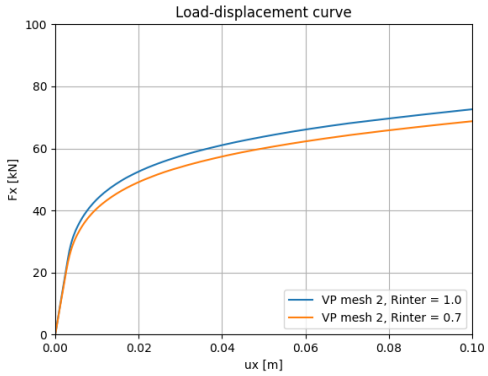

(a) Volume pile method

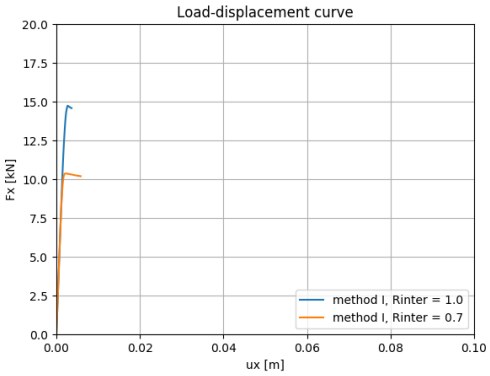

(b) Lateral plasticity method 1 and normal stress limit method I

Figure F.4: Laterally loaded disc model with simplified soil, normal stress limit I

Looking at the occurring failure mechanisms (Figure F.5) shows that they are entirely different. Where the volume pile method is able to capture the desired effect of the soil slipping around the beam, this is not captured with the embedded beam model. Instead of pulling the soil inside the pile radius along, the beam starts moving away from the centre of the pile region. The incorrect failure mechanism is probably the cause for the incorrect failure load.

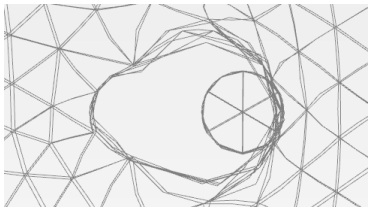

(a) Volume pile method

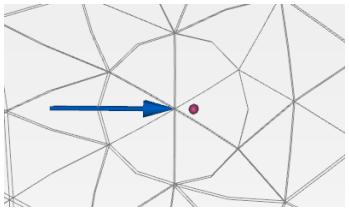

(b) New embedded beam with lateral plasticity method 1 and normal stress limit method I

Figure F.5: Deformed mesh configurations

It is very clear that this implementation of lateral plasticity doesn't result in the desired failure mechanism.

Method II

The second limit that is tried is still based on the stresses in the soil. In this case the vertical stresses in the soil are used, which are converted to maximum horizontal stresses using the following formula from Verruijt (2012):

$$\sigma_1 = K_p \cdot \sigma_3 - 2c\sqrt{K_a} \tag{F.1}$$

Here, σ_1 are the horizontal stresses and σ_3 the vertical stresses in the soil. It must be noted that compression is assumed as positive in this equation. The coefficient of active earth pressure K_p is given by:

$$K_p = \frac{1+\sin\varphi}{1-\sin\varphi} \tag{F.2}$$

The results of this implementation are shown in Figure F.6. The results are slightly better than using the previous method, but the failure load that is found is still too low.

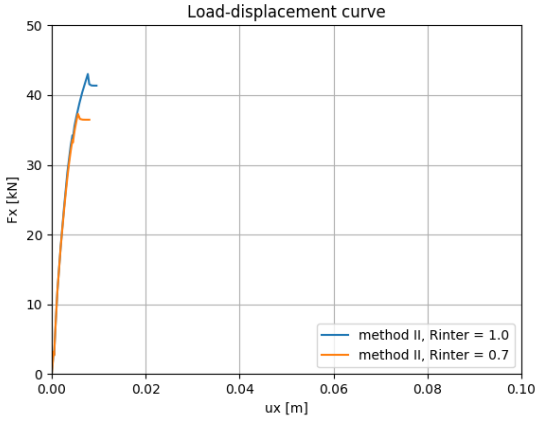

Figure F.6: Laterally loaded disc model with simplified soil, normal stress limit method II

Looking at the deformed mesh (Figure F.7) the same problem can be identified. The beam doesn't pull the elastic zone region along, but moves away. This results in a completely different failure mechanism than is desired.

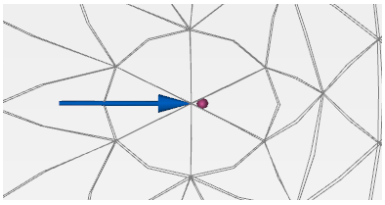

Figure F.7: Deformed mesh configuration of new embedded beam lateral plasticity method 1 and normal stress limit II

Both methods to apply a limit for the compressive normal stresses in the interface don't have the desired effect. Neither resemble the results of the volume pile method. Limiting the normal stresses in the interface using the stresses in the soil is not a solution for the problem. However, this investigation does lead to the cause of the problem; an incorrect failure mechanism is obtained by applying the proposed lateral plasticity method.

G

Case study

G.1. PISA project

Figure G.1 shows that the new 1D parameterised model is in very good agreement with the results of the full 3D finite element model. This holds true for both short and long piles and clay and sand soils. The p-y approach that is used in the current design standards (API/DNV) under-predicts the stiffness and ultimate failure load of the pile in clay significantly. For piles in sand the API/DNV method shows better agreement with the full 3D model than in clay. However, especially for short piles the shape of the curve deviates significantly from the full 3D model curve; a higher initial stiffness is obtained, but a lower failure load. Hence, the new design method is for both soil types an improvement compared to the existing design standards, which results for most cases in smaller necessary dimensions for the monopile foundations.

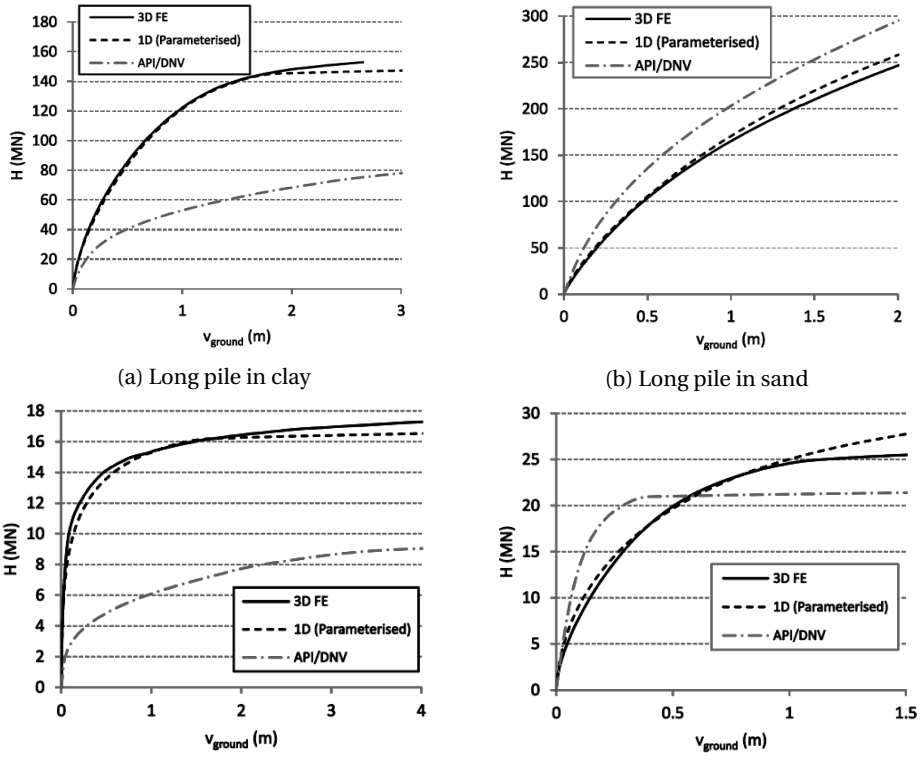

(a) Long pile in clay

(b) Long pile in sand

(c) Short pile in clay

(d) Short pile in sand

Figure G.1: Pile response obtained with different methods. (Byrne et al., 2015)

G.2. PLAXIS MoDeTo

Following the research and results of the PISA project, Plaxis introduced a special Monopile Design Tool (MoDeTo) that is able to capture all the additional soil reaction terms as well. This way it is possible to model monopile foundations with large diameters that are subject to lateral loading accurately. The model is based on a 1D Timoshenko beam and realistic soil reaction curves that are obtained using PLAXIS 3D and measurement data from the field tests.

MoDeTo can be used as a stand-alone tool to apply the proposed PISA design method by the 'rule-base method'; this method is based on previously calibrated soil reaction curves for cases when no detailed constitutive soil behaviour is available. The tool can also be used in combination with PLAXIS 3D to apply the new design method by the 'numerical-based method'; when detailed information about the soil is available, site-specific soil reaction curves can be obtained with PLAXIS 3D and then applied in MoDeTo.

G.3. Model input parameters

	Symbol	Top	Middle	Bottom	Unit
Layer thickness	-	5	25	30	m
Drainage type	-	Undrained(A)	Undrained(A)	Undrained(A)	-
Unit weight	$\gamma_{unsat}/\gamma_{sat}$	21	21	21	kN/m^3
Initial void ratio	e_{init}	0.7570	0.7570	0.7570	-
Secant stiffness	E_{50}^{ref}	$20\cdot10^3$	$20\cdot10^3$	$20\cdot10^3$	kN/m^2
Oedometer stiffness	E_{oed}^{ref}	$15\cdot10^3$	$15\cdot10^3$	$15\cdot10^3$	kN/m^2
Unloading-reloading stiffness	E_{ur}^{ref}	$60\cdot10^3$	$60\cdot10^3$	$60\cdot10^3$	kN/m^2
Poisson's ratio	ν	0.2	0.2	0.2	-
Cohesion	c	80	50	20	kN/m^2
Friction angle	φ	30	30	30	°
Dilatancy angle	ψ	0	0	0	°
Stress dependency power	m	1	1	1	-
	$K_{0,NC}$	0.5	0.5	0.5	-
Threshold shear strain	γ_{07}	$6.5\cdot10^{-3}$	$6.5\cdot10^{-3}$	$6.5\cdot10^{-3}$	-
Small-strain shear stiffness	G_0^{ref}	$90\cdot10^3$	$140\cdot10^3$	$200\cdot10^3$	kN/m^2
Coefficients of permeability	k_x,k_y,k_z	1	1	1	m/day
POP	-	400	200	50	kN/m^2
Tension cut-off	-	selected	selected	selected	-

Table G.1: Soil parameters for the case study. All use HSsmall.

Parameter	Symbol	3D plate	Embedded beam	Unit
Unit weight	γ	78	78	[kN/m^3]
Young's modulus	E	$200\cdot10^6$	$200\cdot10^6$	[kN/m^2]
Poisson's ratio	ν	0.3	-	-
Diameter	-	10	10	[m]
Thickness	d	0.091	0.091	[m]
Axial skin resistance	$T_{skin,max}$	-	Layer-dependent	[kN/m]
Base resistance	F_{max}	-	0	[kN]

Table G.2: Beam parameters for the case study

G.4. Agreement between detailed and simplified model

Figure G.2 shows the results of the detailed model and the simplified model. The mesh of the simplified model is refined in this case, which yields results that are in very good agreement with the detailed model.

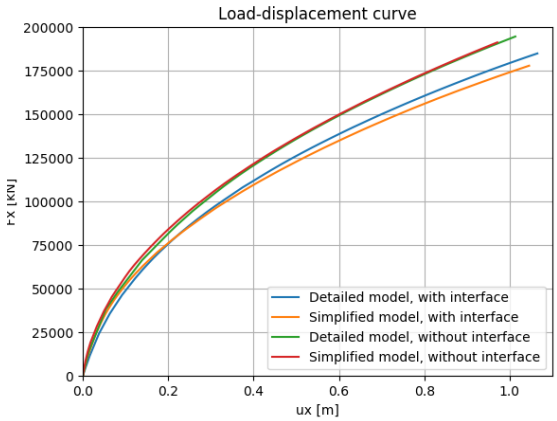

Figure G.2: Results of case study; detailed model and simplified model with refined mesh

G.5. Output results

This section presents additional output results of the case study model.

Deformations of new embedded beam without lateral plasticity

Figure G.3 shows the deformed mesh configuration of the new embedded beam model when the lateral plasticity method is deactivated. Thus, the existing formulation of the correction for plasticity is used; $\sigma_s \leq \left(c - \sigma_{n,soil} \tan\varphi\right) \cdot R_{inter}$. No correction for lateral plasticity takes place. Clearly, the shape of the pile region now remains more exactly circular than when lateral plasticity method 1 is used in the model (Figure 8.5d). Therefore, it is concluded that the shape deformation of the pile region in the new embedded beam model is caused by the use of the lateral plasticity method.

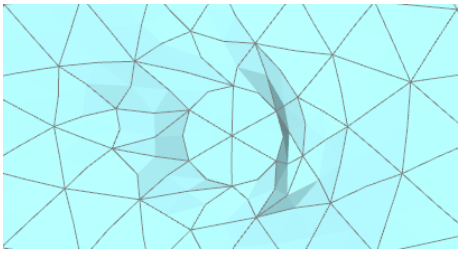

Figure G.3: Deformed mesh of new embedded beam without lateral plasticity method 1

Gap forming between pile and soil

One of the differences between the full 3D model with and without interfaces is the possibility of gap forming at the back of the pile. Only the full 3D model with interfaces is able to capture this behaviour accurately. The influence of the modelling of gap forming is evaluated in this section. The gap forming during loading can be tracked in the full 3D model with interfaces (Figure G.4).

The gap increment at total gap is plotted against the applied force in Figure G.4a. Both curves clearly show that the gap starts forming around a load level of 34 000 kN. This load level is also indicated in Figure G.4b by a horizontal striped grey line. There is not a distinct point where the full 3D model with interfaces starts to deviate from the full 3D model without interfaces, so no conclusion can be drawn on the influence of gap forming in the full 3D model with interfaces. However, it is noteworthy that the total difference in

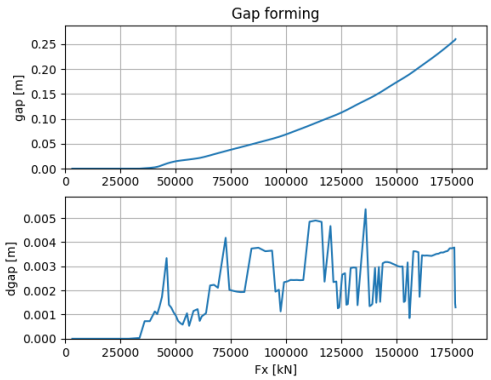

(a) Gap and gap increment vs Fx

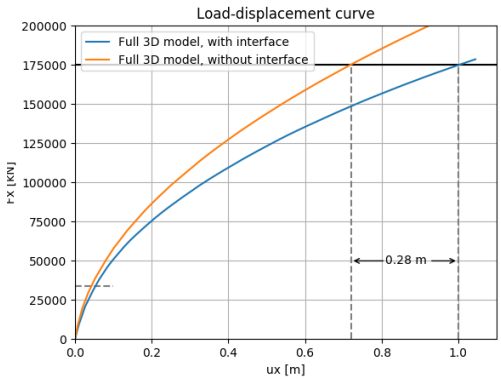

(b) Difference full 3D model with and without interfaces

Figure G.4: Gap forming during loading

displacements between the two models at a load level of 175 000 kN is very close to the size of the total gap that is formed in the full 3D model with interfaces.

Influence strength reduction factor

In case of laterally loaded pile, previous results have shown that R_{inter} doesn't have a large influence on the response of the embedded beam models. This is confirmed by the results shown in Figure G.5. Especially at the head of the pile the influence is negligible. The influence at the base is slightly bigger.

When the interface strength is reduced in the full 3D model, the model fails at a lower load level. This is in agreement with results obtained in Chapter 7.

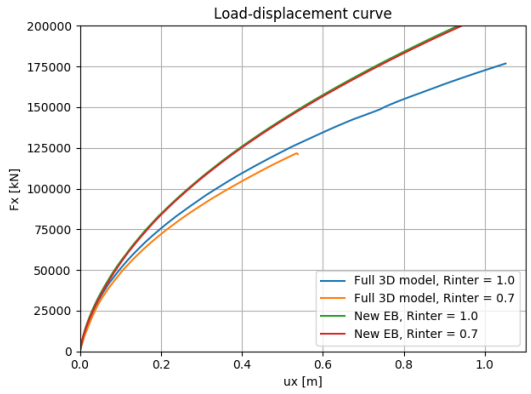

(a) Head of the pile

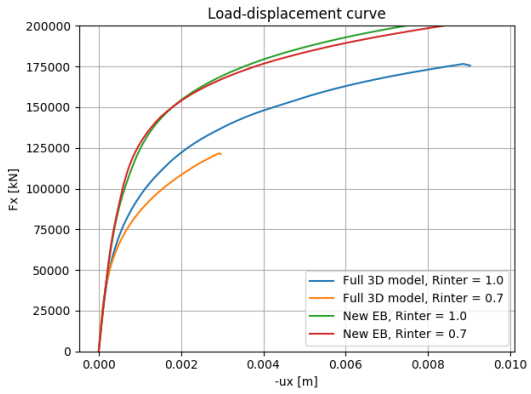

(b) Foot of the pile

Figure G.5: Influence of R_{inter} on case study models